

**CALCULATION OF RELIC DENSITY AND DETECTION
PROSPECTS OF NON-THERMAL DARK MATTER :
A GENERAL STUDY**

By
ARITRA GUPTA
PHYS 08201005002

Harish Chandra Research Institute, Allahabad, India

*A thesis submitted to the
Board of Studies in Physical Sciences
In partial fulfillment of requirements
for the Degree of
DOCTOR OF PHILOSOPHY
of
HOMI BHABHA NATIONAL INSTITUTE*



July, 2017

Homi Bhabha National Institute¹

Recommendations of the Viva Voce Committee

As members of the Viva Voce Committee, we certify that we have read the dissertation prepared by Mr. Aritra Gupta entitled "Calculation of Relic Density and Detection Prospects of Non-Thermal Dark Matter: A General Study" and recommend that it may be accepted as fulfilling the thesis requirement for the award of Degree of Doctor of Philosophy.


Chairman – Prof. Biswarup Mukhopadhyaya
Date: 20.2.18


Guide / Convener – Prof. Raj Gandhi
Date: 20/2/18


Examiner – Prof. Debasish Borah
Date: 20-2-2018


Member 1- Prof. Aresh Krishna Datta
Date: 20-02-2018


Member 2- Prof. Dileep Jatkar
Date: 20-02-2018


Member 3- Prof. Ashoke Sen
Date: 23.02.2018

Final approval and acceptance of this thesis is contingent upon the candidate's submission of the final copies of the thesis to HBNI.

I/We hereby certify that I/we have read this thesis prepared under my/our direction and recommend that it may be accepted as fulfilling the thesis requirement.

Date: February 20, 2018

Place: Allahabad



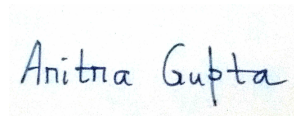
Prof. Raj Gandhi

¹ This page is to be included only for final submission after successful completion of viva voce.

STATEMENT BY AUTHOR

This dissertation has been submitted in partial fulfillment of requirements for an advanced degree at Homi Bhabha National Institute (HBNI) and is deposited in the Library to be made available to borrowers under rules of the HBNI.

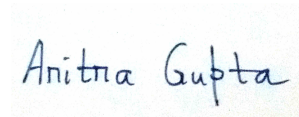
Brief quotations from this dissertation are allowable without special permission, provided that accurate acknowledgement of source is made. Requests for permission for extended quotation from or reproduction of this manuscript in whole or in part may be granted by the Competent Authority of HBNI when in his or her judgment the proposed use of the material is in the interests of scholarship. In all other instances, however, permission must be obtained from the author.



Aritra Gupta

DECLARATION

I, hereby declare that the investigation presented in the thesis has been carried out by me. The work is original and has not been submitted earlier as a whole or in part for a degree / diploma at this or any other Institution / University.

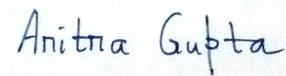


Aritra Gupta

List of Publications arising from the thesis

Journal

1. “The Direct Detection of Boosted Dark Matter at High Energies and PeV events at IceCube.”, Atri Bhattacharya, Raj Gandhi, Aritra Gupta, *Journal of Cosmology and Astroparticle Physics*, **2015**, JCAP03(2015)027, 001-057.
2. “Freeze-in Production of Sterile Neutrino Dark Matter in $U(1)_{B-L}$ Model”, Anirban Biswas, Aritra Gupta., *Journal of Cosmology and Astroparticle Physics*, **2016**, JCAP09(2016)044, 001-047.
3. “Calculation of Momentum Distribution Function of a Non-thermal Fermionic Dark Matter”, Anirban Biswas, Aritra Gupta., *Journal of Cosmology and Astroparticle Physics*, **2017**, JCAP03(2017)033, 001-062.
4. “Boosted Dark Matter and its implications for the features in IceCube HESE data”, Atri Bhattacharya, Raj Gandhi, Aritra Gupta, Satyanarayan Mukhopadhyay, *Journal of Cosmology and Astroparticle Physics*, **2017**, JCAP05(2017)002, 001-056.



Aritra Gupta

Dedicated to

My Parents

Acknowledgements

First and foremost, I would like to thank my parents, whose constant help and support kept me going through this significant journey of my life. I also fondly remember Late Binapani Singha, Late Gopal Singha and Late Ramen Sinha who encouraged me a lot to pursue my career as a physicist.

I owe a very special gratitude to my thesis advisor Prof. Raj Gandhi who provided excellent guidance to me both academically and non-academically. He has helped me a lot to become an independent researcher and always encouraged me to become a good physicist, boosting my confidence in moments of frustration. I am indebted to Prof. Gandhi in a great many ways.

I would like to thank the members of my thesis committee Prof. Biswarup Mukhopadhyaya, Prof. Ashoke Sen, Prof. Dileep Jatkar and Prof. Aseshkrishna Dutta. I sincerely express my gratitude to Prof. Ashoke Sen, Prof. Tirthankar Roychowdhury, Prof. Rajesh Gopakumar and Prof. Jayanta Kumar Bhattacharjee, for the excellent teaching and discussions. I am also highly indebted to Prof. Biswarup Mukhopadhyaya for teaching me a lot of important aspects of particle physics through his courses and also through the projects completed under his supervision. I also thank Prof. Sandhya Choubey for lending out a helping hand whenever necessary.

It gives me immense pleasure to thank my collaborators. I will always be grateful to Dr. Atri Bhattacharya and Dr. Satyanarayan Mukhopadhyaya for their support and help, as well as for teaching me the very basics of dark matter phenomenology. I must express my deepest gratitude to Dr. Anirban Biswas for the long and fruitful discussions we used to have about the minute details of dark matter theory and their applications. I am also highly obliged to Prof. Debashish Borah for many useful discussion sessions. Last but not the least, I will always be indebted to Dr. Arindam Chatterjee from whom I have learnt a lot about the calculational aspects of dark matter theory as well as many new techniques and results. Without his help, my learning would have remained incomplete.

Next, the turn for HRI, where I spent one of the most important and memorable times of my life so far. My wholehearted thanks goes to Subhroneel-da, Swapnamay-da, Atri-da, Dibya, Samrat, Nilay-da, Subha-da, Anirban-da, Masud-da, Hochi(Ujjal)-da, Vuru (Sourav)-da, Joydeep-da, Niyogi-da, Bedo (Arghya)-da, Arpan, Ritabrata, Avirup, Susovan, Nirnoy, Baccha (Titas), Sauri, Rana, Taushif, Udit, Avinanda-di and many others for all the intensive and enjoyable "adda"s/ gossips/ discussions and what not! Especially

to mention is Dibya, Niloy-da, Anirban-da, Hochi-da and Subho-da without whose "little" help and support it would be nearly impossible for me to jump across big hurdles along the course of this journey. My heartfelt thanks goes to Landau (Nabarun-da) for many friendly academic discussions. I will forever be indebted to Hochi-da, Ritabrata, Susovan and Soumyarup for inspiring and helping me to play guitar, which became an integral part of my stay at HRI. Needless to mention Bachha (Titas) who inspired me to learn photography. I also thank my childhood friends Chitrak, Nairit, Avishek (Bhatta), Samit, Titas (Kar), Navoneel (Iku), Aashis and Debtanu for being there when I needed them the most. Likewise, I fondly remember my college friends Asmi, (Aritra) Biswas, Sayonee and Jayita, who were always there to help me whenever required. I will especially remain indebted to Jayita for helping me with various academic and non-academic matters on several occasions. I would also like to thank my good friend Sreemanti who remained by my side during the whole time.

I am thankful to HRI movie club and especially to some of its members like Sauri, Nirnoy, Masud-da, Atri-da, Hochi-da for exposing me to really good and rare movies. I really enjoyed the long discussions we used to have on many film related topics. I am also thankful to innumerable story books and sets of rock music that kept me going through these sometimes difficult journey!

I am also highly grateful to Ritwik Ghatak, Nabarun Bhattacharya, Franz Kafka, Manik Bandopadhyaya and Albert Camus for inspiring me with their lives and works.

Last but not the least, I thank the people in the administration and technical section of HRI. In particular, I would like to mention Amit Khulve, Chandan Kanaujiya, Sanjay Verma, Amit Roy, Archana Tandon and Ravindra Singh, the registrar of HRI. Finally, I would also wish to thank the hard working staffs of HRI, especially Pankaj Bhaia and Mohan Bhaia, who many a times went out of their way to help me.

Thus, HRI had truly become a "Home away from home" for me for the past seven years.

“There is a theory which states that if ever anyone discovers exactly what the Universe is for and why it is here, it will instantly disappear and be replaced by something even more bizarre and inexplicable.

There is another theory which states that this has already happened.”

— Douglas Adams, *The Hitchhiker’s Guide to the Galaxy*.

Contents

Synopsis	xvii
List of Figures	xxi
List of Tables	xxvii
1 Introduction	1
1.1 Dark Matter : Proofs of existence	1
1.1.1 Flat Rotation Curves	1
1.1.2 Gravitational lensing	2
1.1.3 Bullet Cluster	3
1.1.4 Big Bang Nucleosynthesis (BBN)	4
1.1.5 Large Scale Structure of the Universe	6
1.2 Λ CDM cosmology and Dark Matter	7
1.3 Properties of Dark Matter	10
1.4 Candidates of Dark Matter	12
1.4.1 Baryonic Dark Matter	12
1.4.2 Non-Baryonic Dark Matter	12
1.5 Thermal Dark Matter and WIMP miracle	13
1.6 Thermal Dark Matter : Formal solutions	15
1.7 Direct and Indirect searches for Dark Matter	23
1.7.1 Direct searches for (thermal) dark matter	23
1.7.2 Indirect signals and possible hints of dark matter	24
1.8 Non-thermal Dark Matter	26
2 Non-thermal dark matter in $U(1)_{B-L}$ model	31
2.1 Introduction	31
2.2 The $U(1)_{B-L}$ extension of Standard Model	33
2.3 Exploring the Non-thermal Regime	37

2.4	Boltzmann Equation	39
2.4.1	Solution of the complete Boltzmann equation(s) with all production and decay channels	46
2.5	Relic Density of Sterile Neutrino Dark Matter (N_1)	48
2.6	A possible way of detecting the sterile neutrino Dark Matter	53
2.7	Conclusion	55
2.8	Appendix : Analytical expressions for cross sections and decay widths	57
2.8.1	Production processes of N_1 from the decays of SM and BSM particles	57
2.8.2	Production processes of N_1 from annihilation	57
2.8.3	Total decay widths of Z_{BL} , H and h	63
2.8.4	Decay width of $N_1 \rightarrow e^\pm \nu_i$ ($i = 1$ to 3)	65
3	Calculation of Momentum Distribution Function of a Non-thermal Dark Matter	69
3.1	Introduction	69
3.2	A <i>new</i> $U(1)_{B-L}$ extension of Standard Model	71
3.3	The FIMP paradigm	77
3.3.1	Coupled Boltzmann equations and its solution	77
3.4	Results	81
3.5	Constraints	92
3.6	Conclusion	95
3.7	Appendix	96
3.7.1	Relevant Vertex factors	96
3.7.2	Relevant Decay Widths	97
3.7.3	Collision terms	97
4	Indirect imprint of a non-thermal candidate : Boosted dark matter scenario	109
4.1	Introduction	109
4.2	Neutral-current scattering of a relativistic dark matter species with nuclei	111
4.3	The IC events: Characteristics and possible Origins	115
4.3.1	IceCube : Preliminaries	115
4.3.2	988 days of IC data and some of its features	116
4.3.3	PeV events: Fitting the DM-prediction to the IC observation	120
4.3.4	Sub-PeV Events: Neutrinos from extra-galactic sources	121
4.4	Discussion and Conclusions	123

5	Boosted Dark matter and IceCube : Detailed analysis	125
5.1	Introduction and Motivation	125
5.1.1	IceCube High Energy Starting Events (HESE) and features of the 1347-day data	125
5.1.2	Deep Inelastic Scattering of Boosted Dark Matter in IceCube	128
5.2	LDM interaction with quarks: simplified models and current constraints . .	133
5.2.1	Spin-0 mediators	133
5.2.2	Spin-1 mediators	134
5.2.3	Constraints on the couplings and the mass parameters	135
5.3	Scenario I: PeV events caused by LDM scattering on Ice and its implications	140
5.3.1	Pseudoscalar mediator	143
5.3.2	Scalar mediator	147
5.3.3	Vector and axial-vector mediators	149
5.4	Scenario II: Excess events in the 30–100 TeV region caused by LDM scatter- ing on Ice and its implications	153
5.4.1	Gamma-ray constraints on Scenario II	155
5.5	Muon-Track events	157
5.6	Summary and Conclusions	159
6	Conclusion	163
6.1	Non-thermal dark matter in $U(1)_{B-L}$ model	163
6.2	Calculation of momentum distribution functions of non-thermal dark matter	164
6.3	Boosted dark matter scenarios	164

Synopsis

From the measurements carried out by the present day satellite-borne experiments like Planck and WMAP, existence of a mysterious form of matter, namely Dark Matter (DM), is almost certain. But physicists have long been aware of the presence of this dark matter from the days when it was first proposed by Fritz Zwicky, Vera Rubin and others by comparing the observed and predicted (using standard Newtonian mechanics) galaxy rotation curves. With the advancements in precision and experimental techniques more and more evidences pointed towards the presence of dark matter. These mainly involved detection of dark matter through gravitational lensing effects, X-ray observations from elliptical as well as galaxy clusters and measurement of Baryon Acoustic oscillations in the CMB spectrum. According to the latest results from the Planck collaboration (and assuming Λ CDM cosmology), around 26.8% of the total energy budget of the Universe today is due to dark matter. But unfortunately, as it is clear from the above discussion, the (direct) detections of this elusive dark matter is manifested only through its gravitational effects. Very little is known about its particle nature and other microscopic properties. However different experimental observations have led us to believe that most of this unknown matter must be non-baryonic in nature and mostly comprise of non relativistic (cold dark matter) particles. But our knowledge about dark matter beyond this is very limited. Hence, over the years many attractive ideas have been proposed to build models that can explain the dark matter scenario.

A very popular idea is the so called "WIMP hypothesis", where a dark matter particle with a weak scale interaction strength is able to match the experimentally observed relic density quite naturally. Such particles belong to the most widely studied class of dark matter called "Thermal dark matter". In this scenario, the dark matter particles were in thermal (and chemical) equilibrium with the rest of the particles in the early epochs of the Universe. As the Universe cooled, the rate of interaction of these particles became less than the expansion rate of the Universe and consequently they went out of equilibrium from the rest of the thermal plasma and froze to a particular relic abundance. Several direct detection experiments (like LUX, XENON, DAMA, CRESST, EDELWEISS-II etc.)

have been set up over the past decade in order to directly observe these dark matter particles. The non relativistic dark matter particles can scatter off the nuclei in the detector elastically. The recoil energy of the nucleus is measured through different techniques by the detector giving us an idea about the mass and interaction strength of dark matter. Unfortunately we could not find any dark matter type particles in these detectors. Hence, this non observation of dark matter has put a stringent upper bound on the dark matter–nucleon (spin-independent and spin-dependent) coherent scattering cross section. Recent results from LUX even made a four-fold improvement on the previously available results. With this increasing sensitivity of direct detection experiments, in a few years time, we are going to hit the neutrino nucleon coherent scattering cross section limit (commonly dubbed as “neutrino floor”). Hence it will be difficult for us to distinguish neutrino from dark matter. There are three possible way-outs from this problem :

1. Directional searches can help us to distinguish between neutrino and dark matter.
2. Till now direct detection techniques relied on low energy nuclear recoil ($\sim \mathcal{O}(1 \text{ keV})$). We can try to extend our field of view, and search for direct detection of dark matter at other energy scales.
3. The assumption of “thermal” dark matter itself is not sacrosanct. Dark matter can be so feebly interacting that it may never enter into thermal equilibrium, hence explaining the null result in the present direct detection experiments. Direct detection of such non-thermal dark matter candidates is difficult due to such weak interaction strengths, and indirect detection is our only hope.

In my Ph.D. I mainly focused on points 2 and 3 above.

In the first part of my work, we proposed that direct detection of dark matter is indeed possible in the Deep Inelastic Scattering regime in very large neutrino detectors like IceCube. We studied the possibility of detecting dark matter directly via a small but energetic component that is allowed within present-day constraints. Drawing closely upon the fact that neutral current neutrino nucleon interactions are indistinguishable from DM–nucleon interactions at low energies, we extended this feature to high energies for a low mass but highly energetic population of DM particle χ , created via the decay of a significantly more massive and long-lived non-thermal relic Φ , which forms the bulk of DM. We showed that if χ interacts with nucleons, its cross section, like the neutrino-nucleus coherent cross section, can rise sharply with energy leading to deep inelastic scattering, similar to neutral current neutrino-nucleon interactions at high energies. Thus, its direct detection may be possible via cascades in very large neutrino detectors. As a specific example, we applied this notion to the recently reported three ultra-high energy PeV cascade events clustered around 1–2 PeV at IceCube. For definiteness, we took only vector

mediator in this work.

We followed up on this work by a detailed analysis, where we took all four types of mediators (scalar, pseudoscalar, vector and axial vector) and checked their respective viability in simultaneously explaining the PeV events as well as a small excess of events seen around $\sim \mathcal{O}(50 \text{ TeV})$ deposited energy. We show, that our hypothesis, coupled with a standard power-law astrophysical neutrino flux is capable of providing very good fits to the present data, along with a possible explanation of some features in the HESE sample. These features include a) the paucity of events beyond $\sim 2 \text{ PeV}$ b) a spectral feature resembling a dip or a spectral change in the $400 \text{ TeV} - 1 \text{ PeV}$ region and c) an excess in the $50 - 100 \text{ TeV}$ region (as already stated). We consider two different boosted DM scenarios, and determine the allowed mass ranges and couplings for four different types of mediators (scalar, pseudoscalar, vector and axial-vector) which could connect the standard and dark sectors. In the first scenario we tried to explain the TeV excess through a 3-body decay of the scalar dark matter while the PeV excess was explained by the usual two body decay to the lighter relativistic dark matter species. In the second scenario no such assumptions were made and only the two body decay along with the usual astrophysical physical flux were able to explain the IC data. We consider constraints from gamma-ray observations and collider searches. We find that the gamma-ray observations provide the most restrictive constraints, disfavouring the 1σ allowed parameter space from IC fits, while still being consistent with the 3σ allowed region. We also test our proposal and its implications against IC's recent six-year through-going muon track data.

In the second part of my work, we explored in detail the possibility of a non-thermal sterile neutrino DM within the framework of $U(1)_{B-L}$ model. The $U(1)_{B-L}$ model on the other hand is a well-motivated and minimal way of extending the standard model so that it can explain the neutrino masses via Type-I see-saw mechanism. We have shown, besides explaining the neutrino mass, it can also accommodate a non-thermal sterile neutrino DM with correct relic density. In contrast with the existing literature, we have found that W^\pm decay can also be a dominant production mode of the sterile neutrino DM. The new gauge coupling being very small (due to non-thermality), renders the extra gauge boson to remain out of equilibrium as well. This gauge boson is also an important source of production of this sterile neutrino DM. To obtain the comoving number density of dark matter, we have hence solved a coupled set of Boltzmann equations considering all possible decay as well as annihilation production modes of the sterile neutrino dark matter. The framework developed here though has been done for a $U(1)_{B-L}$ model, can be applied quite generally for any models with an extra neutral gauge boson and a fermionic non-thermal dark matter. We have also shown that indirect detection of this dark matter

is possible through the observation of the 511 keV X-ray line.

We have followed up on this work trying to investigate other possible non-thermal dark matter scenarios at the level of momentum distribution functions. If the non-thermal dark matter is itself produced substantially from the decay of another non-thermal mother particle, then their distribution functions may differ in both size and shape from the usual equilibrium distribution function. In this work, we have studied such a non-thermal (fermionic) dark matter scenario in the light of a new type of $U(1)_{B-L}$ model. It is new, because, unlike the usual $U(1)_{B-L}$ model, it does not contain the right handed sterile neutrinos needed for anomaly cancellations. Instead it has four extra chiral fermions which helps in the required cancellation. This $U(1)_{B-L}$ model is interesting, since, besides being anomaly free, it can give rise to neutrino mass by Type-II see-saw mechanism. Moreover, as we will show, it can accommodate a non-thermal fermionic dark matter as well. Starting from the collision terms, we have calculated the momentum distribution function for the dark matter by solving a coupled system of Boltzmann equations. We then used it to calculate the final relic abundance, as well as other relevant physical quantities. We have also compared our result with that obtained from solving the usual Boltzmann (or rate) equations directly in terms of comoving number density, Y . Our findings suggest that the latter approximation is valid only in cases where the system under study is close to equilibrium, and hence should be used with caution.

List of Figures

1.1	Stars in the outer part of M33 galaxy were observed to rotate much faster than expected from the mass estimation based on visible matter. This is what is referred to as the anomalous flattening of rotation curves [1].	3
1.2	Gravitational lensing effect. The foreground cluster is depicted in yellow in the figure while the (multiple) images of the background cluster is shown in blue, and is seen to form a sort of Einstein ring. <i>Image Credit : ESA, NASA, K. Sharon (Tel Aviv University) and E. Ofek (Caltech).</i>	4
1.3	A representation of bullet cluster. The gravitational lens map is shown in blue while the X-ray emissions from the gaseous components are shown in pink. X-ray : [2] and Lensing Map : [3].	5
1.4	Abundance of light elements as predicted by BBN. The uncertainties arise from the determination of nuclear cross sections. Here, $Y_p \equiv \rho(^4\text{He})/\rho_b$, ρ being the energy density. Other abundances are measured relative to that of H. The yellow boxes depict the observed abundances [4].	6
1.5	Temperature power spectrum from Planck, 2015. The blue dots indicate the experimentally observed points. The best fit curve (red one) from the Λ CDM cosmology is shown in red line in the upper plot. The lower plot indicates the residuals with respect to this model. The error bars signify $\pm 1\sigma$ uncertainties. The best fit values are mentioned in the text [5].	8
1.6	Triumph of Λ CDM cosmology and its excellent agreement with independent measurements from Supernovae, Large Scale Structures (clusters), CMB (Left [6]) and BBN (Right [7]). The figure also shows that our universe is almost flat.	10
1.7	Variation of g_* and g_{*s} with temperature (T in GeV) of the universe. The small difference between the two in the low temperature regime (i.e. during the latter part of the universe) occurs due to neutrino decoupling [8]. . .	21

1.8	Variation of comoving number density Y with x for a Weakly interacting massive particle with mass $\sim \mathcal{O}(100)$ GeV. The dotted lines represent the comoving number density after freeze-out, while the solid represents the corresponding equilibrium value [8].	23
1.9	Upper bounds on WIMP-nucleon spin independent cross section from Xenon1T collaboration [9].	24
1.10	Upper bounds DM-nucleon cross section from non-observations in direct detection experiments. Along with this, the neutrino nucleon coherent scattering cross section has also been superposed for comparison [10]. . . .	27
1.11	Contrasting the freeze-in and a typical freeze-out scenario. The final yield increases with the strength of interaction as shown by the upward arrow in case of freeze-in. The trend is opposite for freeze-out as expected. Note, for the freeze in case $x = m_\sigma/T$ while for the freeze-out case $x = m_\chi/T$. The plot has been taken from ref. [11].	29
1.12	Schematic diagram showing the approximate orders of magnitude of coupling strengths (λ, λ') required for thermal and non-thermal scenarios [12]. .	29
2.1	Evolution of comoving number density of Z_{BL} with respect to z	41
2.2	Evolution of comoving number densities of Z_{BL} and N_1	43
2.3	Dependence of $Y_{Z_{BL}}$ and Y_{N_1} on different sets of initial temperatures.	44
2.4	Comparison of comoving number densities of Z_{BL} and N_1 with respect to different sets of chosen model parameters.	45
2.5	Comparison of Z_{BL} and N_1 comoving number density with respect to different sets of chosen parameters.	47
2.6	Relic abundance of N_1 as function of z along with the relative contributions of W^\pm and Z_{BL} decay channels. All the plots are drawn for $M_{N_1} = 1$ MeV. .	49
2.7	Allowed region in g_{BL} Vs α plane satisfying the relic density criteria.	51
2.8	Allowed region in $M_{Z_{BL}}$ Vs g_{BL} plane satisfying the relic density criteria. . .	52
2.9	Values of M_{N_1} and active-sterile mixing angle α allowed by the relic density of N_1 ($0.1172 \leq \Omega_{N_1} h^2 \leq 0.1226$), are shown by the dark cyan points. The points lying within the red coloured band reproduced the flux observed by INTEGRAL/SPI. The points above the red band are ruled out from the observation of too large a flux as compared to that observed by INTEGRAL/SPI. Note, that this rules out the region corresponding to DM production via W -decay.	55

3.1	Non-thermal momentum distribution function $f_{Z_{BL}}$ plotted as a function of the dimensionless variable ξ_p for $\beta = 1$ (left) and $\beta = 10^{-3}$ (right). The curves are shown for different values of $r = \frac{M_{sc}}{T}$	84
3.2	Non-thermal momentum distribution function f_{ψ_1} plotted as a function of the dimensionless variable ξ_p for $\beta = 1$ (left) and $\beta = 10^{-3}$ (right). The curves are shown for different values of $r = \frac{M_{sc}}{T}$	84
3.3	Variation of comoving number density of Z_{BL} and ψ_1 with respect to r . Left: $\beta = 1$ and Right: $\beta = 10^{-3}$	85
3.4	Variation of comoving number density of Z_{BL} and ψ_1 with r corresponding to different values of g_{BL} . Left: $\beta = 1$ and Right: $\beta = 10^{-3}$	86
3.5	Variation of comoving number density of Z_{BL} and ψ_1 with r corresponding to different values of M_{h_2} . Left: $\beta = 1$ and Right: $\beta = 10^{-3}$	87
3.6	Variation of comoving number density of Z_{BL} and ψ_1 with r corresponding to different values of M_{ψ_1} . Left: $\beta = 1$ and Right: $\beta = 10^{-3}$	87
3.7	Variation of comoving number density of Z_{BL} and ψ_1 with r corresponding to different values of $M_{Z_{BL}}$. Left: $\beta = 1$ and Right: $\beta = 10^{-3}$	88
3.8	Comparison of comoving number densities of Z_{BL} and ψ_1 with respect to mixing angles θ_{13} and θ_{23}	89
3.9	Variation of total relic density of ψ_1 with r corresponding to $\beta = 1$ and $\beta = 10^{-3}$	90
3.10	Comparison between the $Y_{Z_{BL}}$ and Y_{ψ_1} obtained from the exact calculation using momentum distribution approach with that of the approximate method using the $\langle \Gamma \rangle_{Th}$ for $\beta = 1$ (left panel) and $\beta = 0.001$ (right panel). . .	92
4.1	(a) Interaction of the incoming TeV mass DM particle χ with a nucleus, mediated by a heavy non-standard boson Z' . (b) The χN DIS interaction cross-section and the corresponding $\langle y(E) \rangle$ are shown for the benchmark value of m_χ and $m_{Z'}$. The overall normalisation to the χN cross-section is set by the product of coupling constants G , and is here arbitrarily chosen to be $G = 0.05$. The real magnitude of G will be determined by comparing event rates to those seen at IC in the succeeding section. For comparison, the νN neutral current cross-section and the corresponding $\langle y \rangle$ are also shown. . . .	113
4.2	Digital Optical Modules used for detecting Cherenkov radiations in Ice-Cube [13].	115

4.3	A layout of IceCube experimental facility at South Pole. The thin grey vertical lines are the 86 strings that are studded with the DOMs. The instrumentation begins from a 1450m below the surface where ice is relatively clear and free from dust particles. AMANDA and DeepCore are also shown in the figure [13].	116
4.4	Left : A track like event record from IceCube. The color coding helps us to understand the temporal behaviour. Red means earliest point of entry, while blue represents latest. We can see that the muon has lit up the DOMs as it passed through the strings. Right : A schematic diagram for a track. . .	117
4.5	Left : A cascade like event record from IceCube. . Right : A schematic diagram for the same.	118
4.6	A schematic diagram of a double bang event as produced by a τ lepton. . .	118
4.7	IC events for 988 days of data collection. The background arising from atmospheric neutrinos is shown in blue shaded and brick red region. The grey and the dashed grey curves are the IC astrophysical best-fit. The latter predicts events in the high energy bins in contrast to what observed [14]. . .	119
4.8	The TeV-scale diffuse neutrino flux and the extra-galactic FDM flux at PeV+ energies for decay lifetime $\tau_\phi = 5 \times 10^{21}$ s. The thick light-gray curve indicates the estimated conventional atmospheric $\nu_\mu + \bar{\nu}_\mu$ flux.	121
4.9	Predicted and observed total event rates at the IceCube. The gray shaded region represents energies at which we expect events predominantly from the DM sector. The green line shows event-rate predictions from our best fit flux to the sub-PeV event-rates observed at IC, with the flux given by Eq. (4.7). The event rates predicted due to the IC best-fit E^{-2} flux (gray dashed line) and the observed data (red diamonds) are shown. The IC-estimate for the atmospheric background events is shown as the yellow shaded region. . .	122
5.1	IC events for 1347 days of data collection. The background arising from atmospheric neutrinos is shown in blue shaded and brick red region. The grey and the dashed grey curves are the IC astrophysical best-fit. The latter predicts events in the high energy bins in contrast to what observed [15]. . .	127
5.2	The interactions corresponding to ϕ decay (left), mediator decay (centre) and χq scattering (right) involving a generic mediator, along with relevant coupling constants.	135

5.3	Representative plots showing the relative behaviour of χN and νN neutral current cross sections (left). Average inelasticities are also plotted for both cases (right).	143
5.4	Relevant fluxes that contribute towards the PeV and the sub-PeV events in Scenario I. The galactic χ flux is not shown since it originates from the two body decay of ϕ , and is given by the simple form in Eq. 5.10, unlike the extra-galactic flux, which exhibits a z dependance. The values of parameters used to calculate the fluxes are given in Table. 5.1.	144
5.5	Best-fit events (stacked bars) from a combination of secondary ν 's, astrophysical ν 's and background in the sub-PeV energies, with LDM events explaining the PeV+ events. The best-fit value of $m_\phi = 5.34$ PeV. Left: Decays to $b\bar{b}$. Right: The mediator mass limited to below $b\bar{b}$ production threshold, so that it can dominantly decay only to $c\bar{c}$ pairs.	145
5.6	1σ and 3σ allowed regions for parameters N_{ψ_1} and m_a (left) and N_{ψ_1} and N_{Ast} (right) for mediator decays to $b\bar{b}$. The solid dot in each case represents the corresponding best-fit point in the parameter subspace.	147
5.7	1σ and 3σ allowed regions for parameters N_{ψ_1} and m_a (left) and N_{ψ_1} and N_{Ast} (right) for mediator decays to $c\bar{c}$. The solid dot in each case represents the corresponding best-fit point in the parameter subspace.	148
5.8	Plot showing allowed regions satisfying gamma ray constraints in the case when pseudoscalar mediator decays to $b\bar{b}$ (Left) and to $c\bar{c}$ (Right). Regions above the red line are constrained by observations of the diffuse gamma ray flux.	149
5.9	Diffuse gamma-ray flux for the best-fit parameter choice in the pseudo-scalar mediator scenario, where the mediator a dominantly decays to $b\bar{b}$ (left) and $c\bar{c}$ (right). The current constraints from Fermi-LAT data at lower energies, and cosmic ray air shower experiment (KASCADE and GRAPES-3) data at higher energies are also shown.	150
5.10	Same as Fig. 5.5, for the scalar mediator scenario, with the mediator dominantly decaying to $c\bar{c}$	150
5.11	Event rates for the benchmark parameter values shown in Table 5.3. In keeping with the description in text, the correspondingly tiny number of events from the astrophysical flux have not been shown here.	151

5.12	Left: PeV events in the vector mediator scenario, with different choices for the Z' mass. A larger value of the Z' mass is more likely to explain the <i>dip</i> at around PeV. Right: PeV events in vector and pseudoscalar case with a mediator mass fixed to 20 GeV. The pseudoscalar scenario, as discussed earlier, explains the <i>dip</i> more accurately because of its sharply falling event rates, unlike in the vector scenario.	151
5.13	Variation of three body branching ratio with g_χ for the vector, axial-vector and the pseudoscalar mediators. The scalar mediator scenario shows a similar behaviour as the pseudo-scalar one.	153
5.14	Relevant fluxes for Scenario II. The corresponding parameters are given in Table 5.4. As before the monochromatic spike at $m_\phi/2$ due to the galactic χ flux is not shown here.	155
5.15	The total event rate is shown as the red solid curve. This comprises events from LDM scattering, astrophysical neutrinos and the atmospheric background. Events from the astrophysical power-law spectrum are shown as orange bars and stacked bars shaded in green show the LDM events over and above the astrophysical events. The other events over and above the green/yellow bars are due to atmospheric neutrinos and muons. The left hand side shows the pseudo-scalar case while the right hand side gives the case of an axial-vector type mediator.	156
5.16	Diffuse gamma-ray flux for pseudo-scalar (left) and axial-vector case (right). The maximum allowed values of $(f_\phi g_\chi^2)/\tau_\phi$ have been used for the flux computation here.	156
5.17	Muon track events for the pseudoscalar case in Scenario I and their comparison with the IC predicted best fit. The black line represents the IC power-law prediction and should be compared to our total prediction for throughgoing track events in the energy region 190 TeV to a few PeV (red line).	158
5.18	Muon track events in Scenario II. Shown for the case of pseudoscalar (left) and axial-vector type mediators (right). In Scenario II, the astrophysical flux is the main contributor to the track events. In our notation $\Phi_{ast} = N_{ast} E^{-\gamma}$. Best fit values of N_{ast} and γ are used in the above plot.	158

List of Tables

2.1	Fractional contributions of different production processes of N_1 through decay for $g_{\text{BL}} = 3.07 \times 10^{-11}$, $\alpha = 4.74 \times 10^{-10}$ rad, $M_{\text{ZBL}} = 10$ GeV, $M_H = 500$ GeV and $M_{N_1} = 1$ MeV.	50
2.2	Fractional contributions of different production processes of N_1 through annihilation for $g_{\text{BL}} = 3.07 \times 10^{-11}$, $\alpha = 4.74 \times 10^{-10}$ rad, $M_{\text{ZBL}} = 10$ GeV, $M_H = 500$ GeV and $M_{N_1} = 1$ MeV.	50
3.1	$\text{SU}(2)_L$, $\text{U}(1)_Y$ and $\text{U}(1)_{\text{B-L}}$ charges and corresponding VEVs of all the fields involved in the present model.	72
3.2	Values of different input parameters used in our analysis. Benchmark corresponding to $\beta = 1$ (left) and $\beta = 10^{-3}$ (right).	83
5.1	The best fit values of relevant parameters in case of a pseudoscalar mediator a , when it dominantly decays to $b\bar{b}$ and $c\bar{c}$ respectively. \tilde{N}_{Ast} is given in units of $\text{GeV cm}^{-2} \text{s}^{-1} \text{sr}^{-1}$	144
5.2	The best fit values of relevant parameters in the case of a scalar mediator a , when it decays dominantly to $c\bar{c}$. The best fit value of m_ϕ here is ~ 5.3 PeV. \tilde{N}_{Ast} is given in terms of $\text{GeV cm}^{-2} \text{s}^{-1} \text{sr}^{-1}$	148
5.3	Benchmark values of relevant parameters in the case of a vector mediator Z' , when it decays to all possible $q\bar{q}$ pairs. The value of m_ϕ used here is ~ 5.0 PeV. As noted in the text, we have chosen a benchmark point in the parameter space that maximises the secondary ν contribution from DM decay, and consequently deems the astrophysical flux negligible. The latter has therefore not been shown here.	152
5.4	The best fit values of relevant parameters in case of a pseudoscalar and axial-vector mediator for Scenario II. \tilde{N}_{ast} is given in units of $\text{GeV cm}^{-2} \text{s}^{-1} \text{sr}^{-1}$	154

Chapter 1

Introduction

One of the principal mysteries that is yet to be resolved is that of dark matter. A lot of studies are being pursued at present to unveil its elusive nature. The presence of dark matter has now been proven from multiple independent observations (to be discussed in detail below). However, its composition from particle physics point of view, is still not known. The very successful theory of particle physics called the Standard Model can not accommodate any dark matter candidate. So to uncover the mystery of the nature of dark matter, we require some insights into Beyond Standard Model theories. The most widely studied class of dark matter is the thermal WIMP (Weakly Interacting Massive Particle). The reason for choosing the latter is a phenomenon called the WIMP miracle which we will discuss in some detail later. In my thesis however, I have tried to investigate some aspects of non thermal dark matter candidates in the setting of some beyond Standard Model theories and also attempted to shed some light on prospects for its indirect detection. But, let us start first, by reviewing some basics of dark matter in general.

1.1 Dark Matter : Proofs of existence

1.1.1 Flat Rotation Curves

Probably the very first hint of existence of some non-luminous matter came from the observations of Fritz Zwicky in 1933 [16] when he measured the dispersion velocity of objects within the Coma Cluster. Later Vera Rubin measured rotation curves of galaxies moving near the fringes of galaxy clusters more accurately [17]. Assuming that almost all of the (visible) matter is concentrated near the center of the cluster, one would expect, upon using classical Newton's laws, the velocities of galaxies should ultimately decrease,

with increasing distance from the center of the cluster. This can be shown easily. Let us consider a test mass (a star, say) of mass m rotating within a galaxy at a distance of r from the center. For simplicity let us assume that it is rotating in a circular orbit. So, from Newton's law :

$$\frac{mv^2(r)}{r} = G \frac{M(r)m}{r^2} \quad (1.1)$$

Here, G is the gravitational constant and $M(r)$ is the mass of the galaxy contained within the radius r . If the star is moving within the galactic bulge, then $M(r) = \frac{4}{3}\pi\rho r^3$, assuming a constant mass density of ρ . Using Eq. 1.1, we get $v(r) \propto r$. Hence, initially the velocity increases as we start moving away from the center. Farther away, if we go beyond the galactic bulge to a place where there is very little visible matter, then $M(r) \simeq M$, M being the net mass of the galaxy. In this case, using Eq. 1.1, we get $v(r) \propto r^{-1/2}$, and hence decreasing. So, we would expect that rotation velocities would increase for $r <$ the radius of the galactic bulge, and then decrease gradually as we move farther away.

But on the contrary, it was observed that the velocity profile seems to flatten out as we go farther out from the center. The estimation of mass contained within the cluster assumed that all the masses were in the form of observable luminous matter. But, the flatness of the rotation curves hinted that the mass contained within the cluster may have been underestimated. Hence, to explain this observations, presence of non-luminous (dark) massive objects was necessary and this, perhaps, was the very first hint about the of a mysterious dark matter. After this puzzling discovery, similar observations were further reported. Observations from local groups of galaxies by Kahn and Woltjer (1959) [18], as well as from many other giant galaxies by Peebles, Yahil and Ostriker (1974) [19], revealed similar mysterious flatness of rotation curves. Similar observations were also made from the spiral galaxies again by V. Rubin et. al. in 1978 and 1985 [20, 21]. This anomalous behaviour is shown schematically in Fig. 1.1 for the M33 spiral galaxy.

1.1.2 Gravitational lensing

Gravitational lensing is the effect observed due to the deflection of photons under the influence of strong gravitational field. In the case of strong lensing [22], the foreground light is bend and due to the presence of large gravitational field between the source and the observer, this light can actually curve back towards the detector revealing the foreground despite of the presence of the obstruction in between. The images usually appear as Einstein Ring around the lens. The ring radius is proportional to the square root of the mass inside the lens. Depending upon the size and shape of the lens as well the offset of the source, the images of the source can be brighter or fainter. An example of such a

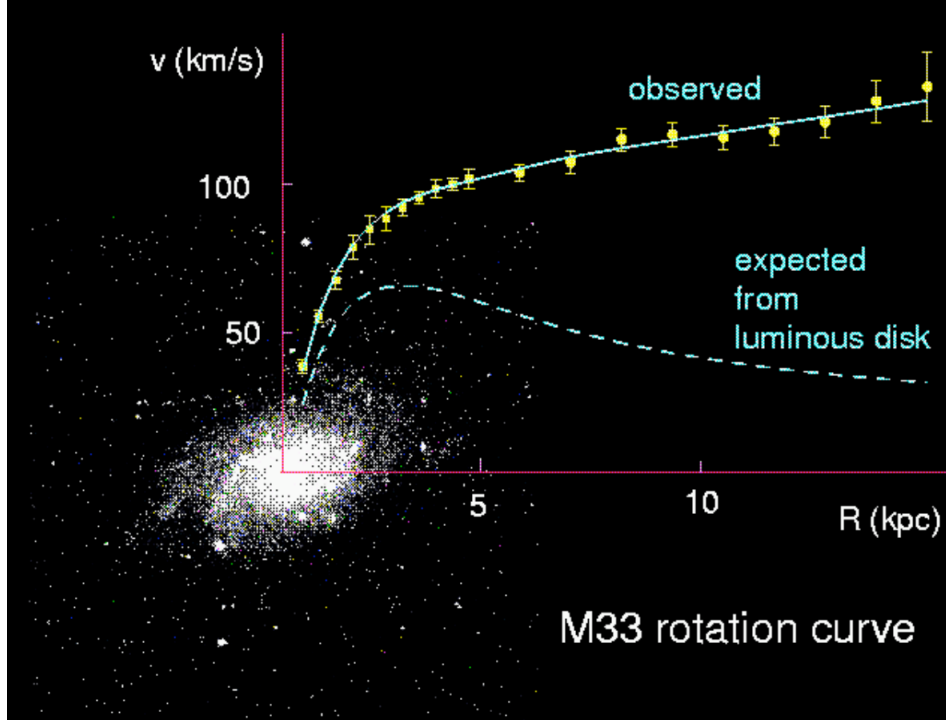


Figure 1.1: Stars in the outer part of M33 galaxy were observed to rotate much faster than expected from the mass estimation based on visible matter. This is what is referred to as the anomalous flattening of rotation curves [1].

lensing effect is seen in Fig. 1.2. The lensed images of the background are shown in blue in the figure. From the amount of lensing, it is concluded that there is much more (invisible) matter present in the center than that estimated from the observation of only the luminous ones. In recent times, we have also obtained hints about the presence of dark matter from weak lensing [23]. Most of the time the light from distant galaxies and stars does not pass near very strong gravitational fields and is not deflected sufficiently, unlike strong lensing. In the weak lensing regime we thus depend on measurement of shear distortion of the source. This shear distortion is proportional to the second derivative of the gravitational potential along the line of sight, and hence gives us an idea of the amount of matter present in the source.

1.1.3 Bullet Cluster

Another hint of the presence of dark matter comes from cosmic supercolliders, i.e. galaxy or cluster mergers. One of the most luminous and hottest of the X-ray clusters is the Bullet cluster (see Fig. 1.3). It is actually a merger formed due to the collision of two

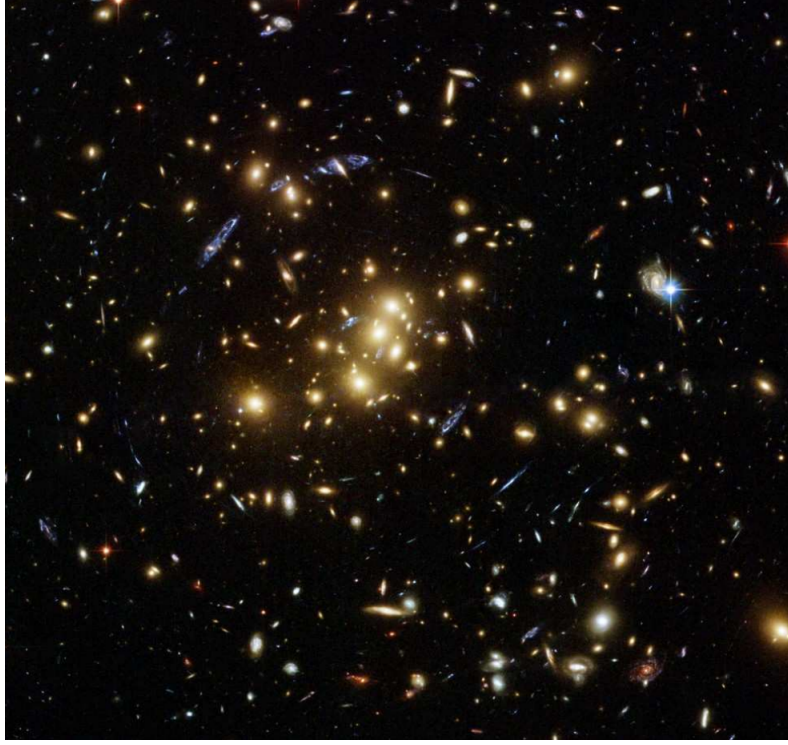


Figure 1.2: Gravitational lensing effect. The foreground cluster is depicted in yellow in the figure while the (multiple) images of the background cluster is shown in blue, and is seen to form a sort of Einstein ring. *Image Credit : ESA, NASA, K. Sharon (Tel Aviv University) and E. Ofek (Caltech).*

galaxy clusters. The gravitational lensing map is shown in blue while the x-ray emission map of the gaseous material is shown in pink. The amount of matter estimated from the gravitational lensing data, is much more than that estimated from the luminous matter only, thereby indicating the presence of dark matter. But the morphology of the bullet cluster also reveals a very important property of dark matter. The dark matter (denoted by the blue regions) have passed right through each other as well as the gaseous clouds. This means that dark matter is very weakly interacting and is almost collisionless [24].

1.1.4 Big Bang Nucleosynthesis (BBN)

As the universe cools down to \mathcal{O} (MeV) temperatures ($t \sim 1$ s), protons, neutrons and electrons begin to combine to form the light elements like Helium (^3He , ^4He), Lithium (^7Li), and Deuterium (D). The abundance of these elements can be well predicted by theory and also well measured from experiments. At early times, the weak interactions occurred



Figure 1.3: A representation of bullet cluster. The gravitational lens map is shown in blue while the X-ray emissions from the gaseous components are shown in pink. X-ray : [2] and Lensing Map : [3].

at a faster rate than the rate of expansion of the universe thus maintaining the neutron to proton ratio (n/p). But around a temperature of 1 MeV, the neutron-proton conversion rate falls below the Hubble expansion rate, ultimately resulting in Big Bang Nucleosynthesis (BBN). The rates of the reactions depend crucially on $\eta \equiv n_b/n_\gamma$. Here, n_b and n_γ are the present day number densities of baryon and photon respectively, the latter being calculable from the CMB temperature of 2.7 K. This very important quantity η is directly proportional to Ω_b , the baryon density of the universe (with $h \equiv H_0/100$, H_0 is the Hubble parameter today in units of $\text{km s}^{-1} \text{Mpc}^{-1}$). Predictions of BBN hence depends on the accurate estimation of these reaction rates as well as that of the Hubble constant. We find excellent agreement with BBN theory from the observation of D/H [25] and $^3\text{He}/\text{H}$ ratios [26] (Fig. 1.4). There is however a discrepancy in $^7\text{Li}/\text{H}$ ratio [27] where BBN actually predict higher abundance than that observed from experiment. The value of η that helps to explain the abundance of light elements is $\sim (5.7 - 6.7) \times 10^{-10}$ (at 95% confidence level) [28]. From the BBN measurements, the amount of baryon fraction, $\Omega_b h^2$ turns to be ~ 0.02 [26] (value of $h \simeq 0.64$).

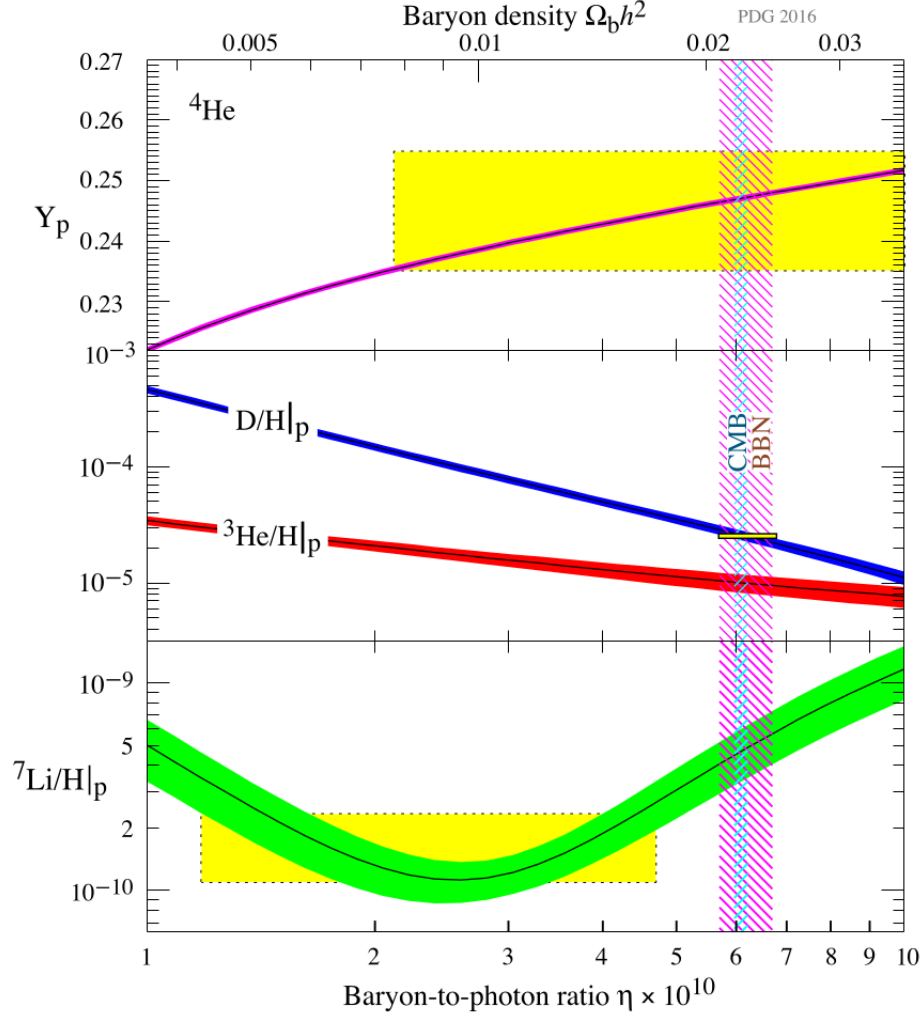


Figure 1.4: Abundance of light elements as predicted by BBN. The uncertainties arise from the determination of nuclear cross sections. Here, $Y_p \equiv \rho(^4\text{He})/\rho_b$, ρ being the energy density. Other abundances are measured relative to that of H. The yellow boxes depict the observed abundances [4].

1.1.5 Large Scale Structure of the Universe

By large scale structure we mean the inhomogeneities present in the universe on scales larger than that of galaxies. Measurements of these can reveal a lot about the quantity and nature of dark matter. Over the last few decades many large scale surveys have unveiled a great deal about the structures of the cosmos. On the other hand, N-body simulations of large scale structures match well with that of the observations if and only if a substantial part of the total energy budget of the universe is due to that of dark matter. Also, the

major portion of this dark matter must be non relativistic (Cold Dark Matter). Otherwise, if it is hot and relativistic, then it will have a larger free streaming length and hence will wash out structures at smaller scales. For example, highly energetic relativistic particles can not form clumps as small as that of galaxies, because they have lower probability of getting entrapped in the gravitational potential due to their high velocities. Galaxies and other smaller structures then should have been formed by repeated splitting of larger structures, leading to what is known as top down approach of structure formation i.e. where larger structures came into existence earlier than the smaller ones. But this is in conflict with the observations which hint towards a bottom-up approach i.e. where larger structures were formed due to the aggregation of smaller ones. The latter is only possible in the presence large amounts of non-relativistic and non-dissipative dark matter particles. The large scale galaxy power spectrum is highly correlated with the total matter density of the universe. Results from the recent surveys indicate a total matter density (luminous as well as dark) $\Omega_m \sim 0.29$. Hence, from the observations of BBN and Large Scale structures we conclude that amount of dark matter in the universe is ~ 0.25 [29].

1.2 Λ CDM cosmology and Dark Matter

Often known as the Standard Model of cosmology, Λ CDM model is one of the biggest successes of the past decade. Measurements of anisotropies of the CMB (Cosmic Microwave Background) almost perfectly agrees with that predicted by the Λ CDM model (Fig. 1.5). The model consists of six independent parameters to be determined from experimental observations. They are : Baryon density ($\Omega_b h^2$), the dark matter density ($\Omega_c h^2$), age of the universe (t_0), scalar spectral index (n_s), curvature fluctuation amplitude (Δ_r^2) and reionization optical depth (τ). All the other important quantities of interest can be derived from these.

Assuming homogeneity and isotropy, the universe can be well described by the FRW metric :

$$ds^2 = dt^2 - R^2(t) \left(\frac{dr^2}{1 - k r^2} + r^2 (d\theta^2 + \sin^2 \theta d\phi^2) \right) \quad (1.2)$$

Here, r, θ, ϕ, t are known as the comoving coordinates. k is related to the curvature of the universe, and when properly scaled it can take the values $0, \pm 1$, corresponding to flat, negative and positive spatial curvatures. Using this metric in the Einstein's equation, we derive the dynamical equations of motion popularly known as the Friedman equations. Einstein's equations of motion reads :

$$\mathcal{R}_{\mu\nu} - \frac{1}{2}\mathcal{R}g_{\mu\nu} = 8\pi G T_{\mu\nu} + \Lambda g_{\mu\nu} \quad (1.3)$$

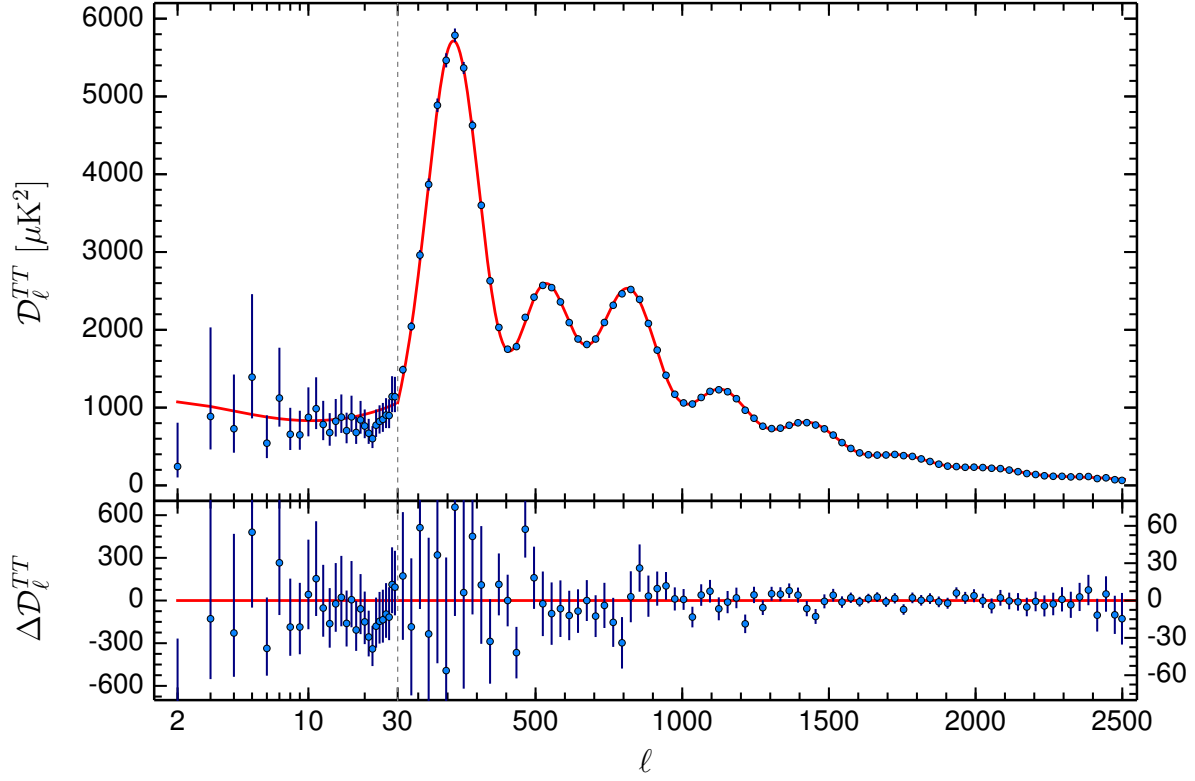


Figure 1.5: Temperature power spectrum from Planck, 2015. The blue dots indicate the experimentally observed points. The best fit curve (red one) from the Λ CDM cosmology is shown in red line in the upper plot. The lower plot indicates the residuals with respect to this model. The error bars signify $\pm 1\sigma$ uncertainties. The best fit values are mentioned in the text [5].

where $\mathcal{R}_{\mu\nu}$ and \mathcal{R} are the Ricci tensor and the Ricci scalar respectively. $T_{\mu\nu}$ is the stress energy tensor, G is the gravitational constant and Λ is the cosmological constant. Assuming the universe to be a perfect fluid, the stress-energy tensor is written as :

$$T_{\mu\nu} = -p g_{\mu\nu} + (p + \rho) u_\mu u_\nu \quad (1.4)$$

Here, p and ρ are the pressure and energy density of the perfect fluid, u is the velocity vector in the comoving co-ordinates. The pressure and energy densities are related by the equation of state and is generically written as $p = w\rho$. The value of w is different for matter, radiation and vacuum energy (related to Λ , the cosmological constant). The dynamical equations for the scale factor $R(t)$ is obtained from the 0-0 and i-i components

of the Einstein's equation. The Friedman equations for $R(t)$ are given by :

$$H^2 \equiv \frac{\dot{R}^2}{R^2} = \frac{8\pi G\rho}{3} - \frac{k}{R^2} + \frac{\Lambda}{3} \quad (1.5)$$

$$\frac{\ddot{R}}{R} = \frac{\Lambda}{3} - \frac{4\pi G}{3}(\rho + 3p) \quad (1.6)$$

where H is the Hubble expansion rate. Using the above two equations, we can derive another useful equation namely,

$$\dot{\rho} = -3H(p + \rho) \quad (1.7)$$

This relation is a simple consequence of the first law of thermodynamics and can be derived directly from it. At this point it is useful to define a quantity called $\rho_c \equiv \frac{3H^2}{8\pi G}$, which is defined to be the total energy density of the universe such that $k = 0$ when $\Lambda = 0$. It takes the value of $1.05 \times 10^{-5} \text{h}^2 \text{ GeV cm}^{-3}$. The rescaled energy densities of matter, radiation and vacuum energy are defined as $\Omega_m = \rho_m/\rho_c$, $\Omega_{rad} = \rho_{rad}/\rho_c$ and $\Omega_{vac} = \Lambda/\rho_c$ respectively. Using these, one can rewrite Eq. 1.5 as follows :

$$\frac{k}{R^2} = H^2 (\Omega_m + \Omega_{rad} + \Omega_{vac} - 1) \quad (1.8)$$

The present day values of these parameters are usually quoted by the experimental collaborations. The values of these at the present epoch is denoted by the suffix 0, and the equation looks like :

$$\frac{k}{R_0^2} = H_0^2 (\Omega_{m,0} + \Omega_{rad,0} + \Omega_{vac,0} - 1) \quad (1.9)$$

Under the assumption that $k \sim 0$ (which turns out to be a very good approximation indeed), Planck measured values of $\Omega_b \sim 0.0486$ and $\Omega_{\text{CDM}} \sim 0.2589$ [5]. These are found to be in excellent agreement with the results obtained from BBN and Large Scale Structure measurements and as a consequence prove the presence of (cold) dark matter almost beyond any doubt. Furthermore, observations from Type I-A supernovae indicate that our universe is accelerating and has a non-zero cosmological constant. Λ CDM cosmology, in agreement with the latter measurements also predicts that at present universe is vacuum energy dominated with $\Omega_{vac} \sim 0.6911$ [5]. This incredible agreement is shown in Fig. 1.6.

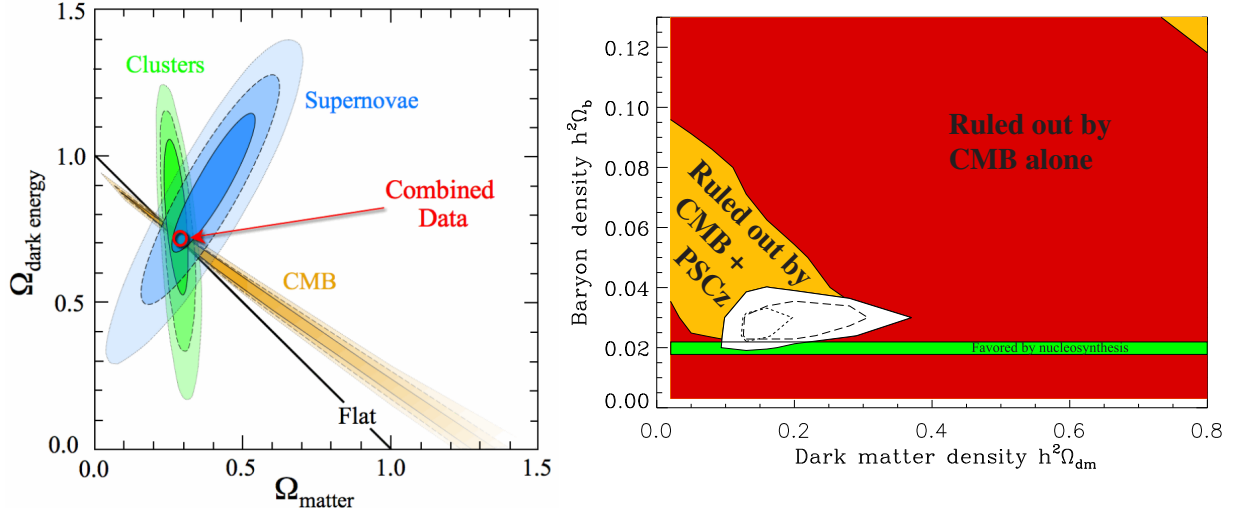


Figure 1.6: Triumph of Λ CDM cosmology and its excellent agreement with independent measurements from Supernovae, Large Scale Structures (clusters), CMB (Left [6]) and BBN (Right [7]). The figure also shows that our universe is almost flat.

1.3 Properties of Dark Matter

From the discussions in the above sections, it is evident that a major portion of our universe must be made up of dark matter. However no one is still sure about its composition. A lot of theories have been put forward to explain the same. Any theory or model that tries to explain dark matter should however satisfy some basic properties. They are listed and discussed below.

Strength and types of interactions

As seen earlier, the most promising hints of dark matter comes from its gravitational interactions. So other types of interactions with ordinary matter (if any), should be extremely weak. The fact that it interacts with ordinary matter very weakly (hence rendering them to be dark), immediately implies that ideally it should be electrically neutral. However, the dark matter particle, in some cases may possess a small amount of charge keeping with astrophysical and cosmological observations (CMB recombination, BBN, supernovae ejections etc). From CMB recombination data, the maximum allowed fractional charge for a dark matter particle is $\sim 10^{-4}$ if its mass is in the GeV range [30]. Furthermore, a new improved constraint has been recently derived for dark matter particles with mass m , from considerations of magnetic fields in galaxy clusters [31]. According

to this study, the maximum allowed charge for such a particle should be $\leq 10^{-14} \frac{m}{\text{GeV}}$ and is considerably stringent than the previous upper bound $\left(10^{-11} \frac{m}{\text{GeV}}\right)$ [32]. Besides electric neutrality, the dark matter also should not have very strong interactions with the baryons. This will leave imprint on the predictions of large scale structures, Baryon Acoustic Peaks among many others.

Although predictions of large scale structures are well explained by the presence of dark matter, there are few problems that are not solved by the same on smaller scales. These are the missing satellite, "too big to fail" and "cusp vs core" problems. However such problems can be alleviated if we consider substantial amount of self interactions between the dark matter particles ($\sigma/m \leq 1\text{cm}^2\text{g}^{-1}$) [33–35].

Stability

Since the major portion of our universe is composed of dark matter, it should be stable, at least on cosmological scales [36]. Dark matter if at all can decay, should have a lifetime larger than the age of the universe. But, there are strong constraints on the lifetime of dark matter decaying directly to standard model particles from the observation of diffuse gamma ray fluxes. However, most of the dark matter models postulate a perfectly stable dark matter. This is usually done by invoking some discrete symmetries like Z_2 . A conserved quantum number related to this symmetry is associated with the dark matter but not with the standard model particles. On the other hand, in some theories, which deals with a dark sector instead of a single dark matter candidate, the dark particles are allowed to decay to the lightest particle in the sector, where the latter plays the role of the stable dark matter.

Relic abundance

The stable dark matter particles as predicted by the models should satisfy the total dark matter energy budget today or in other words, the relic density as measured by experiments. The dark matter relic density, on the other hand, is fixed by its interaction strengths and scattering cross sections all of which is predictable from the theory. The present value of relic density is given by $\Omega_{\text{DM}} h^2 = 0.1186 \pm 0.0020$ [5].

1.4 Candidates of Dark Matter

1.4.1 Baryonic Dark Matter

Dark matter may have some small baryonic contributions, however they cannot comprise the major portion of the total dark matter energy density. Such baryonic dark matters are thought to be present in the galactic disks or within massive dead stars. A very popular candidate for such baryonic dark matter was the class of objects known as the MACHOs (Massive Astrophysical Compact Halo Objects). They are non-luminous massive objects and are usually detected by their gravitational lensing effect. They include black holes, neutron stars as well as brown dwarfs. Around 13–17 MACHOs were discovered in our Milky Way itself [37]. However these MACHOs as the major dark matter candidate has been ruled out by searches for the microlensing effect by them [38]. Other experiments also had put extremely constricting bounds on MACHOs [39, 40]. One such experimental collaboration called EROS has concluded the MACHOs cannot contribute more than 8% to the total mass of the galactic halo [41].

1.4.2 Non-Baryonic Dark Matter

The major portion of dark matter is thus made up of non baryonic constituents. Unfortunately, the Standard Model of Particles which has successfully explained many puzzles, does not possess a suitable dark matter candidate. Most of the particles present within the standard model interact much more strongly than required by a suitable dark matter candidate, with the only exception being the neutrinos. However, because of their almost vanishing mass, neutrinos are highly relativistic even at late times with large free streaming lengths. As discussed earlier, from observations of large scale structures we not only concluded about the presence of dark matter, but also the fact that it should be “cold” i.e. non relativistic. Major portion of the dark matter cannot be composed of ultra-relativistic “hot” particles. On the basis of this free-streaming length (λ_{fs}) dark matter can be categorised as cold ($\lambda_{\text{fs}} < 0.01 \text{ Mpc}$), Warm ($0.01 \text{ Mpc} \leq \lambda_{\text{fs}} \leq 0.1 \text{ Mpc}$) and hot ($\lambda_{\text{fs}} \geq 0.1 \text{ Mpc}$). Hence, neutrinos can be considered as a Hot Dark Matter candidate, but their relic density is much less than the observed value [42]. The abundance of a hot relic like the neutrino is given by :

$$\Omega_{\nu} h^2 \simeq \frac{m_{\nu}}{91.5 \text{ eV}} \quad (1.10)$$

The upper bound on such relics dictates that $\Omega_{\nu} h^2 \leq 0.0062$ (at 95% confidence level) [43] and thus, have very little contribution to the total amount of observed dark matter in the

universe.

Hence, we need to build theories beyond standard model (BSM) to accommodate cold dark matter candidates. The most popular among supersymmetric dark matter candidates is the neutralino [44]. Among the four (chargeless) neutralinos appearing in supersymmetric models (more specifically, in the Minimal Supersymmetric Standard Model *aka* MSSM), the lightest of them is usually taken to be as the dark matter particle. It is stabilised by the conservation of R-parity ($R = (-1)^{3B+L+2S}$), where B, L and S are the baryon number, lepton number and spin respectively.

Another interesting dark matter candidate resides in theories of extra dimensions. The CDM candidate in this case is the lightest Kaluza Klein (KK) particle which appear when the standard model particles propagate in the extra-dimensions. These KK particles are taken to be gauge bosons and they are shown to satisfy relic density as well as direct detection constraints quite well [45]. The stability of these dark matter particles is ensured by the conservation of the quantum number $(-1)^{KK}$, where KK denotes the number of Kaluza Klein towers.

Several other BSM models have also been put forward in view to explain the non baryonic cold dark matter scenario. They include the Inert doublet Model (IDM) [46], models including fermionic [47], vector [48], scalar [49] and gauge singlet scalar dark matter [50]. Usually an externally imposed discrete (global) symmetry like Z_2 stabilises these dark matter candidates. In some other cases the symmetry stabilising the dark matter is derived from the breaking of some imposed local gauge symmetry. In other cases, the dark matter may have a very small decay width and hence stable on cosmological scales. Indirect detection prospects of the latter type of dark matter are much more promising than the rest.

Further, the dark matter and its anti-particle may be different from each other, i.e., an asymmetry is created between them in some early epochs of the universe. The mechanism of asymmetry production is usually taken to be the same as the mechanism producing the observed (and yet unexplained) baryon asymmetry. Such asymmetric dark matter models [51] have also been quite successful in explaining the cold dark matter paradigm.

1.5 Thermal Dark Matter and WIMP miracle

As discussed in section 1.3, an appropriate dark matter candidate should be stable on cosmological scales. In the early universe all the particles present are believed to remain in thermal equilibrium with each other. We know that for particles in equilibrium, their

number density n goes as :

$$n \sim T^3 \quad (m \ll T, \text{ relativistic}) \quad (1.11)$$

$$n \sim (mT)^{3/2} e^{-\frac{m}{T}} \quad (m \gg T, \text{ non-relativistic}) \quad (1.12)$$

The dark matter particles being predominantly non-relativistic, it is obvious from the above expression that they must drop out of the thermal bath, otherwise, their number densities will be exponentially suppressed and will not be present today in copious amounts, thereby contradicting experimental observations. Such dark matter particles which were once in thermal equilibrium but then at some point of time during the evolution of the universe drop off from the thermal plasma are categorised as "thermal dark matter". Dark matter particles will go out of equilibrium if and only if their rate of interaction falls below the Hubble expansion rate at some epoch (commonly known as the freeze-out time, corresponding temperature of the universe is the freeze-out temperature, denoted by T_f). The interaction rate is written as $\Gamma \simeq n \sigma$ where σ is the cross section and n is the number density of the particle under consideration (for non-relativistic particles, the rate is given by $\Gamma \simeq n \sigma v$, v being the relative velocity of the colliding particles). The Hubble parameter, using Friedman's equations, is given by :

$$H(T) = \sqrt{\frac{8\pi G}{3} \rho(T)} \quad (1.13)$$

where ρ is the total energy density of the universe (at a certain epoch). It is generally assumed that the dark matter has decoupled during the radiation dominated epoch. In that case ρ will be replaced by ρ_{rad} with,

$$\rho_{\text{rad}} = g_{\star} \frac{\pi^2}{30} T^4 \quad (1.14)$$

g_{\star} being the number of relativistic degrees of freedom. Hence the Hubble expansion rate in the radiation dominated era is given as $H(T) \simeq \frac{T^2}{M_{\text{pl}}}$, M_{pl} being the Planck mass and $M_{\text{pl}} = 2.4 \times 10^{18} \text{ GeV}$.

The particle drops out of the thermal soup when the interaction rate falls below the rate of the expansion $n \sigma \ll H$. The freeze-out temperature is derived from the relation $n \sigma \sim H$. So, we have :

$$n(T_f) = \frac{T_f^2}{M_{\text{pl}} \sigma} \quad (1.15)$$

Using the expression for number density for non-relativistic particles (Eq. 1.12) and defining a dimensionless quantity $x_f \equiv \frac{m_{\text{DM}}}{T_f}$ in the above equation we get :

$$\sqrt{x_f} (M_{\text{pl}} \times m_{\text{DM}} \times \sigma) e^{-x_f} = 1 \quad (1.16)$$

Taking the cross section to be around weak scale (i.e. $\sigma \sim G_F^2 m_{\text{DM}}^2$) and $m_{\text{DM}} \sim \mathcal{O}(100)$ GeV, we find $x_f \sim 20 - 30$. Now, the present relic density of dark matter particle is :

$$\Omega_{\text{DM}} \equiv \frac{\rho_{\text{DM}}}{\rho_c} = \frac{m_{\text{DM}} n(T_0)}{\rho_c} \quad (1.17)$$

Here, ρ_c is the critical energy density of the universe, ρ_{DM} is the energy density of the dark matter and T_0 is the temperature of the universe today. In the last step of the above equation, the expression for energy density of a non-relativistic particle has been used. From the conservation of entropy of the universe we have :

$$\frac{n(T_f)}{T_f^3} = \frac{n(T_0)}{T_0^3} \quad (1.18)$$

Using the above expression along with Eq. 1.15 in Eq. 1.17 we get :

$$\Omega_{\text{DM}} = \frac{x_f T_0^3}{\sigma \rho_c M_{\text{pl}}} \quad (1.19)$$

After plugging in the numerical values of the constant, this takes the form [52] :

$$\Omega_{\text{DM}} h^2 = 0.12 \left(\frac{x_f}{20} \right) \left(\frac{10^{-8} \text{ GeV}^{-2}}{\sigma} \right) \quad (1.20)$$

This shows that annihilation cross sections in the range of weak interactions, for $\mathcal{O}(100)$ GeV dark matter particles, “miraculously ” gives the correct observed relic density. This is what came to be known as the “WIMP Miracle” and sets a natural benchmark to search for suitable dark matter particles. However, we should not stick to this hypothesis too strictly. It is clear from the derivation above that we can vary the mass and the cross section simultaneously while satisfying the observed relic density, even outside the WIMP miracle regime [53].

1.6 Thermal Dark Matter : Formal solutions

As discussed in the previous section, dark matter species which once formed a part of the cosmic thermal bath, but froze out later when their rate of interaction fell below that of the Hubble expansion, are called thermal dark matter. Hence, the condition for a dark matter to be thermal can be stated as :

$$\begin{aligned} \frac{\Gamma_{\text{DM}}(T)}{H(T)} &< 1 \quad (T < T_f) \\ \frac{\Gamma_{\text{DM}}(T)}{H(T)} &> 1 \quad (T > T_f) \end{aligned} \quad (1.21)$$

After freeze-out since the dark matter goes out of equilibrium, its phase space distribution function has to be solved separately. The evolution of phase distribution function of dark matter (χ , say), is governed by the Boltzmann equation. Schematically it is written as :

$$\hat{L}[f] = C[f] \quad (1.22)$$

Here, $f \equiv f(p^\mu, x^\mu)$ is the distribution function that we are seeking for. It depends generally on the four momentum (p^μ) and the space-time point (x^μ). But under the assumption that space is homogeneous and isotropic (in cosmological scales), the distribution function depends only on energy and time, i.e., $f \equiv f(E, t)$. \hat{L} is the Liouville operator and on the RHS, C is the collision operator containing the microscopic details of the interactions of the particle under study. In a covariant and relativistic theory the Liouville operator can be written in general as :

$$\hat{L} = p^\alpha \frac{\partial}{\partial x^\alpha} - \Gamma_{\beta\gamma}^\alpha p^\beta p^\gamma \frac{\partial}{\partial p^\alpha} \quad (1.23)$$

where, $\Gamma_{\beta\gamma}^\alpha$ is the Christoffel symbol corresponding to the metric under study. For the homogeneous and isotropic universe, using the FRW metric (Eq. 1.2) the Liouville operator takes the form :

$$\hat{L}[f] = E \frac{\partial f}{\partial t} - H(t) p^2 \frac{\partial f}{\partial E} \quad (1.24)$$

Here, $H(t)$ is the Hubble parameter, and is related to the scale factor (R) of the universe as $H \equiv \dot{R}/R$ and p is the modulus of the three-momentum vector \vec{p} of the particle under study. The number density in terms of the phase space density is written as:

$$n(t) = \frac{g}{(2\pi)^3} \int d^3p f(E, t), \quad (1.25)$$

g being the number of internal degrees of freedom.

Using eq. 1.24 in Eq. 1.22, we have :

$$\begin{aligned} E \frac{\partial f}{\partial t} - H(t) p^2 \frac{\partial f}{\partial E} &= C[f] \\ \Rightarrow \frac{\partial f}{\partial t} - H(t) \frac{p^2}{E} \frac{\partial f}{\partial E} &= \frac{C[f]}{E} \end{aligned} \quad (1.26)$$

Next, we integrate both sides of the above equation by $\frac{g}{(2\pi)^3} \int d^3p$. In the LHS of Eq. 1.26, we change variables from d^3p to dE , and after performing integration by parts and throwing away boundary terms (using the fact that distribution functions vanish at $E = 0$ and $E = \infty$), we finally arrive at :

$$\frac{g}{(2\pi)^3} \int \hat{L}[f] \frac{d^3p}{E} = \frac{\partial n}{\partial t} + 3Hn. \quad (1.27)$$

And consequently, Eq. 1.26 becomes :

$$\frac{\partial n}{\partial t} + 3Hn = \frac{g}{(2\pi)^3} \int C[f] \frac{d^3p}{E} \quad (1.28)$$

Thus, the Boltzmann equation has been transformed into a rate equation giving the evolution of number density with time. The collision term on the right hand side depends on the details of the interaction. Let us consider, for simplicity a $2 \rightarrow 2$ process ($\chi + a \rightarrow i + j$, say). RHS of Eq. 1.28 then becomes :

$$\begin{aligned} \frac{g_\chi}{(2\pi)^3} \int C[f] \frac{d^3p_\chi}{E_\chi} = & - \int d\Pi_\chi d\Pi_a d\Pi_i d\Pi_j \times (2\pi)^4 \times \delta^4(p_\chi + p_a - p_i - p_j) \\ & \times \left(|\mathcal{M}|_{\chi+a \rightarrow i+j}^2 f_\chi f_a (1 \pm f_i)(1 \pm f_j) - |\mathcal{M}|_{i+j \rightarrow \chi+a}^2 f_i f_j (1 \pm f_\chi)(1 \pm f_a) \right) \end{aligned} \quad (1.29)$$

Here, f_χ, f_a, f_i, f_j are the phase space distribution functions of the corresponding particles and $d\Pi \equiv \frac{g}{(2\pi)^3} \frac{d^3p}{2E}$ is the phase space factor. $|\mathcal{M}|_{\chi+a \rightarrow i+j}^2$ is the matrix element squared for the process $\chi + a \rightarrow i + j$ and the initial and final spin states were summed up. It includes all the symmetry factors as well.

If the final state particles are fermions, and if a particular phase space state is already occupied, then no other fermions can occupy the same. This leads to the Pauli blocking terms $(1 - f_\chi), (1 - f_a)$ etc. Along similar lines, if the final state particles are bosons then more and more particles will tend to occupy the same state in the phase space. This gives rise to the stimulated emission terms $(1 + f_\chi), (1 + f_a)$ and others.

More generally, the Boltzmann equations should be a coupled set of differential equations and should be solved for the phase space distribution functions of each species. But for most of the cases of interest to us, one or more of the particles under consideration will follow an equilibrium distribution function and hence simplifying the problem.

Eq. 1.29 can be simplified further on basis some legitimate assumptions. They are discussed below :

- **CP invariance** : As with the most dark matter models, the particle is its own antiparticle, and the theory is CP even. Under this assumption :

$$|\mathcal{M}|_{\chi+a \rightarrow i+j}^2 = |\mathcal{M}|_{i+j \rightarrow \chi+a}^2 \equiv |\mathcal{M}|^2 \quad (1.30)$$

Using this, Eq. 1.29 becomes :

$$\begin{aligned} \frac{g_\chi}{(2\pi)^3} \int C[f] \frac{d^3p_\chi}{E_\chi} = & - \int d\Pi_\chi d\Pi_a d\Pi_i d\Pi_j \times (2\pi)^4 \times \delta^4(p_\chi + p_a - p_i - p_j) \\ & \times |\mathcal{M}|^2 \times \left(f_\chi f_a (1 \pm f_i)(1 \pm f_j) - f_i f_j (1 \pm f_\chi)(1 \pm f_a) \right) \end{aligned} \quad (1.31)$$

However, a class of popular models called “Asymmetric dark matter models” exist, where this assumption is relaxed. CP violation is also taken into account in scenarios which try to explain Baryogenesis.

- **Classical Statistical mechanical regime** : For most of the particle species which are in equilibrium with the thermal soup, we will use Maxwell-Boltzmann distribution function instead of Fermi-Dirac or Bose-Einstein distribution. For cold (non relativistic) dark matter scenarios, working within the framework of classical statistical mechanics yields excellent results. In this case, we can neglect the Pauli blocking and stimulated emission terms, i.e. $1 \pm f \simeq 1$. Eq. 1.29 hence gets further simplified to :

$$\begin{aligned} \frac{g_\chi}{(2\pi)^3} \int C[f] \frac{d^3 p_\chi}{E_\chi} &= - \int d\Pi_\chi d\Pi_a d\Pi_i d\Pi_j \times (2\pi)^4 \times \delta^4(p_\chi + p_a - p_i - p_j) \\ &\times |\mathcal{M}|^2 \times \left(f_\chi f_a - f_i f_j \right) \end{aligned} \quad (1.32)$$

- **Particles in the thermal bath follow Maxwell-Boltzmann distribution** : In the above equation, let us assume that particles i and j are in thermal equilibrium and follows a Maxwell-Boltzmann distribution function, i.e. $f_i \sim e^{-\frac{E_i}{T}}$ and $f_j \sim e^{-\frac{E_j}{T}}$. Using this, along with the fact that total energy is conserved, we have :

$$f_i f_j = e^{-\frac{E_i}{T}} \times e^{-\frac{E_j}{T}} = e^{-\frac{E_i + E_j}{T}} = e^{-\frac{E_\chi + E_a}{T}} = e^{-\frac{E_\chi}{T}} \times e^{-\frac{E_a}{T}} = f_\chi^{\text{eq}} f_a^{\text{eq}} \quad (1.33)$$

Note, that in the case when particles a and χ are in equilibrium with the thermal bath composed of particles i and j , the relation $f_i f_j = f_\chi^{\text{eq}} f_a^{\text{eq}}$ follows more generally from the principle of detailed balance. With this, our equation is further simplified to :

$$\begin{aligned} \frac{g_\chi}{(2\pi)^3} \int C[f] \frac{d^3 p_\chi}{E_\chi} &= - \int d\Pi_\chi d\Pi_a d\Pi_i d\Pi_j \times (2\pi)^4 \times \delta^4(p_\chi + p_a - p_i - p_j) \\ &\times |\mathcal{M}|^2 \times \left(f_\chi f_a - f_\chi^{\text{eq}} f_a^{\text{eq}} \right) \end{aligned} \quad (1.34)$$

Here, f_χ^{eq} and f_a^{eq} are the equilibrium phase space distribution functions of χ and a respectively (usually taken to be the Maxwell-Boltzmann distribution).

Under all these assumptions, the final Boltzmann equation thus turns out to be :

$$\begin{aligned} \frac{\partial n_\chi}{\partial t} + 3Hn_\chi &= - \int d\Pi_\chi d\Pi_a d\Pi_i d\Pi_j \times (2\pi)^4 \times \delta^4(p_\chi + p_a - p_i - p_j) \\ &\times |\mathcal{M}|^2 \times \left(f_\chi f_a - f_\chi^{\text{eq}} f_a^{\text{eq}} \right) \end{aligned} \quad (1.35)$$

Now, by definition, the annihilation cross section for the process $\chi + a \rightarrow i + j$ is written as :

$$\sigma_{\chi+a \rightarrow i+j} = \frac{1}{E_\chi E_a g_\chi g_a v} \sum_{\text{spin}} \int d\Pi_i d\Pi_j (2\pi)^4 \delta^4(p_\chi + p_a - p_i - p_j) |\mathcal{M}|_{\chi+a \rightarrow i+j}^2, \quad (1.36)$$

where E_χ , E_a are the energies of the particles χ and a respectively. g_χ and g_a are their internal degrees of freedom. v is the relative velocity between the incoming particles and is given by :

$$v = \frac{\sqrt{(\vec{p}_\chi \cdot \vec{p}_a)^2 - m_\chi^2 m_a^2}}{E_\chi E_a} \quad (1.37)$$

Using this definition of cross section, Eq. 1.35 can be rewritten as :

$$\frac{\partial n_\chi}{\partial t} + 3Hn_\chi = -\langle \sigma_{\chi+a \rightarrow i+j} v \rangle (n_\chi n_a - n_\chi^{\text{eq}} n_a^{\text{eq}}) \quad (1.38)$$

Here $\langle \sigma_{\chi+a \rightarrow i+j} v \rangle$ is called the velocity averaged annihilation cross section and is defined as :

$$\langle \sigma_{\chi+a \rightarrow i+j} v \rangle = \frac{\int \sigma_{\chi+a \rightarrow i+j} v dn_\chi^{\text{eq}} dn_a^{\text{eq}}}{\int dn_\chi^{\text{eq}} dn_a^{\text{eq}}} \quad (1.39)$$

In most of the calculations of dark matter relic density, annihilation processes turns out to be the most dominant ones i.e. processes of the form $\chi + \chi \rightarrow \text{anything}$. For such cases, a closed form analytical expression for the thermally averaged cross section can be derived [54] :

$$\langle \sigma_{\chi+\chi \rightarrow i+j} v \rangle = \frac{1}{8m_\chi^4 T K_2^2(m_\chi/T)} \int_{4m_\chi^2}^{\infty} \sigma_{\chi+\chi \rightarrow i+j} \sqrt{s} (s - 4m_\chi^2) K_1(\sqrt{s}/T) ds \quad (1.40)$$

Here, \sqrt{s} is the center of mass energy of the system and $K_1(x)$, $K_2(x)$ are modified Bessel functions of orders 1 and 2 respectively. An important point to note here is that the above expression is valid only under the *assumption* that the particle χ at some point of time was a part of the thermal background which is well described by a Maxwell-Boltzmann phase space distribution function. If along with $\chi + \chi \rightarrow i + j$, other annihilation channels also exist, then all of them has to added together and $\sigma_{\chi+\chi \rightarrow i+j}$ is replaced simply by σ_{tot} . Eq. 1.38 now takes the form :

$$\frac{\partial n_\chi}{\partial t} + 3Hn_\chi = -\langle \sigma_{\text{tot}} v \rangle (n_\chi^2 - (n_\chi^{\text{eq}})^2) \quad (1.41)$$

The second term in the LHS of the above equation (namely, $3Hn_\chi$) is the dilution factor, that takes into account the expansion of the universe and gives us an idea about the

amount of dilution to the number density of χ due to it. However, it is useful to scale out this effect of expansion by considering the number density of χ per comoving volume, or the comoving number density. The comoving number density is defined as $Y_\chi \equiv \frac{n_\chi}{s}$, s being the entropy density of the universe. Considering the universe to be isentropic, i.e. $sR^3 = \text{constant}$, we have :

$$\frac{\partial n_\chi}{\partial t} + 3Hn_\chi = s \frac{\partial Y_\chi}{\partial t} \quad (1.42)$$

The entropy density, s is given by :

$$s = \frac{2\pi^2}{45} g_{*s} T^3, \quad (1.43)$$

where, g_{*s} is the relativistic degrees of freedom related to entropy density of the universe and

$$g_{*s} = \sum_{i=\text{bosons}} g_i \frac{T_i^3}{T^3} + \frac{7}{8} \sum_{i=\text{fermions}} g_i \frac{T_i^3}{T^3} \quad (1.44)$$

Here, g_i is the internal degrees of freedom of particle i and T_i is its temperature. At most of the epochs during the evolution of the universe $T_i = T$, T being the common temperature of the thermal bath.

At this point we can change the time variable to a dimensional variable $x \equiv \frac{m_\chi}{T}$, T being the temperature of the universe. We *assume* that the dark matter particle (χ) drops out of the thermal bath during the radiation dominated epoch. Hence, the age (time) and temperature of the universe (or, for that matter, the variable x), are related by :

$$t = 0.301 \frac{1}{\sqrt{g_*}} \frac{M_{\text{pl}}}{m_\chi^2} x^2 \quad (1.45)$$

Here, M_{pl} is the Planck mass and has a value of 2.4×10^{18} GeV. g_* is the effective relativistic degrees of freedom related to the energy density of the universe. It is written as :

$$g_* = \sum_{i=\text{bosons}} g_i \frac{T_i^4}{T^4} + \frac{7}{8} \sum_{i=\text{fermions}} g_i \frac{T_i^4}{T^4} \quad (1.46)$$

Here, as usual, g_i is the internal degrees of freedom of the corresponding particle, and T_i is its equilibrium temperature.

As mentioned in section 1.5, the Hubble expansion rate of the universe in the radiation dominated epoch (in terms of x) can be written as $H(x) = \frac{H(m_\chi)}{x^2}$ (upon using Eq. 1.14 in Eq. 1.13), where $H(m_\chi) = 1.67 \sqrt{g_*} \frac{m_\chi^2}{M_{\text{pl}}}$. The relativistic degrees of freedom related to entropy and energy density can be approximately taken to be constant during the early

radiation dominated universe. Using the particle content of the Standard Model and the fact that if $m \gg T_{\text{universe}}$ for any particle with mass m , then that particle can be taken to be non-relativistic and its number density exponentially suppressed. The evolution of g_* and g_{*s} is plotted in Fig. 1.7. Hence, under this assumption, using Eq. 1.42 and Eq. 1.45, one

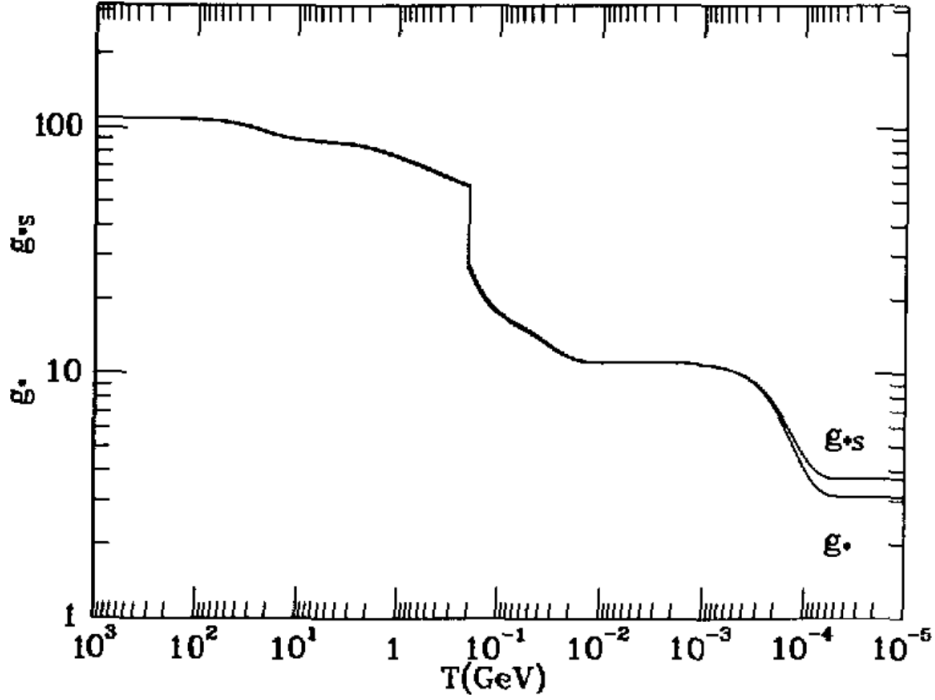


Figure 1.7: Variation of g_* and g_{*s} with temperature (T in GeV) of the universe. The small difference between the two in the low temperature regime (i.e. during the latter part of the universe) occurs due to neutrino decoupling [8].

can write the final workable form of the Boltzmann equation in terms of the comoving number density of χ :

$$\frac{dY_\chi}{dx} = -\frac{x \langle \sigma_{\text{tot}} v \rangle s}{H(m_\chi)} (Y_\chi^2 - (Y_\chi^{\text{eq}})^2) \quad (1.47)$$

For non-relativistic species ($x \gg 1$), $Y_\chi^{\text{eq}} \equiv \frac{n_\chi^{\text{eq}}}{s}$ is given by (assuming Maxwell-Boltzmann distribution) :

$$Y_\chi^{\text{eq}}(x) = 0.145 \frac{g}{g_{*s}} x^{3/2} e^{-x}, \quad (1.48)$$

g_χ being the internal degrees of freedom and s being the entropy density of the universe defined in Eq. 1.43.

Eq. 1.47 is a special form of Riccati equations and in general does not possess any closed form solutions. We can solve this equation very easily numerically to get accurate

results. However, we can also solve this equation analytically making some educated approximations and get results within 5% accuracy. For this, $\langle\sigma_{\text{tot}}v\rangle$ is parametrised as $\langle\sigma_{\text{tot}}v\rangle = \sigma_0 x^{-n}$, where $n=0$ stands for s-wave annihilation, $n=1$ for p-wave annihilation and so on. Next, the departure of comoving number density from its equilibrium value ($\Delta \equiv Y_\chi - Y_\chi^{\text{eq}}$) is tracked for early and late times. In terms of Δ , Eq. 1.47 is rewritten as :

$$\frac{d\Delta}{dx} = -\frac{dY_\chi^{\text{eq}}}{dx} - \lambda x^{-n-2} \Delta (2Y_\chi^{\text{eq}} + \Delta) \quad (1.49)$$

Considering the solutions of the above equation at early ($x \ll x_f$) and late times ($x \gg x_f$), it can be shown easily [8] that :

$$Y_\chi(x = \infty) = \Delta(x = \infty) = \frac{n+1}{\lambda} x_f^{n+1} \quad (1.50)$$

Using the rate of interaction for the χ particles, $\Gamma_{\text{int}} = n_\chi^{\text{eq}} \langle\sigma_{\text{tot}}v\rangle$, one can determine the value of x_f from the condition :

$$\Gamma_{\text{int}}(x_f) \simeq H(x_f), \quad (1.51)$$

$H(x)$ being the Hubble expansion rate. With this solution of x_f , the final comoving number density of χ is found to be :

$$Y_\chi(x = \infty) = \frac{5\sqrt{g_*} x_f^{n+1}}{g_{*s} M_{\text{pl}} m_\chi \sigma_0} \quad (1.52)$$

Finally, knowing this, it is straight forward to calculate the present day relic density of dark matter :

$$\Omega_\chi h^2(x = \infty) = 2.755 \times 10^8 \left(\frac{m_\chi}{\text{GeV}} \right) Y_\chi(x = \infty) \quad (1.53)$$

The variation of comoving number density with x is obtained from Eq. 1.47, and is plotted in Fig. 1.8. It is clear from the plot that if the particle species remains in equilibrium, then its (comoving) number density falls off exponentially with increasing x . Hence for a dark matter particle to match with the present day observed relic, it should drop out of the thermal bath (freeze-out) as shown by the dotted lines. Also it is to be noted, that with increasing $\langle\sigma_{\text{tot}}v\rangle$, the point of freeze-out (i.e the point from where the curve starts to flatten out) shifts more towards right. This is to be expected, because more strongly the particle interacts with the thermal bath, later it will freeze-out. The final value of Y hence also decreases with increasing $\langle\sigma_{\text{tot}}v\rangle$.

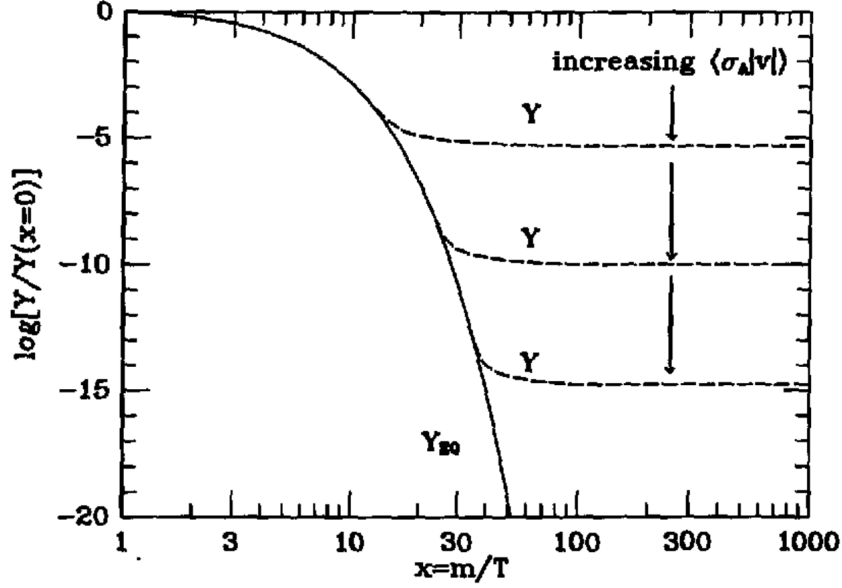


Figure 1.8: Variation of comoving number density Y with x for a Weakly interacting massive particle with mass $\sim \mathcal{O}(100)$ GeV. The dotted lines represent the comoving number density after freeze-out, while the solid represents the corresponding equilibrium value [8].

1.7 Direct and Indirect searches for Dark Matter

1.7.1 Direct searches for (thermal) dark matter

Motivated by the success of thermal WIMP scenarios in explaining the observed relic density naturally, several attempts were made to directly detect the same. The direct detection is mainly based on the measurement of recoil energy of nucleon when it gets hit by a dark matter particle [55]. The collision is usually assumed to be elastic in nature. Based on the type of interaction of dark matter and the quarks (or for that matter, nucleons), the cross section (related to the event rate measured by the experiments) can be classified as spin dependent and spin independent. Vertices of the form $\bar{\chi}\gamma^\mu\chi Z'_\mu$ (Z' being a vector mediator) and $\bar{\chi}\chi A$ (A being a scalar mediator) gives rise to spin independent cross sections, while, vertices of the type $\bar{\chi}\gamma^\mu\gamma^5\chi Z'_\mu$ (Z' being an axial-vector mediator) and $\bar{\chi}\gamma^5\chi A$ (A being a pseudo-scalar mediator) gives rise to spin dependent ones. The presence of DM is being investigated in various direct detection experiments, namely LUX [56], XENON 100 [57], DarkSide-50 [58] etc, and no “real signal” due to a dark matter particle has been observed yet. Although recently, some experiments have claimed to detect dark matter

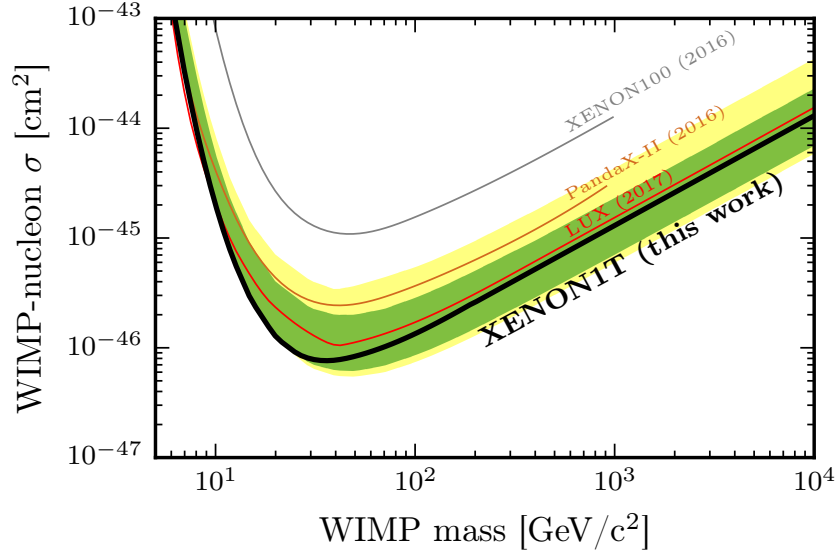


Figure 1.9: Upper bounds on WIMP-nucleon spin independent cross section from Xenon1T collaboration [9].

signals [59, 60], but they are in conflict with the null results obtained from similar other experiments [61, 62]. On the other hand experiments like DAMA/LIBRA claim to have detected dark matter through the observation of an annual modulation in their signals due to the relative motion of earth with respect to the static dark matter halo [63, 64]. However they are in disagreement with other experiments and no definitive conclusions can be reached. Non-observability of dark matter signals from many of the direct detection experiments have put stringent upper bounds on the DM-nucleon cross section (as a function of dark matter mass). The strongest limit for the spin independent DM-nucleon cross section comes from XENON1T [9]. The exclusion plot is shown in Fig. 1.9. For the spin dependent case, the limits are usually weaker. The most updated bound on DM-proton spin dependent cross section is provide by PICO and LUX collaborations [65, 66]. For low mass WIMPs (with mass less than 4 GeV), competitive bounds can be obtained from the PICASSO experiment [67].

1.7.2 Indirect signals and possible hints of dark matter

Besides these direct search experiments people around the world are also trying to look for indirect signals of dark matter. They are usually secondary particles (protons, anti-protons, electrons, neutrinos and photons) created due to dark matter decay or annihilation. The photons are the cleanest and most dependable channel for dark matter detec-

tion, since they are unperturbed by magnetic fields, have almost no interaction with the intergalactic medium, possess small propagation uncertainties and hence retain a lot of information about the source. We briefly mention below some indirect signals which may have originated from dark matter.

1-3 GeV Gamma-ray excess from galactic center

The Fermi-LAT telescope has observed a small excess in the photon spectrum from around the galactic center around an energy of ~ 3 GeV [68–70]. In spite of several astrophysical explanations of the signal [71–73], dark matter origin of the same has not been ruled out completely. It has been shown that a 30–40 GeV dark matter particle annihilating mostly to $b\bar{b}$ or $\tau\bar{\tau}$ can give rise to this excess as well [74].

3.55 keV X-ray line

The XMM-newton telescope has observed an unexplained 3.55 keV X-ray emission line from the Perseus cluster [75]. However, later, similar anomalous line like features were also observed from many other galaxies including Andromeda [76–79]. Since this excess has line-like morphology, most dark matter explanations relied on a decaying dark matter scenario (obviously, the dark matter is stable on cosmological time scales) with mass ~ 7 keV [80,81]. Some other explanations include a two component dark matter scenario with a tree level mass splitting of 3.55 keV. The heavier one can decay (via loop suppressed processes) to the lighter dark matter and a X-ray of energy 3.55 keV [82,83]. Like before, besides the dark matter explanations of the signal, several astrophysical scenarios can also explain the same [84,85]. Recently it is also being believed that the line may have originated due to atomic transitions in potassium present inside the stars. The 3.55 keV line has also been observed from a supernova remnant called Tycho and the latter has very little dark matter content in it [84].

511 keV emission line

In 2003 INTEGRAL/SPI [86] of ESA observed an emission line at an energy of 511 keV mostly from the galactic bulge. Recently, it has been reported that the measured flux from the galactic bulge by INTEGRAL/SPI is $\Phi_{511}^{\text{exp}} = (0.96 \pm 0.07) \times 10^{-3} \text{ph cm}^{-2} \text{s}^{-1}$ at 56σ significance [87]. A possible source of this line is assumed to be the annihilation of electron and positron in the galactic core. In spite of some astrophysical processes explaining the origin of the line [88], the sources of the galactic positrons are not clear yet. Hence a series

of possible explanations have been reported in last ten years involving positrons originating from a decaying [89, 90] or annihilating [91, 92] dark matter. For a brief review of earlier works trying to explain 511 keV line see [93]. Recently the authors of Ref. [94] have shown that the explanation of this anomalous emission line is not possible from the annihilation of thermal dark matter (WIMP) due to conflict with the latest cosmological data and they have preferred a non-thermal origin of dark matter for explaining this long standing puzzle.

Excess amounts of charged particles in cosmic rays

The proton and anti-proton fluxes as measured by AMS-02 show an excess over the estimated background [95]. This can be well explained from dark matter annihilations with mass of dark matter between 20–80 GeV and velocity averaged hadronic cross sections $\sim (0.2 - 5) \times 10^{-26} \text{ cm}^3 \text{ s}^{-1}$ [96]. Astrophysical sources however can also explain this excess satisfactorily [97].

The PAMELA satellite has also reported an excess in the positron fraction $e^+/(e^+ + e^-)$ in the energy range of 10–100 GeV [98]. Later their claim was confirmed by an independent measurement from the FERMI collaboration. They extended the range upto 200 GeV [99]. The signal was shown to be matched well by a dark matter annihilation scenario with mass $\sim 3 \text{ TeV}$. However the annihilation cross section required for the purpose $\sim 2 \times 10^{-22} \text{ cm}^3 \text{ s}^{-1}$, which is too high for a thermal WIMP like scenario [100]. Among the astrophysical sources supernova remnants can also explain this excess as shown in [101].

1.8 Non-thermal Dark Matter

With the increasing sensitivity of the direct detection experiments [102–104], the WIMP-nucleon cross section will soon merge with the coherent elastic neutrino-nucleus cross section (Fig. 1.10) [105, 106]. The floor mostly comprises of 8_B and 7_{Be} solar neutrinos [107]. Hence in future our only probe to distinguish a dark matter signal (assuming that DM is a thermal WIMP) from the neutrino background will be through directional searches [108]. But if we wish to move beyond this thermal WIMP scenario, there is another class of dark matter candidates which are produced through non-thermal processes at an early stage of the Universe. Such possibilities include axino [109–111], gravitino [112, 113], very heavy dark matter candidates like WIMPzillas [114] among many others [115]. As discussed in the earlier sections, thermal dark matters was initially in equilibrium with the cosmic plasma and later when its interaction strengths could not

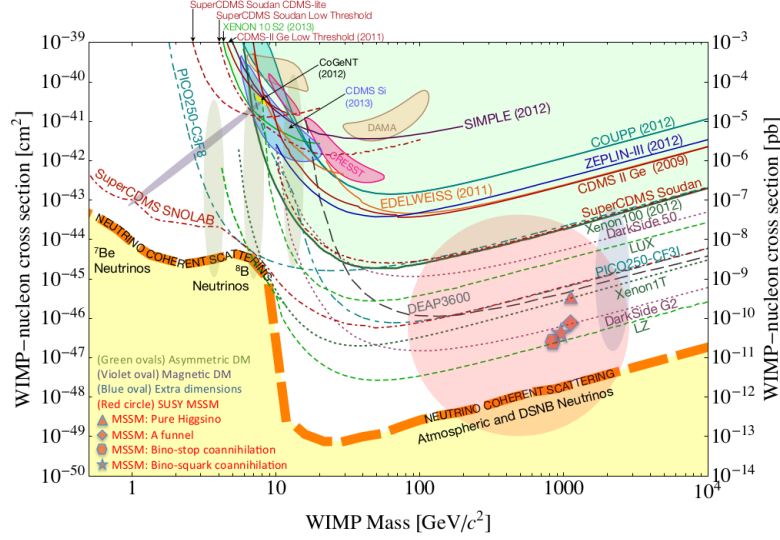


Figure 1.10: Upper bounds DM-nucleon cross section from non-observations in direct detection experiments. Along with this, the neutrino nucleon coherent scattering cross section has also been superposed for comparison [10].

keep up with the Hubble expansion rate, it *froze out*. In this case, however, the particles are so weakly interacting to begin with, that they can never get into equilibrium with the thermal soup. Consequently, their initial number density is extremely tiny and they have to be produced in correct amount so as to match the present day relic abundance. In most of cases they are produced from the decays of heavier particles. These types of dark matter candidates are known as Feebly Interacting Massive Particle or FIMP [12]. In contrast to the commonly discussed “freeze-out” scenario, the relic density of FIMP type dark matter is attained by the so called “freeze-in” mechanism, where the abundance of dark matter steadily rises from an initial negligible amount and finally saturates (freezes in) at the observed value of relic density [12]. The mathematical condition for non-thermality (in contrast to the condition for a thermal dark matter i.e. Eq. 1.21) can be stated as :

$$\frac{\Gamma_{\text{DM}}(T)}{H(T)} \ll 1 \quad (\forall T), \quad (1.54)$$

where, Γ_{DM} is the interaction rate of dark matter.

As mentioned earlier, one of the most common production channels of non-thermal dark matter is from a decay of another heavier mother particle. Following [11, 12], let us

consider the case when non-thermal dark matter particle χ is produced from the decay of σ ($\sigma \rightarrow \chi\chi$). Due to the extremely low abundance of χ , the inverse process can be safely neglected in the analysis. Also, let us assume for simplicity that the mother particle σ is in equilibrium with the thermal soup and follows a Maxwell-Boltzmann distribution function. If σ itself is also out of equilibrium, then calculation of relic density is little more involved, and discussions regarding such scenarios are postponed to a later chapter. Here, the rate equation can thus be written as :

$$\frac{dn_\chi}{dt} + 3Hn_\chi = 2 \frac{K_1(m_\sigma/T)}{K_2(m_\sigma/T)} \Gamma_\sigma n_\sigma^{\text{eq}}, \quad (1.55)$$

where Γ_σ is the decay width of $\sigma \rightarrow \chi\chi$ process and n_σ^{eq} is the equilibrium number density of σ . As was done in section 1.6, we now rewrite the above equation in terms of variables $Y_\chi \equiv n_\chi/s$ and $x \equiv m_\sigma/T$. We hence have :

$$\frac{dY_\chi}{dx} = 2 Y_\sigma^{\text{eq}} \frac{\Gamma_\sigma}{H x} \frac{K_1(m_\sigma/T)}{K_2(m_\sigma/T)} \quad (1.56)$$

An approximate solution of this equation is given by :

$$\Omega_{\chi,0} h^2 = 4.48 \times 10^8 \frac{g_\sigma}{g_{*s} \sqrt{g_*}} \left(\frac{m_\chi}{\text{GeV}} \right) \frac{M_{\text{pl}} \Gamma_\sigma}{m_\sigma^2} \quad (1.57)$$

Here, $\Omega_{\chi,0} h^2$ is the present day relic density, m_χ and m_σ are the masses of χ and σ respectively. All the other symbols have their usual meaning. The decay width in terms of strength of interaction y (coupling constant) is given by $\Gamma_\sigma = \frac{y^2 m_\sigma}{8\pi}$. Hence,

$$\Omega_{\chi,0} h^2 = 1.78 \times 10^7 \frac{g_\sigma}{g_{*s} \sqrt{g_*}} \left(\frac{m_\chi}{\text{GeV}} \right) \frac{y^2 M_{\text{pl}}}{m_\sigma} \quad (1.58)$$

Note, in contrast to Eq. 1.20, the final relic density in case of freeze-in is proportional to the strength of interaction i.e. y (in case of freeze-out, relic density was inversely proportional to the cross section, and consequently with the interaction strength). The difference between the two scenarios is shown in Fig. 1.11.

From Eq. 1.58, we can get an idea about the smallness of the coupling constants required for non-thermal scenarios. Eq. 1.58 can be written as [11] :

$$y = 10^{-12} \left(\frac{\Omega_{\chi,0} h^2}{0.12} \right)^{1/2} \left(\frac{g_*}{100} \right)^{3/4} \left(\frac{m_\sigma}{m_\chi} \right)^{1/2} \quad (1.59)$$

Here it is assumed that $g_* \simeq g_{*s}$ (see Fig. 1.7). The range of couplings usually required for a system to be a non-thermal or a thermal one is represented schematically in Fig. 1.12

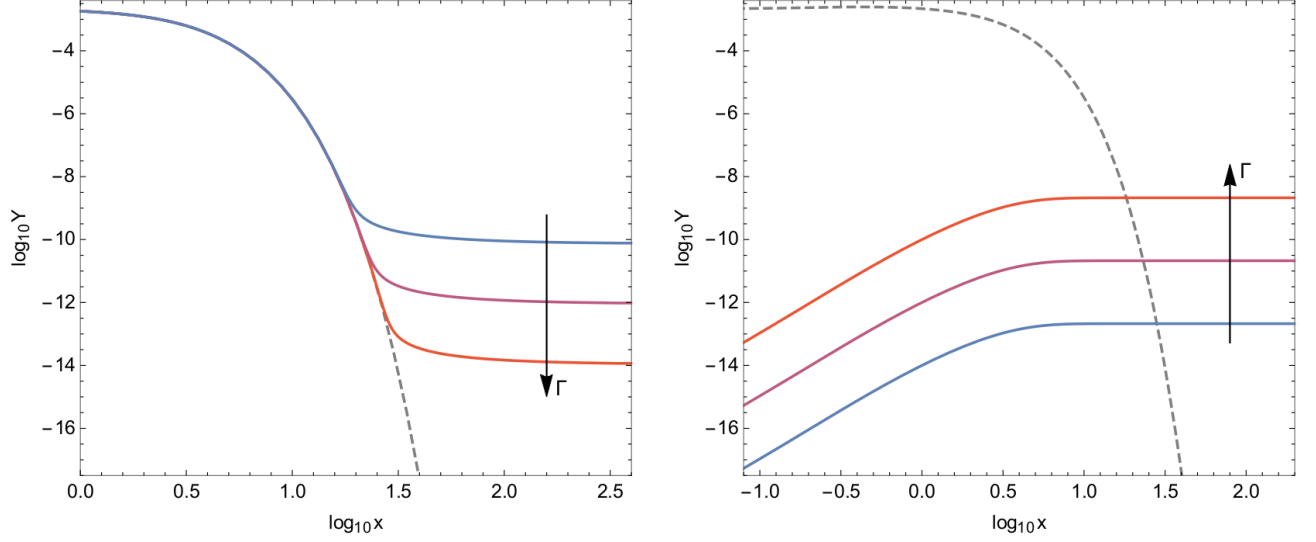


Figure 1.11: Contrasting the freeze-in and a typical freeze-out scenario. The final yield increases with the strength of interaction as shown by the upward arrow in case of freeze-in. The trend is opposite for freeze-out as expected. Note, for the freeze in case $x = m_\sigma/T$ while for the freeze-out case $x = m_\chi/T$. The plot has been taken from ref. [11].

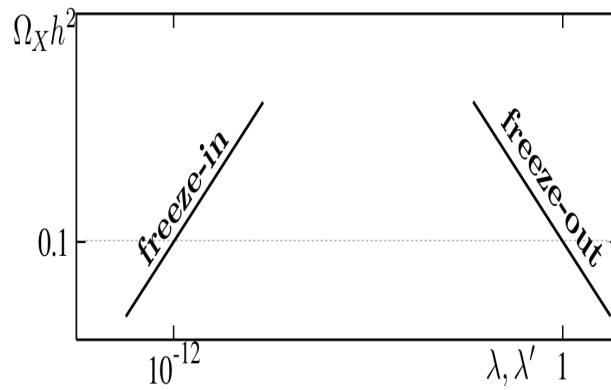


Figure 1.12: Schematic diagram showing the approximate orders of magnitude of coupling strengths (λ, λ') required for thermal and non-thermal scenarios [12].

Unlike the thermal freeze-out mechanism where the relic density depends on the final abundance of dark matter, in case of freeze-in, DM relic density is sensitive to its initial production history (for a nice review see [11, 116]). In the literature two types of freeze-in mechanisms are usually discussed, IR (infra-red) freeze-in [80, 117, 118] and UV (ultra-violet) freeze-in [119–121]. Unlike the former, the DM relic density in UV Freeze-in depends explicitly on the reheat temperature (T_R). Production of the non-thermal DM candidate, as already stated, usually occurs via a decay of a heavy mother particle (e.g. from inflaton decay and decay of heavy Moduli fields [122, 123]).

In the following chapters we will describe in detail methodology of calculating the relic density of non thermal dark matter (even when the mother particle goes out equilibrium) in the setting of some popular models. Also, we will try to provide indirect ways of detecting these feebly interacting particles, which due to their low coupling strengths almost always escape conventional direct detection techniques.

Chapter 2

Non-thermal dark matter in $U(1)_{B-L}$ model

2.1 Introduction

In this chapter we will study a FIMP type dark matter candidate in the $U(1)_{B-L}$ extension of the Standard Model of particle physics. $U(1)_{B-L}$ extension of SM is a very well motivated beyond standard model theory as it provides the explanation of non-zero neutrino mass through Type-I sea-saw mechanism [124]. In this model besides the usual SM gauge ($SU(3)_c \times SU(2)_L \times U(1)_Y$) symmetry, an additional local $U(1)_{B-L}$ symmetry invariance is also imposed on the Lagrangian where B and L respectively represent the baryon and lepton number of a particle. In order to obtain an “anomaly free gauge theory”, three additional right handed neutrinos ($N_i, i = 1, 3$) are required to be added to the particle spectrum of SM. Moreover, we also require a complex scalar (Ψ) which is a singlet under the SM gauge group but possesses a suitable nonzero $U(1)_{B-L}$ charge. Majorana masses for the three right handed neutrinos are generated through the spontaneous breaking of the local $B - L$ symmetry by the vacuum expectation value (VEV) of complex scalar singlet Ψ . The lightest one (N_1) among the three right handed neutrinos can be a viable dark matter candidate.

The dark matter candidate N_1 in $U(1)_{B-L}$ model can be produced through both thermal as well as non-thermal processes. In the former case, the interaction strengths of DM particles with others in the early Universe are such that they are able to maintain their thermal as well as chemical equilibrium. The decoupling of the DM particles occur when their interaction rates fall short of the expansion rate of the Universe. If n_{eq} and $\langle\sigma v\rangle$ are the equilibrium number density and the thermally averaged annihilation cross section of

N_1 then the decoupling condition requires $\frac{n_{\text{eq}} \langle \sigma v \rangle}{H} < 1$ with H being the Hubble parameter. Being out of equilibrium, the relic density of N_1 freezes to a particular value which depends upon the interaction strength as well as the temperature of the Universe at which the decoupling occurred (freeze-out temperature). The thermally produced N_1 as a dark matter candidate, in the $U(1)_{B-L}$ extension of SM, has been studied in Refs. [125–128]. In these works most of the authors have shown that the relic abundance of dark matter particle satisfied the WMAP or Planck limit only when the mass of DM is nearly half the masses of mediating scalar particles (at or near resonances). This requires significant fine tuning as there is no symmetry, in the Lagrangian, which can relate the masses of dark matter and the scalar sector particles in the above mentioned way (however, extra discrete symmetries are imposed to stabilise the dark matter candidate). Hence, with respect to the above discussions, it is natural to think about a dark matter particle, in this $U(1)_{B-L}$ model, which is produced through some non-thermal interactions at the early stage of the Universe. Non-thermal sterile neutrino production from the oscillation of active neutrinos was first proposed by Dodelson-Widrow [129], but this idea is now in conflict with the X-ray observations [130]. Other mechanisms of sterile neutrino production like Shi-Fuller mechanism [131] can alleviate some of these problems producing a colder dark matter spectrum. In contrast with the existing literature, we have found here that W^\pm decay can also be a dominant production mode of the sterile neutrino DM. To obtain the comoving number density of dark matter, we have solved here a coupled set of Boltzmann equations considering all possible decay as well as annihilation production modes of the sterile neutrino dark matter. Although, strictly speaking, this method is valid only in those parameter regions where the system under consideration is not far off from a thermal one. We have checked that this conclusion is indeed true for the benchmark values chosen here. If it would have been a highly non thermal system then we should not use rate equations, (*i.e.* differential equation direction in terms of comoving number density Y) instead we had to solve for distribution functions directly. But that is a more involved process and let us postpone discussions regarding this until the next chapter.

Several other models have also successfully discussed non-thermal sterile neutrino dark matter. They include some Supersymmetric models [132], models using warped extra-dimensions [133] and decay from charged [134] and neutral scalars [135, 136] or from extra gauge bosons [137, 138]. Most of the studies involving production of sterile neutrino from extra gauge boson assume the gauge boson to be in thermal equilibrium with the other SM particles. However, in this chapter we have moved way from this assumption (details later). Several non-thermal models of sterile neutrino dark matter

under the assumption of low reheating temperature have also been studied in [139–141] which is also not the case we are considering here.

Additionally, unlike what is usually done in building a dark matter model, we do not impose any extra symmetry to stabilise our dark matter candidate. For an \mathcal{O} (MeV) sterile neutrino dark matter we have a dominant decay mode to e^\pm and ν with a very large life time (larger than the age of the Universe for the parameters we consider here) which in turn helps us to propose a possible indirect detection signal of the 511 keV line observed by INTEGRAL/SPI [86] of ESA.

The rest of the chapter is organised as follows: In Section 2.2 we briefly describe the $U(1)_{B-L}$ model. In Section 2.3 we describe the production mechanism of non-thermal sterile neutrino dark matter in detail. Section 2.4 describes the Boltzmann equation(s) needed to compute the comoving number densities of both Z_{BL} and N_1 . Calculation of relic density of sterile neutrino dark matter is given in Section 2.5. Section 2.6 deals with a possible indirect detection mode of our dark matter particle N_1 . Finally our conclusion is given in Section 7. All analytic expressions of decay widths and annihilation cross sections used in this chapter are listed in the 2.8.

2.2 The $U(1)_{B-L}$ extension of Standard Model

Here we have considered a *minimal* $U(1)_{B-L}$ extension of the Standard Model where the SM gauge sector is enhanced by an additional local $U(1)_{B-L}$ gauge symmetry with B and L are known as the baryon and lepton number of a particle. Therefore, under the $U(1)_{B-L}$ gauge group all SM leptons (including neutrinos) and quarks have charges -1 and $\frac{1}{3}$ respectively. Besides the SM fields, this model requires the presence of three right handed neutrinos (N_i , $i = 1$, to 3) with $U(1)_{B-L}$ charge -1 for anomaly cancellation. On the other hand, as the SM Higgs doublet (Φ) does not possess any $B - L$ charge, hence in order to spontaneously break the local $B - L$ symmetry one needs to introduce a scalar field which transforms nontrivially under the $U(1)_{B-L}$ symmetry group. As a result, the scalar sector of the present model is composed of a usual Higgs doublet (doublet under $SU(2)_L$) Φ and a complex scalar singlet Ψ . To generate Majorana mass terms in a gauge invariant manner for the three right handed neutrinos one needs the $B - L$ charge of Ψ is $+2$. $B - L$ symmetry is spontaneously broken when Ψ acquires VEV v_{BL} while the remnant electroweak symmetry ($SU(2)_L \times U(1)_Y$) of the Lagrangian breaks spontaneously through the usual Higgs mechanism. In unitary gauge, the expressions of Φ and Ψ , after

getting VEVs v and v_{BL} respectively, are

$$\Phi = \begin{pmatrix} 0 \\ \frac{\phi+v}{\sqrt{2}} \end{pmatrix}, \quad \Psi = \frac{\psi + v_{\text{BL}}}{\sqrt{2}}. \quad (2.1)$$

The gauge invariant and renormalisable Lagrangian of the scalar sector is thus given by

$$\mathcal{L}_{\text{scalar}} = (D_{\phi_\mu} \Phi)^\dagger (D_{\phi}^\mu \Phi) + (D_{\psi_\mu} \Psi)^\dagger (D_{\psi}^\mu \Psi) - V(\Phi, \Psi), \quad (2.2)$$

with

$$\begin{aligned} V(\Phi, \Psi) = & \mu_1^2 (\Phi^\dagger \Phi) + \lambda_1 (\Phi^\dagger \Phi)^2 + \mu_2^2 (\Psi^\dagger \Psi) + \lambda_2 (\Psi^\dagger \Psi)^2 \\ & + \lambda_3 (\Phi^\dagger \Phi) (\Psi^\dagger \Psi), \end{aligned} \quad (2.3)$$

where

$$\begin{aligned} D_{\phi_\mu} \Phi &= \left(\partial_\mu + i \frac{g}{2} \sigma^a W_{a\mu} + i \frac{g'}{2} B_\mu \right) \Phi, \\ D_{\psi_\mu} \Psi &= (\partial_\mu + i Q_{\text{BL}}(\Psi) g_{\text{BL}} Z_{\text{BL}\mu}) \Psi, \end{aligned} \quad (2.4)$$

are the covariant derivatives of the scalar doublet Φ and complex scalar singlet Ψ respectively while $Q_{\text{BL}}(\Psi) = +2$ is the B - L charge of Ψ . Gauge couplings of $\text{SU}(2)_L$, $\text{U}(1)_Y$ and $\text{U}(1)_{\text{B-L}}$ are denoted by g , g' and g_{BL} . The corresponding gauge fields are $W_{a\mu}$ ($a = 1, 2, 3$), B_μ and $Z_{\text{BL}\mu}$. After spontaneous breaking of $\text{SU}(2)_L \times \text{U}(1)_Y \times \text{U}(1)_{\text{B-L}}$ symmetry by the VEVs of Φ and Ψ we get two physical neutral scalar fields h and H which can be expressed as a linear combinations of ϕ and ψ in the following way

$$\begin{pmatrix} h \\ H \end{pmatrix} = \begin{pmatrix} \cos \theta & -\sin \theta \\ \sin \theta & \cos \theta \end{pmatrix} \begin{pmatrix} \phi \\ \psi \end{pmatrix}, \quad (2.5)$$

where θ is the mixing angle between the neutral scalars h and H . The expressions of mixing angle (θ) and masses (M_h, M_H) of h and H are given by

$$\begin{aligned} \theta &= \frac{1}{2} \tan^{-1} \left(\frac{\lambda_3 v_{\text{BL}} v}{\lambda_2 v_{\text{BL}}^2 - \lambda_1 v^2} \right), \\ M_h^2 &= \lambda_1 v^2 + \lambda_2 v_{\text{BL}}^2 - \sqrt{(\lambda_1 v^2 - \lambda_2 v_{\text{BL}}^2)^2 + (\lambda_3 v v_{\text{BL}})^2}, \\ M_H^2 &= \lambda_1 v^2 + \lambda_2 v_{\text{BL}}^2 + \sqrt{(\lambda_1 v^2 - \lambda_2 v_{\text{BL}}^2)^2 + (\lambda_3 v v_{\text{BL}})^2}. \end{aligned} \quad (2.6)$$

We have considered the physical scalar h as the SM-like Higgs boson which was discovered recently by ATLAS [142] and CMS [143] collaborations and consequently we have

fixed the value of M_h at 125.5 GeV. Also according to the measured values of Higgs boson signal strengths (for its various decay modes) the mixing angle θ between the SM-like Higgs boson h and extra scalar boson H should be very small. As this mixing angle does not play any significant role in the present context, we have kept θ fixed at 0.1 rad [144], throughout this chapter, such that it satisfies all results from both ATLAS and CMS collaborations. Besides this, in order to obtain a stable vacuum the quartic couplings of the Lagrangian (Eq. 2.3) must satisfy the following inequalities,

$$\begin{aligned}\lambda_1 &\geq 0, \\ \lambda_2 &\geq 0, \\ \lambda_3 &\geq -2\sqrt{\lambda_1\lambda_2}.\end{aligned}\tag{2.7}$$

Moreover, as both Φ and Ψ have nonzero VEVs, this requires $\mu_i^2 < 0$ ($i = 1, 2$).

The gauge sector Lagrangian of the present model is given as ¹

$$\mathcal{L}_{\text{gauge}} = \mathcal{L}_{\text{gauge}}^{\text{SM}} - \frac{1}{4}Z'_{\mu\nu}Z'^{\mu\nu}.\tag{2.8}$$

Here, $\mathcal{L}_{\text{gauge}}^{\text{SM}}$ is the Lagrangian of the SM gauge sector while the second term represents the kinetic term for the B – L gauge bosons Z_{BL} and in terms of Z_{BL} the field strength tensor $Z'^{\mu\nu}$ for an abelian gauge field is defined as

$$Z'^{\mu\nu} = \partial^\mu Z_{\text{BL}}^\nu - \partial^\nu Z_{\text{BL}}^\mu.\tag{2.9}$$

The gauge invariant Lagrangian for the three right handed neutrinos can be written as:

$$\mathcal{L}_{\text{RN}} = i \sum_{i=1}^3 \bar{N}_i \not{D}_N N_i - \lambda_{R_i} \bar{N}_i^c N_i \Psi + \sum_{\alpha=1}^3 \sum_{i=1}^3 y_{\alpha i} \bar{L}_\alpha \tilde{\Phi} N_i,\tag{2.10}$$

where $\tilde{\Phi} = -i\tau_2\Phi^*$ and $\not{D}_N = \gamma_\mu D_N^\mu$ with

$$D_\mu^{N_i} N_i = (\partial_\mu - i g_{\text{BL}} Z_{\text{BL}\mu}) N_i\tag{2.11}$$

is the covariant derivative for the right handed neutrino N_i . After $U(1)_{\text{B-L}}$ symmetry breaking the masses of right handed neutrinos and Z_{BL} are given by

$$M_{Z_{\text{BL}}}^2 = 4g_{\text{BL}}^2 v_{\text{BL}}^2,\tag{2.12}$$

$$M_{N_i} = \sqrt{2}\lambda_{R_i} v_{\text{BL}}.\tag{2.13}$$

¹In general we may also have a kinetic mixing term given by $\kappa Z_{\mu\nu}Z'^{\mu\nu}$. The value of κ is however severely constrained by electroweak precision measurements ($\kappa \lesssim 10^{-4}$ [145]). So for calculational simplicity we have restricted ourselves to a parameter space where $\kappa < g_{\text{BL}}$, hence neglecting its contribution. These type of scenarios where kinetic mixing term is neglected has been previously studied under the name of “Minimal/Pure” $U(1)_{\text{B-L}}$ model [125, 126, 146].

Using above two equations one can write the coupling λ_{R_i} in terms of g_{BL} , M_{N_i} and $M_{Z_{\text{BL}}}$ which is

$$\lambda_{R_i} = \sqrt{2} \left(\frac{M_{N_i}}{M_{Z_{\text{BL}}}} \right) g_{\text{BL}}. \quad (2.14)$$

From Eq. (2.10) it is possible to generate neutrino masses via Type-I see-saw mechanism. In our analysis we want to focus on the viability of lightest sterile neutrino (N_1) as a dark matter candidate. So for simplicity we have neglected intergenerational mixing between the active and sterile neutrinos. The mass of the other two sterile neutrinos are also not constrained by our analysis, and in principle can be very heavy aiding neutrino mass generation by the see-saw mechanism. From Eq. (2.10) and Eq. (2.13), one can find the expression of active-sterile mixing angle α_i per generation as

$$\tan 2\alpha_i = -\frac{\sqrt{2} y_i v}{M_{N_i}}. \quad (2.15)$$

For simplicity, throughout this chapter we have denoted the first generation active-sterile mixing angle α_1 by only α .

The non-observation of the extra neutral gauge boson in the LEP experiment [147, 148] imposes following constraint² on the ratio of $M_{Z_{\text{BL}}}$ and g_{BL} :

$$\frac{M_{Z_{\text{BL}}}}{g_{\text{BL}}} = 2v_{\text{BL}} \geq 6 - 7 \text{ TeV}. \quad (2.16)$$

In our analysis independent parameters are:

Mass of the extra singlet Higgs M_H , Masses of all three RH neutrinos M_{N_i} , mass of extra neutral gauge boson $M_{Z_{\text{BL}}}$, scalar mixing angle θ , the new gauge coupling g_{BL} and active-sterile mixing angle α . In terms of our chosen independent set of model parameters, the other parameters appearing in Eq. (2.3) can be written as

$$\mu_1^2 = -\frac{v(M_h^2 + M_H^2) + (M_h^2 - M_H^2)(v \cos 2\theta - v_{\text{BL}} \sin 2\theta)}{4v}, \quad (2.17)$$

$$\mu_2^2 = \frac{-v^3(M_h^2 + M_H^2) + (M_h^2 - M_H^2)(v^3 \cos 2\theta + v_{\text{BL}}^3 \sin 2\theta)}{4v v_{\text{BL}}^2}, \quad (2.18)$$

$$\lambda_1 = \frac{M_h^2 + \cos 2\theta(M_h^2 - M_H^2) + M_H^2}{4v^2}, \quad (2.19)$$

$$\lambda_2 = \frac{\cos 2\theta(M_H^2 - M_h^2) + M_h^2 + M_H^2}{4v_{\text{BL}}^2}, \quad (2.20)$$

$$\lambda_3 = \frac{\sin \theta \cos \theta (M_H^2 - M_h^2)}{v v_{\text{BL}}}. \quad (2.21)$$

²For recent bounds on $M_{Z_{\text{BL}}}$ and g_{BL} from the LHC experiment see Ref. [149].

2.3 Exploring the Non-thermal Regime

Non-thermal production mechanism has been discussed in some detail in Chapter 1. Their characteristic behaviour comes from the very low cross section with the Standard Model particles in the early Universe. Due to this very low cross section (lower than that of WIMPs), the non-thermal dark matter particles can never reach in thermal equilibrium with the Standard Model particles. Hence their evolution in the early Universe is studied differently than the thermal scenario. In the thermal scenario, the abundance of a relic particle (called WIMP) remains nonzero in the present epoch due to the “Freeze-out” mechanism [54], whereas in the case of a non-thermal production of DM (called FIMP), a different mechanism known as “Freeze-in” [150] is responsible for their relic abundance. In the non-thermal case, due to very low interaction cross section, the initial abundance of the dark matter is taken to be zero. As the Universe cools, they are dominantly produced by the decay of other SM/BSM particles. They can also be produced by the scattering of SM/BSM particles, but with a sub-dominant contribution. Once the non-thermal dark matter is produced, due to extremely low interaction strength, they do not thermalise with the rest of the thermal soup. Since most of the production of DM particles in the non-thermal regime occur from the decays of heavier particles, non-thermality condition will be satisfied when the rate of production from the decaying mother particle (decay width) is less than the expansion rate of the Universe at around a temperature $T \sim M$, where M is the mass of the decaying particle [151]. Mathematically this can be written as

$$\frac{\Gamma}{H} < 1 \quad (\text{for } T \sim M), \quad (2.22)$$

where, Γ is the relevant decay width and H is the Hubble parameter. However in some cases, if the production of DM particles may occur mainly from the annihilation of other particles in the thermal bath (production from decay can be forbidden due to kinematical condition or by some symmetry in the Lagrangian). Γ will then be replaced by:

$$\Gamma = n_{eq} \langle \sigma v \rangle, \quad (2.23)$$

where, $\langle \sigma v \rangle$ is the thermally averaged annihilation cross section of the particles in the thermal bath and n_{eq} is their *equilibrium* number density.

In this $U(1)_{B-L}$ model, to calculate the relic density of a non-thermal sterile neutrino dark matter (N_1), the principal ingredient is its production from various decay and annihilation channels. This gives the required comoving number density of N_1 upon solving the relevant Boltzmann equation. The main production channels of the sterile neutrino

(via decay) are :

$$W^\pm \rightarrow N_1 e^\pm, Z \rightarrow N_1 \bar{N}_1, Z_{\text{BL}} \rightarrow N_1 \bar{N}_1, H \rightarrow N_1 \bar{N}_1, h \rightarrow N_1 \bar{N}_1.$$

The corresponding decay widths are given in the Appendix 2.8.1. As discussed earlier, non-thermal dark matter particles can also be produced from the scattering of the SM/BSM particles in the thermal soup. The rate of the back reactions are negligible, since the number density of N_1 is extremely small in the early Universe. The annihilation channels along with corresponding cross sections aiding the production of N_1 are also given in the Appendix 2.8.2. As we will see later, in the present case W^\pm and Z_{BL} decays are main production channels of N_1 . Using the non-thermality condition given in Eq. (2.22) we find that the extra gauge coupling g_{BL} and the active-sterile mixing angle α must be less than 10^{-9} and 10^{-7} (rad) respectively for an $\mathcal{O}(\text{MeV})$ sterile neutrino with the mass of Z_{BL} lying in 1 GeV to 100 GeV range. Although this is a simple way to estimate the order of magnitude of g_{BL} and α required for the dark matter candidate (N_1) to be non-thermal, this sets a very first upper limit on these quantities. However, more stringent upper bound on α ($\alpha \lesssim 10^{-9}$ rad) arises from the stability of DM over the cosmological time scale.

Moreover, an upper bound on the active-sterile mixing angle α is also obtained from the invisible decay of the Standard Model Z boson. Following Ref. [152] we find:

$$\frac{\Gamma(Z \rightarrow \text{inv})}{\Gamma(Z \rightarrow \nu\nu)} = 2.990 \pm 0.007. \quad (2.24)$$

In the limit when active-sterile mixing angle is small and $M_Z \gg M_{N_1}$, from the above equation we get $\sin^4 \alpha < 0.007$. As we will see later that for us, this condition is indeed being satisfied. In the present scenario since $M_h < 2 M_H$, SM Higgs boson can decay *invisibly* only into a pair of lightest sterile neutrino N_1 . From the expression of the decay width given in Eq. (2.37) we find that it is suppressed by g_{BL}^2 and hence very small. Thus this decay width easily satisfies the bound on invisible decay of SM Higgs boson from LHC [153]. Furthermore, due to sufficiently small interaction strength with the SM particles, non-thermally produced N_1 always satisfies all the existing bounds on spin independent as well as spin dependent scattering cross sections from dark matter direct detection experiments [56].

We have mentioned earlier that for the non-thermal production of the sterile neutrinos, the coupling constant g_{BL} should be very small ($< 10^{-9}$). As is usually done, while considering the production of dark matter from a decay of any SM/BSM particle, the latter is implicitly assumed to be in thermal equilibrium. Hence we usually do not need to solve a system of *coupled* Boltzmann equations, since the equilibrium number density is assumed for the decaying mother particle. But, here due to very low interaction strength of Z_{BL}

(due to small g_{BL}), it will not be in thermal equilibrium with the rest of the particles. Also, the decay of Z_{BL} is a mode of production of the our sterile neutrino dark matter N_1 . So, first, we find the comoving number density of Z_{BL} by solving its Boltzmann equation. Then we use this to find the relic density of our sterile neutrino dark matter. Thus, in our case we have to solve a set of two *coupled* Boltzmann equations, one for the sterile neutrino dark matter, and another for the Z_{BL} .

In any model with a sterile neutrino we will have an active-sterile mixing in general. Hence in such model *production* of the sterile neutrino via W^\pm decay is a very generic feature. But, it is usually not taken into account since it is suppressed by the square of the small active-sterile mixing angle. However, here, in our favoured parameter space, we find that a sizeable contribution (to the relic-density of N_1) even from the W^\pm decay is present (see Section 2.4.1).

Another important feature which will be present for a generic model having an nonzero active sterile mixing is the production of sterile neutrino through the Dodelson-Widrow (DW) mechanism. Here the production of sterile neutrino occurs via the oscillations of active neutrinos to the sterile ones. But this mechanism suffers serious drawbacks from the Lyman- α bounds [154] as well as X-ray observations [130]. It is now known [155, 156] that sterile neutrino produced by this mechanism cannot comprise the whole of the dark matter of the Universe. The contribution arising to the relic abundance of a sterile neutrino from the DW mechanism is given by [157]

$$\Omega_{\text{DW}} h^2 \approx 0.3 \times \left(\frac{\sin^2 2\alpha}{10^{-10}} \right) \left(\frac{M_{N_1}}{100 \text{ keV}} \right)^2, \quad (2.25)$$

where, α is the active sterile mixing angle and M_{N_1} is the mass of the sterile neutrino. In our case we find (see Section 2.5 for details) that in order to satisfy relic density, α should be less than 10^{-10} rad for sterile neutrino mass lying between 1 MeV and 10 MeV. From Eq. (2.25) we see that the corresponding DW contribution to the relic density is $\lesssim 1.2 \times 10^{-6}$ and hence negligible.

2.4 Boltzmann Equation

In this section, we write the two coupled Boltzmann equations that dictates the final relic abundance of the sterile neutrino dark matter N_1 . The Boltzmann equation for the evolu-

tion of Z_{BL} which, as already discussed is very weakly interacting is given by³:

$$\frac{dY_{Z_{\text{BL}}}}{dz} = \frac{2M_{pl}}{1.66 M_h^2} \frac{z \sqrt{g_*(z)}}{g_s(z)} \left(\langle \Gamma_{H \rightarrow Z_{\text{BL}} Z_{\text{BL}}} \rangle Y_H^{eq} - \langle \Gamma_{Z_{\text{BL}} \rightarrow \text{all}} \rangle Y_{Z_{\text{BL}}} \right). \quad (2.26)$$

Here, $Y_{Z_{\text{BL}}} \equiv \frac{n_{Z_{\text{BL}}}}{s}$ is the comoving number density of the extra gauge boson with $n_{Z_{\text{BL}}}$ and s being the number density of Z_{BL} and the entropy density of the Universe respectively. Also $z \equiv \frac{\Lambda}{T}$ where Λ is a mass scale and T is the temperature of the Universe. For simplicity we have taken $\Lambda \sim M_h$, the mass of SM Higgs boson while M_{pl} is the usual Planck mass. The function $g_*(z)$ is given by:

$$\sqrt{g_*(z)} = \frac{g_s(z)}{\sqrt{g_\rho(z)}} \left(1 - \frac{1}{3} \frac{d \ln g_s(z)}{d \ln z} \right),$$

where, $g_\rho(z)$ and $g_s(z)$ are the effective degrees of freedom related to the energy density ρ and the entropy density s of the Universe respectively. The quantity $\langle \Gamma_{A \rightarrow BB} \rangle$ denotes the thermally averaged decay width for the process $A \rightarrow BB$ and its expression, in terms of decay width $\Gamma_{A \rightarrow BB}$, is given by [81]⁴:

$$\langle \Gamma_{A \rightarrow BB} \rangle = \frac{K_1(z)}{K_2(z)} \Gamma_{A \rightarrow BB}. \quad (2.27)$$

Here, $K_1(z)$ and $K_2(z)$ are the modified Bessel functions of order 1 and 2 respectively. The expressions for the relevant decay widths are given in Appendix 2.8.3.

The SM particles acquire their masses after the process of EWSB whereas the BSM particles like $U(1)_{\text{B-L}}$ gauge boson Z_{BL} and the additional Higgs boson (H) gain their masses after the breaking of $U(1)_{\text{B-L}}$ symmetry. Therefore, in the early Universe the main production channel of the new gauge boson is mainly through the decay of H , while the latter is in thermal equilibrium with the plasma. The first term in Eq. (2.26) denotes this contribution to the production of Z_{BL} (i.e. increase in number density of Z_{BL}) and hence

³In general the first term of Eq. (2.26) will look like: $\langle \Gamma_{H \rightarrow Z_{\text{BL}} Z_{\text{BL}}} \rangle (Y_H^{eq} - Y_{Z_{\text{BL}}}^2)$, but since the initial abundance of Z_{BL} is very small, we have neglected the inverse process i.e. $Z_{\text{BL}} Z_{\text{BL}} \rightarrow H$, and consequently dropping the $\langle \Gamma_{H \rightarrow Z_{\text{BL}} Z_{\text{BL}}} \rangle Y_{Z_{\text{BL}}}^2$ term in our analysis.

⁴For a more rigorous approach, when the decaying particle is Z_{BL} , one should use its non-thermal distribution function ($f_{Z_{\text{BL}}}$) for calculating this thermally averaged decay width. The expression will look like: $\langle \Gamma_{Z_{\text{BL}} \rightarrow BB} \rangle = \frac{\int (\frac{M_{Z_{\text{BL}}}}{E_{Z_{\text{BL}}}}) \Gamma_{Z_{\text{BL}} \rightarrow BB} f_{Z_{\text{BL}}}(p, T) d^3p}{\int f_{Z_{\text{BL}}}(p, T) d^3p}$. The non-thermal distribution function $f_{Z_{\text{BL}}}$ should be obtained first by solving the appropriate Boltzmann equation.

comes with a positive sign. Since in our case, both the masses of Z_{BL} and H are free parameters, we have adopted the values of M_H in a range such that it always satisfy the kinematical condition $M_H \geq 2 M_{Z_{BL}}$. Although in the early stage of the Universe, the decay of H is the main production channel of Z_{BL} , in principle it can also be produced from the annihilation processes, involving both SM as well as BSM particles, like $hh \rightarrow Z_{BL}Z_{BL}$, $W^+W^- \rightarrow Z_{BL}Z_{BL}$, $ZZ \rightarrow Z_{BL}Z_{BL}$, $HH \rightarrow Z_{BL}Z_{BL}$, $N_{2,3}\bar{N}_{2,3} \rightarrow Z_{BL}Z_{BL}$ etc. However, contribution of these annihilation processes is subleading to that of decay. The number density of extra gauge boson Z_{BL} is also depleted mainly through its decay modes to $N_1\bar{N}_1$ (other two sterile neutrinos are assumed to be heavy for simplicity), $\nu_x\bar{\nu}_x$ and $f\bar{f}$. It is denoted by the second term in the Boltzmann equation (Eq. (2.26)), and as expected it comes with a negative sign, since it signifies the depletion of Z_{BL} number density. These two competing processes (production vs. depletion) decide the final comoving number density of Z_{BL} . Numerically solving Eq. (2.26), we graphically show the evolution of comoving number density of Z_{BL} with $z = \frac{M_h}{T}$ in Fig. 2.1.

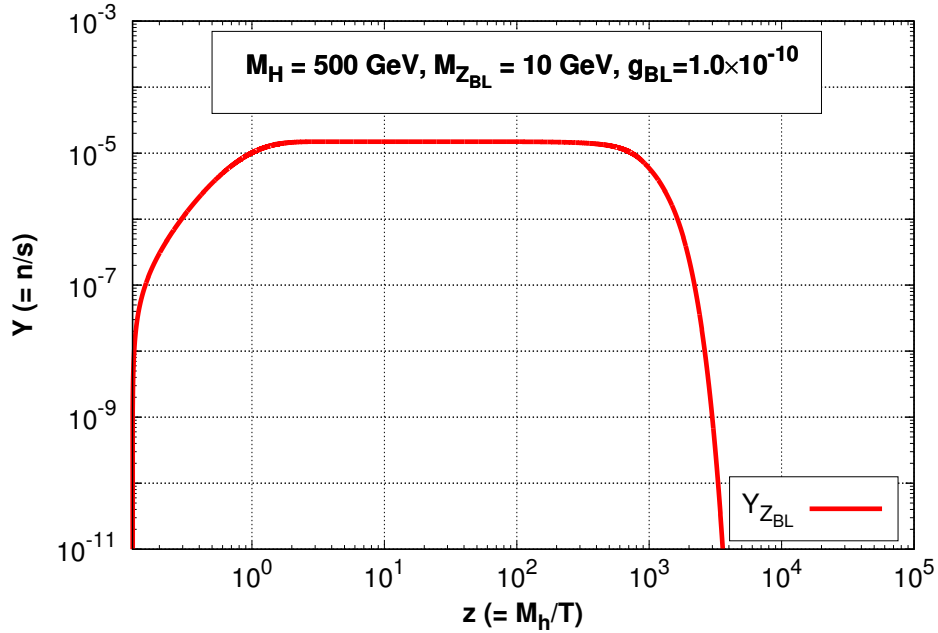


Figure 2.1: Evolution of comoving number density of Z_{BL} with respect to z .

From the above plot it is seen that, the comoving number density of Z_{BL} first rises due to the production term (first term in the R.H.S. of Eq. (2.26)) and then after a certain time it falls when the depletion term (i.e. the second term in the R.H.S. of Eq. (2.26)) begins to dominate. This situation arises because, at that time the temperature of the Universe becomes much smaller than M_H ($T \ll M_H$) and hence, being a non relativistic

species, the equilibrium number density of H is exponentially suppressed. Therefore, the production of Z_{BL} ceases. The middle “plateau” like portion occurs when both the production and the depletion terms are comparable and hence compensating each other. The plot is generated for the following chosen set of relevant parameters: $M_H = 500$ GeV, $M_{Z_{\text{BL}}} = 10$ GeV and $g_{\text{BL}} = 10^{-10}$.

Now, we proceed to write the Boltzmann equation of the lightest sterile neutrino N_1 . This will govern the number density of the dark matter candidate (N_1) and consequently its relic abundance at the present epoch. Similar to Eq. (2.26), the Boltzmann equation for N_1 is given by :

$$\begin{aligned} \frac{dY_{N_1}}{dz} = & \frac{2M_{pl}}{1.66 M_h^2} \frac{z\sqrt{g_*(z)}}{g_s(z)} \left(\langle \Gamma_{W^\pm \rightarrow e^\pm N_1} \rangle (Y_W^{eq} - Y_{N_1}) + \langle \Gamma_{Z_{\text{BL}} \rightarrow N_1 N_1} \rangle (Y_{Z_{\text{BL}}} - Y_{N_1}^2) \right. \\ & + \sum_{i=H,h,Z} \langle \Gamma_{i \rightarrow N_1 N_1} \rangle (Y_i^{eq} - Y_{N_1}^2) \left. \right) + \frac{4\pi^2}{45} \frac{M_{pl} M_h}{1.66} \frac{\sqrt{g_*(T)}}{z^2} \times \\ & \left(\sum_{x=W,Z,f,H} \langle \sigma_{V_{x\bar{x} \rightarrow N_1 N_1}} \rangle (Y_x^{eq\ 2} - Y_{N_1}^2) + \langle \sigma_{V_{Z_{\text{BL}} Z_{\text{BL}} \rightarrow N_1 N_1}} \rangle (Y_{Z_{\text{BL}}}^2 - Y_{N_1}^2) \right). \end{aligned} \quad (2.28)$$

As discussed in Eq. (2.26), since the initial abundance of the sterile neutrino dark matter N_1 is very small, the Y_{N_1} term in the above equation may be neglected [135, 150]. Here $\langle \sigma_{V_{x\bar{x} \rightarrow N_1 N_1}} \rangle$ is the thermally averaged cross section for the production of N_1 from the annihilation of x particle. The expression of $\langle \sigma_{V_{x\bar{x} \rightarrow N_1 N_1}} \rangle$ is given by [54]⁵

$$\langle \sigma_{V_{x\bar{x} \rightarrow N_1 N_1}} \rangle = \frac{1}{8M_x^4 T K_2^2 \left(\frac{M_x}{T} \right)} \int_{4M_x^2}^{\infty} \sigma_{x\bar{x} \rightarrow N_1 N_1} (s - 4M_x^2) \sqrt{s} K_1 \left(\frac{\sqrt{s}}{T} \right) ds. \quad (2.29)$$

The expressions for the relevant decay widths and annihilation cross sections are given in the Appendix 2.8.1 and 2.8.2 respectively.

In order to get the comoving number density (Y_{N_1}) of N_1 at the present epoch, we have to solve the coupled set of Boltzmann equations given in Eq. (2.26, 2.28). To be more precise, the value of $Y_{Z_{\text{BL}}}(z)$ for each z obtained by solving Eq. (2.26) is to be fed into Eq. (2.28). For understanding the physics behind this coupled set of Boltzmann equations better, let us first assume that the lightest sterile neutrinos are *only* produced from the decay of Z_{BL} , whereas Z_{BL} is produced and depleted according to Eq. (2.26). We plot the result in Fig. 2.2. In Fig. 2.2, initially at the early stage of the Universe there are no Z_{BL}

⁵As previously discussed, in a strict sense, one should use a definition of $\langle \sigma_{V_{Z_{\text{BL}} Z_{\text{BL}} \rightarrow N_1 N_1}} \rangle$ based on the non-equilibrium density function $f_{Z_{\text{BL}}}$.

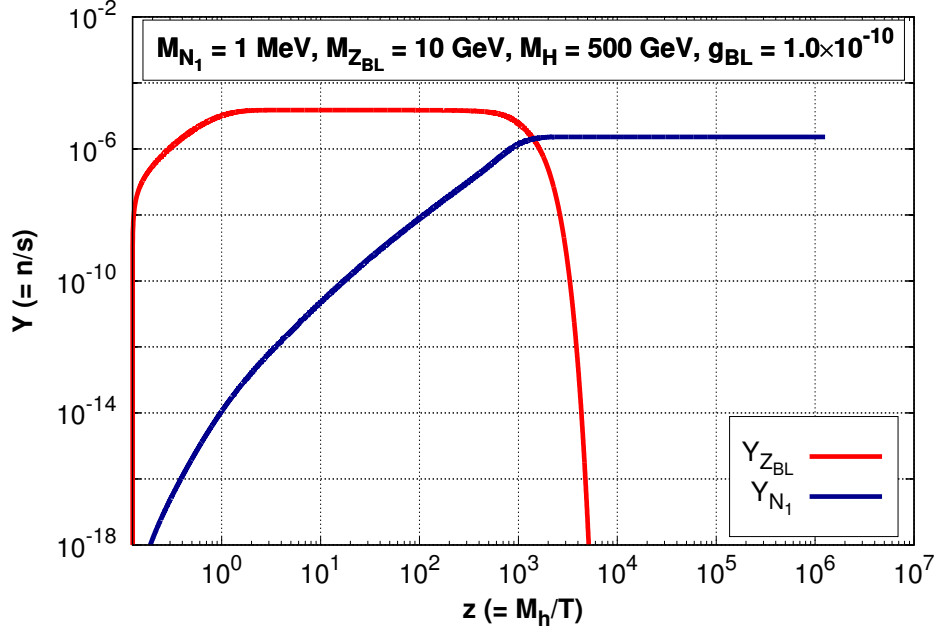


Figure 2.2: Evolution of comoving number densities of Z_{BL} and N_1 .

particles and hence no N_1 , since for simplicity we have switched off all other production channels of N_1 , except Z_{BL} . Then, when Z_{BL} is produced from the decay of H , we also find an increase in the number density of N_1 from the decay of Z_{BL} . Finally, the number density of Z_{BL} begins to fall due to its dominating decay modes (production of Z_{BL} terminates as the the number density of H becomes negligibly small), and consequently the number density of N_1 also saturates since now there are no Z_{BL} left to aid the production of N_1 . This plot is also generated for the following chosen set of relevant parameters: $M_H = 500$ GeV, $M_{Z_{BL}} = 10$ GeV, $M_{N_1} = 1$ MeV and $g_{BL} = 10^{-10}$.

In Fig. 2.2 we have taken the initial temperature (T_i) to be 1 TeV. The final abundances of Z_{BL} and N_1 will not depend on this as long as $T_i \gtrsim M_H$. The maximum production of Z_{BL} from H decay occurs around a temperature of $\sim M_H$. However, if T_i becomes less than M_H then, since H is in thermal equilibrium, its own abundance will be exponentially suppressed (as it becomes non-relativistic) and thereby reducing $Y_{Z_{BL}}$ and Y_{N_1} . All these are shown in Fig. 2.3 where we see as discussed above, for $T_i \gtrsim M_H$, there is no change in the final values of $Y_{Z_{BL}}$ and Y_{N_1} (red, green, blue, cyan solid lines). While for $T_i \lesssim M_H$ both the final abundances are reduced (black solid line) from their previous values.

We now show the variation of Fig. 2.2 with different sets of chosen model parameters. In Fig. 2.4(a) we show the variation of $Y_{Z_{BL}}$ and Y_{N_1} with z for two different values of $U(1)_{B-L}$ gauge coupling g_{BL} . In this plot, we find that with increase in the value of g_{BL} the

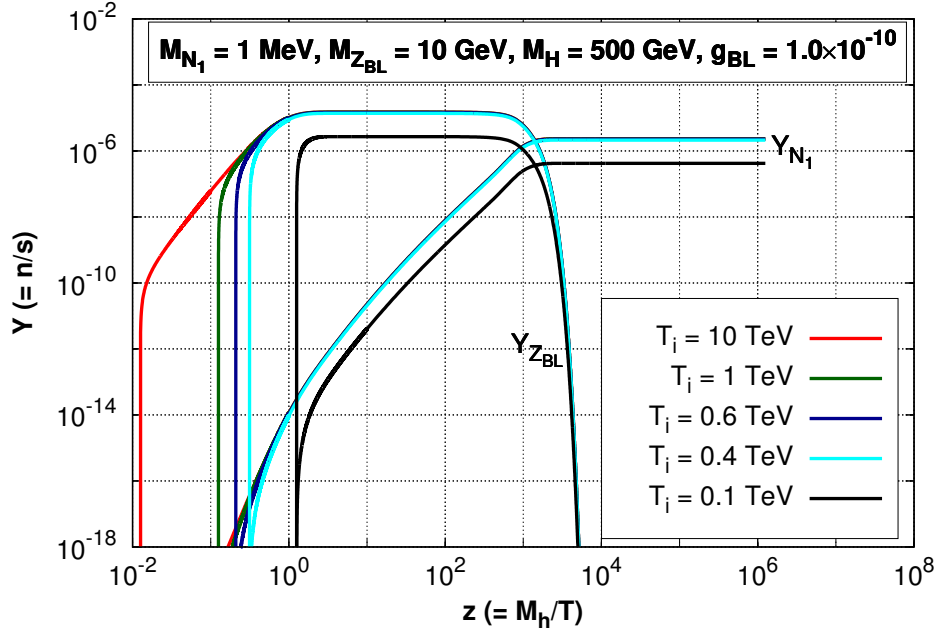


Figure 2.3: Dependence of $Y_{Z_{BL}}$ and Y_{N_1} on different sets of initial temperatures.

number density of Z_{BL} also increases initially. This is understandable, because the decay width $\Gamma_{H \rightarrow Z_{BL} Z_{BL}}$ increases with g_{BL} , and hence resulting in an increased number density of the extra gauge boson. But the depletion rate of Z_{BL} (proportional to its total decay width) also increases with g_{BL} , and hence will result in a faster fall of its comoving number density. This is also evident from the figure where the green line starts to fall earlier than the red one. On the other hand, the production rate of sterile neutrino dark matter (N_1) is proportional to $\Gamma_{Z_{BL} \rightarrow N_1 N_1}$ and $Y_{Z_{BL}}$ (see Eq. (2.28)) and both of these quantities increase with g_{BL} . Therefore, the comoving number density of N_1 increases as the value of g_{BL} changes from 1×10^{-10} to 5×10^{-10} .

In Fig. 2.4(b), we show the variation of $Y_{Z_{BL}}$ and Y_{N_1} with z for two different values of M_H . Now, with a decrease in M_H , we expect a corresponding decrease in decay width $\Gamma_{H \rightarrow Z_{BL} Z_{BL}}$ (Z_{BL} production rate), and hence the initial number density of Z_{BL} will be smaller. This feature is seen in plot (b) where initially ($z \lesssim 10^3$) $Y_{Z_{BL}}$ for $M_H = 500$ GeV (green line) is larger than that for $M_H = 50$ GeV (red line). However, the total decay width of Z_{BL} (and consequently its depletion rate) does not depend on the mass of H . Hence both the red and green lines will start to fall off around the same time. Another noticeable change due to the variation of M_H is that the width of the “plateau” becomes narrower with the decrease in mass difference between M_H and $M_{Z_{BL}}$. Further, as the $Y_{Z_{BL}}$ increases with an increase in M_H , which in turn produces more N_1 (from the decay of Z_{BL}) in the

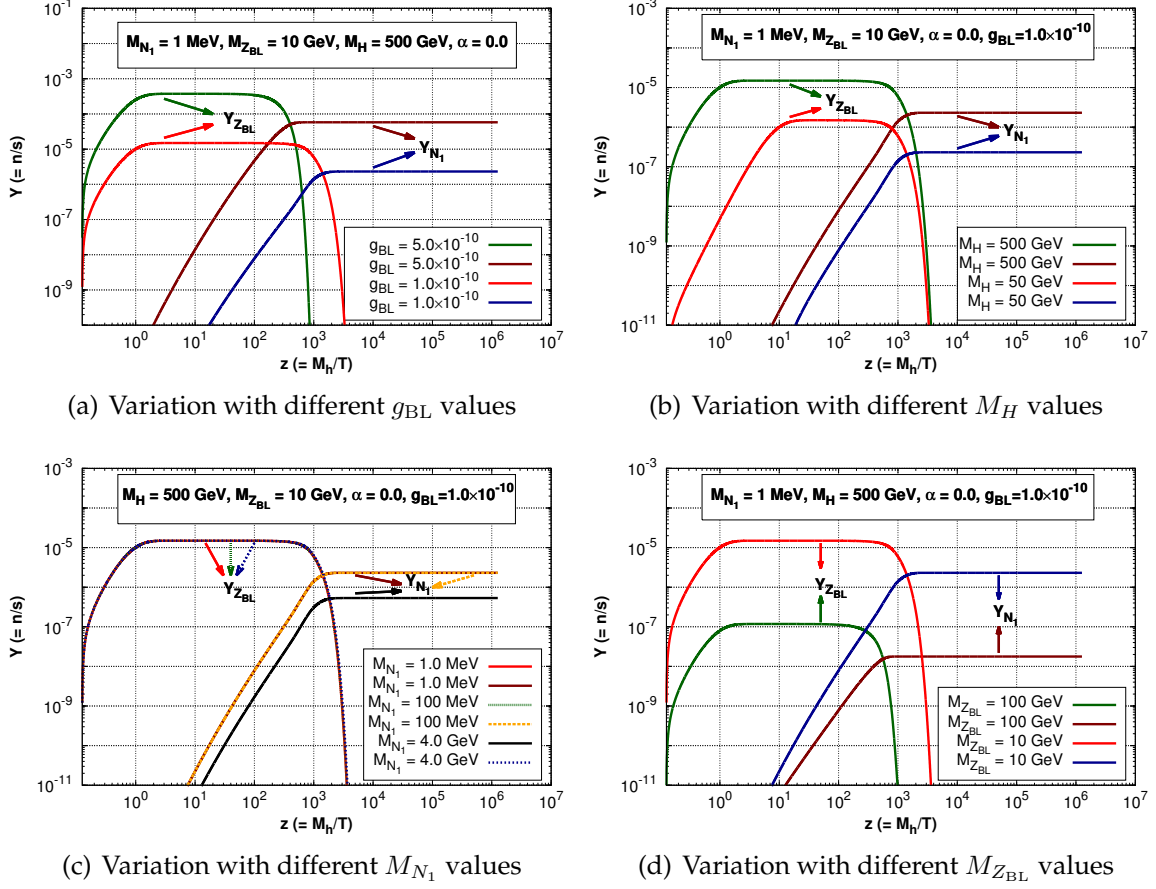


Figure 2.4: Comparison of comoving number densities of Z_{BL} and N_1 with respect to different sets of chosen model parameters.

final state and hence the comoving number density Y_{N_1} also increases with M_H . In Fig. 2.4(c) we have shown the variation of $Y_{Z_{BL}}$ and Y_{N_1} for three different values of sterile neutrino dark matter mass. From this plot we find that there is not much variation in $Y_{Z_{BL}}$ with changing M_{N_1} . This is because the decay width $\Gamma_{Z_{BL} \rightarrow N_1 N_1}$ is subdominant with respect to the other decays modes of Z_{BL} . Increasing the mass of N_1 will lead to a further decrease of $\Gamma_{Z_{BL} \rightarrow N_1 N_1}$ and hence will not affect the depletion rate which is dominantly controlled by the other decay channels of Z_{BL} . But since in this case (when other production channels of N_1 are switched off) $\Gamma_{Z_{BL} \rightarrow N_1 N_1}$ solely controls the production rate of N_1 , Y_{N_1} changes with M_{N_1} . It is seen from Fig. 2.4(c) that if we increase the sterile neutrino mass from 1 MeV to 4 GeV (M_{N_1} tends to $M_{Z_{BL}}/2$), then Y_{N_1} decreases. The decrease in the decay width results in a corresponding decrease of Y_{N_1} as expected. However we find no visible change in Y_{N_1} when M_{N_1} goes from 1 MeV to 100 MeV. This is because in

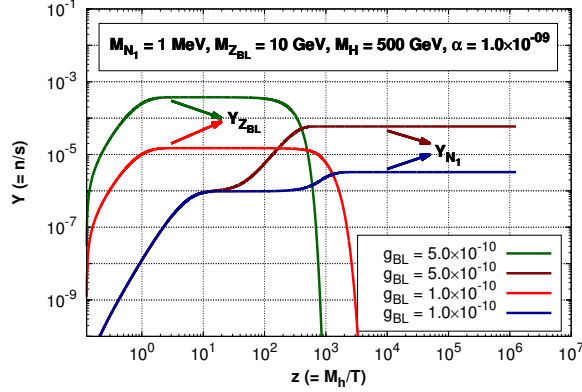
both of these cases $M_{Z_{BL}} \gg 2M_{N_1}$, therefore the decay width $\Gamma_{Z_{BL} \rightarrow N_1 N_1}$ and hence Y_{N_1} is practically insensitive to M_{N_1} ($M_{N_1} = 1 \text{ MeV to } 100 \text{ MeV}$).

Finally, the effect of the variation of gauge boson mass $M_{Z_{BL}}$ on $Y_{Z_{BL}}$ and Y_{N_1} is shown in Fig. 2.4(d). The increase in $M_{Z_{BL}}$ results in the decrease of $\Gamma_{H \rightarrow Z_{BL} Z_{BL}}$ and an increase of $\Gamma_{Z_{BL} \rightarrow all}$, which is manifested through a smaller rise and a faster fall of $Y_{Z_{BL}}$. This nature of $Y_{Z_{BL}}$ is corroborated in the plot as well, where $M_{Z_{BL}}$ varies from 10 GeV (red line) to 100 GeV (green line). On the other hand the quantity Y_{N_1} follows the evolution of $Y_{Z_{BL}}$ in the usual way as discussed earlier. Since all these cases were shown to demonstrate the validity of the coupled Boltzmann equations, for simplicity the active sterile mixing angle (α) is set to zero.

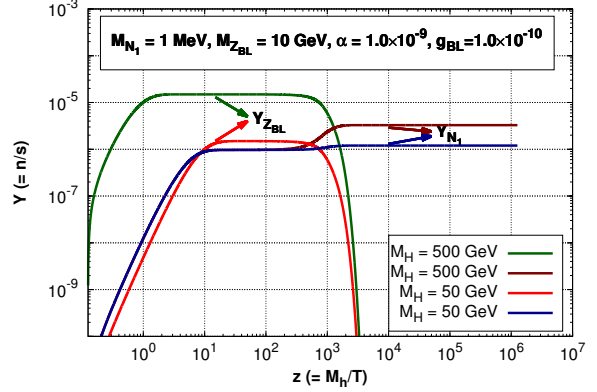
2.4.1 Solution of the complete Boltzmann equation(s) with all production and decay channels

In the previous section, we demonstrated the validity of the coupled set of Boltzmann equations needed to solve for the relic abundance of the sterile neutrino dark matter N_1 . For simplicity, we assumed that the only production channel of N_1 is the decay from Z_{BL} . However in general, all the possible production modes of N_1 including decays as well as annihilations of SM and BSM particles, as given in Eq. (2.28), have to be taken into account. Therefore, the active-sterile mixing angle is now nonzero. The noticeable feature when the active sterile mixing is nonzero is the production of N_1 from the decay of W^\pm bosons ($W^\pm \rightarrow e^\pm N_1$). It may a priori seem that due to small value of active-sterile mixing angle the contribution from the decay of W^\pm will be negligible, but we have to remember that in this non-thermal scenario, the extra gauge coupling (g_{BL}) is also required to be very small ($\sim 10^{-10}$), and hence the production of N_1 from the decay of Z_{BL} may also compete with the former. We will show this quantitatively later. Also note the decay of W^\pm is solely governed by the active-sterile mixing angle α and does not depend on $U(1)_{B-L}$ gauge coupling g_{BL} , hence if g_{BL} is made very low, the *only* dominant production channel of N_1 will be from W^\pm decay. In Fig. 2.5((a)-(d)) we show the variation Y_{N_1} and $Y_{Z_{BL}}$ with respect to different sets of independent parameters as before.

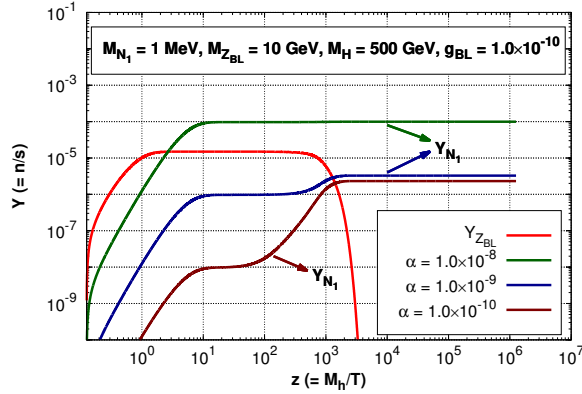
Interesting feature of Fig. 2.5((a)-(d)) when contrasted with Fig. 2.4((a)-(d)) is the existence of a “double plateau”. The reason behind this is the presence of another the production mode of N_1 from W^\pm decay which was neglected in previous section for simplicity. The onset of N_1 production as seen in these plots is a little early than those seen in Fig. 2.4. The initial onset here is due to the presence of W^\pm decay and is independent of g_{BL} , $M_{Z_{BL}}$ and M_H (Eq. (2.33)), and only depends on α which is the sole parameter that controls the



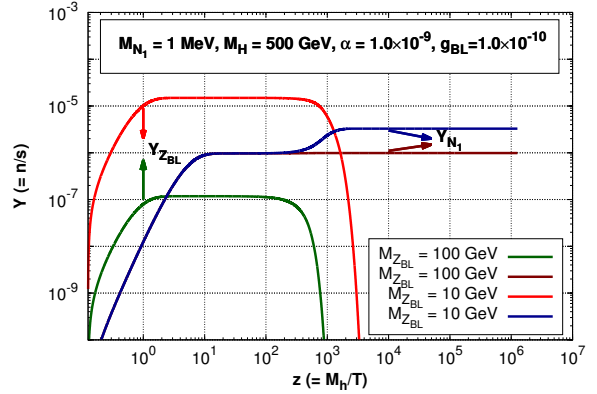
(a) Variation with different g_{BL} values



(b) Variation with different M_H values



(c) Variation with different α values



(d) Variation with different $M_{Z_{BL}}$ values

Figure 2.5: Comparison of Z_{BL} and N_1 comoving number density with respect to different sets of chosen parameters.

$W^\pm \rightarrow e^\pm N_1$ decay. The first plateau occurs when the number density of W boson begins to fall and hence there is a decreased rate of production of N_1 . However it again begins to rise sharply when the production from Z_{BL} starts to dominate. Then as before, we can see by comparing with the accompanying $Y_{Z_{BL}}$ lines that the second plateau results when the Z_{BL} number density starts to deplete. It is to be noted that this “two plateau” feature will be visible only when the production from W and Z_{BL} are comparable to each other at some point of $z (= \frac{M_h}{T})$. If either one of them remains dominant for all z , then it will result in single plateau like feature. For example, the green solid line in plot (c) of Fig. 2.5 has only a single plateau. This is because, due to a very high value of α the decay channels of W^\pm remain the most dominant production mode of N_1 for all z . The corresponding variation of Z_{BL} number density is also shown by red solid line and since α has no effect on the production and decay channels of Z_{BL} we find no variation of $Y_{Z_{BL}}$ with α . However

the variation of Y_{N_1} is different for different values of α , as the active-sterile mixing angle α controls the production mode of N_1 from W^\pm decay.

2.5 Relic Density of Sterile Neutrino Dark Matter (N_1)

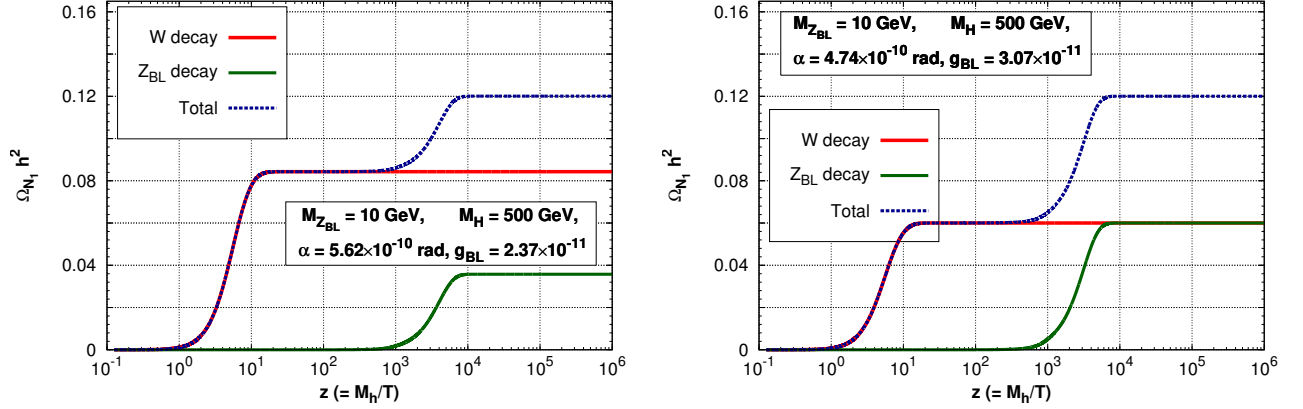
In order to compute the relic abundance ($\Omega_{N_1} h^2$) of the lightest sterile neutrino (N_1) we need to find the value of its comoving number density (Y_{N_1}) at the present epoch ($T = T_0$, $T_0 \sim 2.73$ K). The value of $Y_{N_1}(T_0)$ can be obtained by solving the two coupled Boltzmann equations (Eqs.(2.26, 2.28)), which we have discussed elaborately in Section 2.4. The expression of $\Omega_{N_1} h^2$ in terms of $Y_{N_1}(T_0)$ is given by [158],

$$\Omega_{N_1} h^2 = 2.755 \times 10^8 \left(\frac{M_{N_1}}{\text{GeV}} \right) Y_{N_1}(T_0) . \quad (2.30)$$

Here, we take all decay and annihilation channels of both SM as well as BSM particles for the production of N_1 . In Fig. 2.6 we show the relative contributions to $\Omega_{N_1} h^2$ from W^\pm (red solid line) and Z_{BL} decay (green solid line) for some chosen sets of model parameters. The total relic abundance of N_1 is also shown by the blue solid line. For some combinations of model parameters we find W^\pm decay can be the leading production channel of N_1 (plot (a)) while for some others it can be the subleading one (plot (c)). However in all three plots (a-c) of Fig. 2.6, the total relic density of N_1 has the saturation value ~ 0.12 which is in conformity with the value of dark matter relic density measured by the satellite borne experiment Planck. In plot (b) of Fig. 2.6 we show a situation when the relative contributions to $\Omega_{N_1} h^2$ from both W^\pm and Z_{BL} decays are equal. In this case we have adopted the following values of relevant model parameters: $g_{\text{BL}} = 3.07 \times 10^{-11}$, $\alpha = 4.74 \times 10^{-10}$ rad, $M_{Z_{\text{BL}}} = 10$ GeV and $M_H = 500$ GeV. For this set of model parameters we have also listed the fractional contributions to $\Omega_{N_1} h^2$ arising from all the possible decay and annihilation channels in Table 5.1, 2.2.

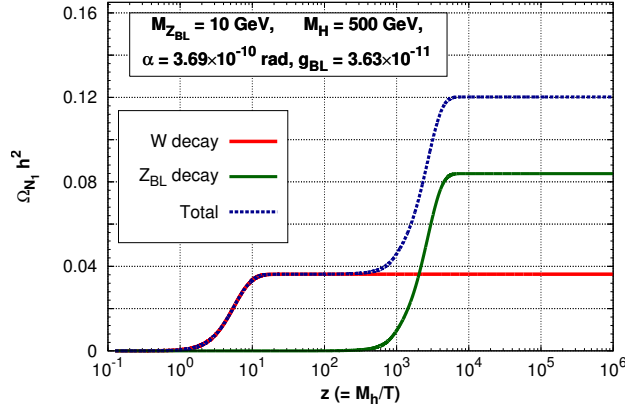
From Table 5.1 it is seen that for the small values of $g_{\text{BL}} \sim 10^{-11}$ and $\alpha \sim 10^{-10}$ (which are required for the non-thermality of N_1) the contributions of other production channels of N_1 through the decays of Z , H and h are negligible. Similarly, Table 2.2 shows that within this adopted ranges of model parameters the annihilation processes of SM as well as BSM particles do not contribute significantly to the production of sterile neutrino dark matter N_1 and hence we can safely consider the decays of W^\pm and Z_{BL} as the two most efficient production mechanisms of N_1 .

In Fig. 2.7, we plot the allowed values of B – L gauge coupling g_{BL} and active sterile mixing angle α which satisfy the relic density criteria ($0.1166 \leq \Omega_{N_1} h^2 \leq 0.1206$) [5]. Dur-



(a) W contribution to $\Omega_{N_1} h^2 \sim 70\%$ while Z_{BL} contribution $\sim 30\%$

(b) W contribution to $\Omega_{N_1} h^2 \sim Z_{BL}$ contribution



(c) W contribution to $\Omega_{N_1} h^2 \sim 30\%$ while Z_{BL} contribution $\sim 70\%$

Figure 2.6: Relic abundance of N_1 as function of z along with the relative contributions of W^\pm and Z_{BL} decay channels. All the plots are drawn for $M_{N_1} = 1$ MeV.

ing the computation of Fig. 2.7 we have varied the relevant parameters in the following range.

$$\begin{aligned}
 0.1 \text{ GeV} &\leq M_{Z_{BL}} \leq 250 \text{ GeV} , \\
 1.2 \text{ MeV} &\leq M_{N_1} \leq 10 \text{ MeV} , \\
 10^{-8} &\leq g_{BL} \leq 10^{-15} , \\
 10^{-7} \text{ rad} &\leq \alpha \leq 10^{-17} \text{ rad} ,
 \end{aligned}
 \tag{2.31}$$

and we have kept the mass of the extra Higgs boson H fixed at 500 GeV. From Fig. 2.7, we see that for very small values of the extra gauge coupling g_{BL} ($\sim 10^{-12}$ to 10^{-15}) the relic

Decay Channel	Fractional contribution to $\Omega_{\text{DM}} h^2$
W^\pm	0.5000
Z_{BL}	0.4999
H	0.2590×10^{-10}
h	0.1177×10^{-11}
Z	0.6276×10^{-19}

Table 2.1: Fractional contributions of different production processes of N_1 through decay for $g_{\text{BL}} = 3.07 \times 10^{-11}$, $\alpha = 4.74 \times 10^{-10}$ rad, $M_{Z_{\text{BL}}} = 10$ GeV, $M_H = 500$ GeV and $M_{N_1} = 1$ MeV.

Annihilation Channel	Fractional contribution to $\Omega_{\text{DM}} h^2$
$t\bar{t}$	0.3745×10^{-12}
$h h$	0.1650×10^{-13}
$W^+ W^-$	0.3606×10^{-14}
$Z Z$	0.3562×10^{-14}
$H H$	0.4403×10^{-19}
$Z_{\text{BL}} Z_{\text{BL}}$	0.4515×10^{-30}
$N_2 \bar{N}_2$	0.1987×10^{-35}
$N_3 \bar{N}_3$	0.1987×10^{-35}

Table 2.2: Fractional contributions of different production processes of N_1 through annihilation for $g_{\text{BL}} = 3.07 \times 10^{-11}$, $\alpha = 4.74 \times 10^{-10}$ rad, $M_{Z_{\text{BL}}} = 10$ GeV, $M_H = 500$ GeV and $M_{N_1} = 1$ MeV.

density condition of N_1 is always satisfied for a active-sterile mixing angle $\alpha \sim 10^{-10}$ rad. This is expected since for very small values of g_{BL} the production of N_1 from the decay of Z_{BL} is highly suppressed and in this situation decay of W^\pm becomes the principal production channel, since the latter is *not* suppressed by the extra gauge coupling (see Eqs. (2.33), (2.35)). Earlier works about the non-thermal production of sterile neutrino have

not touched upon this point in detail (production of N_1 from W^\pm decay), since most of the previous authors have ignored the N_1 production mode from W^\pm decay in their works by assuming extremely small values of active-sterile mixing angle α . However, such an assumption needs careful attention when other couplings in the theory can also be very small. On the other hand for the higher values of g_{BL} ($\sim 10^{-9}$ to 10^{-11}) the decay of Z_{BL} becomes the dominant contributor and hence in this case small values of α are required to suppress the contribution of W^\pm decay to $\Omega_{N_1} h^2$ such that the total relic density of N_1 lies within the range prescribed by the Planck experiment. Since the production of sterile neutrino from W^\pm decay depends only on the mixing angle α , in Fig. 2.7 we get only a narrow band of α which satisfies the relic density of N_1 (for small values of g_{BL}). But when Z_{BL} is the main production channel of N_1 then for a given g_{BL} and α we can make N_1 to satisfy the relic density by adjusting the Z_{BL} mass. Hence we get a relatively wider band of allowed values of g_{BL} for a fixed α . For the chosen mass range of sterile neutrino (i.e. $\mathcal{O}(\text{MeV})$), from Fig. 2.7 we find that the maximum allowed value of α is $\sim 10^{-10}$ rad. Such a sterile neutrino is free from all the constraints arising from X-ray and BBN as seen from Fig. 1 of Ref. [116].

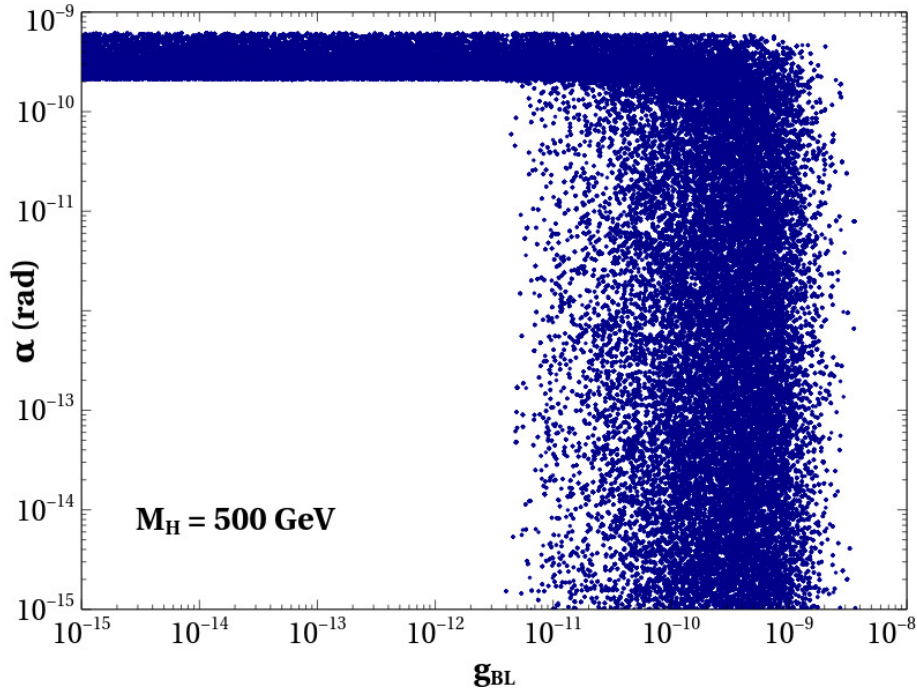


Figure 2.7: Allowed region in g_{BL} Vs α plane satisfying the relic density criteria.

The allowed region in $M_{Z_{\text{BL}}} - g_{\text{BL}}$ plane is shown in Fig. 2.8. Like the previous plot in Fig. 2.7, here also all the points in $M_{Z_{\text{BL}}} - g_{\text{BL}}$ plane produce the correct relic density of N_1

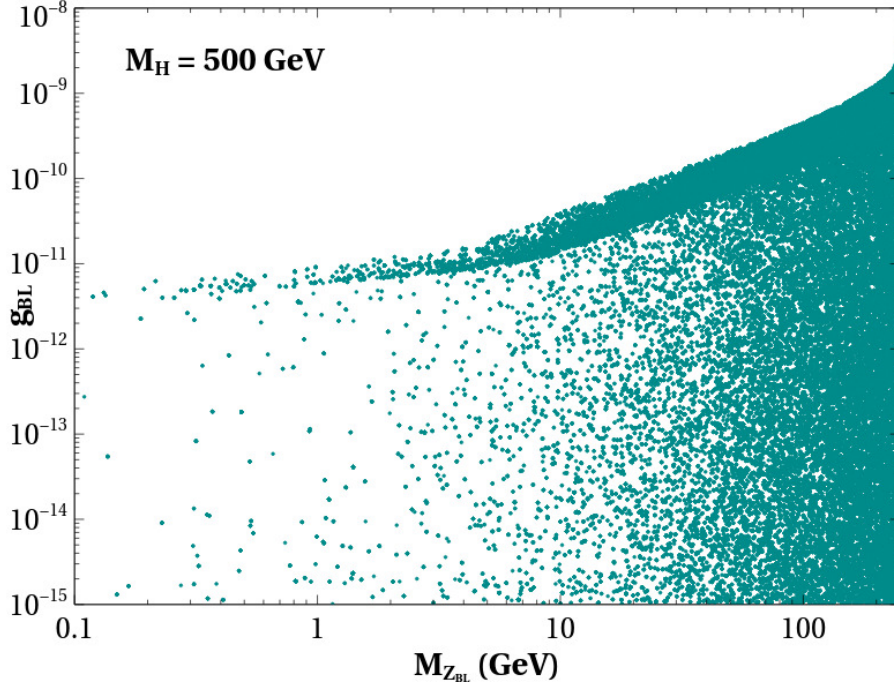


Figure 2.8: Allowed region in $M_{Z_{BL}}$ Vs g_{BL} plane satisfying the relic density criteria.

($0.1172 \leq \Omega_{N_1} h^2 \leq 0.1226$). In this case we have also varied the other relevant parameters (M_{N_1}, α) in the range given in Eq. (2.31). From this figure it is seen that the allowed values of g_{BL} increases with $M_{Z_{BL}}$. This nature of $M_{Z_{BL}} - g_{BL}$ plane can be explained in the following way. We know that the contribution of Z_{BL} to Y_{N_1} depends on both $\Gamma_{Z_{BL} \rightarrow N_1 N_1}$ and $Y_{Z_{BL}}$ (see Eq. (2.28)) where the latter quantity increases with $\Gamma_{H \rightarrow Z_{BL} Z_{BL}}$ (Eq. (2.26)) as the extra gauge bosons Z_{BL} are produced mainly from the decay of H . However the decay width $\Gamma_{H \rightarrow Z_{BL} Z_{BL}}$ is suppressed by $M_{Z_{BL}}^{-2}$ and thereby reducing the comoving number density of Z_{BL} with its mass (see Eq. (2.55) and Fig. 2.5(d)). In order to keep the contribution to $\Omega_{N_1} h^2$ arising from Z_{BL} decay unaltered, this decrement in $Y_{Z_{BL}}$ must be compensated by a corresponding increment in $\Gamma_{Z_{BL} \rightarrow N_1 N_1}$ which is proportional to g_{BL}^2 (Eq. (2.35)). Hence with an increase in $M_{Z_{BL}}$, g_{BL} should also increase to satisfy the relic density constraint.

Simulations using the standard Λ CDM cosmology requires that most of the dark matter candidates should be *cold* to satisfy constraints from the structure formation [159, 160]. In our case, to get an idea about the *coldness* of the sterile neutrino dark matter we try to compute its free-streaming length defined by [154]:

$$\lambda_{fs} = \int_{t_{in}}^{t_0} \frac{\langle v(t) \rangle}{a(t)} dt ,$$

where t_{in} is the initial time, t_0 is the present time, $v(t)$ is the mean velocity of the dark matter, and $a(t)$ is the scale factor of the Universe. Following Ref. [135], the hot, cold and warm dark matters are classified as:

$$\begin{aligned}\text{Cold Dark Matter (CDM)} & : \lambda_{\text{fs}} < 0.01 \text{ Mpc} \\ \text{Warm Dark Matter (WDM)} & : 0.01 \text{ Mpc} < \lambda_{\text{fs}} < 0.1 \text{ Mpc} \\ \text{Hot Dark Matter (HDM)} & : \lambda_{\text{fs}} > 0.1 \text{ Mpc}\end{aligned}$$

For the case where both W^\pm and Z_{BL} contribute equally to the final dark matter relic density (Fig. 2.6b), we have calculated the free-streaming length for dark matter produced from W^\pm as well as Z_{BL} decay separately. In both the cases we find that $\lambda_{\text{fs}}^{W^\pm} \sim 0.003 \text{ Mpc}$ and $\lambda_{\text{fs}}^{Z_{\text{BL}}} \sim 0.007 \text{ Mpc}$. Hence following the above classification of hot, cold and warm dark matter, we find that all of our sterile neutrino is *cold* and thus satisfying the structure formation constraints.

2.6 A possible way of detecting the sterile neutrino Dark Matter

As mentioned briefly in section 1.7.2, an unexplained anomalous line like signal round 511 keV has been detected by INTEGRAL/SPI in 2003. We again stress upon the point that this anomalous feature is not explained well from annihilating thermal dark matter scenarios and a non-thermal genesis of dark matter is hence anticipated [94]. Earlier people have tried to explain this INTEGRAL anomaly from the decay of light sterile neutrino dark matter [141, 161]. In this chapter, in the case of sterile neutrino dark matter in a non-thermal setting, we have also found that such an explanation is indeed possible. The decaying dark matter scenarios however require a more cuspy density profile than the annihilation models [162]. The seed mechanism behind this 511 keV emission line is the decay of sterile neutrino (N_1) into a e^\pm pair and an active neutrino. The e^\pm pair thus produced, get slowed down to non relativistic velocities due to several energy loss mechanisms within the galactic bulge [163] and thereby producing 511 keV *gamma-line* from their pair annihilation. The mass of the sterile neutrino favourable to explain this signal is $\sim 1\text{-}10 \text{ MeV}$ [163]. In the present $U(1)_{\text{B-L}}$ model, there are six possible Feynman diagrams contributing to this three body decay of which those which are mediated by Z_{BL} , h and H are sub dominant due to the suppression by the very low value of $U(1)_{\text{B-L}}$ gauge coupling g_{BL} . Therefore, we have used the remaining three diagrams i.e. those mediated by Z and W^\pm bosons to calculate the three body decay width. The expression of matrix

amplitude squared and corresponding decay width $\Gamma_{N_1 \rightarrow e^\pm \nu}$ is given in Appendix 2.8.4. A more simpler analytical expression (using some approximation) for this three body decay width can be found in Ref. [161]. The expression for the gamma ray flux obtained from the galactic bulge due the decay $N_1 \rightarrow e^\pm \nu$ is given by [161]:

$$\Phi_{511}^{theory} = 2 \frac{1}{4\pi} \frac{\Gamma_{N_1 \rightarrow e^\pm \nu}}{M_{N_1}} \frac{\int_{\Delta\Omega} \int_{l.o.s} \rho_{DM}(r(s, \Omega)) ds d\Omega}{\int_{\Delta\Omega} d\Omega}. \quad (2.32)$$

Here, $\Gamma_{N_1 \rightarrow e^\pm \nu}$ is the decay width of $N_1 \rightarrow e^\pm \nu$ and $\rho_{DM}(s, \Delta\Omega)$ is the dark matter density profile in the galaxy. During our analysis, we have taken Einasto profile [164] with $\alpha_{einasto} = 0.17$ for the computation of gamma-ray flux. The angular integration over the solid angle $\Delta\Omega$ is performed within the 2° angular resolution of the spectrometer while the spacial integration is over the line of sight (l.o.s) distance of galactic bulge from the position of solar system. The extra factor of 2 appearing in Eq. (2.32) is due to the production of two photons per decay of N_1 .

Using Eq. (2.32) we have computed the photon flux for different values of M_{N_1} and α . In Fig. (2.9) the red band shows the correct combination of M_{N_1} and α which is needed to explain the INTEGRAL observed flux. The dark cyan region is for those values of M_{N_1} and α which satisfies only the relic density constraint of N_1 . From Fig. 2.9, we can see that in the chosen range of M_{N_1} ($\sim 1 - 10$ MeV) the active-sterile mixing angle α required to explain *both* the relic density as well as the INTEGRAL anomaly is $\sim 10^{-12} - 10^{-14}$ rad.

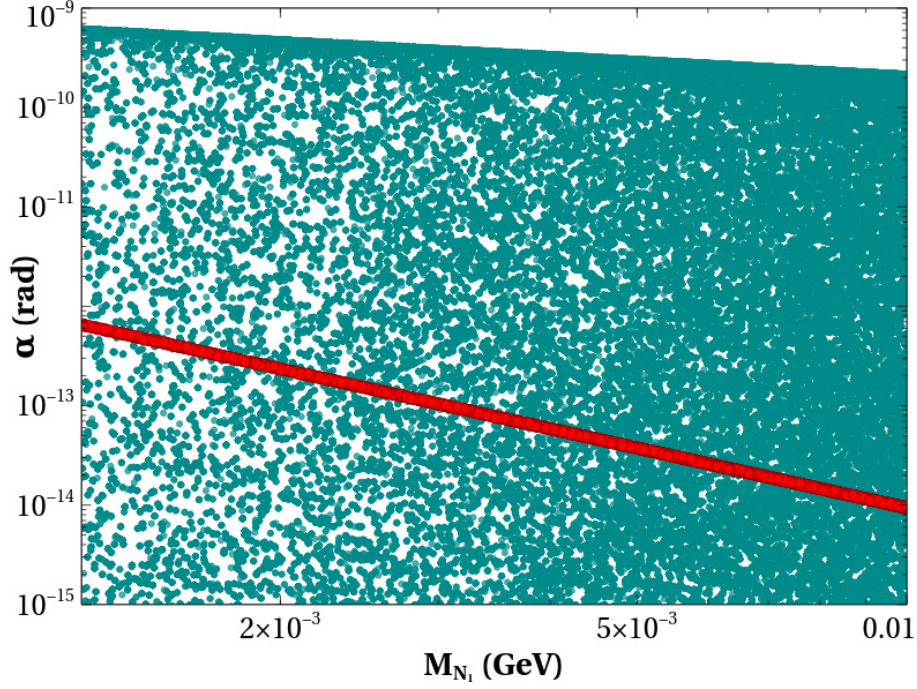


Figure 2.9: Values of M_{N_1} and active-sterile mixing angle α allowed by the relic density of N_1 ($0.1172 \leq \Omega_{N_1} h^2 \leq 0.1226$), are shown by the dark cyan points. The points lying within the red coloured band reproduced the flux observed by INTEGRAL/SPI. The points above the red band are ruled out from the observation of too large a flux as compared to that observed by INTEGRAL/SPI. Note, that this rules out the region corresponding to DM production via W-decay.

2.7 Conclusion

In this chapter we have shown that non-thermal sterile neutrino in $U(1)_{B-L}$ model can be a viable dark matter candidate. But the formalism developed here is in general applicable to any $U(1)_X$ extension of the Standard Model. Any such model trying to describe a non-thermal dark matter scenario (through IR Freeze-in) will have in general a very weakly coupled Z' as well as a feebly coupled dark matter candidate. Under such circumstances (i.e. when the mother particle responsible for most of the production of the dark matter has itself gone out of thermal equilibrium), we have shown how to solve a set of coupled Boltzmann equations to calculate the final relic density. Although, strictly speaking, in such cases we should solve the Boltzmann equations at the level distribution functions themselves, and a thorough analysis along this line is discussed in the next chapter. The approach taken here is valid as long as the non-thermal distribution functions do not dif-

fer much in shape and size from the equilibrium one, and we have explicitly checked that this assumption is indeed true for the benchmarks chosen. We have seen that the sterile neutrinos are mostly produced from the decay of Z_{BL} and W^\pm . We have also shown that though the contribution from W^\pm was neglected in the previous works (under the assumption of smallness of the active-sterile mixing angle), it can actually be sizeable (even dominating over the production from Z_{BL} decay for some values of α and g_{BL}) depending on the parameter space we are focussing on. Note that for generic values of α we use here, one of the active neutrinos has to be very light. However this is allowed by the data available from the various present day neutrino experiments. Finally for completeness, we have also checked that such an $\mathcal{O}(\text{MeV})$ mass non-thermal sterile neutrino can explain the 511 keV line observed by INTEGRAL/SPI. The α required to explain this signal falls in the region where the dark matter production is mostly dominated by Z_{BL} decay. The decay width required has a corresponding life time $\sim 10^{25}$ s, which is much larger than the present age of the Universe ($\sim 10^{17}$ s).

2.8 Appendix : Analytical expressions for cross sections and decay widths

2.8.1 Production processes of N_1 from the decays of SM and BSM particles

In this section, we give the expressions of all the relevant decay widths which are needed to solve the coupled Boltzmann equation for N_1 (Eqs. (2.28)).

$$\Gamma(W^+ \rightarrow N_1 e^+) = \frac{2(2M_W^4 - (M_e^2 - M_{N_1}^2)^2 - (M_e^2 + M_{N_1}^2)M_W^2) \sin^2 \alpha}{3v^2} \times \frac{\sqrt{1 - \left(\frac{M_e + M_{N_1}}{M_W}\right)^2} \sqrt{1 - \left(\frac{M_e - M_{N_1}}{M_W}\right)^2}}{16\pi M_W}, \quad (2.33)$$

$$\Gamma(Z \rightarrow N_1 \bar{N}_1) = \frac{M_Z^3 \sin^4 \alpha}{24\pi v^2} \left(1 - \frac{4M_{N_1}^2}{M_Z^2}\right)^{3/2}, \quad (2.34)$$

$$\Gamma(Z_{\text{BL}} \rightarrow N_1 \bar{N}_1) = \frac{M_{Z_{\text{BL}}}^3}{24\pi} ((\sin^2 \alpha - \cos^2 \alpha)^2 g_{\text{BL}}^2) \left(1 - \frac{4M_{N_1}^2}{M_{Z_{\text{BL}}}^2}\right)^{3/2}, \quad (2.35)$$

$$\Gamma(H \rightarrow N_1 \bar{N}_1) = \frac{g_{HN_1 N_1}^2 M_H}{16\pi} \left(1 - \frac{4M_{N_1}^2}{M_H^2}\right)^{3/2}, \quad (2.36)$$

$$\Gamma(h \rightarrow N_1 \bar{N}_1) = \frac{g_{hN_1 N_1}^2 M_h}{16\pi} \left(1 - \frac{4M_{N_1}^2}{M_h^2}\right)^{3/2}, \quad (2.37)$$

where M_x denotes the mass of particle x , α is the active-sterile mixing angle of first generation (i.e. mixing of ν_1 with N_1) while $g_{HN_1 N_1}$ and $g_{hN_1 N_1}$ are vertex factors corresponding to the vertices $HN_1 N_1$ and $hN_1 N_1$ respectively. With respect to our chosen set of independent parameters, these vertex factors are given as:

$$\begin{aligned} g_{HN_1 N_1} &= 2 \cos \alpha \left(\sin \theta \sin \alpha \frac{\sqrt{M_{N_1} m_{\nu_1}}}{v} - \cos \theta \cos \alpha \frac{g_{\text{BL}} M_{N_1}}{M_{Z_{\text{BL}}}} \right), \\ g_{hN_1 N_1} &= 2 \cos \alpha \left(\cos \theta \sin \alpha \frac{\sqrt{M_{N_1} m_{\nu_1}}}{v} + \sin \theta \cos \alpha \frac{g_{\text{BL}} M_{N_1}}{M_{Z_{\text{BL}}}} \right). \end{aligned} \quad (2.38)$$

2.8.2 Production processes of N_1 from annihilation

In this section, we present the expressions of all the relevant annihilation cross sections i.e. the production processes of N_1 through the annihilations of SM as well as BSM particles. In all the expressions given below, M_X and Γ_X denote the mass and total decay

width of the particle X while g_{ijk} denotes the coupling of the vertex involving fields i, j, k . Further, \sqrt{s} is the center of mass energy of a particular annihilation process. All the annihilation cross sections given below are written in terms of our chosen set of independent parameters.

$$\underline{\mathbf{W}^+ \mathbf{W}^- \rightarrow \mathbf{N}_1 \bar{\mathbf{N}}_1}$$

In this annihilation process, three s -channel diagrams mediated by h , H and Z and one electron mediated t -channel diagram are possible. However, Z boson and electron mediated diagrams are suppressed respectively by the fourth and second power of the active-sterile mixing angle α . Therefore we have considered other two s -channel diagrams only.

$$\begin{aligned} g_{WW h} &= \frac{2M_W^2}{v} \cos \theta, \\ g_{WW H} &= \frac{2M_W^2}{v} \sin \theta, \\ A_{WW} &= \frac{g_{WW h} g_{h N_1 N_1} ((s - M_h^2) - i M_h \Gamma_h)}{(s - M_h^2)^2 + (M_h \Gamma_h)^2} + \frac{g_{WW H} g_{H N_1 N_1} ((s - M_H^2) - i M_H \Gamma_H)}{(s - M_H^2)^2 + (M_H \Gamma_H)^2}, \\ |M_{WW}|^2 &= \frac{4}{9} (s - 4M_{N_1}^2) \left(1 + \frac{(s - 2M_W^2)^2}{8M_W^4} \right) |A_{WW}|^2, \\ \sigma_{WW} &= \frac{1}{32\pi s} \frac{\sqrt{1 - \frac{4M_{N_1}^2}{s}}}{\sqrt{1 - \frac{4M_W^2}{s}}} |M_{WW}|^2. \end{aligned} \tag{2.39}$$

$$\underline{\mathbf{Z} \mathbf{Z} \rightarrow \mathbf{N}_1 \bar{\mathbf{N}}_1}$$

There are two s -channel diagrams and two t -channel diagrams for $Z Z \rightarrow N_1 \bar{N}_1$ annihilation process. The t -channel diagrams mediated by active and sterile neutrinos are suppressed by fourth and eighth power of α respectively. Hence we have considered only

two s -channel diagrams mediated by h and H .

$$\begin{aligned}
g_{ZZh} &= \frac{2M_Z^2}{v} \cos \theta, \\
g_{ZZH} &= \frac{2M_Z^2}{v} \sin \theta, \\
A_{ZZ} &= \frac{g_{ZZh} g_{hN_1N_1} ((s - M_h^2) - i M_h \Gamma_h)}{(s - M_h^2)^2 + (M_h \Gamma_h)^2} + \frac{g_{ZZH} g_{HN_1N_1} ((s - M_H^2) - i M_H \Gamma_H)}{(s - M_H^2)^2 + (M_H \Gamma_H)^2}, \\
|M_{ZZ}|^2 &= \frac{4}{9} (s - 4M_{N_1}^2) \left(1 + \frac{(s - 2M_Z^2)^2}{8M_Z^4} \right) |A_{ZZ}|^2, \\
\sigma_{ZZ} &= \frac{1}{32\pi s} \frac{\sqrt{1 - \frac{4M_{N_1}^2}{s}}}{\sqrt{1 - \frac{4M_Z^2}{s}}} |M_{ZZ}|^2.
\end{aligned} \tag{2.40}$$

$f \bar{f} \rightarrow N_1 \bar{N}_1$ (where f denotes any SM quarks or leptons)

In this annihilation process four s -channel diagrams, mediated by Z , Z_{BL} , h and H , are possible. However, the Z boson mediated diagram is suppressed by α^4 and consequently we have neglected it.

$$\begin{aligned}
g_{ffh} &= -\frac{M_f}{v} \cos \theta, \\
g_{ffH} &= -\frac{M_f}{v} \sin \theta, \\
A_{ff} &= \frac{g_{ffh} g_{hN_1N_1} ((s - M_h^2) - i M_h \Gamma_h)}{(s - M_h^2)^2 + (M_h \Gamma_h)^2} + \frac{g_{ffH} g_{HN_1N_1} ((s - M_H^2) - i M_H \Gamma_H)}{(s - M_H^2)^2 + (M_H \Gamma_H)^2}, \\
|M_{ff}|^2 &= \frac{g_{BL}^4 q_f^2 \left(\frac{8(s - 4M_{N_1}^2)(s + 2M_f^2)}{3n_c} \right)}{(s - M_{Z_{BL}}^2)^2 + (\Gamma_{Z_{BL}} M_{Z_{BL}})^2} + \frac{2}{n_c} |A_{ff}|^2 (s - 4M_{N_1}^2)(s - 4M_f^2) \\
\sigma_{ff} &= \frac{1}{64\pi s} \frac{\sqrt{1 - \frac{4M_{N_1}^2}{s}}}{\sqrt{1 - \frac{4M_f^2}{s}}} |M_{ff}|^2,
\end{aligned} \tag{2.41}$$

where n_c is the colour charge of the corresponding fermion (f).

Although, the annihilation processes $HH \rightarrow N_1 \bar{N}_1$, $hh \rightarrow N_1 \bar{N}_1$ consist of two t -channel and two s -channel diagrams, we consider only the two dominant s -channel diagrams mediated by H and h .

$\mathbf{H H} \rightarrow \mathbf{N_1 \bar{N}_1}$

$$\begin{aligned}
g_{HHh} &= 2 \sin \theta \cos^2 \theta (3\lambda_2 - \lambda_3) v_{\text{BL}} - \lambda_3 v \cos^3 \theta + 2 \cos \theta \sin^2 \theta (\lambda_3 - 3\lambda_1) v + \lambda_3 v_{\text{BL}} \sin^3 \theta, \\
g_{HHH} &= -3 (\lambda_3 \sin \theta \cos^2 \theta v + 2 \cos^3 \theta \lambda_2 v_{\text{BL}} + \sin^2 \theta \cos \theta \lambda_3 v_{\text{BL}} + 2 \sin^3 \theta \lambda_1 v), \\
A_{HH} &= \frac{g_{HHh} g_{hN_1 N_1} ((s - M_h^2) - i M_h \Gamma_h)}{(s - M_h^2)^2 + (M_h \Gamma_h)^2} + \frac{g_{HHH} g_{HN_1 N_1} ((s - M_H^2) - i M_H \Gamma_H)}{(s - M_H^2)^2 + (M_H \Gamma_H)^2}, \\
|M_{HH}|^2 &= 2 (s - 4M_{N_1}^2) |A_{ZZ}|^2, \\
\sigma_{HH} &= \frac{1}{32\pi s} \frac{\sqrt{1 - \frac{4M_{N_1}^2}{s}}}{\sqrt{1 - \frac{4M_H^2}{s}}} |M_{HH}|^2.
\end{aligned} \tag{2.42}$$

$\mathbf{h h} \rightarrow \mathbf{N_1 \bar{N}_1}$

$$\begin{aligned}
g_{hhH} &= 2 \sin \theta \cos^2 \theta (\lambda_3 - 3\lambda_1) v - \lambda_3 v_{\text{BL}} \cos^3 \theta + 2 \cos \theta \sin^2 \theta (\lambda_3 - 3\lambda_2) v_{\text{BL}} - \lambda_3 v \sin^3 \theta, \\
g_{hhh} &= 3 (\lambda_3 \sin \theta \cos^2 \theta v_{\text{BL}} - 2 \cos^3 \theta \lambda_1 v - \sin^2 \theta \cos \theta \lambda_3 v + 2 \sin^3 \theta \lambda_2 v_{\text{BL}}), \\
A_{hh} &= \frac{g_{hhh} g_{hN_1 N_1} ((s - M_h^2) - i M_h \Gamma_h)}{(s - M_h^2)^2 + (M_h \Gamma_h)^2} + \frac{g_{hhH} g_{HN_1 N_1} ((s - M_H^2) - i M_H \Gamma_H)}{(s - M_H^2)^2 + (M_H \Gamma_H)^2}, \\
|M_{hh}|^2 &= 2 (s - 4M_{N_1}^2) |A_{hh}|^2, \\
\sigma_{hh} &= \frac{1}{32\pi s} \frac{\sqrt{1 - \frac{4M_{N_1}^2}{s}}}{\sqrt{1 - \frac{4M_h^2}{s}}} |M_{hh}|^2.
\end{aligned} \tag{2.43}$$

$\lambda_1, \lambda_2, \lambda_3$ has been previously expressed in terms of the independent parameters (Eqs. (2.19-2.21)).

$\mathbf{Z_{BL} Z_{BL}} \rightarrow \mathbf{N_1 \bar{N}_1}$

This annihilation process is also mediated by two s -channel diagrams and two t -channel diagrams. However the t -channel diagram mediated by active neutrino is suppressed by α^4 . Therefore we have considered two s -channel diagrams and one t -channel diagram mediated by H, h and N_1 respectively. For simplicity, due to smallness of α , we have considered $\cos \alpha \simeq 1$ and consequently $\sin \alpha \simeq 0$ in the following expressions (Eq.

(2.44)-(2.51)).

$$\begin{aligned}
A_1 = & \left[-2g_{\text{BL}}^4 \left(- (4M_{N_1}^2 - s)^{3/2} (4M_{\text{ZBL}}^2 - s)^{3/2} \left(s^2 M_{\text{ZBL}}^4 + 20s M_{\text{ZBL}}^6 - 48M_{\text{ZBL}}^8 + \right. \right. \right. \\
& 2M_{N_1}^4 (-56s M_{\text{ZBL}}^2 + 16M_{\text{ZBL}}^4 + s^2) + M_{N_1}^2 (16s^2 M_{\text{ZBL}}^2 - 102s M_{\text{ZBL}}^4 + 184M_{\text{ZBL}}^6 + s^3) \Big) \\
& + 12M_{\text{ZBL}}^4 (2M_{\text{ZBL}}^2 - 8M_{N_1}^2 - s) (M_{N_1}^2 (s - 4M_{\text{ZBL}}^2) + M_{\text{ZBL}}^4) \\
& \left. \left. 2(s - 4M_{\text{ZBL}}^2)(4M_{N_1}^2 - s) \log \left(\frac{s - \sqrt{4M_{N_1}^2 - s} \sqrt{4M_{\text{ZBL}}^2 - s - 2M_{\text{ZBL}}^2}}{s + \sqrt{4M_{N_1}^2 - s} \sqrt{4M_{\text{ZBL}}^2 - s - 2M_{\text{ZBL}}^2}} \right) \right) \right] \times \\
& \frac{1}{27M_{\text{ZBL}}^4 (4M_{N_1}^2 - s)^{3/2} (4M_{\text{ZBL}}^2 - s)^{3/2} (M_{N_1}^2 (s - 4M_{\text{ZBL}}^2) + M_{\text{ZBL}}^4)}, \tag{2.44}
\end{aligned}$$

$$\begin{aligned}
A_2 = & \left[\sqrt{4M_{N_1}^2 - s} (2M_{\text{ZBL}}^2 - s) \sqrt{4M_{\text{ZBL}}^2 - s} \left(M_{N_1}^2 (88M_{\text{ZBL}}^2 - 46s) + s (20M_{\text{ZBL}}^2 + s) \right) + \right. \\
& 48s (M_{N_1} - M_{\text{ZBL}}) (M_{\text{ZBL}} + M_{N_1}) (M_{N_1}^2 (4M_{\text{ZBL}}^2 - s) - M_{\text{ZBL}}^4) \times \\
& \left. \log \left(\frac{1 + \frac{\sqrt{4M_{N_1}^2 - s} (s - 2M_{\text{ZBL}}^2) \sqrt{4M_{\text{ZBL}}^2 - s}}{M_{N_1}^2 (8M_{\text{ZBL}}^2 - 2s) - 4s M_{\text{ZBL}}^2 + 2M_{\text{ZBL}}^4 + s^2}}{1 - \frac{\sqrt{4M_{N_1}^2 - s} (s - 2M_{\text{ZBL}}^2) \sqrt{4M_{\text{ZBL}}^2 - s}}{M_{N_1}^2 (8M_{\text{ZBL}}^2 - 2s) - 4s M_{\text{ZBL}}^2 + 2M_{\text{ZBL}}^4 + s^2}} \right) \right] \frac{2g_{\text{BL}}^4}{27M_{\text{ZBL}}^4 \sqrt{4M_{N_1}^2 - s} (s - 2M_{\text{ZBL}}^2) \sqrt{4M_{\text{ZBL}}^2 - s}}, \tag{2.45}
\end{aligned}$$

$$\begin{aligned}
A_3 = & \left[\left(\sqrt{s - 4M_{N_1}^2} \sqrt{s - 4M_{\text{ZBL}}^2} (-2s M_{\text{ZBL}}^2 + 4M_{\text{ZBL}}^4 + s^2) \right. \right. \\
& + 2(M_{N_1}^2 (-4s M_{\text{ZBL}}^2 + 8M_{\text{ZBL}}^4 + s^2) - 2M_{\text{ZBL}}^6) \times \\
& \left. \left. \log \left(\frac{s - \sqrt{s - 4M_{N_1}^2} \sqrt{s - 4M_{\text{ZBL}}^2} - 2M_{\text{ZBL}}^2}{s + \sqrt{s - 4M_{N_1}^2} \sqrt{s - 4M_{\text{ZBL}}^2} - 2M_{\text{ZBL}}^2} \right) \right) \right. \\
& \left. 64g_{\text{BL}}^4 \sin^2 \theta M_{N_1}^2 (M_h^2 - s) \right] \times \\
& \frac{1}{9M_{\text{ZBL}}^4 \sqrt{s - 4M_{N_1}^2} \sqrt{s - 4M_{\text{ZBL}}^2} (\Gamma_h^2 M_h^2 + (M_h^2 - s)^2)}, \tag{2.46}
\end{aligned}$$

$$\begin{aligned}
A_4 = & \left[\left(\sqrt{s - 4M_{N_1}^2} \sqrt{s - 4M_{Z_{BL}}^2} (-2sM_{Z_{BL}}^2 + 4M_{Z_{BL}}^4 + s^2) \right. \right. \\
& + 2 \left(M_{N_1}^2 (-4sM_{Z_{BL}}^2 + 8M_{Z_{BL}}^4 + s^2) - 2M_{Z_{BL}}^6 \right) \times \\
& \left. \log \left(\frac{s - \sqrt{s - 4M_{N_1}^2} \sqrt{s - 4M_{Z_{BL}}^2} - 2M_{Z_{BL}}^2}{s + \sqrt{s - 4M_{N_1}^2} \sqrt{s - 4M_{Z_{BL}}^2} - 2M_{Z_{BL}}^2} \right) \right) \\
& \left. 64 g_{BL}^4 \cos^2 \theta M_{N_1}^2 (M_H^2 - s) \right] \times \\
& \frac{1}{9M_{Z_{BL}}^4 \sqrt{s - 4M_{N_1}^2} \sqrt{s - 4M_{Z_{BL}}^2} (\Gamma_H^2 M_H^2 + (M_H^2 - s)^2)}, \tag{2.47}
\end{aligned}$$

$$A_5 = \frac{32 g_{BL}^4 \sin^4 \theta M_{N_1}^2 (s - 4M_{N_1}^2) (s^2 - 4sM_{Z_{BL}}^2 + 12M_{Z_{BL}}^4)}{9 M_{Z_{BL}}^4 (\Gamma_h^2 M_h^2 + (M_h^2 - s)^2)}, \tag{2.48}$$

$$A_6 = \frac{32 g_{BL}^4 \cos^4 \theta M_{N_1}^2 (s - 4M_{N_1}^2) (s^2 - 4sM_{Z_{BL}}^2 + 12M_{Z_{BL}}^4)}{9 M_{Z_{BL}}^4 (\Gamma_H^2 M_H^2 + (M_H^2 - s)^2)}, \tag{2.49}$$

$$\begin{aligned}
A_7 = & \left[64 g_{BL}^4 \sin^2 \theta \cos^2 \theta M_{N_1}^2 (s - 4M_{N_1}^2) (s^2 - 4sM_{Z_{BL}}^2 + 12M_{Z_{BL}}^4) \times \right. \\
& \left. (\Gamma_h M_h \Gamma_H M_H + (s - M_h^2) (s - M_H^2)) \right] \times \\
& \frac{1}{9M_{Z_{BL}}^4 (\Gamma_h^2 M_h^2 + (M_h^2 - s)^2) (\Gamma_H^2 M_H^2 + (M_H^2 - s)^2)}, \tag{2.50}
\end{aligned}$$

$$\sigma_{Z_{BL}, Z_{BL}} = \frac{1}{32\pi s} \frac{\sqrt{1 - \frac{4M_{N_1}^2}{s}}}{\sqrt{1 - \frac{4M_{Z_{BL}}^2}{s}}} \sum_{i=1}^7 A_i \tag{2.51}$$

$N_x \bar{N}_x \rightarrow N_1 \bar{N}_1$ (where N_x s are the other two sterile neutrinos with $x = 2, 3$)

In this annihilation process we have considered the only Z_{BL} mediated s -channel diagram as it contributes dominantly over the other possible diagrams.

$$\begin{aligned}
g_{N_x N_x Z_{\text{BL}}} &= -g_{\text{BL}}(\cos \alpha_x^2 - \sin \alpha_x^2), \\
g_{N_1 N_1 Z_{\text{BL}}} &= -g_{\text{BL}}(\cos \alpha^2 - \sin \alpha^2), \\
\sigma_{N_x N_x} &= \frac{(g_{N_x N_x Z_{\text{BL}}} \times g_{N_1 N_1 Z_{\text{BL}}})^2}{256 \pi s \left[(s - M_{Z_{\text{BL}}}^2)^2 + (\Gamma_{Z_{\text{BL}}} M_{Z_{\text{BL}}})^2 \right]} \frac{\sqrt{s - 4M_{N_1}^2}}{\sqrt{s - 4M_{N_x}^2}} \times \\
&\quad \left[\frac{32 (4M_{N_1}^2 (M_{N_x}^2 (-6s M_{Z_{\text{BL}}}^2 + 7M_{Z_{\text{BL}}}^4 + 3s^2) - s M_{Z_{\text{BL}}}^4) + s M_{Z_{\text{BL}}}^4 (s - 4M_{N_x}^2))}{3M_{Z_{\text{BL}}}^4} \right].
\end{aligned} \tag{2.52}$$

Here, α_x is the active-sterile neutrino mixing angle of ν_x with N_x with $x = 1, 2, 3$ and α_1 has been denoted simply by α .

2.8.3 Total decay widths of Z_{BL} , H and h

The total decay width of different particles used in the expressions for the annihilation cross section are given below :

Total Decay width of Z_{BL}

$$\begin{aligned}
\Gamma(Z_{\text{BL}} \rightarrow f \bar{f}) &= \frac{M_{Z_{\text{BL}}}}{12 \pi} n_c (q_f g_{\text{BL}})^2 \left(1 + \frac{2 M_f^2}{M_{Z_{\text{BL}}}^2} \right) \sqrt{1 - \frac{4 M_f^2}{M_{Z_{\text{BL}}}^2}}, \\
\Gamma(Z_{\text{BL}} \rightarrow \nu_x \bar{\nu}_x) &= \frac{M_{Z_{\text{BL}}}}{24 \pi} ((\cos^2 \alpha_x - \sin^2 \alpha_x)^2 g_{\text{BL}}^2) \left(1 - \frac{4 M_{\nu_x}^2}{M_{Z_{\text{BL}}}^2} \right)^{3/2}, \\
\Gamma(Z_{\text{BL}} \rightarrow N_x \bar{N}_x) &= \frac{M_{Z_{\text{BL}}}}{24 \pi} ((\sin^2 \alpha_x - \cos^2 \alpha_x)^2 g_{\text{BL}}^2) \left(1 - \frac{4 M_{N_x}^2}{M_{Z_{\text{BL}}}^2} \right)^{3/2}.
\end{aligned} \tag{2.53}$$

$$\Gamma_{Z_{\text{BL}}} = \sum_f \Gamma(Z_{\text{BL}} \rightarrow f \bar{f}) + \sum_{x=1}^3 \left(\Gamma(Z_{\text{BL}} \rightarrow \nu_x \bar{\nu}_x) + \Gamma(Z_{\text{BL}} \rightarrow N_x \bar{N}_x) \right). \tag{2.54}$$

Total Decay width of H

$$\begin{aligned}
\Gamma(H \rightarrow V V) &= \frac{G_F M_H^3 \sin^2 \theta \delta V}{16\sqrt{2} \pi} \sqrt{1 - \frac{4 M_V^2}{M_H^2}} \left(1 - \frac{4 M_V^2}{M_H^2} + \frac{12 M_V^4}{M_H^4} \right), \\
\Gamma(H \rightarrow Z_{\text{BL}} Z_{\text{BL}}) &= \frac{g_{\text{BL}}^2 M_H^3 \cos^2 \theta}{8 \pi M_{Z_{\text{BL}}}^2} \sqrt{1 - \frac{4 M_{Z_{\text{BL}}}^2}{M_H^2}} \left(1 - \frac{4 M_{Z_{\text{BL}}}^2}{M_H^2} + \frac{12 M_{Z_{\text{BL}}}^4}{M_H^4} \right), \quad (2.55) \\
\Gamma(H \rightarrow f \bar{f}) &= \frac{n_c M_H}{8 \pi} \left(\frac{M_f \sin \theta}{v} \right)^2 \left(1 - \frac{4 M_f^2}{M_H^2} \right)^{3/2}, \\
\Gamma(H \rightarrow h h) &= \frac{g_{hhH}^2}{32 \pi M_H} \sqrt{1 - \frac{4 M_h^2}{M_H^2}}, \\
\Gamma(H \rightarrow N_x \bar{N}_x) &= \frac{g_{HN_x N_x}^2 M_H}{16 \pi} \left(1 - \frac{4 M_{N_x}^2}{M_H^2} \right)^{3/2}, \\
\Gamma(H \rightarrow \nu_x \bar{\nu}_x) &= \frac{g_{H\nu_x \nu_x}^2 M_H}{16 \pi} \left(1 - \frac{4 M_{\nu_x}^2}{M_H^2} \right)^{3/2}, \quad (2.56)
\end{aligned}$$

$$\begin{aligned}
\Gamma_H &= \sum_f \Gamma(H \rightarrow f \bar{f}) + \sum_{x=1}^3 \left(\Gamma(H \rightarrow \nu_x \bar{\nu}_x) + \Gamma(H \rightarrow N_x \bar{N}_x) \right) \\
&\quad + \sum_{V=W, Z} \Gamma(H \rightarrow V V) + \Gamma(H \rightarrow Z_{\text{BL}} Z_{\text{BL}}), \quad (2.57)
\end{aligned}$$

where, $\delta V = 2$ for W boson and 1 for Z boson and

$$\begin{aligned}
g_{HN_x N_x} &= 2 \cos \alpha_x \left(\sin \theta \sin \alpha_x \frac{\sqrt{M_{N_x} m_{\nu_x}}}{v} - \cos \theta \cos \alpha_x \frac{g_{\text{BL}} M_{N_x}}{M_{Z_{\text{BL}}}} \right), \\
g_{H\nu_x \nu_x} &= 2 \sin \alpha_x \left(\sin \theta \cos \alpha_x \frac{\sqrt{M_{N_x} m_{\nu_x}}}{v} + \cos \theta \sin \alpha_x \frac{g_{\text{BL}} M_{N_x}}{M_{Z_{\text{BL}}}} \right).
\end{aligned}$$

Total Decay width of h

$$\begin{aligned}
\Gamma(h \rightarrow Z_{\text{BL}} Z_{\text{BL}}) &= \frac{g_{\text{BL}}^2 M_h^3 \sin^2 \theta}{8 \pi M_{Z_{\text{BL}}}^2} \sqrt{1 - \frac{4 M_{Z_{\text{BL}}}^2}{M_h^2}} \left(1 - \frac{4 M_{Z_{\text{BL}}}^2}{M_h^2} + \frac{12 M_{Z_{\text{BL}}}^4}{M_h^4} \right), \\
\Gamma(h \rightarrow H H) &= \frac{g_{HHh}^2}{32 \pi M_h} \sqrt{1 - \frac{4 M_H^2}{M_h^2}}, \\
\Gamma(h \rightarrow N_x \bar{N}_x) &= \frac{g_{hN_x N_x}^2 M_h}{16 \pi} \left(1 - \frac{4 M_{N_x}^2}{M_h^2} \right)^{3/2}, \\
\Gamma(h \rightarrow \nu_x \bar{\nu}_x) &= \frac{g_{h\nu_x \nu_x}^2 M_h}{16 \pi} \left(1 - \frac{4 M_{\nu_x}^2}{M_h^2} \right)^{3/2},
\end{aligned}$$

$$\begin{aligned}\Gamma_h &= \cos^2 \theta \Gamma_h^{\text{SM}} + \Gamma(h \rightarrow Z_{\text{BL}} Z_{\text{BL}}) + \Gamma(h \rightarrow H H) \\ &+ \sum_{x=1}^3 \left(\Gamma(h \rightarrow \nu_x \bar{\nu}_x) + \Gamma(h \rightarrow N_x \bar{N}_x) \right),\end{aligned}\quad (2.58)$$

where $\Gamma_h^{\text{SM}} = 4.14 \times 10^{-3} \text{ MeV}$ [165] is the decay width of SM Higgs boson with mass 125.5 GeV and

$$\begin{aligned}g_{hN_x N_x} &= 2 \cos \alpha_x \left(\cos \theta \sin \alpha_x \frac{\sqrt{M_{N_x} m_{\nu_x}}}{v} + \sin \theta \cos \alpha_x \frac{g_{\text{BL}} M_{N_x}}{M_{Z_{\text{BL}}}} \right), \\ g_{h\nu_x \nu_x} &= 2 \sin \alpha_x \left(\cos \theta \cos \alpha_x \frac{\sqrt{M_{N_x} m_{\nu_x}}}{v} - \sin \theta \sin \alpha_x \frac{g_{\text{BL}} M_{N_x}}{M_{Z_{\text{BL}}}} \right).\end{aligned}$$

2.8.4 Decay width of $N_1 \rightarrow e^\pm \nu_i$ ($i = 1$ to 3)

In this section, we have calculated the three body decay width of sterile neutrino dark matter N_1 into e^\pm and ν_i . In this calculation we have considered only W^\pm and Z bosons mediated diagrams as these three diagrams contribute dominantly to this decay process of N_1 . Also in our calculation, for simplicity, we have neglected terms involving neutrino masses as these are extremely tiny compared to the masses of other particles. Further, we have neglected the intergenerational mixing between active and sterile neutrinos. We have define two quantities X and Y in terms of four momentums of ν_i , e^\pm and N_1 as

$$X = (P - p_1)^2, \quad (2.59)$$

$$Y = (P - p_2)^2, \quad (2.60)$$

where P is four momentum of N_1 while that of ν_i and e^\pm are p_1 and p_2 respectively. Now,

$$\begin{aligned}B_1 &= \frac{8}{M_Z^4} \left(a_2^2 \left(M_Z^4 (4Y M_e^2 - 2M_e^4 + M_{N_1}^2 (X + 2Y) - X^2 - 2XY - 2Y^2) \right) + a_3^2 \left(M_{N_1}^2 (M_Z^4 \times \right. \right. \\ &\quad (X + 2Y) - 2M_e^2 (-2X M_Z^2 + 2M_Z^4 + X^2)) + 2M_e^2 M_{N_1}^4 (X - 2M_Z^2) + M_Z^4 (-(-4M_e^2 \times \\ &\quad (X + Y) + 2M_e^4 + X^2 + 2XY + 2Y^2)) \left. \left. \right) \right),\end{aligned}\quad (2.61)$$

$$\begin{aligned}
B_2 = & -\frac{16}{M_W^4} \left(M_e^4 (-M_{N_1}^2 (8M_W^2 + 7(X+Y)) + 5M_{N_1}^4 + 4M_W^2 (M_W^2 + X) + (X+Y)^2) \right. \\
& + M_e^2 (M_{N_1}^2 (4M_W^2 (M_W^2 + Y) + (X+Y)^2) - M_{N_1}^4 (X+Y) - 8YM_W^4) - 2M_e^6 (-3M_{N_1}^2 \\
& \left. + X+Y) + M_e^8 + 4YM_W^4 (Y - M_{N_1}^2) \right), \tag{2.62}
\end{aligned}$$

$$\begin{aligned}
B_3 = & -\frac{16}{M_W^4} \left(M_e^4 (YM_{N_1}^2 + M_{N_1}^4 + 4M_W^2 (M_W^2 + X) + Y^2) + M_e^2 (M_{N_1}^2 (-4M_W^2 (X+Y) + 4M_W^4 \right. \\
& + Y^2) - M_{N_1}^4 (Y - 4M_W^2) - 8M_W^4 (X+Y)) - 2M_e^6 (M_{N_1}^2 + Y) + M_e^8 + 4M_W^4 (X+Y) \\
& \left. (-M_{N_1}^2 + X+Y) \right), \tag{2.63}
\end{aligned}$$

$$\begin{aligned}
B_4 = & -\frac{8}{M_W^2 M_Z^2} \left(a_2 M_Z^2 \left(M_e^4 (M_{N_1}^2 + 2M_W^2 - X - 2Y) + M_e^2 (-M_{N_1}^2 (3X + 2Y) + 2M_{N_1}^4 + 2M_W^2 \times \right. \right. \\
& (X - 2Y) + (X+Y)^2) + M_e^6 + 2YM_W^2 (Y - M_{N_1}^2) \Big) + a_3 \left(M_{N_1}^2 (M_Z^2 (-M_e^2 (4M_W^2 + 3X \right. \\
& + 4Y) + 5M_e^4 + 2YM_W^2) + XM_e^2 (-2M_e^2 + 2M_W^2 + X+Y)) + M_e^2 M_{N_1}^4 (M_e^2 - 2M_W^2 + 2M_Z^2 \\
& - X) + M_Z^2 (-2M_W^2 (-M_e^2 (X+2Y) + M_e^4 + Y^2) - M_e^4 (3X+2Y) + M_e^2 (X+Y)^2 + M_e^6) \Big) \Big), \tag{2.64}
\end{aligned}$$

$$\begin{aligned}
B_5 = & -\frac{8}{M_W^2 M_Z^2} \left(a_2 M_Z^2 \left(M_e^2 (-XM_{N_1}^2 + M_{N_1}^4 - 2M_W^2 (X+2Y) + Y^2) + M_e^4 (-M_{N_1}^2 + 2M_W^2 + X \right. \right. \\
& - 2Y) + M_e^6 + 2M_W^2 (X+Y) (-M_{N_1}^2 + X+Y) \Big) + a_3 \left(M_e^2 (M_{N_1}^2 (M_Z^2 (-4M_W^2 + X+2Y) \right. \\
& + 2XM_W^2 - XY) + M_{N_1}^4 (- (2M_W^2 + M_Z^2)) + M_Z^2 (M_W^2 (6X+4Y) + Y^2)) + M_e^4 (M_{N_1}^4 - M_Z^2 \times \\
& (M_{N_1}^2 + 2M_W^2 + X+2Y)) + M_e^6 M_Z^2 - 2M_W^2 M_Z^2 (X+Y) (-M_{N_1}^2 + X+Y) \Big) \Big), \tag{2.65}
\end{aligned}$$

Also,

$$\begin{aligned}
f_1 &= \left(\frac{e \sin 2\alpha}{2 \sin 2\theta_W} \right)^2, \\
f_2 &= \left(\frac{e^2 \sin 2\alpha}{16 \sin^2 \theta_W} \right)^2, \\
f_3 &= -\frac{e^3 \sin^2 2\alpha}{32 \sin^2 \theta_W \sin 2\theta_W},
\end{aligned} \tag{2.66}$$

and

$$\begin{aligned}
D_1 &= (X - M_Z^2)^2 + (\Gamma_Z M_Z)^2, \\
D_2 &= (M_{N_1}^2 + M_{\nu_1}^2 + 2M_e^2 - X - Y - M_W^2)^2 + (\Gamma_W M_W)^2, \\
D_3 &= (Y - M_W^2)^2 + (\Gamma_W M_W)^2, \\
D_4 &= D_1 D_2, \\
D_5 &= D_1 D_3,
\end{aligned} \tag{2.67}$$

with Γ_W and Γ_Z are the total decay widths of W^\pm and Z bosons respectively.

Therefore,

$$\begin{aligned}
|M_1^2| &= \frac{1}{2} \frac{B_1 f_1}{D_1} \times \left(\sum_{\alpha=1}^3 U_{e\alpha}^2 \right), \\
|M_2^2| &= \frac{1}{2} \frac{B_2 f_2}{D_2} \times \left(\sum_{\alpha=1}^3 U_{e\alpha}^4 \right), \\
|M_3^2| &= \frac{1}{2} \frac{B_3 f_2}{D_3} \times \left(\sum_{\alpha=1}^3 U_{e\alpha}^4 \right), \\
|M_4^2| &= \frac{B_4 f_3 [(M_{N_1}^2 + M_{\nu_1}^2 + 2M_e^2 - X - Y - M_W^2)(X - M_Z^2) + \Gamma_W \Gamma_Z M_W M_Z]}{D_4} \times \left(\sum_{\alpha=1}^3 U_{e\alpha}^3 \right), \\
|M_5^2| &= \frac{B_5 f_3 [(Y - M_W^2)(X - M_Z^2) + \Gamma_W \Gamma_Z M_W M_Z]}{D_5} \times \left(\sum_{\alpha=1}^3 U_{e\alpha}^3 \right),
\end{aligned} \tag{2.68}$$

where $U_{e\alpha}$ s are the elements of PMNS matrix of neutrino mixing and in terms of neutrino mixing angles these are defined as (assuming Dirac CP phase $\delta = 0$)

$$U_{e1} = \cos \theta_{12} \cos \theta_{13}, \quad U_{e2} = \sin \theta_{12} \cos \theta_{13}, \quad U_{e3} = \sin \theta_{13}. \quad (2.69)$$

Finally, the expression of Matrix amplitude square for the process $N_1 \rightarrow e^\pm \nu_i$ is given by,

$$|M^2| = \sum_1^5 |M_i^2|. \quad (2.70)$$

The corresponding decay width in terms of $|M^2|$ is given by,

$$\Gamma_{N_1 \rightarrow e^\pm \nu_i} = \frac{1}{2\pi^3} \frac{1}{32 M_{N_1}^3} \int_{Y_{min}}^{Y_{max}} \int_{X_{min}}^{X_{max}} |M^2| dX dY. \quad (2.71)$$

The upper and lower limits of the quantities X and Y are given below

$$\begin{aligned} X_{min} &= (x+y)^2 - \left(\sqrt{x^2 - M_e^2} - \sqrt{y^2 - M_e^2} \right)^2, \\ X_{max} &= (x+y)^2 - \left(\sqrt{x^2 - M_e^2} + \sqrt{y^2 - M_e^2} \right)^2, \end{aligned} \quad (2.72)$$

with

$$\begin{aligned} x &= \frac{Y + M_e^2}{2\sqrt{Y}}, \\ y &= \frac{M_{N_1}^2 - Y - M_e^2}{2\sqrt{Y}}, \end{aligned} \quad (2.73)$$

and

$$\begin{aligned} Y_{min} &= M_e^2, \\ Y_{max} &= (M_{N_1} - M_e)^2. \end{aligned} \quad (2.74)$$

Chapter 3

Calculation of Momentum Distribution Function of a Non-thermal Dark Matter

3.1 Introduction

In this chapter we study the viability of a non-thermal dark matter candidate within the framework of a recently proposed model called the *new* $U(1)_{B-L}$ model [166]. It is *new* in the sense that this model unlike the usual $U(1)_{B-L}$ model has no right handed neutrinos. Four chiral fermions are however introduced for anomaly cancellations. These chiral fermions linearly combine together in mass basis to give rise to two Dirac fermions namely ψ_1 and ψ_2 . Two extra scalars were introduced in order to give masses to these fermions. The charge assignment of the new particles under the $U(1)_{B-L}$ gauge group is consequently different from the usual model. Since the model is symmetric under a local gauge group (i.e. $U(1)_{B-L}$), it naturally has an extra gauge boson (Z_{BL}), which gets mass after this extra gauge symmetry is broken spontaneously. We will take the lightest of the two Dirac fermions (ψ_1) as our non-thermal dark matter candidate.

Another novel feature of this new model (as was already noted in [166]) is that it can explain the generation of neutrino mass through a Type II see-saw mechanism upon the introduction of a new scalar triplet (Δ) with suitable B-L charge.

The study assuming the lightest Dirac fermion to be a thermal dark matter has already been done in Ref. [166]. We see from their analysis that the relic density constraint is actually satisfied within very small regions. It is satisfied either when $M_{DM} \sim M_{Z_{BL}}/2$ (i.e. near the resonance) or when dark matter mass is ~ 4 TeV. But a priori there is no reason for the dark matter mass to be $\sim M_{Z_{BL}}/2$ as there is no symmetry in the Lagrangian, which can relate the masses of dark matter (ψ_1) and Z_{BL} in the above mentioned way. This

naturally motivates one to study the implications of a non-thermal dark matter candidate within this frame work. Imposing the non-thermality condition implies that unlike in the thermal case, the dark matter particles are so feebly interacting that they never attain thermal equilibrium. An approximate mathematical statement in this regard will be $\frac{n_{eq}\langle\sigma v\rangle}{H} < 1$, which means that the interaction rate for scattering of dark matter particles is less than the expansion rate of the Universe and hence the particles fail to scatter with other particles within the thermal plasma and so remains out of the thermal soup. We have shown here that, this model can indeed accommodate a non-thermal dark matter candidate with correct relic density. We have solved a coupled set of Boltzmann equations to find the momentum distribution function for the dark matter particles. Knowledge of the non-equilibrium momentum distribution function (unlike in the usual scenarios where only the comoving number density ($Y = n/s$) is solved for) will allow us to calculate all the relevant quantities of interest like the relic density (from freeze in), constraints from structure formation, bounds from relativistic degrees of freedom etc. It is well known that, if the particles under consideration are produced from a non-thermal source (e.g. from the decay of an out of equilibrium mother particle) then solving the usual Boltzmann equations in terms of Y is only an approximate method to find the comoving number density. This formalism will provide roughly the correct result as long as we do not move far from equilibrium. In light of this, we have also discussed and compared results from our exact calculations with that obtained from the above mentioned approximate method.

An important difference with the earlier work is that unlike in [166], here all the (three) mixing angles between the three scalars (i.e. SM Higgs, and the two non-standard Higgs) are taken into account and we have found that in some cases, two of them significantly control the final DM abundance.

The rest of the chapter is divided as follows: In Section 3.2 we have discuss the *new* $U(1)_{B-L}$ model in detail. Section 3.3 deals with the FIMP scenario and also with the coupled Boltzmann equations needed to solve the non-thermal momentum distribution function of DM. The results that we have found by solving the coupled Boltzmann equations are presented in Section 3.4. In Section 3.5 we discuss about the relevant theoretical as well as experimental constraints on this non-thermal dark matter scenario. Finally the conclusion is given Section 3.6. The detailed derivations all the collision terms as well as the relevant vertex factors and decay widths are given in the Appendix.

3.2 A new $U(1)_{B-L}$ extension of Standard Model

We consider a *new* $U(1)_{B-L}$ extension of the Standard Model of particle physics. The model has been proposed in Ref. [166]. This model does not contain any sterile neutrino like the *minimal* $U(1)_{B-L}$ model [167] which is usually studied in the literature. The gauge group however is the same i.e. $SU(2)_L \times U(1)_Y \times U(1)_{B-L}$. But in the absence of the three sterile neutrinos we need some extra chiral fermions for the cancellation of axial vector anomaly [168] and mixed gravitational-gauge anomaly [169]. Hence four chiral fermions namely ξ_L, η_L, χ_{1R} and χ_{2R} with suitable $B - L$ charges are introduced. In order to generate Dirac type mass terms for these chiral fermions in a gauge invariant manner we need two distinct scalar fields (ϕ_1, ϕ_2) with different $B - L$ charges. All the fields and their corresponding charges under $SU(2)_L, U(1)_Y$ and $U(1)_{B-L}$ gauge groups are given in Table 3.1. The presence of a new gauge symmetry ($U(1)_{B-L}$) also introduces its corresponding gauge boson (Z_{BL}) to the particle spectrum and Z_{BL} becomes massive whenever the proposed $B - L$ symmetry is broken spontaneously by the VEVs of scalar fields.

The gauge invariant Lagrangian for these new fields is given by:

$$\begin{aligned} \mathcal{L}_{BL} = & i \bar{\eta}_L \gamma_\mu D_\eta^\mu \eta_L + i \bar{\xi}_L \gamma_\mu D_\xi^\mu \xi_L + i \sum_{i=1}^2 \bar{\chi}_{iR} \gamma_\mu D_{\chi_i}^\mu \chi_{iR} - \frac{1}{4} F_{Z_{BL}}^{\mu\nu} F_{Z_{BL} \mu\nu} \\ & + \sum_{i=1}^2 (D_{\phi_i}^\mu \phi_i)^\dagger (D_{\phi_i \mu} \phi_i) - \sum_{i=1}^2 (y_{\xi_i} \bar{\xi}_L \chi_{iR} \phi_2 + y_{\eta_i} \bar{\eta}_L \chi_{iR} \phi_1 + h.c.) \\ & - V(H, \phi_1, \phi_2) + \mathcal{L}_\Delta, \end{aligned} \quad (3.1)$$

where D_{ψ_μ} is the covariant derivative for the field ψ ($\psi = \eta_L, \xi_L, \chi_{iR}$ and ϕ_i). General expression of D_{ψ_μ} for a field ψ with a $B - L$ charge $Q_{B-L}(\psi)$ is given by

$$D_{\psi_\mu} = (\partial_\mu + i Q_{BL}(\psi) g_{BL} Z_{BL\mu} \gamma^\mu) .$$

Here g_{BL} is the new gauge coupling corresponding to the gauge group $U(1)_{B-L}$ while $F_{Z_{BL}}^{\mu\nu}$ is the usual field tensor of the new gauge boson Z_{BL} . The Yukawa couplings of the chiral fermions are denoted by y_{ξ_i} and y_{η_i} . These chiral fermions η_L, ξ_L, χ_{1R} and χ_{2R} in gauge basis do not represent any physical fermionic field. In mass basis, they combine together to give rise new physical states ψ_1 and ψ_2 with masses M_{ψ_1} and M_{ψ_2} respectively. The scalar potential including all possible gauge invariant as well as renormalisable interac-

	Field	SU(2) _L charge	U(1) _Y charge	U(1) _{B-L} charge	VEV
SM Fermions	$l_L \equiv (\nu_L \ e_L)^T$	2	$-\frac{1}{2}$	-1	0
	$Q_L \equiv (u_L \ d_L)^T$	2	$\frac{1}{6}$	$\frac{1}{3}$	
	e_R	1	-1	-1	
	u_R	1	$\frac{2}{3}$	$\frac{1}{3}$	
	d_R	1	$-\frac{1}{3}$	$\frac{1}{3}$	
BSM Fermions	ξ_L	1	0	$\frac{4}{3}$	0
	η_L	1	0	$\frac{1}{3}$	
	χ_{1R}	1	0	$-\frac{2}{3}$	
	χ_{2R}	1	0	$-\frac{2}{3}$	
Scalars	H	2	$\frac{1}{2}$	0	v
	ϕ_1	1	0	1	v_1
	ϕ_2	1	0	2	v_2
	Δ	3	1	-2	v_Δ

Table 3.1: SU(2)_L, U(1)_Y and U(1)_{B-L} charges and corresponding VEVs of all the fields involved in the present model.

tion terms among H , ϕ_1 and ϕ_2 is given by:

$$\begin{aligned}
V(H, \phi_1, \phi_2) = & \mu_H^2 H^\dagger H + \lambda_H (H^\dagger H)^2 + \mu_1^2 \phi_1^\dagger \phi_1 + \lambda_1 (\phi_1^\dagger \phi_1)^2 + \mu_2^2 \phi_2^\dagger \phi_2 + \lambda_2 (\phi_2^\dagger \phi_2)^2 \\
& + \rho_1 (H^\dagger H) (\phi_1^\dagger \phi_1) + \rho_2 (H^\dagger H) (\phi_2^\dagger \phi_2) + \lambda_3 (\phi_1^\dagger \phi_1) (\phi_2^\dagger \phi_2) \\
& + \mu \left(\phi_2 \phi_1^{\dagger 2} + \phi_2^\dagger \phi_1^2 \right), \tag{3.2}
\end{aligned}$$

where H is the usual Standard Model Higgs doublet, while ϕ_1 and ϕ_2 are the new scalars which are required to generate fermion masses in a gauge invariant way after symmetry breaking. The U(1)_{B-L} symmetry is assumed to be broken spontaneously above the electroweak phase transition scale. The scalar potential defined above should be bounded from below. In other words, it should have stable minima. The existence of a stable minimum of the potential puts some conditions on the quartic couplings. These are known as

the vacuum stability condition, and are given by:

$$\begin{aligned}
\lambda_H, \lambda_1, \lambda_2 &\geq 0, \\
\rho_1 + \sqrt{\lambda_H \lambda_1} &\geq 0, \\
\rho_2 + \sqrt{\lambda_H \lambda_2} &\geq 0, \\
\lambda_3 + \sqrt{\lambda_1 \lambda_2} &\geq 0,
\end{aligned} \tag{3.3}$$

and

$$\begin{aligned}
&\sqrt{\lambda_H \lambda_1 \lambda_2} + \rho_1 \sqrt{\lambda_2} + \rho_2 \sqrt{\lambda_1} + \lambda_3 \sqrt{\lambda_H} + \\
&\sqrt{2(\rho_1 + \sqrt{\lambda_H \lambda_1})(\rho_2 + \sqrt{\lambda_H \lambda_2})(\lambda_3 + \sqrt{\lambda_1 \lambda_2})} \geq 0.
\end{aligned} \tag{3.4}$$

The neutral component of the Higgs doublet (H^0) and the other two scalars acquire VEVs after symmetry breaking:

$$\begin{aligned}
H^0 &= \frac{1}{\sqrt{2}}(v + \tilde{h}) + \frac{i}{\sqrt{2}}\tilde{G}, \\
\phi_1 &= \frac{1}{\sqrt{2}}(v_1 + \tilde{h}_1) + \frac{i}{\sqrt{2}}\tilde{A}_1, \\
\phi_2 &= \frac{1}{\sqrt{2}}(v_2 + \tilde{h}_2) + \frac{i}{\sqrt{2}}\tilde{A}_2,
\end{aligned} \tag{3.5}$$

where v, v_1 and v_2 are the respective VEVs, \tilde{h}, \tilde{h}_1 and \tilde{h}_2 are the CP-even scalars, while \tilde{G}, \tilde{A}_1 and \tilde{A}_2 are the CP-odd counterparts. From the minimisation condition, i.e. equating the first order derivative of the scalar potential $V(H, \phi_1, \phi_2)$ to zero with respect to each of the scalars, we get the following equations:

$$\begin{aligned}
\mu_H^2 &= -\left(\lambda_H v^2 + \frac{\rho_1}{2}v_1^2 + \frac{\rho_2}{2}v_2^2\right), \\
\mu_1^2 &= -\left(\lambda_1 v_1^2 + \frac{\rho_1}{2}v^2 + \frac{\lambda_3}{2}v_2^2 + \sqrt{2}v_2\mu\right), \\
\mu_2^2 &= -\left(\lambda_2 v_2^2 + \frac{\rho_2}{2}v^2 + \frac{\lambda_3}{2}v_1^2 + \frac{1}{\sqrt{2}}\frac{v_1^2\mu}{v_2}\right).
\end{aligned} \tag{3.6}$$

After the spontaneous breaking of all the gauge symmetries that we have imposed on the model Lagrangian (Eq. (3.1)), three CP-even scalars ($\tilde{h}, \tilde{h}_1, \tilde{h}_2$) mix among themselves. With respect to the basis states $\tilde{h}-\tilde{h}_1-\tilde{h}_2$ (gauge basis), the mass matrix of the CP-even scalars is given by

$$\mathcal{M}_{\text{CP even}}^2 = \begin{pmatrix} 2\lambda_H v^2 & \rho_1 v v_1 & \rho_2 v v_2 \\ \rho_1 v v_1 & 2\lambda_1 v_1^2 & (\lambda_3 v_2 + \sqrt{2}\mu) v_1 \\ \rho_2 v v_2 & (\lambda_3 v_2 + \sqrt{2}\mu) v_1 & (2\lambda_2 v_2^2 - \frac{\mu v_1^2}{\sqrt{2}v_2}) \end{pmatrix}. \tag{3.7}$$

It should be noted that, while deriving the mass matrix, we have used the conditions obtained from extremising the scalar potential i.e. Eq. (3.6). Now, in order to find the physical scalar states and their respective masses we have to find a new basis states (h_1, h_2, h_3) with respect to which the above mass matrix becomes diagonal. This new basis states are known as the mass basis. As in this case, the CP-even scalars mass matrix is a real symmetric one (assuming all the parameters in the Lagrangian are real), the gauge basis and mass basis states must be related by an orthogonal matrix which is the PMNS matrix with zero complex phase. The three mixing angles are $\theta_{12}, \theta_{13}, \theta_{23}$. So we have:

$$\mathcal{U}_{\text{PMNS}}(\theta_{12}, \theta_{23}, \theta_{13}) = \begin{pmatrix} \cos \theta_{12} \cos \theta_{13} & \sin \theta_{12} \cos \theta_{13} & \sin \theta_{13} \\ -\sin \theta_{12} \cos \theta_{23} - \cos \theta_{12} \sin \theta_{23} \sin \theta_{13} & \cos \theta_{12} \cos \theta_{23} - \sin \theta_{12} \sin \theta_{23} \sin \theta_{13} & \sin \theta_{23} \cos \theta_{13} \\ \sin \theta_{12} \sin \theta_{23} - \cos \theta_{12} \cos \theta_{23} \sin \theta_{13} & -\cos \theta_{12} \sin \theta_{23} - \sin \theta_{12} \cos \theta_{23} \sin \theta_{13} & \cos \theta_{23} \cos \theta_{13} \end{pmatrix},$$

and hence the gauge basis and the mass basis states are related by:

$$\begin{pmatrix} h_1 \\ h_2 \\ h_3 \end{pmatrix} = \mathcal{U}_{\text{PMNS}}(\theta_{12}, \theta_{23}, \theta_{13}) \begin{pmatrix} \tilde{h} \\ \tilde{h}_1 \\ \tilde{h}_2 \end{pmatrix}. \quad (3.8)$$

Like the the CP-even scalar sector, the CP odd sector also exhibits mixing between the pseudo scalars. However in this case, only the pseudo scalars (\tilde{A}_1, \tilde{A}_2) of the singlets ϕ_1 and ϕ_2 mix with each other. This is because the CP odd scalar (\tilde{G}) of the Higgs doublet H does not mix with the CP odd portion of the other two complex scalars (ϕ_1 and ϕ_2), which are $\text{SU}(2)_L$ singlets. This is due to the fact that with a doublet and a complex singlet scalar we cannot write a gauge invariant term in the Lagrangian and also all the VEVs are assumed to be real and associated with the CP even sector. Hence terms involving odd powers of \tilde{G} is absent here. The CP odd scalars mixing matrix is thus given by:

$$\mathcal{M}_{CP\text{-odd}}^2 = \sqrt{2} \begin{pmatrix} -2\mu v_2 & \mu v_1 \\ \mu v_1 & -\frac{\mu v_1^2}{2v_2} \end{pmatrix}. \quad (3.9)$$

On diagonalisation we find that one of the eigenvalues of the matrix is zero as expected and which corresponds to a massless Goldstone mode. The mass of only physical pseudo scalar is given by:

$$M_A^2 = -\frac{\mu v_2}{\sqrt{2}\beta^2} (1 + 4\beta^2), \quad (3.10)$$

where $\beta = \frac{v_2}{v_1}$, the ratio of VEVs of ϕ_2 and ϕ_1 . Since mass of this pseudo scalar is always positive, the above equation implies that $\mu < 0$. Also in terms of the mixing angle α between A_1 and A_2 , the expression of M_A^2 can also be written in the following form

$$M_A^2 = -2\sqrt{2} \frac{\mu v_2}{\sin^2 \alpha} \quad (3.11)$$

with mixing angle $\alpha = \tan^{-1} 2\beta$.

The fermions in the present model also get masses after the spontaneous breaking of the $U(1)_{B-L}$ gauge symmetry. The masses of the fermions arise from the Yukawa interaction terms appearing in Eq. (3.1), when ϕ_1 and ϕ_2 get their VEVs. The Yukawa interaction terms involving only chiral fermions in Eq. (3.1), can also be written in the following matrix form

$$\mathcal{L}_{\text{fermion-mass}} = \begin{pmatrix} \overline{\xi_L} & \overline{\eta_L} \end{pmatrix} \mathcal{M}_{\text{fermion}} \begin{pmatrix} \chi_{1R} \\ \chi_{2R} \end{pmatrix} + h.c., \quad (3.12)$$

where

$$\mathcal{M}_{\text{fermion}} = \begin{pmatrix} y_{\xi_1} v_2 & y_{\xi_2} v_2 \\ y_{\eta_1} v_1 & y_{\eta_2} v_1 \end{pmatrix} \quad (3.13)$$

is the mass matrix for the chiral fermions, which can in general be diagonalised by a bi-unitary transformation. From the expression of mass matrix, one can notice that the $\mathcal{M}_{\text{fermion}}$ is not a symmetric matrix (Dirac type). Hence in the mass basis we have two physical Dirac fermions (ψ_1 and ψ_2). The mass and gauge basis states are related by:

$$\begin{pmatrix} \xi_L \\ \eta_L \end{pmatrix} = \mathcal{U}_L \begin{pmatrix} \psi_{2L} \\ \psi_{1L} \end{pmatrix}, \quad \begin{pmatrix} \chi_{1R} \\ \chi_{2R} \end{pmatrix} = \mathcal{U}_R \begin{pmatrix} \psi_{2R} \\ \psi_{1R} \end{pmatrix}. \quad (3.14)$$

Where $\mathcal{U}_{L,R}$ are two unitary matrices and for the case when all the Yukawa couplings (y_{ξ_i} and y_{η_i}) are real numbers, these matrices can be the usual 2×2 rotation matrix. Therefore, for this case $\mathcal{U}_{L,R}$ can be written as

$$\mathcal{U}_{L,R} = \begin{pmatrix} \cos \theta_{L,R} & \sin \theta_{L,R} \\ -\sin \theta_{L,R} & \cos \theta_{L,R} \end{pmatrix} \quad (3.15)$$

with $\theta_{L,R}$ are the respective mixing angles for the left chiral and the right chiral states. In the mass basis, the two physical fermionic states are $\psi_1 = \psi_{1L} + \psi_{1R}$, $\psi_2 = \psi_{2L} + \psi_{2R}$ and

the lightest one would automatically be stable, hence can serve as a viable dark matter candidate. Without any loss of generality, we assume the lightest fermion ψ_1 is our dark matter candidate.

The breaking of $U(1)_{B-L}$ symmetry, besides giving masses to the fermions also makes the extra gauge boson Z_{BL} massive. Its mass is given by :

$$M_{Z_{BL}}^2 = \left(\frac{g_{BL} v_2}{\beta} \right)^2 (1 + 4\beta^2). \quad (3.16)$$

The set of independent parameters relevant for our analysis are as follows:

$\theta_{12}, \theta_{13}, \theta_{23}, \theta_L, \theta_R, M_{h_2}, M_{h_3}, M_A, M_{\psi_1}, M_{\psi_2}, M_{Z_{BL}}, g_{BL}$ and β . Other model parameters can be written in terms of all these independent variables. In addition, we have chosen h_1 as the SM-like Higgs boson which has recently been discovered by ATLAS [142], CMS [143] collaborations of LHC at CERN and consequently we have kept fixed M_{h_1} and v at 125.5 GeV and 246 GeV respectively. The relevant vertex factors (in terms of the independent parameters) that we will need in our further calculations of DM distribution function as well as its comoving number density, are given in the Appendix 3.7.1.

As there are no right handed neutrinos in this new $U(1)_{B-L}$ model, which are usually present in $U(1)_{B-L}$ extended Standard Model to cancel gauge anomaly, light active neutrinos remain massless. We can overcome this situation by using Type-II see-saw mechanism [170–172] for which one has to introduce a scalar field Δ which is a triplet under $SU(2)_L$. In Eq. (3.1) the term \mathcal{L}_Δ represents the Lagrangian for the triplet Δ field. The Δ field also has $B - L$ charge -2, which is required to write a gauge invariant Yukawa term involving Δ and two lepton doublet (l_L) via $\mathcal{L}_\Delta \supset Y_{\nu_{\alpha\beta}} l_{\alpha L}^T C i \sigma_2 \Delta l_{\beta L}$, where $l_{\alpha L}$ is the usual left handed lepton doublet of flavour α while C is the charge conjugation matrix. Therefore, neutrinos become massive with $m_{\nu_{ij}} = Y_{\nu_{ij}} \frac{v_t}{\sqrt{2}}$, when the neutral component of Δ acquires a VEV v_t . However, the VEV of Δ field is related to that of SM Higgs doublet through the relation $v_t \sim \frac{\mu v^2}{\sqrt{2} M_\Delta^2}$ [173] (when $v \gg v_t$, required for ρ parameter to be equal to 1). Here M_Δ^2 is the coefficient for the quadratic term (mass term) of Δ in the \mathcal{L}_Δ ($\supset -M_\Delta^2 \text{Tr}(\Delta^\dagger \Delta)$) while μ is the coefficient of the trilinear term between two Higgs doublet H and a Δ . In our present case such term is although forbidden, but can be generated from a term like $\lambda' H^T i \sigma_2 \Delta^\dagger H \phi_2^\dagger$ in a gauge invariant manner, when ϕ_2 gets its VEV. Therefore in our case $\mu = \lambda' \frac{v_2}{\sqrt{2}}$ and consequently $m_{\nu_{ij}} = Y_{\nu_{ij}} \frac{\lambda' v_2 v^2}{2\sqrt{2} M_\Delta^2}$. Hence, in order to produce neutrino masses $\sim \mathcal{O}(0.1)$ eV, we need $M_\Delta \sim 10^8$ GeV for $Y_\nu \sim 10^{-1}$ and $\lambda' v_2 \sim 1$ TeV (possible as we have assumed before that the $B - L$ symmetry breaking occurs well above the EWPT). As a results the masses of the scalar fields within the triplet

Δ will be several orders of magnitude higher than those of particles we are considering here. Hence the effect of the formers will be negligibly small at that epoch of the Universe (Temperature ≤ 10 TeV) where we have done our analysis.

3.3 The FIMP paradigm

Now we turn to the problem of investigating a non-thermal fermionic dark matter candidate (ψ_1) within the framework of this new $U(1)_{B-L}$ model. As already discussed before, since the thermal scenario is only viable either near the resonance, or near the high mass range where mass of dark matter $\sim \mathcal{O}(4 \text{ TeV})$, hunt for a non-thermal dark matter candidate is quite natural. As mentioned in the earlier chapters, non-thermal dark matters are usually produced from the decay of heavier particles and in that case we can use Eq. 2.22 as a condition for non-thermality. Using the criterion we find that for a decaying particle of mass $\mathcal{O}(\text{TeV})$, the extra gauge coupling g_{BL} must be less than 10^{-7} . Most of the earlier studies involving calculation of DM relic abundance have attempted to solve the Boltzmann equation in terms of the comoving number density $Y = \frac{n}{s}$ of the relic particle. But this approach is valid as long as the decaying and the annihilating particles (except one whose comoving number density is being solved) are in thermal equilibrium or at least their distribution functions are similar in shape to the equilibrium distribution function and do not vary much from the latter. However this situation is certainly not guaranteed here, since one of the decaying particles (Z_{BL}) is not in equilibrium. Thus in order to compute the DM relic density, first we need to calculate the momentum distribution function of Z_{BL} followed by that of ψ_1 . Hence, we have solved a set of coupled Boltzmann equations at the level of momentum distribution functions for each of Z_{BL} and ψ_1 (other decaying particles are assumed to be in thermal equilibrium) following Ref. [174]. Once we have the knowledge about both the distribution functions, it is straight forward to calculate the other physical quantities like comoving number density, relic density etc.

3.3.1 Coupled Boltzmann equations and its solution

The Boltzmann equation for the distribution function $f(p)$, in its most general form can be written in terms of the Liouville operator (\hat{L}) and the collision term (\mathcal{C}). Symbolically, it is written as:

$$\hat{L} f = \mathcal{C}[f].$$

For an isotropic and homogeneous Universe, using the FRW metric we find that $\hat{L} = \frac{\partial}{\partial t} - H p \frac{\partial}{\partial p}$, where $p = |\vec{p}|$ is the absolute value of the particle's three momentum. As in Ref. [174] making the transformation of variable:

$$r = \frac{m_0}{T}, \quad (3.17)$$

$$\xi_p = \left(\frac{g_s(T_0)}{g_s(T)} \right)^{1/3} \frac{p}{T}, \quad (3.18)$$

where m_0 and T_0 are some reference mass and temperature, we find that the Liouville operator takes the following form:

$$\hat{L} = r H \left(1 + \frac{T g'_s}{3 g_s} \right)^{-1} \frac{\partial}{\partial r}, \quad (3.19)$$

where $g_s(T)$ is the effective number of degrees of freedom related to the entropy density of the Universe while g'_s denotes differentiation of g_s with respect to temperature T .

The main production channels for the non-thermal dark matter ψ_1 are from the decays of h_1 , h_2 and Z_{BL} . All of these BSM particles have been assumed to have mass of $\sim \mathcal{O}(\text{TeV})$. Among the three decaying particles, Z_{BL} is itself very feebly interacting (due to very low value of g_{BL}) and remains outside the thermal soup. The BSM scalar h_2 can be in thermal equilibrium, as it can interact with the SM particles through its mixing with h_1 , which need not be too small even in the non-thermal scenario. In whole of the analysis that will follow, (for simplicity) we have assumed that the CP odd scalar A , the extra fermion ψ_2 and one of the three CP even scalars (say h_3) are much heavier than rest of the particles. This can be done by appropriately choosing the model parameters so that their masses are higher than the reheat temperature of the universe and consequently they will have negligible effect on the production of the non-thermal dark matter. So, ψ_1 is partly produced from the decay of h_1 and h_2 which are in thermal equilibrium, and consequently the usual equilibrium Boltzmann distribution function has been assumed for them. ψ_1 is also produced from the decay of Z_{BL} which is out of equilibrium, and hence we have to solve for its non-equilibrium distribution function separately. Hence we have to solve two coupled Boltzmann equations. From the first one we calculate the non-equilibrium momentum distribution function of Z_{BL} . This solution is then used in the second equation to find the final non-equilibrium momentum distribution function of ψ_1 . The scattering terms contribute very little in the freeze-in scenario and hence left out in rest of the analysis [136, 175]. The coupled set of Boltzmann equations necessary for

calculating the momentum distribution function of ψ_1 are as follows:

$$\hat{L} f_{Z_{BL}} = \mathcal{C}^{h_2 \rightarrow Z_{BL} Z_{BL}} + \mathcal{C}^{Z_{BL} \rightarrow all}, \quad (3.20)$$

$$\hat{L} f_{\psi_1} = \sum_{s=h_1, h_2} \mathcal{C}^{S \rightarrow \bar{\psi}_1 \psi_1} + \mathcal{C}^{Z_{BL} \rightarrow \bar{\psi}_1 \psi_1}. \quad (3.21)$$

Here $\mathcal{C}^{A \rightarrow BB}$ s are the collision terms corresponding to the interaction depicted in the superscript. Before proceeding further, let us pause here to discuss a small subtlety. We know that the SM higgs boson gains its vacuum expectation value (VEV) after electroweak phase transition (EWPT) which occurs when the temperature of the Universe is $T_{EWPT} \sim 153$ GeV [49]. So while evolving the Boltzmann equations, as written above, from an initial temperature $T_{in} (> T_{EWPT})$ we have to bear in mind that when $T_{Universe} > T_{EWPT}$, the decay of SM Higgs boson (h_1) is not allowed. This is because the $h_1 \bar{\psi}_1 \psi_1$ vertex is proportional to the standard model VEV (v), the latter being zero before EWPT. More precisely, the mixing angles θ_{13} and θ_{12} vanish in the limit $v \rightarrow 0$ (Eq. 3.7) and this in turn makes $g_{h_1 \bar{\psi}_1 \psi_1}$ tend to zero as well (see Eq. 3.37). Its decay will be an important factor when the Universe cools down below T_{EWPT} . On the other hand, the BSM scalar h_2 can however always decay since it gets its vev from the spontaneous breaking of the new $U(1)_{B-L}$ symmetry which is assumed to occur at a much higher temperature than T_{EWPT} .

As discussed earlier, the simplistic form of the Liouville operator in Eq. (3.19) can be used only when we are in a specially chosen coordinate system defined by ξ_p and r . The final solution of the momentum distribution function will thus, in general be a function of both $r \equiv \frac{M_{sc}}{T}$ (where M_{sc} is some reference mass scale which we fix to be at the mass of the SM Higgs boson) and ξ_p defined in Eqs. ((3.17)–(3.18)). For example, $f_{Z_{BL}} = f_{Z_{BL}}(\xi_p, r)$. For our convenience, let us further define:

$$\left(\frac{g_s(T)}{g_s(T_0)} \right)^{1/3} = \left(\frac{g_s(M_{sc}/r)}{g_s(M_{sc}/r_0)} \right)^{1/3} \equiv \mathcal{B}(r) \quad (3.22)$$

where, T_0 (and the corresponding r_0) is some reference temperature, which we take to be equal to the initial temperature T_{in} . The collision terms corresponding to Eq. (3.20) are as

follows:

$$\begin{aligned} \mathcal{C}^{h_2 \rightarrow Z_{\text{BL}} Z_{\text{BL}}} &= \frac{r}{8\pi M_{sc}} \frac{\mathcal{B}^{-1}(r)}{\xi_p \sqrt{\xi_p^2 \mathcal{B}(r)^2 + \left(\frac{M_{Z_{\text{BL}}} r}{M_{sc}}\right)^2}} \frac{g_{h_2 Z_{\text{BL}} Z_{\text{BL}}}^2}{6} \left(2 + \frac{(M_{h_2}^2 - 2M_{Z_{\text{BL}}}^2)^2}{4M_{Z_{\text{BL}}}^4}\right) \\ &\times \left(e^{-\sqrt{(\xi_k^{\min})^2 \mathcal{B}(r)^2 + \left(\frac{M_{h_2} r}{M_{sc}}\right)^2}} - e^{-\sqrt{(\xi_k^{\max})^2 \mathcal{B}(r)^2 + \left(\frac{M_{h_2} r}{M_{sc}}\right)^2}} \right), \end{aligned} \quad (3.23)$$

$$\mathcal{C}^{Z_{\text{BL}} \rightarrow \text{all}} = - \frac{\Gamma_{Z_{\text{BL}} \rightarrow \text{all}} M_{Z_{\text{BL}}} r}{M_{sc} \sqrt{\xi_p^2 \mathcal{B}(r)^2 + \left(\frac{M_{Z_{\text{BL}}} r}{M_{sc}}\right)^2}} f_{Z_{\text{BL}}}(\xi_p, r). \quad (3.24)$$

Here, in the above two equations $\xi_k \equiv \frac{1}{\mathcal{B}(r)} \frac{k}{T}$ is the variable corresponding to the three momentum k of the decaying particle (i.e. h_2). It is integrated over from ξ_k^{\min} to ξ_k^{\max} where each of these are functions of ξ_p and r (and also of masses of the particles involved in the corresponding process). M_{sc} , as already mentioned, is some reference mass scale, which we take to be equal to M_{h_1} . The quantity $\Gamma_{Z_{\text{BL}} \rightarrow \text{all}}$ is the total decay width of Z_{BL} . Explicit expression of the total decay width as well as the detailed derivation of the collision term $\mathcal{C}^{h_2 \rightarrow Z_{\text{BL}} Z_{\text{BL}}}$ are given in the Appendix (3.7.2, 3.7.3). Further, $g_{h_2 Z_{\text{BL}} Z_{\text{BL}}}$ is the vertex factor of an interaction vertex containing fields $h_2 Z_{\text{BL}} Z_{\text{BL}}$ and its expression in terms of chosen set of independent parameters is also given in the Appendix 3.7.1. The detailed derivation of other collision term $\mathcal{C}^{Z_{\text{BL}} \rightarrow \text{all}}$ is also given in Appendix 3.7.3.

The collision terms appearing in Eq. (3.21) can similarly be written as:

$$\begin{aligned} \mathcal{C}^{s \rightarrow \bar{\psi}_1 \psi_1} &= \frac{r}{8\pi M_{sc}} \frac{\mathcal{B}^{-1}(r)}{\xi_p \sqrt{\xi_p^2 \mathcal{B}(r)^2 + \left(\frac{M_{\psi_1} r}{M_{sc}}\right)^2}} g_{s \bar{\psi}_1 \psi_1}^2 (M_s^2 - 4M_{\psi_1}^2) \\ &\times \left(e^{-\sqrt{(\hat{\xi}_k^{\min})^2 \mathcal{B}(r)^2 + \left(\frac{M_s r}{M_{sc}}\right)^2}} - e^{-\sqrt{(\hat{\xi}_k^{\max})^2 \mathcal{B}(r)^2 + \left(\frac{M_s r}{M_{sc}}\right)^2}} \right), \end{aligned} \quad (3.25)$$

$$\begin{aligned} \mathcal{C}^{Z_{\text{BL}} \rightarrow \bar{\psi}_1 \psi_1} &= \frac{r}{4\pi M_{sc}} \frac{\mathcal{B}(r)}{\xi_p \sqrt{\xi_p^2 \mathcal{B}(r)^2 + \left(\frac{M_{\psi_1} r}{M_{sc}}\right)^2}} \times (M_{Z_{\text{BL}}}^2 (a_{\psi_1}^2 + b_{\psi_1}^2) + 2M_{\psi_1}^2 (a_{\psi_1}^2 - 2b_{\psi_1}^2)) \\ &\times \int_{\tilde{\xi}_k^{\min}}^{\tilde{\xi}_k^{\max}} \frac{\xi_k f_{Z_{\text{BL}}}(\xi_k, r) d\xi_k}{\sqrt{\xi_k^2 \mathcal{B}(r)^2 + \left(\frac{M_{Z_{\text{BL}}} r}{M_{sc}}\right)^2}}, \end{aligned} \quad (3.26)$$

where the superscript s is a generic symbol denoting the decay of ψ_1 from any of the scalars h_1, h_2 . As we mentioned above, the expressions of the coupling $g_{s\bar{\psi}_1\psi_1}$ in terms of the independent parameters are given in the Appendix 3.7.1. The value of the function $f_{Z_{BL}}$ in Eq. (3.26) is obtained by solving the first Boltzmann equation, i.e. Eq. (3.20). The derivation of these collision terms are also roughly sketched in Appendix 3.7.3 and 3.7.3.

3.4 Results

Having developed the structure of the coupled set of Boltzmann equations that we will use to find the momentum distribution functions of Z_{BL} and ψ_1 , we can now proceed further to solve them numerically. For our numerical calculation we have always taken $\frac{M_{h_1}}{2} \leq M_{Z_{BL}} \leq \frac{M_{h_2}}{2}$, so that the extra gauge boson can be produced from the decay of h_2 only. Introduction of another decay mode only complicates the numerics while giving rise to no extra interesting features. The present section can be broadly categorised in two parts, i) $\beta = 1$ and ii) $\beta \ll 1$, depending on the relative contributions of different decay modes in the final relic abundance of ψ_1 . For definiteness, we have chosen $\beta = 10^{-3}$ as a representative value in the $\beta \ll 1$ case. All of our arguments and discussions in this section are with respect to two benchmarks, one corresponding to $\beta = 1$ and the other corresponding to $\beta = 10^{-3}$.

Once the momentum distribution function for ψ_1 is calculated (solving Eq. (3.20) and Eq. (3.21)), it is then easy to calculate other quantities of physical importance. The first order moment of the distribution function for e.g. gives an idea about the number density of the concerned particle, i.e. $n \sim \int d^3p f(p)$ or in terms of ξ_p , it is given by:

$$n(r) = \frac{g T^3}{2\pi^2} \mathcal{B}(r)^3 \int d\xi_p \xi_p^2 f_{\psi_1}(\xi_p), \quad (3.27)$$

where g is the internal degree of freedom of the particle under consideration and $\mathcal{B}(r)$ is defined in Eq. (3.22). Other symbols have their usual meaning. Our primary quantity of interest in the rest of this section is the comoving number density $Y = \frac{n}{s}$, where s is the entropy density of the Universe, given by:

$$s = \frac{2\pi^2}{45} g_s(T) T^3. \quad (3.28)$$

Here T is the temperature and $g_s(T)$ is degrees of freedom corresponding to the entropy density s of the Universe. The relic abundance of our dark matter ψ_1 is simply related to

the comoving number density Y by [176]:

$$\Omega_{\psi_1} h^2 = 2.755 \times 10^8 \left(\frac{M_{\psi_1}}{\text{GeV}} \right) Y_{\psi_1}(T_{\text{Now}}), \quad (3.29)$$

where T_{Now} is the temperature of the Universe at the present epoch. In the present scenario, the temperature T can be easily calculated if $r \left(\equiv \frac{M_{sc}}{T} \right)$ is known.

The values of different independent parameters in our benchmark scenarios have been tabulated in Table 5.4 (left) for $\beta = 1$ and Table 5.4 (right) for $\beta = 10^{-3}$. The two benchmarks are so chosen such that the final Y_{ψ_1} calculated using these parameters give the correct relic density when plugged in Eq. (3.29). As we will see later, in the $\beta = 1$ scenario, if we fix the scalars mixing angles to values of $\mathcal{O}(0.1)$ rad or less¹, the contributions arising from the scalar decay channels to the total comoving number density (Y_{ψ_1}) become quite low. Almost the whole of ψ_1 is produced from the decay of Z_{BL} . The percentage contribution of the scalar decay modes to Y_{ψ_1} , in this case, is thus not much sensitive to the values of the mixing angles ($\theta_s \leq 0.1$ rad). This can be easily understood from the expressions of $g_{h_1 \bar{\psi}_1 \psi_1}$ and $g_{h_2 \bar{\psi}_1 \psi_1}$ given in the Appendix 3.7.1. The situation is however different when $\beta = 10^{-3}$. For our chosen benchmark, values of the dark matter–scalar couplings now become sizeable and also sensitive to θ_{13} ($h_1 \bar{\psi}_1 \psi_1$ coupling) and θ_{23} ($h_2 \bar{\psi}_1 \psi_1$ coupling). The benchmark in this case is chosen in such a way so that we can have equal contributions to the final comoving number density of the dark matter (Y_{ψ_1}) from h_1 , h_2 and Z_{BL} decays. For definiteness, the value of the arbitrary mass scale M_{sc} has been fixed at the Standard Model Higgs mass.

Let us now try to solve the Boltzmann equations (Eqs. ((3.20)–(3.21))) numerically. The first step, of course, is to solve the non-equilibrium momentum distribution function of Z_{BL} . Using Eq. (3.20) along with Eqs. ((3.23) and (3.24)), we solve for the non-thermal momentum distribution function of Z_{BL} i.e. $f_{Z_{\text{BL}}}$ as shown in Fig. 3.1 (left) for $\beta = 1$. In the y-axis we have plotted $\xi_p^2 f_{Z_{\text{BL}}}(\xi_p, r)$, since area under this curve will readily give us an idea about the number density of the particle species under consideration (at a fixed temperature). Initially, at the onset, as r increases (i.e. the temperature of the Universe decreases), we expect that more and more Z_{BL} will be produced from the decay of h_2 . In other words, the area under the curve should increase. This is exactly what we see as we go from $r = 0.02$ (red solid line) to $r = 0.05$ (green solid line) in the plot. Then, with further lowering of temperature (increment in r), the process of depletion of Z_{BL} through its decay starts to compete with the production, and hence, no appreciable change in the number density is expected. This is reflected in the curves corresponding to $r = 0.2$ (blue

¹to satisfy the bounds on the signal strength of SM Higgs boson [177].

Input Parameters	Corresponding values	Input Parameters	Corresponding values
$M_{Z_{BL}}$	1 TeV	$M_{Z_{BL}}$	1 TeV
M_{h_2}	5 TeV	M_{h_2}	5 TeV
M_{ψ_1}	10 GeV	M_{ψ_1}	10 GeV
g_{BL}	4.87×10^{-11}	g_{BL}	1.75×10^{-11}
θ_{12}	0.1 rad	θ_{12}	0.1000 rad
θ_{13}	0.1 rad	θ_{13}	9.58×10^{-3} rad
θ_{23}	0.1 rad	θ_{23}	6.18×10^{-2} rad
$\theta_L = \theta_R$	$\pi/4$ rad	$\theta_L = \theta_R$	$\pi/4$ rad

Table 3.2: Values of different input parameters used in our analysis. Benchmark corresponding to $\beta = 1$ (left) and $\beta = 10^{-3}$ (right).

solid line) and $r = 2.0$ (brown solid line). At a much lower temperature, production of Z_{BL} almost ceases due the Boltzmann suppression of h_2 abundance. So Z_{BL} gets depleted through its decay, and number density is expected to fall. This is observed in Fig. 3.1 (left) for the black dotted line corresponding to $r = 700$. Similar plot for the $\beta = 10^{-3}$ case is also shown in Fig. 3.1 (right).

With this, we now proceed to find the non-equilibrium distribution function for our dark matter particle ψ_1 using Eq. (3.21). It is shown in Fig. 3.2 (left) for $\beta = 1$. Similar to the Z_{BL} case, here also with the decrease of temperature more and more ψ_1 particles are produced from the decays massive bosons such as h_1 , h_2 and Z_{BL} . Hence the area under the curves increases as we go from $r = 0.02$ to $r = 1000$. With further increase in r we expect that the *rate* of production of ψ_1 should decrease and consequently the (comoving) number density will cease to change, since for this high value of r (low temperature) the number densities of all the decaying bosons have become extremely dilute and also ψ_1 itself is stable. This can be verified, if we compare the curves corresponding to $r = 10^3$ and $r = 10^4$. Similar features are also observed for $\beta = 10^{-3}$ case which has been shown in Fig. 3.2 (right).

All of the features that we have discussed so far with respect to the momentum distribution functions are reflected clearly if we plot the variation of the comoving number density of Z_{BL} and ψ_1 with respect to r . The comoving number density Y is easily calcu-

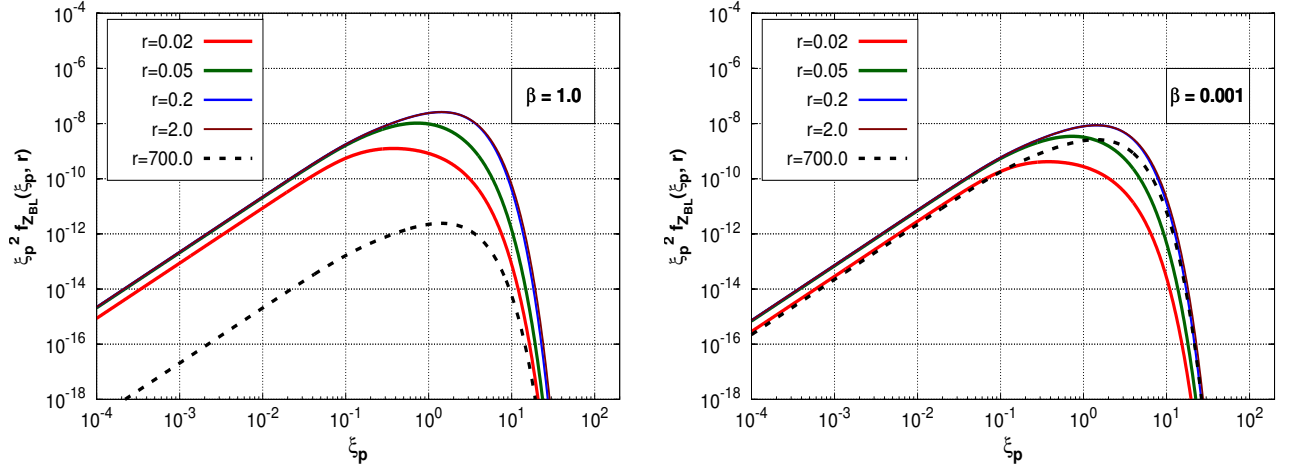


Figure 3.1: Non-thermal momentum distribution function $f_{Z_{BL}}$ plotted as a function of the dimensionless variable ξ_p for $\beta = 1$ (left) and $\beta = 10^{-3}$ (right). The curves are shown for different values of $r = \frac{M_{sc}}{T}$.

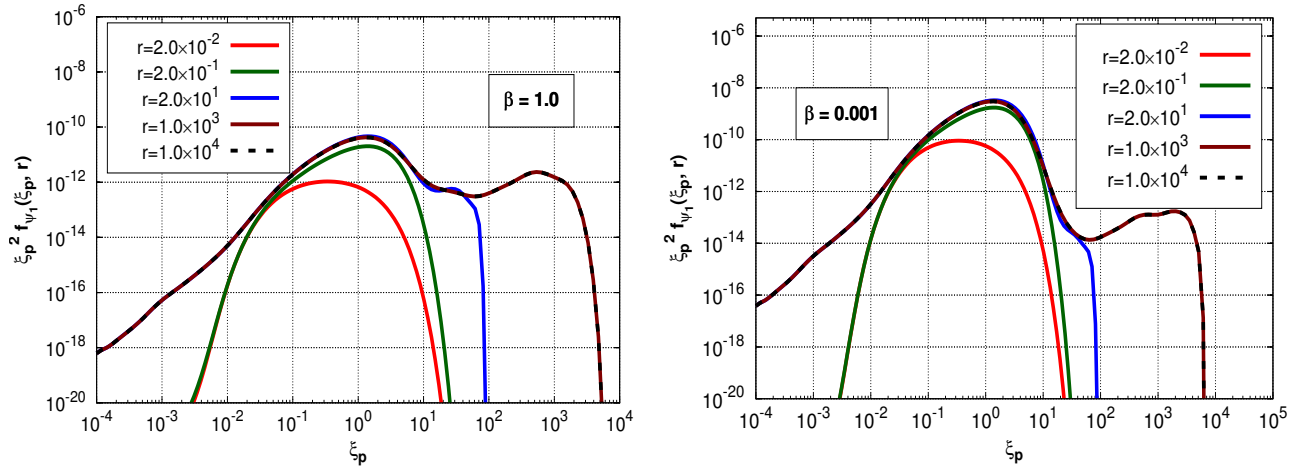


Figure 3.2: Non-thermal momentum distribution function f_{ψ_1} plotted as a function of the dimensionless variable ξ_p for $\beta = 1$ (left) and $\beta = 10^{-3}$ (right). The curves are shown for different values of $r = \frac{M_{sc}}{T}$.

lable by using Eqs. ((3.27) and (3.28)), once the momentum distribution function of the corresponding species is known. We plot our numerical results in both panels of Fig. 3.3.

For the $\beta = 1$ case, the scalars h_1 and h_2 contribute minimally to the comoving number density of ψ_1 . The bulk of the contribution comes from Z_{BL} . In the left panel of Fig. 3.3, we find that the comoving number density of Z_{BL} first rises with r . Initially, there is also

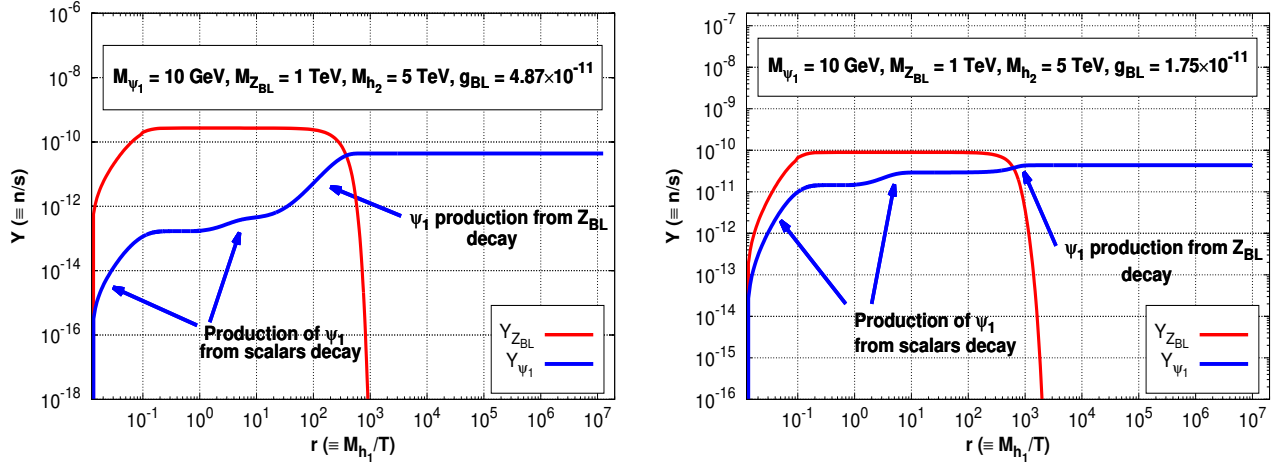


Figure 3.3: Variation of comoving number density of Z_{BL} and ψ_1 with respect to r . **Left:** $\beta = 1$ and **Right:** $\beta = 10^{-3}$.

a similar rise in the number density of ψ_1 as well. However, the rate of increment of Y_{ψ_1} is small compared to $Y_{Z_{BL}}$ for $r \leq 0.1$ since in this regime, the main production channel of ψ_1 is the decay from BSM scalar h_2 , which is presently contributing very little to Y_{ψ} . Then as r increases, the number density of Z_{BL} flattens out due to the competing decay and production terms while Y_{ψ_1} rises slightly due to its production from the decay of SM-like Higgs boson h_1 . With the further increase of r , the Z_{BL} number density falls off as the decay modes of Z_{BL} become dominant over its production process (i.e. production from the Boltzmann suppressed h_2). Consequently, there is a sharp rise in Y_{ψ} as more and more ψ_1 starts producing dominantly from Z_{BL} decay. Finally, for $r > 10^3$ there is practically no Z_{BL} is left for decay to ψ_1 , and hence in absence of any sources Y_{ψ_1} freezes-in to a constant value. For the other case i.e. when $\beta = 10^{-3}$, the situation is exactly same as with $\beta = 1$ except in this case all the production modes of ψ_1 including those from the decays of h_1 and h_2 contribute equally to Y_{ψ_1} . Therefore for $r \leq 10^2$, Y_{ψ_1} increases significantly since in this regime ψ_1 is mainly produced from scalars decay. Moreover unlike Z_{BL} , as the h_1 and h_2 are in thermal equilibrium, in both panels, bulk of their contribution to the number density of ψ_1 occurs when the temperatures of the Universe are around $T \sim M_{h_1}$ ($r \sim 1.0$) and $T \sim M_{h_2}$ ($r \sim 0.03$) respectively.

Let us now try to understand how the comoving number density varies with different model parameters. Parameters have varied one at a time, while keeping the others fixed at their benchmark values. In Fig. 3.4, we plot the variation of Y with varying g_{BL} . Increasing g_{BL} will result in an increase in the collision term corresponding to $h_2 \rightarrow Z_{BL} Z_{BL}$

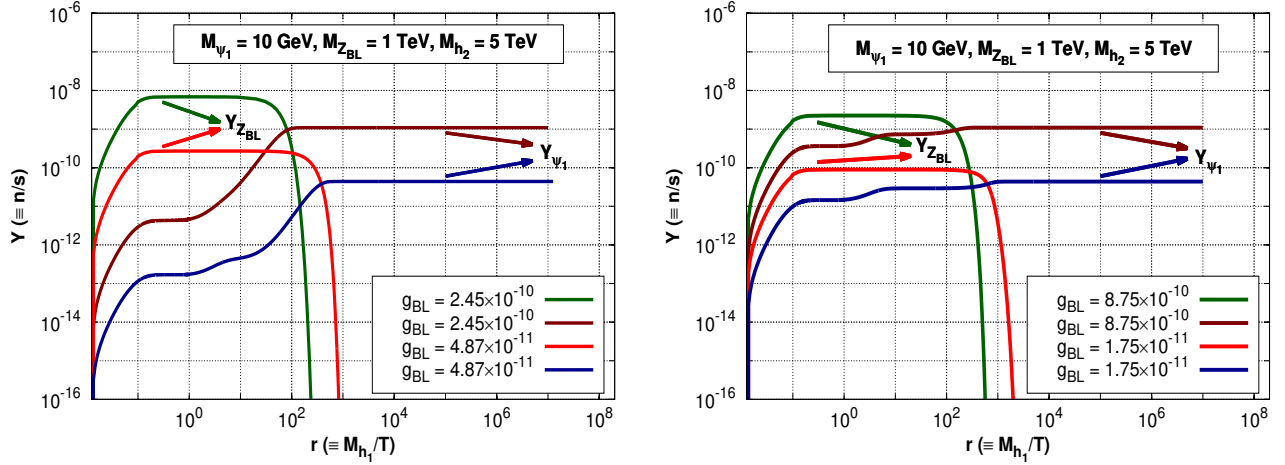


Figure 3.4: Variation of comoving number density of Z_{BL} and ψ_1 with r corresponding to different values of g_{BL} . **Left:** $\beta = 1$ and **Right:** $\beta = 10^{-3}$.

(since $g_{h_2 Z_{BL} Z_{BL}}$ increases, see Appendix 3.7.1) and hence an enhanced initial production of Z_{BL} . Also, increasing g_{BL} will enlarge the total decay width of Z_{BL} (see Appendix 3.7.2 for the expression of $Z_{BL} \rightarrow all$), and consequently we expect that the produced Z_{BL} will start to deplete earlier in the case where g_{BL} is higher. The curves corresponding to Y_{ψ_1} follow the rise of Z_{BL} and in the case where g_{BL} is higher, more ψ_1 is produced in the final state (since there is a corresponding increment in the production of Z_{BL}). As Z_{BL} depletes off, ψ_1 freezes in to a particular value of Y_{ψ_1} as expected. In the right panel of Fig. 3.4, the initial sharp rise of Y_{ψ_1} for $r \leq 10$ is due to the significant production of DM from the decaying scalars h_2 and h_1 respectively.

In Fig. 3.5, we have plotted the variations in Y by changing M_{h_2} . Increasing M_{h_2} will again increase $\mathcal{C}^{h_2 \rightarrow Z_{BL} Z_{BL}}$ like the previous case. But unlike before, $Y_{Z_{BL}}$ curves corresponding to the two M_{h_2} values start falling around the same epoch. This is because, changing the mass of h_2 has no bearing upon the total decay width of $Z_{BL} \rightarrow all$, while the latter process is responsible for the fall off. Since more Z_{BL} is produced initially when M_{h_2} is increased, the yield of ψ_1 in this case is also higher, as is evident from the figure. A qualitative difference between the right and left panel of Fig. 3.5 is that, the final abundances of ψ_1 in $\beta = 1$ case are quite different from each other for different values of M_{h_2} , while in $\beta = 10^{-3}$ case, we see that they are almost identical. This is because, in the $\beta = 1$ case, the contribution of the scalars are sub-dominant compared to Z_{BL} , while abundance of the latter and consequently that of ψ_1 increases with increasing M_{h_2} . Hence the amount of splitting in the two Y_{ψ_1} curves (left panel) is almost same as the difference observed in

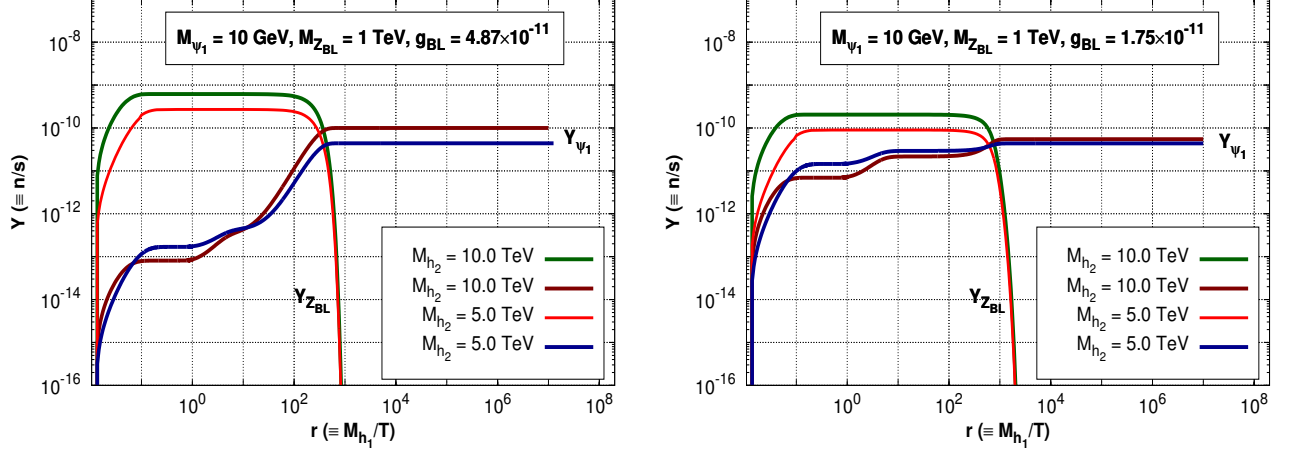


Figure 3.5: Variation of comoving number density of Z_{BL} and ψ_1 with r corresponding to different values of M_{h_2} . **Left:** $\beta = 1$ and **Right:** $\beta = 10^{-3}$.

the corresponding $Y_{Z_{BL}}$ curves. But in the $\beta = 10^{-3}$ scenario, things are a little different. Here, both the scalars as well as Z_{BL} contribute substantially to the final abundance of ψ_1 . The contribution to the final abundance from the decays of the two scalars compensates to reduce the splitting amongst the Y_{ψ_1} curves arising from the increment of $Y_{Z_{BL}}$.

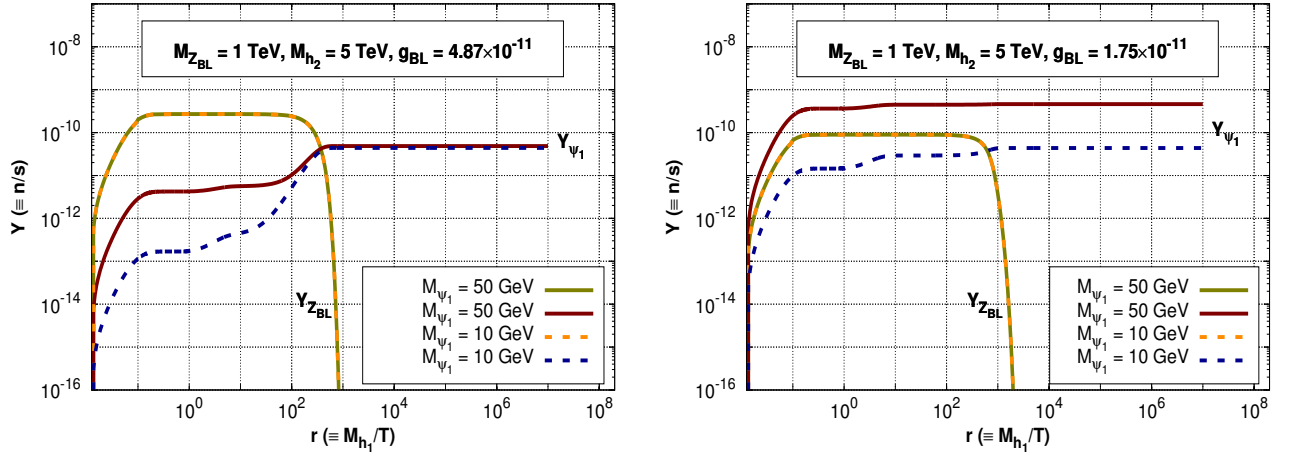


Figure 3.6: Variation of comoving number density of Z_{BL} and ψ_1 with r corresponding to different values of M_{ψ_1} . **Left:** $\beta = 1$ and **Right:** $\beta = 10^{-3}$.

In Fig. 3.6, the variation of $Y_{Z_{BL}}$ and Y_{ψ_1} have been studied by changing the mass of dark matter itself i.e. M_{N_1} . Now in the present scenario with $M_{Z_{BL}} \gg M_{\psi_1}$, any change in the mass of dark matter will in no way affect $Y_{Z_{BL}}$, since M_{ψ_1} neither affects the Z_{BL} total

decay width nor does it change $h_2 \rightarrow Z_{\text{BL}} Z_{\text{BL}}$ collision term. But the production of ψ_1 from the scalars decay is however affected. It is clear from the expression of the scalar–dark matter couplings given in Appendix 3.7.1, that with increase in M_{N_1} , the value of the coupling increases and there by yielding more ψ_1 . This observation is corroborated if we look at the blue dashed line (corresponding to $M_{N_1} = 10 \text{ GeV}$) and the solid grey line (corresponding to $M_{N_1} = 50 \text{ GeV}$) in the left panel of Fig. 3.6. For more massive dark matter, the yield of ψ_1 is higher from the scalars decay. But there is no effect on the production of ψ_1 from Z_{BL} decay, which is expected, since the couplings between Z_{BL} and ψ_1 do not depend on the mass of the latter and also here $M_{Z_{\text{BL}}} \gg M_{\psi_1}$. Let us now contrast this case with the right panel of Fig. 3.6. Here again as before the contribution of the scalars become important. As already mentioned, the benchmark for $\beta = 10^{-3}$ scenario is chosen in such a way, so that h_1, h_2 and Z_{BL} contribute equally in the final relic abundance. Increase in scalar–dark matter couplings (due to an increase in M_{N_1}), hence makes the contribution from the scalars decay, larger than that from the Z_{BL} .

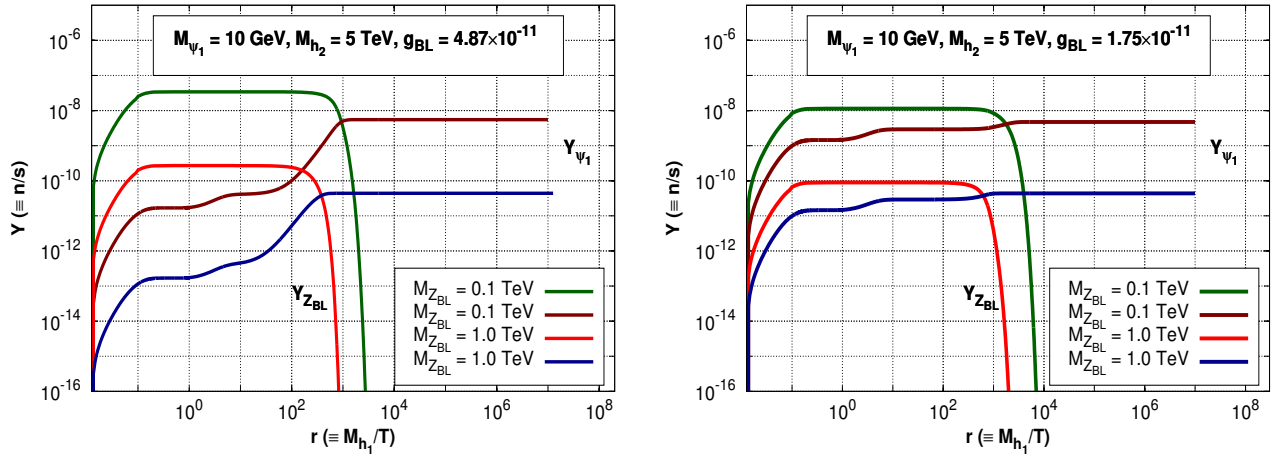
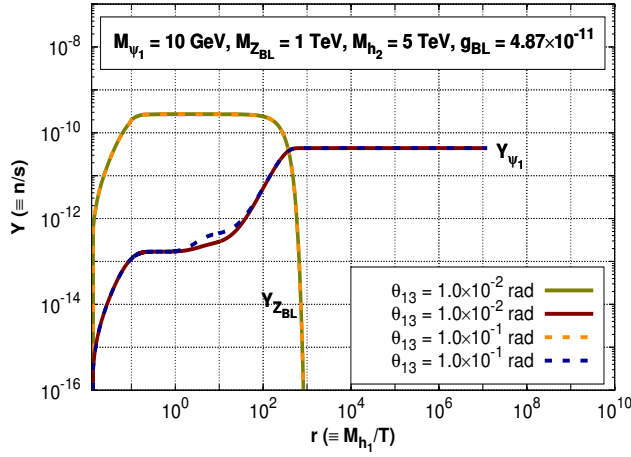


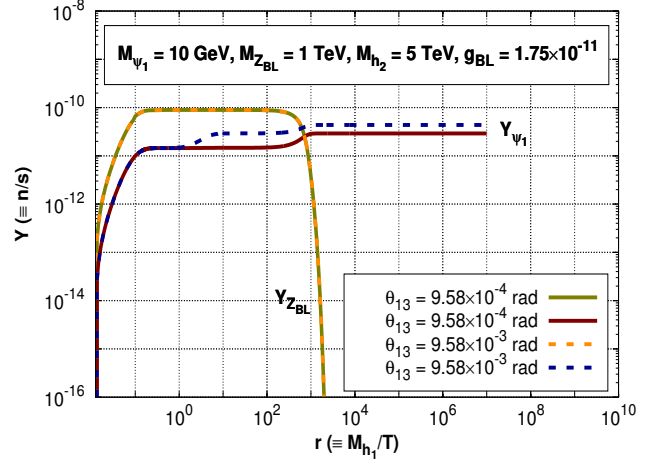
Figure 3.7: Variation of comoving number density of Z_{BL} and ψ_1 with r corresponding to different values of $M_{Z_{\text{BL}}}$. **Left:** $\beta = 1$ and **Right:** $\beta = 10^{-3}$.

In Fig. 3.7, variation with respect to $M_{Z_{\text{BL}}}$ is demonstrated. With an increase in $M_{Z_{\text{BL}}}$, the total decay width $Z_{\text{BL}} \rightarrow \text{all}$ increases leading to an earlier fall in the comoving number density of Z_{BL} . Also increasing $M_{Z_{\text{BL}}}$ suppresses the production of Z_{BL} via h_2 decay. Y_{ψ_1} , on the other hand tracks the rise and fall of $Y_{Z_{\text{BL}}}$ (since Z_{BL} is the main production channel of ψ_1 in the left panel with $\beta = 1$ case). For $\beta = 10^{-3}$ (right panel), $Y_{Z_{\text{BL}}}$ exhibits similar features. The scalar–dark matter couplings on the other hand increases with an decrease in $M_{Z_{\text{BL}}}$. This leads to higher yield of ψ_1 from scalars decay. The yield from Z_{BL}

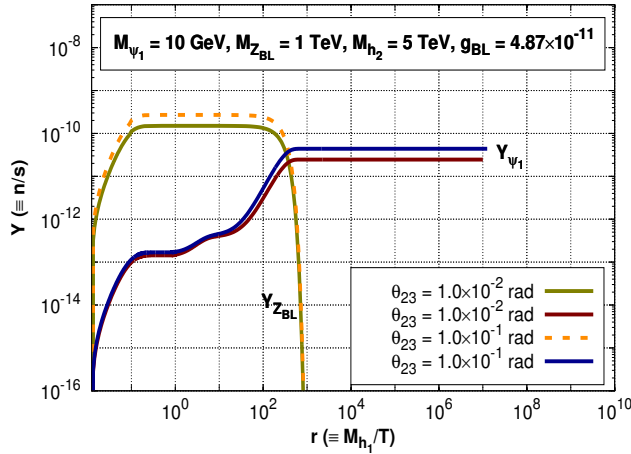
decay, for reasons discussed before, also increases due to a decrease in $M_{Z_{BL}}$. All these are shown in the right panel of Fig. 3.7.



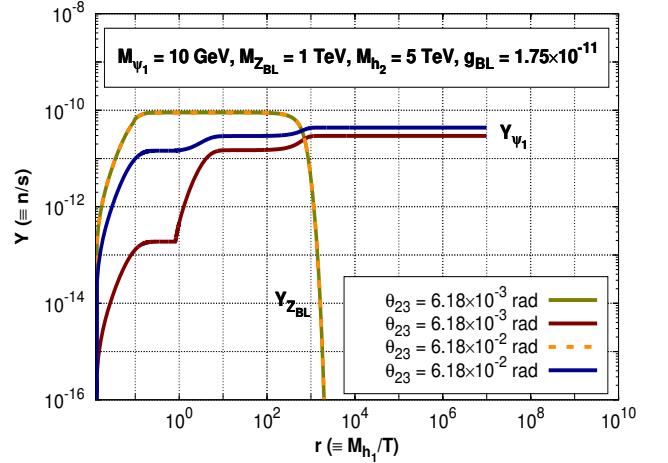
(a) Variation with different θ_{13} values for $\beta = 1$



(b) Variation with different θ_{13} values for $\beta = 10^{-3}$



(c) Variation with different θ_{23} values for $\beta = 1$



(d) Variation with different θ_{23} values for $\beta = 1$

Figure 3.8: Comparison of comoving number densities of Z_{BL} and ψ_1 with respect to mixing angles θ_{13} and θ_{23} .

Let us now discuss the variation of Y with respect to mixing angles. These are shown in Fig. 3.8 (a)–3.8 (d). As mentioned earlier, when $\beta = 1$, the mixing angles have very little effect on the comoving number density of Z_{BL} and ψ_1 . In Fig. 3.8 (a), on increasing θ_{13} , we find that there is only a small increase in the production of ψ_1 from the SM Higgs (h_1) due to an increase in $g_{h_1\psi_1\psi_1}$ coupling. On the other hand, $g_{h_2Z_{BL}Z_{BL}}$ is however insensitive to variations in θ_{13} and hence $Y_{Z_{BL}}$ remains unchanged. The $g_{h_2Z_{BL}Z_{BL}}$ coupling, however,

is sensitive to θ_{23} (because of the presence of the term like $\cos \theta_{13} \sin \theta_{23}$). So we find a corresponding increase in Z_{BL} yield on increasing θ_{23} in Fig. 3.8 (c). Consequently, an increase in Y_{ψ_1} is also noted.

Variation in the yield of Z_{BL} and ψ_1 with these mixing angles is more pronounced in the $\beta = 10^{-3}$ scenario. Increasing θ_{13} in Fig. 3.8 (b), we find that the production of dark matter from SM Higgs decay is enhanced while the production from h_2 is almost unaffected. This happens since the coupling $g_{h_1 \bar{\psi}_1 \psi_1}$ is more sensitive to changes in θ_{13} as is seen from its expression in the Appendix 3.7.1. On the contrary, the coupling $g_{h_2 \bar{\psi}_1 \psi_1}$ is sensitive to θ_{23} . So production of ψ_1 from h_2 is enhanced in the case where θ_{23} is increased (Fig. 3.8 (d)). Yield of Z_{BL} in this case ($\beta = 10^{-3}$), however remains unaffected because the effect of the mixing angle θ_{13} on the coupling $g_{h_2 Z_{\text{BL}} Z_{\text{BL}}}$ is always suppressed due to its nature of occurrence within the trigonometric functions while the low value of β makes the $h_2 Z_{\text{BL}} Z_{\text{BL}}$ coupling insensitive to the other mixing angle θ_{23} .

Finally, to contrast the two scenarios, we have plotted the relic density corresponding to the two benchmarks given in Table 5.4. The equal contribution of the scalars as well as Z_{BL} to the final DM relic abundance is clearly visible in Fig. 3.9 for $\beta = 10^{-3}$ case. In the other scenario, all most all of the contribution to the final abundance of ψ_1 comes from the decay of Z_{BL} .

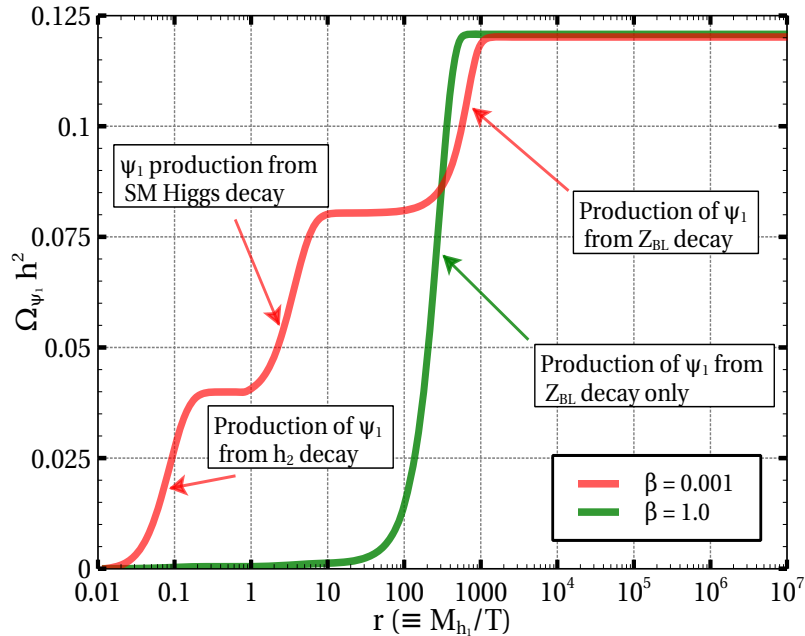


Figure 3.9: Variation of total relic density of ψ_1 with r corresponding to $\beta = 1$ and $\beta = 10^{-3}$.

A major portion of this chapter is focussed on deriving the distribution function of the dark matter particle ψ_1 . A natural question may hence arise about the need of following such a procedure. Naively, one may expect to follow the usual procedure of solving the Boltzmann equation written in terms of the comoving number density Y [178, 179]. If the decaying mother particle is not in thermal equilibrium, then we need to solve a separate Boltzmann equation for the comoving number density of this out of equilibrium mother particle first. But the usual form of the Boltzmann equation in terms of Y depends on the fact that the species under study is at least close to thermal equilibrium. For example, in case of decay, the thermal average decay width $\langle\Gamma\rangle_{\text{Th}}$ appearing in the Boltzmann equation, is usually given by $\frac{K_1(z)}{K_2(z)}\Gamma$, where K_1 and K_2 are the modified Bessel functions of order 1 and 2 respectively. However, while deriving the above expression of thermally averaged decay width one assumes that the corresponding decaying particle is either in thermal equilibrium or at least it is close to thermal equilibrium such that it obeys Maxwell-Boltzmann distribution. If this is not the case, such a thermal average is not guaranteed to give correct results and relic density should not be computed directly by solving the Boltzmann equation for Y . In such cases average value of the decay width itself requires the information about the non-equilibrium momentum distribution function of the decaying mother particle. Under such circumstances, $\langle\Gamma\rangle_{\text{Th}}$ should be replaced by non-thermal average, $\langle\Gamma\rangle_{\text{NTh}} = \frac{\int \Gamma f_{\text{non-eq}}(p) d^3p}{\int f_{\text{non-eq}}(p) d^3p}$. So we should first solve the distribution function of the mother particle (here Z_{BL}), then use it to calculate the distribution function of the dark matter directly. Once this is known, we can calculate other quantities of interest as we have discussed elaborately earlier. Thus, finally we make a comparative study (for both the benchmark points $\beta = 1$ and $\beta = 0.001$) of the differences in the results obtained from the exact calculation and that obtained by assuming the system to be close to an equilibrium one. The findings are plotted in both the panels of Fig. 3.10 where left panel is for $\beta = 1$ case while the right one corresponds to $\beta = 0.001$. In both plots, we find considerable differences in the final abundance of ψ_1 computed using $\langle\Gamma\rangle_{\text{NTh}}$ (solid lines) and $\langle\Gamma\rangle_{\text{Th}}$ (dashed lines). We also find that the difference in Y_{ψ_1} depends on the contribution of Z_{BL} to comoving number density of ψ_1 . For $\beta = 1$ case, almost all the DM is produced from the decay of Z_{BL} and hence in this case, Y_{ψ_1} obtained from exact calculation is 7.98 times lower than that obtained from the approximate one. For the other scenario, with $\beta = 0.001$, contribution of Z_{BL} is only 33%. So now, the final value of Y_{ψ_1} from the exact calculation using distribution functions is 3.32 times smaller than the value of Y_{ψ_1} obtained using the approximate method.

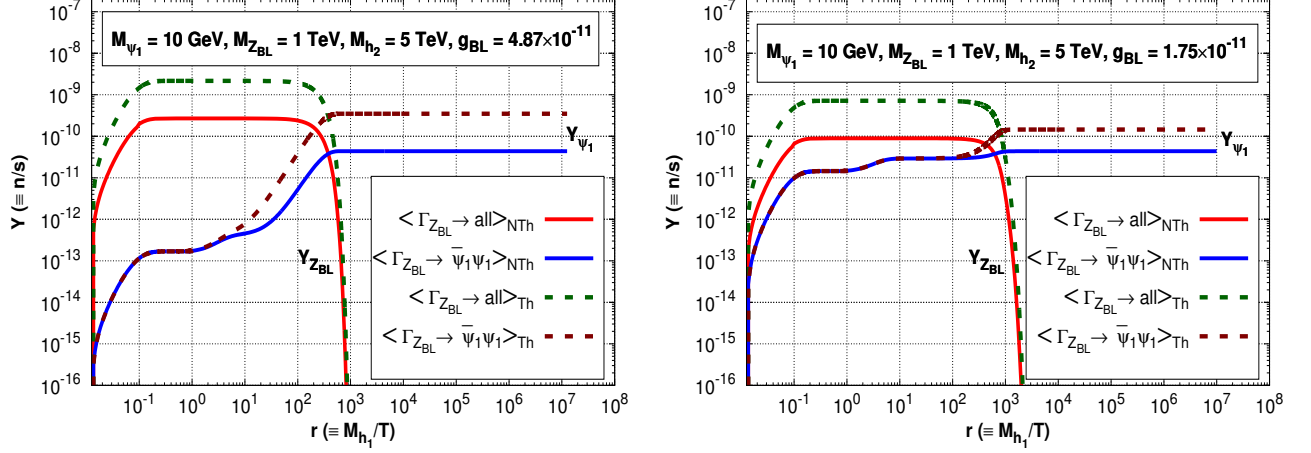


Figure 3.10: Comparison between the $Y_{Z_{BL}}$ and Y_{ψ_1} obtained from the exact calculation using momentum distribution approach with that of the approximate method using the $\langle \Gamma \rangle_{Th}$ for $\beta = 1$ (left panel) and $\beta = 0.001$ (right panel).

3.5 Constraints

In this section, we will discuss about the relevant constraints on the model parameters arising from theoretical as well as experiment and observational results. To start with, we should first satisfy the nontrivial theoretical constraints arising from the vacuum stability criterion. The conditions we need to satisfy are listed in Eqs. ((3.3)–(3.4)) (copositivity conditions [180]) For a general 3×3 scalar mixing matrix it is difficult to write closed form analytical expressions of the different λ 's (Eq. (3.1)) in terms of our chosen set of independent parameters. We have however checked numerically that for our benchmark points the conditions are indeed satisfied.

Among the experimental constraints let us first discuss the implication of the constraint related to the invisible decay width of SM Z boson. As given in [152],

$$\frac{\Gamma(Z \rightarrow \text{invisible})}{\Gamma(Z \rightarrow \nu \bar{\nu})} = 2.990 \pm 0.007. \quad (3.30)$$

In our chosen model, in absence of kinetic mixing terms between the Standard Model Z boson and the extra gauge boson Z_{BL} , the former do not decay to any BSM particles. Hence Eq. (3.30) is trivially satisfied.

The Standard Model Higgs boson (h_1) in the representative benchmarks is lighter than the other two scalars (h_2 and h_3) as well as Z_{BL} . As already discussed, the fermion ψ_2 and pseudo scalar A are assumed to be very heavy for simplicity. Hence only allowed invisible

decay mode of h_1 is to $h_1 \rightarrow \bar{\psi}_1 \psi_1$. But this channel is highly suppressed because of the very small value of the extra gauge coupling g_{BL} required to satisfy the non-thermality condition (see Eq. 3.37). Thus this decay width evades the bound from LHC on the invisible decay of SM Higgs boson [177].

The scattering cross section ψ_1 with the Standard Model particles is also very weak in this non-thermal regime hence the spin independent DM nucleon coherent scattering cross sections lie much below the present day direct detection bounds [181].

From cosmological point of view, the most important constraints arise from the structure formation and somewhat related to it, the bounds from dark radiation. The presence of highly relativistic particles around the Big Bang Nucleosynthesis (BBN) epoch can upset the observed structures of the galaxies. Dark matter particles if at all produced around that epoch then it has to be non-relativistic and hence should not alter the onset of BBN. Dark matter momentum distribution functions $f_{\psi_1}(\xi_p, r)$ can provide us with the vital information on whether the particle is Hot or Cold. A suitable quantity to calculate in this regard is the free-streaming horizon length denoted commonly by λ_{fs} [154]. It is defined by:

$$\lambda_{fs} \equiv \int_{T_{\text{production}}}^{T_{\text{now}}} \frac{\langle v(T) \rangle}{a(T)} \frac{dt}{dT} dT, \quad (3.31)$$

where $T_{\text{production}}$ is the temperature when almost all of the dark matter particles have been produced and the DM comoving number density already has frozen in. T_{Now} is the present temperature of the Universe. $\langle v(T) \rangle$ is the average velocity of the dark matter particle and is calculable once its distribution function is known. The term $\frac{dt}{dT}$ can be found from the time-temperature relationship and in the radiation dominated era $\frac{dt}{dT} = - \left(1 + \frac{1}{4} \frac{d \ln g_\rho(T)}{d \ln T} \right) \frac{1}{H T}$, where $H(T)$ is the Hubble parameter while $g_\rho(T)$ is the number of degrees of freedom related to the energy density of the Universe. At this point we transform the variable T to our usual dimensionless variable $r = \frac{M_{sc}}{T}$. With this Eq. (3.31) becomes:

$$\lambda_{fs} = \int_{r_{\text{production}}}^{r_{\text{now}}} \frac{\langle v(r) \rangle}{a(r)} \frac{\tilde{g}_\rho(r)}{H(r)} \frac{dr}{r}, \quad (3.32)$$

where $\tilde{g}_\rho(r) = \left(1 - \frac{1}{4} \frac{d \ln g_\rho(r)}{d \ln r} \right)$ and $r_{\text{production (now)}} \equiv \frac{M_{sc}}{T_{\text{production (now)}}}$. The average veloc-

ity $\langle v(r) \rangle$ is defined as:

$$\langle v(r) \rangle = \mathcal{B}(r) \frac{\int_0^\infty d\xi \frac{\xi^3 f_{\psi_1}(\xi, r)}{\sqrt{\mathcal{B}(r)^2 \xi^2 + r^2 \frac{M_{\psi_1}^2}{M_{sc}^2}}}}{\int_0^\infty d\xi \xi^2 f_{\psi_1}(\xi, r)}. \quad (3.33)$$

The scale factor $a(r)$ is obtained by using the conservation of total entropy of the Universe in a comoving volume. It is given by:

$$a(r) = \left(\frac{43}{11 g_s(r)} \right)^{1/3} \frac{r}{r_{\text{now}}}. \quad (3.34)$$

The Hubble parameter in terms of r is written as:

$$H(r) = \frac{M_{sc}^2}{M_0(r) r^2}, \quad (3.35)$$

with $M_0(r) = \left(\frac{45 M_{Pl}^2}{4\pi^3 g_p(r)} \right)^{1/2}$. Using all these in Eq. (3.32) we calculated the free streaming horizon length. According to Ref. [135], if $\lambda_{fs} < 0.01$ Mpc, then we can attribute the dark matter as ‘‘Cold’’. In our case we have found out that $\lambda_{fs} \ll 0.01$ Mpc for all the benchmark points, and hence respects the structure formation constraints.

Another cosmological quantity of interest that measures the amount of relativistic particles that can be injected without disrupting the precise experimental observations around BBN and CMB is the effective number of neutrinos, denoted by N_{eff} . Its standard value is given by 3.046 [182]. This number will change if the highly relativistic particles are introduced at around the time of BBN and CMB. Stringent bounds on the amount of *extra* relativistic degree of freedom that can be added is given by ΔN_{eff} . The present experimental constraints on this quantity are $\Delta N_{eff}(T_{\text{BBN}}) < 0.85$ [25] and $\Delta N_{eff}(T_{\text{CMB}}) < 0.32$ [5]. This quantity can be also calculated using the knowledge of momentum distribution function of ψ_1 following [136]. The expression of ΔN_{eff} is given by :

$$\Delta N_{eff}(r) = \frac{60}{7\pi^4} \left(\frac{r_\nu}{r} \right)^4 \frac{M_{\psi_1} r}{M_{sc}} \mathcal{B}(r)^3 \int_0^\infty d\xi_p \xi_p^2 \left(\sqrt{1 + \left(\frac{\mathcal{B}(r) \xi_p M_{sc}}{M_{\psi_1} r} \right)^2} - 1 \right) f_{\psi_1}(\xi_p, r) \quad (3.36)$$

The factor $\left(\frac{r_\nu}{r} \right)^4 = \left(\frac{T}{T_\nu} \right)^4$ is neglected for $T \gtrsim 1$ MeV since the neutrinos had the same temperature with the background photon bath during that epoch. For our benchmarks,

the calculated value of this ΔN_{eff} (at both the epochs of BBN and CMB) lies well below the existing upper bounds. It is expected that our scenario will not disturb the evolution of Universe during BBN and CMB. This is because in our chosen benchmarks, the mass of dark matter is $\mathcal{O}(\text{Gev})$ and most of it are produced at around a temperature of $\mathcal{O}(100 \text{ MeV})$. Hence by the time the Universe is cooled to lower temperatures most of these particles will become non-relativistic and hence wont affect either structure formation or CMB.

3.6 Conclusion

In this chapter we have calculated the momentum distribution function of a non-thermal fermionic dark matter. Calculation of momentum distribution function is a general feature of any non-thermal dark matter scenario if the dark matter particle under study originates from a parent particle that itself is outside the thermal soup. On the other hand, the momentum distribution function of DM is a key quantity for the computations of all the relevant thermodynamic quantities. We have demonstrated its use in the calculations of cosmological constraints, which, though weak in our case, can become important for other different combination of model parameters. The model chosen here is also well motivated, since it is anomaly free and also explains the genesis of neutrino mass, besides accommodating a non-thermal fermionic dark matter candidate as well. For the two chosen benchmark scenarios there are noticeable structural differences in the plots. In one scenario (with $\beta = 1$), the dominant production of dark matter is seen to be pronounced from Z_{BL} decay and hence the final abundances is not much sensitive to the scalars mixing angles. In the other scenario (with $\beta(\ll 1) = 10^{-3}$), however all decay modes can contribute substantially, resulting in a characteristic multi-plateau feature in the variation of comoving number density (Y_{ψ_1}) with r . Finally, we have also checked that our non-thermal dark matter scenario does not violate any experimental or theoretical constraints.

3.7 Appendix

3.7.1 Relevant Vertex factors

We denote the vertex factor by g_{abc} for a vertex containing fields a, b, c . Vertex factors for the interactions of ψ_1 with CP-even scalars are given below

$$g_{h_1 \bar{\psi}_1 \psi_1} = 2\sqrt{2} \frac{g_{\text{BL}} \sqrt{1+4\beta^2}}{\beta M_{Z_{\text{BL}}}} (\beta \sin \theta_{12} \cos \theta_{13} \cos^2 \theta_L M_{\psi_1} + \sin \theta_{13} \sin^2 \theta_L M_{\psi_1}) \quad (3.37)$$

$$g_{h_2 \bar{\psi}_1 \psi_1} = 2\sqrt{2} \frac{g_{\text{BL}} \sqrt{1+4\beta^2}}{\beta M_{Z_{\text{BL}}}} (\beta (\cos \theta_{12} \cos \theta_{23} - \sin \theta_{12} \sin \theta_{23} \sin \theta_{13}) \cos^2 \theta_L M_{\psi_1} + \sin \theta_{23} \cos \theta_{13} \sin^2 \theta_L M_{\psi_1}) \quad (3.38)$$

$$g_{h_3 \bar{\psi}_1 \psi_1} = 2\sqrt{2} \frac{g_{\text{BL}} \sqrt{1+4\beta^2}}{\beta M_{Z_{\text{BL}}}} (-\beta (\cos \theta_{12} \sin \theta_{23} + \sin \theta_{12} \cos \theta_{23} \sin \theta_{13}) \cos^2 \theta_L M_{\psi_1} + \cos \theta_{23} \cos \theta_{13} \sin^2 \theta_L M_{\psi_1}) \quad (3.39)$$

Vertex factors for the interactions between CP-even scalars and B – L gauge boson (Z_{BL}):

$$g_{h_1 Z_{\text{BL}} Z_{\text{BL}}} = 2 \frac{g_{\text{BL}} M_{Z_{\text{BL}}}}{\sqrt{1+4\beta^2}} (\sin \theta_{12} \cos \theta_{13} + 4\beta \sin \theta_{13}) \quad (3.40)$$

$$g_{h_2 Z_{\text{BL}} Z_{\text{BL}}} = 2 \frac{g_{\text{BL}} M_{Z_{\text{BL}}}}{\sqrt{1+4\beta^2}} (\cos \theta_{12} \cos \theta_{23} - \sin \theta_{12} \sin \theta_{23} \sin \theta_{13} + 4\beta \cos \theta_{13} \sin \theta_{23}) \quad (3.41)$$

$$g_{h_3 Z_{\text{BL}} Z_{\text{BL}}} = 2 \frac{g_{\text{BL}} M_{Z_{\text{BL}}}}{\sqrt{1+4\beta^2}} (-(\cos \theta_{12} \sin \theta_{23} + \sin \theta_{12} \cos \theta_{23} \sin \theta_{13}) + 4\beta \cos \theta_{13} \cos \theta_{23}) \quad (3.42)$$

The interaction vertex of the dark matter ψ_1 with the new gauge boson can be written as: $\frac{g_{\text{BL}}}{6} \bar{\psi}_1 \gamma^\mu (a - b \gamma_5) \psi_1$, where $a = (1 - 3 \sin^2 \theta_L)$ and $b = -3 (1 + \sin^2 \theta_L)$.

The Yukawa couplings of the fermions i.e. the y_{ξ_i} 's and y_{η_i} 's are also listed below for completeness.

$$y_{\xi_1} = \sqrt{2} \frac{g_{\text{BL}} \sqrt{1+4\beta^2}}{\beta M_{Z_{\text{BL}}}} (\cos \theta_L \cos \theta_R M_{\psi_2} + \sin \theta_L \sin \theta_R M_{\psi_1}), \quad (3.43)$$

$$y_{\xi_2} = \sqrt{2} \frac{g_{\text{BL}} \sqrt{1+4\beta^2}}{\beta M_{Z_{\text{BL}}}} (-\cos \theta_L \sin \theta_R M_{\psi_2} + \sin \theta_L \cos \theta_R M_{\psi_1}), \quad (3.44)$$

$$y_{\eta_1} = \sqrt{2} \frac{g_{\text{BL}} \sqrt{1+4\beta^2}}{M_{Z_{\text{BL}}}} (-\sin \theta_L \cos \theta_R M_{\psi_2} + \cos \theta_L \sin \theta_R M_{\psi_1}), \quad (3.45)$$

$$y_{\eta_2} = \sqrt{2} \frac{g_{\text{BL}} \sqrt{1+4\beta^2}}{M_{Z_{\text{BL}}}} (\sin \theta_L \sin \theta_R M_{\psi_2} + \cos \theta_L \cos \theta_R M_{\psi_1}). \quad (3.46)$$

3.7.2 Relevant Decay Widths

The only relevant decay widths that we need during the computation of dark matter momentum distribution functions are those corresponding to the decay of the extra gauge boson Z_{BL} to fermions.

$$\Gamma_{Z_{BL} \rightarrow f\bar{f}} = \frac{M_{Z_{BL}}}{16\pi} \frac{4}{3} (a_f^2 + b_f^2) \left(1 + \frac{2(a_f^2 - 2b_f^2)}{(a_f^2 + b_f^2)} \frac{M_f^2}{M_{Z_{BL}}^2} \right) \sqrt{1 - \frac{4M_f^2}{M_{Z_{BL}}^2}}. \quad (3.47)$$

If f is a Standard Model fermion then $b_f = 0$ and $a_f = g_{BL} Q_{BL}(f)$, where $Q_{BL}(f)$ is the $B - L$ charge corresponding to the fermion f (see Table 3.1). If, on the other hand f is a beyond Standard Model particle (say, $f = \psi_1$), we have $a_{\psi_1} = \frac{g_{BL}}{6} (1 - 3\sin^2 \theta_L)$ and $b_{\psi_1} = \frac{g_{BL}}{2} (1 + \sin^2 \theta_L)$. Hence the total decay width (assuming other BSM particles such as ψ_2 , A and h_3 are heavier than Z_{BL}) is given as the sum of the individual decay widths to all these individual SM and BSM channels i.e.

$$\Gamma_{Z_{BL} \rightarrow all} = \left(\sum_{\text{SM fermions}} \Gamma_{Z_{BL} \rightarrow f\bar{f}} \right) + \Gamma_{Z_{BL} \rightarrow \psi_1 \bar{\psi}_1}. \quad (3.48)$$

Note, that this expression of decay width is valid only in the rest frame of the decaying particle (here Z_{BL}). In a reference frame where Z_{BL} is not at rest but moving with an energy $E_{Z_{BL}}$, the total decay width is given by:

$$\Gamma'_{Z_{BL} \rightarrow all} = \Gamma_{Z_{BL} \rightarrow all} \frac{M_{Z_{BL}}}{E_{Z_{BL}}} \quad (3.49)$$

3.7.3 Collision terms

The first step while solving the Boltzmann equation is to derive the collision terms ($\mathcal{C}[f]$). The generic form of the collision term in case of $1 \rightarrow 2$ decay process (say, $\chi \rightarrow a b$) is given by [54, 183]:

$$\begin{aligned} \mathcal{C}[f_\chi(p)] &= \frac{1}{2E_p} \int \frac{g_a d^3 p'}{(2\pi)^3 2E_{p'}} \frac{g_b d^3 q'}{(2\pi)^3 2E_{q'}} (2\pi)^4 \delta^4(\tilde{p} - \tilde{p}' - \tilde{q}') \times \overline{|\mathcal{M}|^2} \\ &\quad \times [f_a f_b (1 \pm f_\chi) - f_\chi (1 \pm f_a) (1 \pm f_b)]. \end{aligned} \quad (3.50)$$

In this expression p, p', q' are the absolute values of three momenta of χ , a and b respectively. The corresponding four momenta are given by \tilde{p} , \tilde{p}' and \tilde{q}' while E_p , $E_{p'}$ and $E_{q'}$ are the energies of χ , a and b respectively. These energies are of course related to the absolute value of the corresponding three momenta by the usual relativistic dispersion relation.

For e.g. $E_p = \sqrt{p^2 + m_\chi^2}$ and so on. The internal degrees of freedom corresponding to the particles a and b are indicated by g_a and g_b respectively. The matrix element squared denoted by $|\overline{\mathcal{M}}|^2$ for the corresponding process (here, $\chi \rightarrow a b$) is averaged over the spins of both the initial as well as final state particles. The distribution function corresponding to the particle x is denoted by f_x and $(1 \pm f_x)$ are the Pauli blocking and the stimulated emission factors respectively. These factors can be approximated ~ 1 in absence of Bose condensation and Fermi degeneracy. If any of the particles a or b is in thermal equilibrium then the corresponding f can be approximated by the Maxwell-Boltzmann distribution function i.e. $f \sim e^{-\frac{E}{T}}$, where E is the energy of the particle and T is the temperature of the Universe.

$\mathcal{C}^{Z_{\text{BL}} \rightarrow \text{all}}$

As a concrete example let us try to calculate $\mathcal{C}^{Z_{\text{BL}} \rightarrow \text{all}}$ (the second collision term in Eq. (3.20)). Let us first calculate the collision term for a specific channel, say $\mathcal{C}^{Z_{\text{BL}} \rightarrow f\bar{f}}$, where f is any fermion. In Eq. (3.20), we are interested in solving the non-equilibrium distribution function for Z_{BL} . Hence this collision term denotes the depletion of the particle under study. If we neglect the back reactions i.e. the inverse decay processes (which is a legitimate approximation for a particle in non-thermal regime [81, 136]) and approximate the Pauli blocking factors and stimulated emission terms to be ~ 1 , then from Eq. (3.50) we have:

$$\begin{aligned} \mathcal{C}^{Z_{\text{BL}} \rightarrow f\bar{f}}[f_{Z_{\text{BL}}}(p)] &= \frac{1}{2 E_p} \int \frac{g_f d^3 p'}{(2\pi)^3 2 E_{p'}} \frac{g_f d^3 q'}{(2\pi)^3 2 E_{q'}} (2\pi)^4 \delta^4(\tilde{p} - \tilde{p}' - \tilde{q}') \times \overline{|\mathcal{M}|^2} \\ &\quad \times [-f_{Z_{\text{BL}}}(p)], \\ &= -f_{Z_{\text{BL}}}(p) \times \frac{1}{2 E_p} \int \frac{g_f d^3 p'}{(2\pi)^3 2 E_{p'}} \frac{g_f d^3 q'}{(2\pi)^3 2 E_{q'}} (2\pi)^4 \delta^4(\tilde{p} - \tilde{p}' - \tilde{q}') \times \overline{|\mathcal{M}|^2}. \end{aligned} \quad (3.51)$$

But we know that the decay width (in an arbitrary frame) for the process $Z_{\text{BL}} \rightarrow f\bar{f}$ is given by the expression:

$$\Gamma'_{Z_{\text{BL}} \rightarrow f\bar{f}} = \frac{1}{2 E_p} \int \frac{g_f d^3 p'}{(2\pi)^3 2 E_{p'}} \frac{g_f d^3 q'}{(2\pi)^3 2 E_{q'}} (2\pi)^4 \delta^4(\tilde{p} - \tilde{p}' - \tilde{q}') \times \overline{|\mathcal{M}|^2} \Big|_{Z_{\text{BL}} \rightarrow f\bar{f}}, \quad (3.52)$$

where, as discussed before, p , p' and q' are the three momenta corresponding to Z_{BL} , f and \bar{f} respectively. Now using Eq. (3.52) in Eq. (3.50) and making the change of variables

$\xi_p \equiv \frac{1}{\mathcal{B}(r)} \frac{p}{T}$ and $r_{Z_{\text{BL}}} \equiv \frac{M_{Z_{\text{BL}}}}{T}$, we get

$$\begin{aligned} \mathcal{C}^{Z_{\text{BL}} \rightarrow f \bar{f}}[f_{Z_{\text{BL}}}(\xi_p)] &= -f_{Z_{\text{BL}}}(\xi_p) \times \Gamma_{Z_{\text{BL}} \rightarrow f \bar{f}} \times \frac{M_{Z_{\text{BL}}}}{E_{Z_{\text{BL}}}}, \\ &= -f_{Z_{\text{BL}}}(\xi_p) \times \Gamma_{Z_{\text{BL}} \rightarrow f \bar{f}} \times \frac{r_{Z_{\text{BL}}}}{\sqrt{\xi_p^2 \mathcal{B}(r)^2 + r_{Z_{\text{BL}}}^2}}, \end{aligned} \quad (3.53)$$

where we have used Eq. (3.49). Hence the collision term $\mathcal{C}^{Z_{\text{BL}} \rightarrow \text{all}}$ is now simply given by:

$$\mathcal{C}^{Z_{\text{BL}} \rightarrow \text{all}} = -f_{Z_{\text{BL}}}(\xi_p) \times \Gamma_{Z_{\text{BL}} \rightarrow \text{all}} \times \frac{r_{Z_{\text{BL}}}}{\sqrt{\xi_p^2 \mathcal{B}(r)^2 + r_{Z_{\text{BL}}}^2}}. \quad (3.54)$$

We can easily rewrite the above equation in terms of $r \equiv \frac{M_{sc}}{T}$ by writing $r_{Z_{\text{BL}}} = \frac{M_{Z_{\text{BL}}}}{M_{sc}} r$.

The derivation of this collision term is greatly simplified by the use of the expression of the decay width (Eq. (3.52)). This simplification is possible because the distribution function of the particle we are interested in (i.e. Z_{BL}) is itself the decaying particle.

However, the situation may be such that the particle whose non-equilibrium momentum distribution function we are interested in, is the daughter particle produced from the decay of another mother particle (where it is assumed that the distribution function of the latter is already known). In that case, the final expression for the collision term will not be so simple. We will illustrate such a case now with a definite example. Let us hence derive the first collision term in Eq. (3.20) i.e. $\mathcal{C}^{h_2 \rightarrow Z_{\text{BL}} Z_{\text{BL}}}$.

$\mathcal{C}^{h_2 \rightarrow Z_{\text{BL}} Z_{\text{BL}}}$

The starting point is again Eq. (3.50). This is actually the first collision term in Eq. (3.20). Proceeding as before we now have:

$$\begin{aligned} \mathcal{C}^{h_2 \rightarrow Z_{\text{BL}} Z_{\text{BL}}}[f_{Z_{\text{BL}}}(p)] &= 2 \times \frac{1}{2 E_p} \int \frac{g_{h_2} d^3 k}{(2\pi)^3 2 E_k} \frac{g_{Z_{\text{BL}}} d^3 q'}{(2\pi)^3 2 E_{q'}} (2\pi)^4 \delta^4(\tilde{k} - \tilde{p} - \tilde{q}') \times \overline{|\mathcal{M}|^2} \Big|_{h_2 \rightarrow Z_{\text{BL}} Z_{\text{BL}}} \\ &\quad \times [f_{h_2} (1 \pm f_{Z_{\text{BL}}}) (1 \pm f_{Z_{\text{BL}}}) - f_{Z_{\text{BL}}} f_{Z_{\text{BL}}} (1 \pm f_{h_2})]. \end{aligned} \quad (3.55)$$

Here k is the three momentum of the decaying particle (h_2) while p and q' are the three momenta of the final state particles (Z_{BL}). The factor of 2 in front is due the production of two Z_{BL} in the final state from h_2 decay. $g_{Z_{\text{BL}}}$ and g_{h_2} are the internal degrees of freedom for the extra gauge boson and extra scalar respectively. Hence, $g_{Z_{\text{BL}}} = 3$ and $g_{h_2} = 1$.

Using the usual approximations of neglecting the back reactions as well as the Pauli blocking and stimulated emission factors, we finally get:

$$\mathcal{C}^{h_2 \rightarrow Z_{\text{BL}} Z_{\text{BL}}}[f_{Z_{\text{BL}}}(p)] = 2 \times \frac{1}{2 E_p} \int \frac{g_{h_2} d^3 k}{(2\pi)^3 2 E_k} \frac{g_{Z_{\text{BL}}} d^3 q'}{(2\pi)^3 2 E_{q'}} (2\pi)^4 \delta^4(\vec{k} - \vec{p} - \vec{q}') \times \overline{|\mathcal{M}|^2} \Big|_{h_2 \rightarrow Z_{\text{BL}} Z_{\text{BL}}} \times [f_{h_2}(k)]. \quad (3.56)$$

The matrix element squared average for the decay process $h_2 \rightarrow Z_{\text{BL}} Z_{\text{BL}}$ is given by:

$$\overline{|\mathcal{M}|^2} \Big|_{h_2 \rightarrow Z_{\text{BL}} Z_{\text{BL}}} = \frac{g_{h_2 Z_{\text{BL}} Z_{\text{BL}}}^2}{2 \times 9} \left(2 + \frac{(E_p E_{q'} - \vec{p} \cdot \vec{q}')^2}{M_{Z_{\text{BL}}}^4} \right). \quad (3.57)$$

In Eq. (3.56), $\delta^{(4)}(\vec{k} - \vec{p} - \vec{q}')$ can be written as $\delta^{(3)}(\vec{k} - \vec{p} - \vec{q}') \delta(E_k - E_p - E_{q'})$. We can then do the integral over q' . So we should replace every occurrence of \vec{q}' with $\vec{k} - \vec{p}$. As already stated earlier that, to simplify notations we will write $|\vec{k}| = k$ and so on. Hence now $E_{q'}$ has become a function of p and k (and of the masses of the corresponding particles which have three momenta \vec{p} and \vec{k} respectively), i.e. $E_{q'} = E_{q'}(p, k)$. Therefore Eq. (3.56) becomes:

$$\mathcal{C}^{h_2 \rightarrow Z_{\text{BL}} Z_{\text{BL}}}[f_{Z_{\text{BL}}}(p)] = \frac{g_{h_2 Z_{\text{BL}} Z_{\text{BL}}}^2}{6 (4\pi)^2} \frac{1}{E_p} \int \frac{d^3 k}{E_k E_{q'}(p, k)} \delta(E_k - E_p - E_{q'}(p, k)) \times \left(2 + \frac{(E_p E_{q'}(k, p) + p^2 - p k \cos \theta)^2}{M_{Z_{\text{BL}}}^4} \right) \times [f_{h_2}(k)], \quad (3.58)$$

where θ is the angle between the \vec{k} and \vec{p} . Also, we have, $E_{q'} = \sqrt{k^2 + p^2 + M_{Z_{\text{BL}}}^2 - 2 p k \cos \theta}$. At this point let us transform variables to $\xi_k = \frac{1}{\mathcal{B}(r)} \frac{k}{T}$, $\xi_p = \frac{1}{\mathcal{B}(r)} \frac{p}{T}$ and $\cos \theta = y$, where $\mathcal{B}(r)$ is defined by Eq. (3.22). Also $r_{Z_{\text{BL}}} = \frac{M_{Z_{\text{BL}}}}{T}$ and $r_{h_2} = \frac{M_{h_2}}{T}$. Hence,

$$E_{q'} = T \sqrt{\xi_k^2 \mathcal{B}(r)^2 + \xi_p^2 \mathcal{B}(r)^2 + r_{Z_{\text{BL}}}^2 - 2 \mathcal{B}(r)^2 \xi_k \xi_p y} \equiv T H_1(\xi_k, \xi_p, y). \quad (3.59)$$

From here onwards, for notational fluidity, we will suppress the explicit dependence on $r \equiv \frac{M_{sc}}{T}$. Every occurrence of $r_{Z_{\text{BL}}}$ and/or r_{h_2} should be replaced by $r_{Z_{\text{BL}}} = \frac{M_{Z_{\text{BL}}}}{M_{sc}} r$ and $r_{h_2} = \frac{M_{h_2}}{M_{sc}} r$. Hence it is easy to identify the functional dependence on r . Eq. (3.58) now

simplifies to:

$$\begin{aligned} \mathcal{C}^{h_2 \rightarrow Z_{\text{BL}} Z_{\text{BL}}}[f_{Z_{\text{BL}}}(\xi_p)] &= \frac{g_{h_2 Z_{\text{BL}} Z_{\text{BL}}}^2}{48\pi T} \frac{\mathcal{B}(r)^3}{\sqrt{\xi_p^2 \mathcal{B}(r)^2 + r_{Z_{\text{BL}}}^2}} \int \frac{\xi_k^2 d\xi_k dy}{\sqrt{\xi_k^2 \mathcal{B}(r)^2 + r_{h_2}^2} H_1(\xi_k, \xi_p, y)} \delta(\mathcal{F}(\xi_k, \xi_p, y)) \\ &\times \left(2 + \frac{\left(\sqrt{\xi_p^2 \mathcal{B}(r)^2 + r_{Z_{\text{BL}}}^2} H_1(\xi_k, \xi_p, y) + \xi_p^2 \mathcal{B}(r)^2 - \mathcal{B}(r)^2 \xi_p \xi_k y \right)^2}{r_{Z_{\text{BL}}}^4} \right) \times [f_{h_2}(\xi_k)]. \end{aligned} \quad (3.60)$$

For convenience we have defined:

$$\mathcal{F}(\xi_k, \xi_p, y) \equiv \sqrt{\xi_k^2 + r_{h_2}^2} - \sqrt{\xi_p^2 \mathcal{B}(r)^2 + r_{Z_{\text{BL}}}^2} - H_1(\xi_k, \xi_p, y). \quad (3.61)$$

Also let,

$$H_2(\xi_k, \xi_p, y) \equiv \frac{\left(\sqrt{\xi_p^2 \mathcal{B}(r)^2 + r_{Z_{\text{BL}}}^2} H_1(\xi_k, \xi_p, y) + \xi_p^2 \mathcal{B}(r)^2 - \mathcal{B}(r)^2 \xi_p \xi_k y \right)^2}{r_{Z_{\text{BL}}}^4}. \quad (3.62)$$

The y integral in Eq. (3.60) can easily be done. For this, we have used the well known property of δ function which is $\delta(\mathcal{F}(\xi_k, \xi_p, y)) = \frac{\delta(y - y_0)}{|\mathcal{F}'(\xi_k, \xi_p, y_0)|}$, $\mathcal{F}'(\xi_k, \xi_p, y_0)$ denotes differentiation of $\mathcal{F}(\xi_k, \xi_p, y)$ with respect to y at $y = y_0$ where y_0 is the root of the equation $\mathcal{F}(\xi_k, \xi_p, y) = 0$. The expression of y_0 is given by:

$$y_0(\xi_k, \xi_p) = \frac{1}{2 \mathcal{B}(r)^2 \xi_k \xi_p} \left(2 \sqrt{\xi_k^2 \mathcal{B}(r)^2 + r_{h_2}^2} \sqrt{\xi_p^2 \mathcal{B}(r)^2 + r_{Z_{\text{BL}}}^2} - r_{h_2}^2 \right). \quad (3.63)$$

Using this we find that

$$\mathcal{F}'(\xi_k, \xi_p) = \frac{\mathcal{B}(r)^2 \xi_k \xi_p}{\sqrt{\xi_k^2 \mathcal{B}(r)^2 + r_{h_2}^2} - \sqrt{\xi_p^2 \mathcal{B}(r)^2 + r_{Z_{\text{BL}}}^2}} \equiv F(\xi_k, \xi_p). \quad (3.64)$$

But since y_0 is a function of ξ_k itself, integration over y puts a limit on the ξ_k integral as well. The limit(s) can be derived by remembering that y_0 is actually $\cos \theta_0$, and hence $|y_0| \leq 1$. The minimum and maximum limits on ξ_k turn out to be:

$$\xi_k^{\min}(\xi_p) = \frac{1}{2 \mathcal{B}(r) r_{Z_{\text{BL}}}} \left| \eta(\xi_p) - \mathcal{B}(r) \frac{\xi_p r_{h_2}^2}{r_{Z_{\text{BL}}}} \right|, \quad (3.65)$$

$$\xi_k^{\max}(\xi_p) = \frac{1}{2 \mathcal{B}(r) r_{Z_{\text{BL}}}} \left(\eta(\xi_p) + \mathcal{B}(r) \frac{\xi_p r_{h_2}^2}{r_{Z_{\text{BL}}}} \right), \quad (3.66)$$

where

$$\eta(\xi_p) \equiv r_{h_2} \sqrt{\left(\frac{M_{h_2}^2}{M_{Z_{BL}}^2} - 4\right)} \sqrt{\left(\xi_p^2 \mathcal{B}(r)^2 + r_{Z_{BL}}^2\right)}.$$

So, finally when the smoke clears, Eq. (3.60) reduces to:

$$\begin{aligned} \mathcal{C}^{h_2 \rightarrow Z_{BL} Z_{BL}}[f_{Z_{BL}}(\xi_p)] &= \frac{g_{h_2 Z_{BL} Z_{BL}}^2}{48\pi M_{sc}} \frac{r \mathcal{B}(r)^3}{\sqrt{\xi_p^2 \mathcal{B}(r)^2 + \left(\frac{M_{Z_{BL}} r}{M_{sc}}\right)^2}} \times \\ &\int_{\xi_k^{min}}^{\xi_k^{max}} \frac{\xi_k^2 f_{h_2}(\xi_k) d\xi_k}{\sqrt{\xi_k^2 \mathcal{B}(r)^2 + \left(\frac{M_{h_2} r}{M_{sc}}\right)^2} H_1(\xi_k, \xi_p, y_0(\xi_k, \xi_p))} \times \frac{1}{F(\xi_k, \xi_p)} \left(2 + H_2(\xi_k, \xi_p, y_0(\xi_k, \xi_p))\right). \end{aligned} \quad (3.67)$$

For completeness, let us now plug back in the explicit dependence of the functions in Eq. (3.67) on r and list them below:

$$F(\xi_k, \xi_p, r) = \frac{\mathcal{B}(r)^2 \xi_k \xi_p}{\sqrt{\xi_k^2 \mathcal{B}(r)^2 + \left(\frac{M_{h_2} r}{M_{sc}}\right)^2} - \sqrt{\xi_p^2 \mathcal{B}(r)^2 + \left(\frac{M_{Z_{BL}} r}{M_{sc}}\right)^2}}, \quad (3.68)$$

$$y_0(\xi_k, \xi_p, r) = \frac{1}{2\mathcal{B}(r)^2 \xi_k \xi_p} \left(2\sqrt{\xi_k^2 \mathcal{B}(r)^2 + \left(\frac{M_{h_2} r}{M_{sc}}\right)^2} \sqrt{\xi_p^2 \mathcal{B}(r)^2 + \left(\frac{M_{Z_{BL}} r}{M_{sc}}\right)^2} - \left(\frac{M_{h_2} r}{M_{sc}}\right)^2\right), \quad (3.69)$$

$$H_1(\xi_k, \xi_p, r) = \sqrt{\xi_k^2 \mathcal{B}(r)^2 + \left(\frac{M_{h_2} r}{M_{sc}}\right)^2} - \sqrt{\xi_p^2 \mathcal{B}(r)^2 + \left(\frac{M_{Z_{BL}} r}{M_{sc}}\right)^2}, \quad (3.70)$$

$$H_2(\xi_k, \xi_p, r) = \frac{\left(\sqrt{\xi_p^2 \mathcal{B}(r)^2 + \left(\frac{M_{Z_{BL}} r}{M_{sc}}\right)^2} H_1(\xi_k, \xi_p, r) + \xi_p^2 \mathcal{B}(r)^2 - \mathcal{B}(r)^2 \xi_p \xi_k y_0(\xi_k, \xi_p, r)\right)^2}{\left(\frac{M_{Z_{BL}} r}{M_{sc}}\right)^4} \quad (3.71)$$

The limits of the integration are as follows:

$$\xi_k^{min}(\xi_p, r) = \frac{M_{sc}}{2\mathcal{B}(r)rM_{Z_{BL}}} \left| \eta(\xi_p, r) - \frac{\mathcal{B}(r) \times M_{h_2}^2}{M_{Z_{BL}} \times M_{sc}} \xi_p r \right|, \quad (3.72)$$

$$\xi_k^{max}(\xi_p, r) = \frac{M_{sc}}{2\mathcal{B}(r)rM_{Z_{BL}}} \left(\eta(\xi_p, r) + \frac{\mathcal{B}(r) \times M_{h_2}^2}{M_{Z_{BL}} \times M_{sc}} \xi_p r \right), \quad (3.73)$$

where

$$\eta(\xi_p, r) = \left(\frac{M_{h_2} r}{M_{sc}}\right) \sqrt{\frac{M_{h_2}^2}{M_{Z_{BL}}^2} - 4} \sqrt{\xi_p^2 \mathcal{B}(r)^2 + \left(\frac{M_{Z_{BL}} r}{M_{sc}}\right)^2}. \quad (3.74)$$

With the explicit forms of the functions at hand (Eqs. ((3.68)–(3.74))) and remembering that $f_{h_2}(\xi_k)$ is the equilibrium distribution function (here Maxwell-Boltzmann distribution function), Eq. (3.67) can be greatly simplified. The final form of the collision term after performing the integral over ξ_k thus turns out to be:

$$\begin{aligned} \mathcal{C}^{h_2 \rightarrow Z_{BL} Z_{BL}} = & \frac{r}{8\pi M_{sc}} \frac{\mathcal{B}^{-1}(r)}{\xi_p \sqrt{\xi_p^2 \mathcal{B}(r)^2 + \left(\frac{M_{Z_{BL}} r}{M_{sc}}\right)^2}} \frac{g_{h_2 Z_{BL} Z_{BL}}^2}{6} \left(2 + \frac{(M_{h_2}^2 - 2M_{Z_{BL}}^2)^2}{4M_{Z_{BL}}^4}\right) \\ & \times \left(e^{-\sqrt{(\xi_k^{\min})^2 \mathcal{B}(r)^2 + \left(\frac{M_{h_2} r}{M_{sc}}\right)^2}} - e^{-\sqrt{(\xi_k^{\max})^2 \mathcal{B}(r)^2 + \left(\frac{M_{h_2} r}{M_{sc}}\right)^2}} \right). \end{aligned} \quad (3.75)$$

Having derived in detail all the collision terms in Eq. (3.20), it is now a straight forward exercise to derive the expressions for the other collision terms appearing in Eq. (3.21). Hence, for rest of the collision terms, we will simply write the analytical expressions for the different functions analogous to those in Eqs. ((3.68)–(3.71)) without going into the detailed derivations. Finally, we will provide the most simplified forms of the corresponding collision terms (where ever possible).

$$\mathcal{C}^{s \rightarrow \bar{\psi}_1 \psi_1}$$

In this case, the matrix element squared average is given by:

$$\overline{|\mathcal{M}|^2} \Big|_{s \rightarrow \bar{\psi}_1 \psi_1} = (g_{s\bar{\psi}_1 \psi_1})^2 (E_p E_q - \vec{p} \cdot \vec{q} - m_{\psi_1}^2), \quad (3.76)$$

where \vec{p} , \vec{q} are the three momenta of the final state particles and E_p , E_q are the corresponding energies. The generic form of this collision term is given as:

$$\begin{aligned} \mathcal{C}^{s \rightarrow \bar{\psi}_1 \psi_1} = & \frac{(g_{s\bar{\psi}_1 \psi_1}^2)}{8\pi r} \frac{M_{sc}}{\sqrt{\xi_p^2 \mathcal{B}(r)^2 + \left(\frac{M_{\psi_1} r}{M_{sc}}\right)^2}} \times [\mathcal{B}(r)]^3 \times g_s g_{\psi_1} \times \\ & \int_{\hat{\xi}_k^{\min}}^{\hat{\xi}_k^{\max}} \frac{\xi_k^2 f_s(\xi_k) \hat{H}_2^s(\xi_k, \xi_p, r) d\xi_k}{\sqrt{\xi_k^2 \mathcal{B}(r)^2 + \left(\frac{M_s r}{M_{sc}}\right)^2} \hat{H}_1^s(\xi_k, \xi_p, r) \hat{F}(\xi_k, \xi_p, r)}, \end{aligned} \quad (3.77)$$

where g_{ψ_1} , g_s are the internal degrees of freedom of scalar ($s = h_1, h_2$) and fermion (ψ_1) respectively. Below we list the expressions of all the relevant functions which have ap-

peared in Eq. (3.77).

$$\widehat{F}(\xi_k, \xi_p, r) = \frac{\mathcal{B}(r)^2 \xi_k \xi_p}{\sqrt{\xi_k^2 \mathcal{B}(r)^2 + \left(\frac{M_s r}{M_{sc}}\right)^2} - \sqrt{\xi_p^2 \mathcal{B}(r)^2 + \left(\frac{M_{\psi_1} r}{M_{sc}}\right)^2}}, \quad (3.78)$$

$$\widehat{y}_0(\xi_k, \xi_p, r) = \frac{1}{2 \mathcal{B}(r)^2 \xi_k \xi_p} \left(2 \sqrt{\xi_k^2 \mathcal{B}(r)^2 + \left(\frac{M_s r}{M_{sc}}\right)^2} \sqrt{\xi_p^2 \mathcal{B}(r)^2 + \left(\frac{M_{\psi_1} r}{M_{sc}}\right)^2} - \left(\frac{M_s r}{M_{sc}}\right)^2 \right), \quad (3.79)$$

$$\widehat{H}_1^s(\xi_k, \xi_p, r) = \sqrt{\xi_k^2 \mathcal{B}(r)^2 + \left(\frac{M_s r}{M_{sc}}\right)^2} - \sqrt{\xi_p^2 \mathcal{B}(r)^2 + \left(\frac{M_{\psi_1} r}{M_{sc}}\right)^2}, \quad (3.80)$$

$$\begin{aligned} \widehat{H}_2^s(\xi_k, \xi_p, r) = & \left(\sqrt{\xi_p^2 \mathcal{B}(r)^2 + \left(\frac{M_{\psi_1} r}{M_{sc}}\right)^2} \widehat{H}_1^s(\xi_k, \xi_p, r) + \xi_p^2 \mathcal{B}(r)^2 \right. \\ & \left. - \mathcal{B}(r)^2 \xi_p \xi_k \widehat{y}_0(\xi_k, \xi_p, r) - \left(\frac{M_{\psi_1} r}{M_{sc}}\right)^2 \right). \end{aligned} \quad (3.81)$$

Here, $s = h_1, h_2$ and M_s is the mass of the of the scalar under consideration. All of these functions (except \widehat{H}_2^s) have the same structural form as those in the expression of $\mathcal{C}^{h_2 \rightarrow Z_{BL} Z_{BL}}$ (i.e. Eqs. ((3.68)–(3.70))). The only difference is that the masses of the particles have been modified accordingly. This is because, if we look into the derivation of collision term as presented in the above section, we will see that these functions are mostly derived from kinematical conditions. The functions \widehat{H}_2^s (Eq. (3.81)) and H_2 (Eq. (3.71)) are however different since they depend on the dynamics of the processes concerned (i.e. the type of the interaction involved).

The limits of the integration are given by:

$$\widehat{\xi}_k^{\min}(\xi_p, r) = \frac{M_{sc}}{2 \mathcal{B}(r) r M_{\psi_1}} \left| \widehat{\eta}(\xi_p, r) - \frac{M_s^2 \times \mathcal{B}(r)}{M_{\psi_1} \times M_{sc}} \xi_p r \right|, \quad (3.82)$$

$$\widehat{\xi}_k^{\max}(\xi_p, r) = \frac{M_{sc}}{2 \mathcal{B}(r) r M_{\psi_1}} \left(\widehat{\eta}(\xi_p, r) + \frac{M_s^2 \times \mathcal{B}(r)}{M_{\psi_1} \times M_{sc}} \xi_p r \right) \quad (3.83)$$

where

$$\widehat{\eta}(\xi_p, r) = \left(\frac{M_s r}{M_{sc}} \right) \sqrt{\frac{M_s^2}{M_{\psi_1}^2} - 4} \sqrt{\xi_p^2 \mathcal{B}(r)^2 + \left(\frac{M_{\psi_1} r}{M_{sc}}\right)^2}. \quad (3.84)$$

Like the previous case, here also using Eqs. ((3.78)–(3.81)) we can simplify Eq. (3.77). The final expression (after putting in the numerical values of the internal degrees of freedom) for the collision term hence turns out to be:

$$\begin{aligned} \mathcal{C}^{s \rightarrow \bar{\psi}_1 \psi_1} &= \frac{r}{8\pi M_{sc}} \frac{\mathcal{B}^{-1}(r)}{\xi_p \sqrt{\xi_p^2 \mathcal{B}(r)^2 + \left(\frac{M_{\psi_1} r}{M_{sc}}\right)^2}} g_{s\bar{\psi}_1\psi_1}^2 (M_s^2 - 4M_{\psi_1}^2) \\ &\times \left(e^{-\sqrt{(\hat{\xi}_k^{\min})^2 \mathcal{B}(r)^2 + \left(\frac{M_s r}{M_{sc}}\right)^2}} - e^{-\sqrt{(\hat{\xi}_k^{\max})^2 \mathcal{B}(r)^2 + \left(\frac{M_s r}{M_{sc}}\right)^2}} \right). \end{aligned} \quad (3.85)$$

$$\mathcal{C}^{Z_{BL} \rightarrow \bar{\psi}_1 \psi_1}$$

The matrix element squared average for the decay mode $Z_{BL} \rightarrow \bar{\psi}_1 \psi_1$ is given by:

$$\overline{|\mathcal{M}|^2} \Big|_{Z_{BL} \rightarrow \bar{\psi}_1 \psi_1} = \frac{1}{3} \left((a_{\psi_1}^2 + b_{\psi_1}^2)(\tilde{p}_1 \cdot \tilde{p}_2) + 3M_{\psi_1}^2 (a_{\psi_1}^2 - b_{\psi_1}^2) + 2 \frac{(a_{\psi_1}^2 + b_{\psi_1}^2)}{M_{Z_{BL}}^2} (\tilde{p}_1 \cdot \tilde{k})(\tilde{p}_2 \cdot \tilde{k}) \right), \quad (3.86)$$

where \tilde{p}_1 and \tilde{p}_2 are the four momenta of the final state particles while \tilde{k} is the corresponding four momenta for the mother particle (Z_{BL}) and $\tilde{k} = \tilde{p}_1 + \tilde{p}_2$. The couplings $a_{\psi_1} = \frac{g_{BL}}{6} (1 - 3\sin^2 \theta_L)$ and $b_{\psi_1} = \frac{g_{BL}}{2} (1 + \sin^2 \theta_L)$. The masses of ψ_1 and Z_{BL} are M_{ψ_1} and $M_{Z_{BL}}$ respectively.

As before, the collision term has the following form:

$$\begin{aligned} \mathcal{C}^{Z_{BL} \rightarrow \bar{\psi}_1 \psi_1} &= \frac{1}{24\pi r} \frac{M_{sc}}{\sqrt{\xi_p^2 \mathcal{B}(r)^2 + \left(\frac{M_{\psi_1} r}{M_{sc}}\right)^2}} \times [\mathcal{B}(r)]^3 \times g_{Z_{BL}} g_{\psi_1} \times \\ &\int_{\tilde{\xi}_k^{\min}}^{\tilde{\xi}_k^{\max}} \frac{\xi_k^2 f_{Z_{BL}}(\xi_k, r) \mathcal{H}_2(\xi_k, \xi_p, r) d\xi_k}{\sqrt{\xi_k^2 \mathcal{B}(r)^2 + \left(\frac{M_{Z_{BL}} r}{M_{sc}}\right)^2} \mathcal{H}_1(\xi_k, \xi_p, r) \mathcal{F}(\xi_k, \xi_p, r)}. \end{aligned} \quad (3.87)$$

As expected, the functions \mathcal{H}_1 and \mathcal{F} in Eq. (3.87) are structurally quite similar to those in Eqs. ((3.68)–(3.70)) and Eqs. ((3.78)–(3.80)), since they arise from kinematical considerations. Only the masses will change in accordance with the particles involved. Thus we have:

$$\mathcal{F}(\xi_k, \xi_p, r) = \frac{\mathcal{B}(r)^2 \xi_k \xi_p}{\sqrt{\xi_k^2 \mathcal{B}(r)^2 + \left(\frac{M_{Z_{BL}} r}{M_{sc}}\right)^2} - \sqrt{\xi_p^2 \mathcal{B}(r)^2 + \left(\frac{M_{\psi_1} r}{M_{sc}}\right)^2}}, \quad (3.88)$$

$$\mathcal{Y}_0(\xi_k, \xi_p, r) = \frac{1}{2 \mathcal{B}(r)^2 \xi_k \xi_p} \left(2 \sqrt{\xi_k^2 \mathcal{B}(r)^2 + \left(\frac{M_{Z_{BL}} r}{M_{sc}} \right)^2} \sqrt{\xi_p^2 \mathcal{B}(r)^2 + \left(\frac{M_{\psi_1} r}{M_{sc}} \right)^2} - \left(\frac{M_{Z_{BL}} r}{M_{sc}} \right)^2 \right), \quad (3.89)$$

$$\mathcal{H}_1(\xi_k, \xi_p, r) = \sqrt{\xi_k^2 \mathcal{B}(r)^2 + \left(\frac{M_{Z_{BL}} r}{M_{sc}} \right)^2} - \sqrt{\xi_p^2 \mathcal{B}(r)^2 + \left(\frac{M_{\psi_1} r}{M_{sc}} \right)^2}. \quad (3.90)$$

To write down the exact analytical form of \mathcal{H}_2 defined in Eq. (3.87) in a compact way, it is useful to define some auxiliary functions first. They are:

$$\begin{aligned} G_1(\xi_k, \xi_p, r) = & \left(\sqrt{\xi_p^2 \mathcal{B}(r)^2 + \left(\frac{M_{\psi_1} r}{M_{sc}} \right)^2} \mathcal{H}_1(\xi_k, \xi_p, r) + \xi_p^2 \mathcal{B}(r)^2 \right. \\ & \left. - \mathcal{B}(r)^2 \xi_p \xi_k \mathcal{Y}_0(\xi_k, \xi_p, r) - \left(\frac{M_{\psi_1} r}{M_{sc}} \right)^2 \right), \end{aligned} \quad (3.91)$$

$$G_2(\xi_k, \xi_p, r) = \sqrt{\xi_k^2 \mathcal{B}(r)^2 + \left(\frac{M_{Z_{BL}} r}{M_{sc}} \right)^2} \sqrt{\xi_p^2 \mathcal{B}(r)^2 + \left(\frac{M_{\psi_1} r}{M_{sc}} \right)^2} - \mathcal{B}(r)^2 \xi_p \xi_k \mathcal{Y}_0(\xi_k, \xi_p, r), \quad (3.92)$$

$$G_3(\xi_k, \xi_p, r) = \sqrt{\xi_k^2 \mathcal{B}(r)^2 + \left(\frac{M_{Z_{BL}} r}{M_{sc}} \right)^2} \mathcal{H}_1(\xi_k, \xi_p, r) - \xi_k^2 \mathcal{B}(r)^2 + \mathcal{B}(r)^2 \xi_p \xi_k \mathcal{Y}_0(\xi_k, \xi_p, r). \quad (3.93)$$

Therefore using Eqs. ((3.91)–(3.93)) we have:

$$\begin{aligned} \mathcal{H}_2(\xi_k, \xi_p, r) = & (a_{\psi_1}^2 + b_{\psi_1}^2) G_1(\xi_k, \xi_p, r) + 2 \left(\frac{M_{\psi_1} r}{M_{sc}} \right)^2 (2 a_{\psi_1}^2 - b_{\psi_1}^2) \\ & + 2 \frac{(a_{\psi_1}^2 + b_{\psi_1}^2)}{\left(\frac{M_{Z_{BL}} r}{M_{sc}} \right)^2} G_2(\xi_k, \xi_p, r) G_3(\xi_k, \xi_p, r). \end{aligned} \quad (3.94)$$

However, using Eqs. ((3.88)–(3.90)), G_1 , G_2 and G_3 are greatly simplified :

$$G_1 = \frac{1}{2} \left(\frac{M_{Z_{BL}} r}{M_{sc}} \right)^2 - 2 \left(\frac{M_{\psi_1} r}{M_{sc}} \right)^2, \quad (3.95)$$

$$G_2 = G_3 = \frac{1}{2} \left(\frac{M_{Z_{BL}} r}{M_{sc}} \right)^2. \quad (3.96)$$

Consequently, \mathcal{H}_2 is also simplified to:

$$\mathcal{H}_2 = \left(\frac{M_{Z_{\text{BL}}} r}{M_{sc}} \right)^2 (a_{\psi_1}^2 + b_{\psi_1}^2) + 2 \left(\frac{M_{\psi_1} r}{M_{sc}} \right)^2 (a_{\psi_1}^2 - 2 b_{\psi_1}^2). \quad (3.97)$$

The limits of the integration are given by:

$$\tilde{\xi}_k^{\min}(\xi_p, r) = \frac{M_{sc}}{2 \mathcal{B}(r) r M_{\psi_1}} \left| \tilde{\eta}(\xi_p, r) - \frac{M_{Z_{\text{BL}}}^2 \times \mathcal{B}(r)}{M_{\psi_1} \times M_{sc}} \xi_p r \right|, \quad (3.98)$$

$$\tilde{\xi}_k^{\max}(\xi_p, r) = \frac{M_{sc}}{2 \mathcal{B}(r) r M_{\psi_1}} \left(\tilde{\eta}(\xi_p, r) + \frac{M_{Z_{\text{BL}}}^2 \times \mathcal{B}(r)}{M_{\psi_1} \times M_{sc}} \xi_p r \right). \quad (3.99)$$

where,

$$\tilde{\eta}(\xi_p, r) = \left(\frac{M_{Z_{\text{BL}}} r}{M_{sc}} \right) \sqrt{\frac{M_{Z_{\text{BL}}}^2}{M_{\psi_1}^2} - 4} \sqrt{\xi_p^2 \mathcal{B}(r)^2 + \left(\frac{M_{\psi_1} r}{M_{sc}} \right)^2}. \quad (3.100)$$

Finally, using Eqs. ((3.88)–(3.90)) and Eq. (3.97) in Eq. (3.87), we get:

$$\begin{aligned} \mathcal{C}^{Z_{\text{BL}} \rightarrow \bar{\psi}_1 \psi_1} &= \frac{r}{4 \pi M_{sc}} \frac{\mathcal{B}(r)}{\xi_p \sqrt{\xi_p^2 \mathcal{B}(r)^2 + \left(\frac{M_{\psi_1} r}{M_{sc}} \right)^2}} \times (M_{Z_{\text{BL}}}^2 (a_{\psi_1}^2 + b_{\psi_1}^2) + 2 M_{\psi_1}^2 (a_{\psi_1}^2 - 2 b_{\psi_1}^2)) \\ &\quad \times \int_{\tilde{\xi}_k^{\min}}^{\tilde{\xi}_k^{\max}} \frac{\xi_k f_{Z_{\text{BL}}}(\xi_k, r) d\xi_k}{\sqrt{\xi_k^2 \mathcal{B}(r)^2 + \left(\frac{M_{Z_{\text{BL}}} r}{M_{sc}} \right)^2}}. \end{aligned} \quad (3.101)$$

Unlike the previous cases, here the integration over ξ_k can not be analytically performed since, we do not apriori know the distribution function of Z_{BL} . The Boltzmann equation (Eq. (3.20)) has been solved for finding this $f_{Z_{\text{BL}}}$ and hence the integration has been done numerically.

Chapter 4

Indirect imprint of a non-thermal candidate : Boosted dark matter scenario

4.1 Introduction

In this chapter we will study the possibility of detecting (a non-thermal) dark matter indirectly via a small but energetic component (decay product of the non-thermal mother candidate) that is allowed within present-day constraints. Unlike in the previous two chapters where we calculated the relic density of the non-thermal dark matter (under different frameworks) in detail, here, we shift our focus to the indirect detection of the same. While theoretical biases have served as a guide for searches and model-building for dark matter, in principle, very little is known about its nature and properties. Specifically, the DM mass can span the range 10^{-15} – 10^{15} GeV, and its interaction cross-section with nucleons and annihilation cross-section into SM particles can lie in the range 10^{-76} – 10^{-41} cm².

Since the bulk of DM is known to be non-relativistic, its direct detection has focussed on its low-energy coherent scattering off nuclei, leading to nuclear recoils which have energies of a few keV, making them very challenging to detect over backgrounds. In general, most efforts have been directed towards exploring the parameter space spanned by thermal DM masses in the 10–100 GeV range with weak-scale interaction cross-sections with nucleons. Recent experiments have, however, significantly constrained this space for such particles (also called WIMPS).¹ When combined with results from indirect DM searches and colliders, it is fair to say that credible reasons for seriously considering “non-WIMP” and possibly non-thermal candidates for DM exist (for a review, see [185]). In

¹For recent reviews, see [184].

addition, we note that Big Bang Nucleosynthesis (BBN) constraints derived from the primordial Helium and Deuterium abundances [186], indicate that the number of effective relativistic species is $\Delta N_{eff}(T_{BBN}) < 0.85$ [25]. Constraints derived from observations of the Cosmic Microwave Background (CMB) by the Planck experiment [187] similarly favor the presence of some “dark radiation” over and above the three standard model neutrinos, with $\Delta N_{eff}(T_{CMB}) < 0.32$ [5]. Significantly, when combined, these two sets of constraints with very different origins rule out the presence of a full sterile neutrino, $\Delta N_{eff} = 1$ at $> 99\%$ C.L, whereas the absence of any additional neutrino coupled relativistic species is disfavoured at $> 98\%$ C.L. [186]. Relativistic non-thermal DM particles could be one possible way of resolving this [188].

The possibility that DM may be a multi-particle sector has, of course, been extensively studied in the literature under various assumptions. Due to the reasons mentioned above, it is possible that the bulk of this sector may comprise of a non-thermal (and non-relativistic) component, and may also contain a small component that may be relativistic and highly energetic. In what follows, we focus on the detection of DM via this latter component. Specifically, we explore the possibility of directly detecting (highly energetic) DM in existing large neutrino detectors at energies much higher than presently considered. After further motivating this idea, we explore its consequences qualitatively and quantitatively when specifically applied to the recently announced IceCube (IC) PeV events.

We note that coherent elastic neutrino-nucleus scattering [189], a process not yet experimentally observed due to the very small nuclear recoil measurement required to detect it, is expected to be an irreducible background for future DM direct detection experiments [190]. Thus DM and neutral current (NC) neutrino interactions mimic each other at low energies. One can expect that this analogy holds with rising energies, and in particular at the highest energies at which neutrinos are presently detected.

Here, we assume the heavy PeV dark matter to be primarily non-thermal. Unitarity bounds constrain particles with mass $m \gtrsim 300$ TeV to remain out of thermal equilibrium throughout its history as discussed in [191]. The bulk of DM is comprised of a very massive relic ϕ (with mass m_ϕ and a lifetime τ_ϕ greater than the age of the Universe) which decays preferentially to another much lighter DM particle χ (as opposed to decaying to standard model (SM) daughters). This leads to a small but significant population of ultra-high energy relativistic DM particles, non-thermally created in the narrow energy region spanning m_ϕ .

Drawing closely upon the similarity between neutrino NC and DM interactions, we further assume that χ interacts with SM particles with cross-sections much smaller than

standard weak interactions via the exchange of a heavy gauge boson which connects the SM and DM sectors. The assumption of a small strength interaction between DM and SM is of course empirically required, and the assumption about the existence of a heavy neutral gauge boson provides a simple way to implement it. At high energies, this will result in deeply inelastic interactions (DIS) of DM with SM particles, and mimic UHE neutrino-nucleon NC interactions [192, 193] in a detector like IC, creating cascades which are indistinguishable from those created by neutrinos. To summarise, the non-thermal heavy dark matter ϕ can be detected indirectly in IC through the direct observation of its decay product χ , the latter being a highly energetic sub-dominant dark matter candidate.

In what follows, we quantitatively implement the above proposal of looking for DM at high energies in neutrino detectors by performing a flux and cross-section calculation. While the approach is generic, it can be modified in specific ways to perform a broader and more general study, vis a vis choices of a mediator (scalar versus a vector boson, for instance), coupling strengths, masses etc. Our choices below are pertinent to our chosen application, which are the recently observed PeV IC events. We calculate the DM-nucleon cross section at high energies in analogy with the neutrino-nucleon NC cross-section. We then focus on the three PeV events in IC, and assuming that their cascades originate in DM interactions with ice nuclei, we determine the ramifications for DM mass and flux which result from this. Finally, we discuss the general features that would distinguish this scenario from others in which all the events in IC-like detectors are due to neutrino scattering.

4.2 Neutral-current scattering of a relativistic dark matter species with nuclei

We assume that the DM sector consists of at least two particle species with the following properties:

- A co-moving non-relativistic real scalar species ϕ , with a mass of $\mathcal{O}(10 \text{ PeV})$, which is unstable but decays with a very large lifetime to χ , and does not have any decay channels to SM particles. We call this (non-thermal) species the PeV Dark Matter (PDM), and it comprises the bulk of present-day DM.
- A lighter fermionic DM species (FDM), χ with mass $m_\chi \ll m_\phi$, which we assume is produced in a monochromatic pair when the PDM decays, *i.e.*, $\phi \rightarrow \bar{\chi}\chi$, each with

energies of $m_\phi/2$.²

The lifetimes for the decay of heavy DM particles to standard model species are strongly constrained ($\tau \gtrsim 10^{27}\text{--}10^{28}\text{s}$) by diffuse gamma-ray and neutrino observations [194, 195]. However, since in our scenario ϕ does not decay to SM particles, constraints relevant here are only those based on cosmology, which limits the total relativistic particle density of the universe at the respective epochs, independent of what those particles are, and are significantly weaker. Specifically, these include limits from the observed CMB anisotropies [196], light nuclei abundances during Big-Bang Nucleosynthesis (BBN) [121, 186] and from structure formation (see, *e.g.*, [197] for a review).³ Consistent with these constraints, and with present-day relic abundance considerations, we assume that the PDM decays with a lifetime of $\tau_\phi \gtrsim 10^{17}\text{s}$, *i.e.*, greater than the lifetime of the universe. Additionally, the lighter (and stable) FDM species is assumed to be produced only non-thermally, via the decay of the long-lived PDM. Its contribution to the DM mass density is thus expected to be small.

The FDM flux is composed of galactic and extragalactic components of comparable magnitudes [198]. Thus, the total flux $\Phi = \Phi^G + \Phi^{\text{EG}}$, where, Φ^G and Φ^{EG} respectively represent the galactic and extra-galactic components of this flux [198, 199]):

$$\Phi^G = \int_{E_{\min}}^{E_{\max}} dE_\chi D_G \frac{dN_\chi}{dE_\chi}, \quad (4.1)$$

and,

$$\Phi^{\text{EG}} = \frac{\Omega_{DM} \rho_c}{4\pi m_\phi \tau_\phi} \int_{E_{\min}}^{E_{\max}} dE_\chi \int_0^\infty dz \frac{1}{H(z)} \frac{dN_\chi}{dE_\chi} [(1+z)E_\chi] \quad (4.2a)$$

$$= D_{\text{EG}} \int_{E_{\min}}^{E_{\max}} dE_\chi \int_0^\infty dz \frac{1}{\sqrt{\Omega_\Lambda + \Omega_m(1+z)^3}} \times \frac{dN_\chi}{dE_\chi} [(1+z)E_\chi], \quad (4.2b)$$

with

$$D_G = 1.7 \times 10^{-8} \left(\frac{1 \text{ TeV}}{m_\phi} \right) \left(\frac{10^{26} \text{ s}}{\tau_\phi} \right) \text{ cm}^{-2} \text{ s}^{-1} \text{ sr}^{-1}$$

²As mentioned above, the choice of a PeV scale mass for DM and subsequent choices of couplings and a mediator is based on our application below to recent IC events, but they are representative of a concept that may have broader applicability.

³BBN is also sensitive to the electron-positron pair production rate in DM annihilation, but for both the PDM and FDM these interaction strengths are tiny.

and

$$D_{\text{EG}} = 1.4 \times 10^{-8} \left(\frac{1 \text{ TeV}}{m_\phi} \right) \left(\frac{10^{26} \text{ s}}{\tau_\phi} \right) \text{ cm}^{-2} \text{ s}^{-1} \text{ sr}^{-1}.$$

Here, z represents the red-shift of the source, $\rho_c = 5.6 \times 10^{-6} \text{ GeV cm}^{-3}$ denotes the critical density of the universe, and we have used $H(z) = H_0 \sqrt{\Omega_\Lambda + \Omega_m(1+z)^3}$, and $\Omega_\Lambda = 0.6825$, $\Omega_m = 0.3175$, $\Omega_{DM} = 0.2685$ and $H_0 = 67.1 \text{ km s}^{-1} \text{ Mpc}^{-1}$ from the recent PLANCK data [187]. For the two-body decay $\phi \rightarrow \bar{\chi}\chi$

$$\frac{dN_\chi}{dE_\chi} = 2\delta \left(E_\chi - \frac{1}{2}m_\phi \right), \quad (4.3)$$

where, E_χ denotes the energy of each of the produced χ particle.

The FDM interacts with the nucleus within the IceCube detector via a neutral current interaction mediated by a beyond-SM heavy gauge boson, Z' (Fig. 4.1(a)) that couples to both the χ and quarks and gluons.

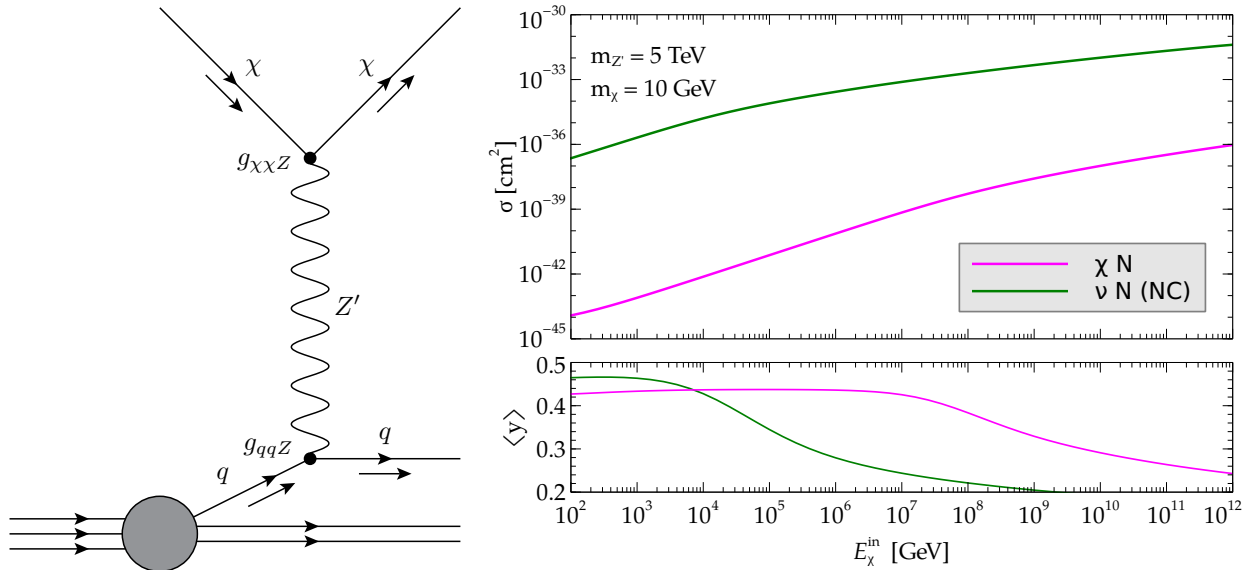


Figure 4.1: (a) Interaction of the incoming TeV mass DM particle χ with a nucleus, mediated by a heavy non-standard boson Z' . (b) The χN DIS interaction cross-section and the corresponding $\langle y(E) \rangle$ are shown for the benchmark value of m_χ and $m_{Z'}$. The overall normalisation to the χN cross-section is set by the product of coupling constants G , and is here arbitrarily chosen to be $G = 0.05$. The real magnitude of G will be determined by comparing event rates to those seen at IC in the succeeding section. For comparison, the νN neutral current cross-section and the corresponding $\langle y \rangle$ are also shown.

For both the $\chi\chi Z'$ and qqZ' interactions we assume the interaction vertex to be vector-like, with hitherto undetermined coupling constants $g_{\chi\chi Z}$ and g_{qqZ} respectively.⁴ The DIS cross-section for $\chi N \rightarrow \chi X$ is then computed in the lab-frame, with the product $G = g_{\chi\chi Z} g_{qqZ}$ as the undetermined parameter, over a broad range of incoming FDM energies, $100 \text{ GeV} \leq E_\chi^{\text{in}} \leq 10 \text{ PeV}$, using tree-level CT10 parton distribution functions [202]. We set the Z' mass to be 5 TeV. For Z' with mass $\geq 2.9 \text{ TeV}$, the couplings $g_{\chi\chi Z}$ and g_{qqZ} are largely unconstrained by collider searches [203], thus are limited only by unitarity. We note here that due to the presence of $\chi\chi Z'$ vertex, the possibility that Z' -bremsstrahlung affects the two-body $\phi \rightarrow \chi\chi$ decay and thus the energies of the outgoing χ -particles becomes worth considering. We have verified by means of explicit calculations that, for the value of the parameters G^2 and τ_ϕ that we require in order to fit the predicted events from χN NC scattering with IC observations (see section 4.3.3), Z' bremsstrahlung-included decay rate is about 5% of the total decay rate and therefore negligible. A presentation of the full computation is beyond the scope of this work, but closely follows a similar computation made in [204].

Since the IC can only measure the deposited energy E^{dep} for neutral current events, it is important to determine the nature of the inelasticity parameter, relating the deposited energy to the incoming particle energy (E_χ^{in}):

$$y = \frac{E_\chi^{\text{in}} - E_\chi^{\text{out}}}{E_\chi^{\text{in}}} = \frac{E^{\text{dep}}}{E_\chi^{\text{in}}}, \quad (4.4)$$

where, E_χ^{out} represents the energy of the outgoing χ in the scattering process. The DIS differential cross-section with respect to the inelasticity parameter is then expressed as

$$\frac{d\sigma}{dy}(E_\chi^{\text{in}}, y) = G^2 f(E_\chi^{\text{in}}, y). \quad (4.5)$$

The results for the total cross-section and the mean inelasticity parameter,

$$\langle y(E_\chi^{\text{in}}) \rangle = \frac{1}{\sigma(E_\chi^{\text{in}})} \int_0^1 dy y \frac{d\sigma(E_\chi^{\text{in}}, y)}{dy},$$

are shown in Fig. 4.1(b).

⁴We have deliberately tried to avoid limiting the scenario to any particular theoretical model in order to focus solely on the phenomenological signatures of the two-sector DM that we have discussed here. Theoretical models that encompass our DM spectrum have been discussed in the literature in terms of Z or Z' portal sectors with the Z' vector boson typically acquiring mass through the breaking of an additional $U(1)$ gauge group at the high energies (see *e.g.*, [200, 201]).

4.3 The IC events: Characteristics and possible Origins

4.3.1 IceCube : Preliminaries

IceCube is the largest neutrino observatory in the world. It has been build at the geographic South Pole with a total instrumented volume of 1km^3 . It consists of 86 strings with a separation of 125m between them. Extremely high energy neutrinos will hit the ice nucleus thereby shattering them (Deep Inelastic Scattering, DIS) producing large amounts of hadronic secondary charged particles which radiate Cherenkov light. To detect these Cherenkov radiations Digital Optical Modules (DOMs) are placed on each of the 86 strings at a separation of 17m between 1450m and 2450m below the ice surface. An example of a DOM is shown in Fig. 4.2. The detector is designed to detect neutrinos with



Figure 4.2: Digital Optical Modules used for detecting Cherenkov radiations in IceCube [13].

deposited energy of 100 GeV or greater. The DOMs transform the Cherenkov light to electric signals using photoelectric effect. These are then digitized and sent to IceCube research facility for further analysis. In Fig. 4.3, we provide a schematic picture of IceCube detector along with its prototype AMANDA. The DeepCore is a small region within the detector which has more closely placed strings (thereby increasing the resolution). It is targeted to measure atmospheric neutrinos with a lower energy threshold of 10 GeV.

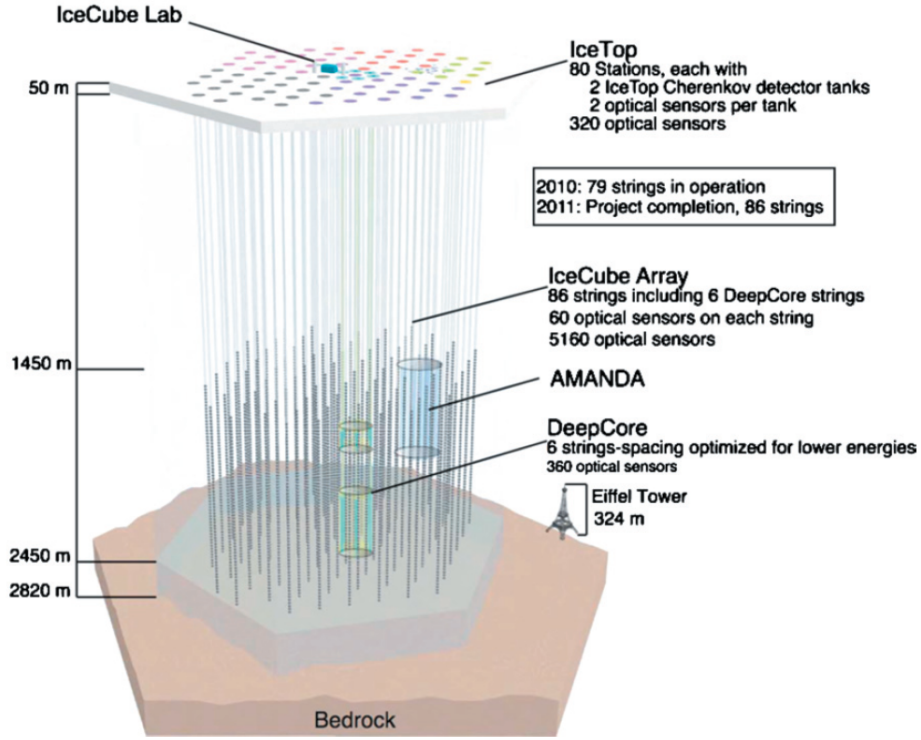


Figure 4.3: A layout of IceCube experimental facility at South Pole. The thin grey vertical lines are the 86 strings that are studded with the DOMs. The instrumentation begins from a 1450m below the surface where ice is relatively clear and free from dust particles. AMANDA and DeepCore are also shown in the figure [13].

4.3.2 988 days of IC data and some of its features

Prior to applying our proposal, we recapitulate the basic observations and features of the IC data below.

The observation of ultra-high energy (UHE, $E_\nu \geq 30$ TeV) neutrino events at IceCube (IC) [14, 205] is one of the most striking of recent experimental results in all of physics. When statistically buttressed by imminent additional observations by IC and other high energy neutrino observatories like ANTARES [206], AUGER [207] and the upcoming KM3NET [208] they promise to open hitherto unprecedented windows of understanding on the highest energy processes in our Universe.

IceCube is sensitive to high energy neutrinos via their electroweak charge and neutral current (CC and NC respectively) deep inelastic (DIS) interactions with nucleons in ice, which result in the deposition of detectable energy in the form of Cerenkov radiation. An

event may thus be classified as :

- *a track*, produced by ν_μ CC and a subset of ν_τ CC interactions (where a produced τ decays to a μ) , characterized by a highly energetic charged lepton traversing a significant length of the detector. Energy reconstruction (i.e. reconstructing the energy of the incoming particle from the knowledge of its deposited energy) is poor for a track like event. But a lot can be concluded about the directionality of the incoming particle. Fig. 4.4 shows an actual event record (left) and a schematic diagram for a cascade time event.

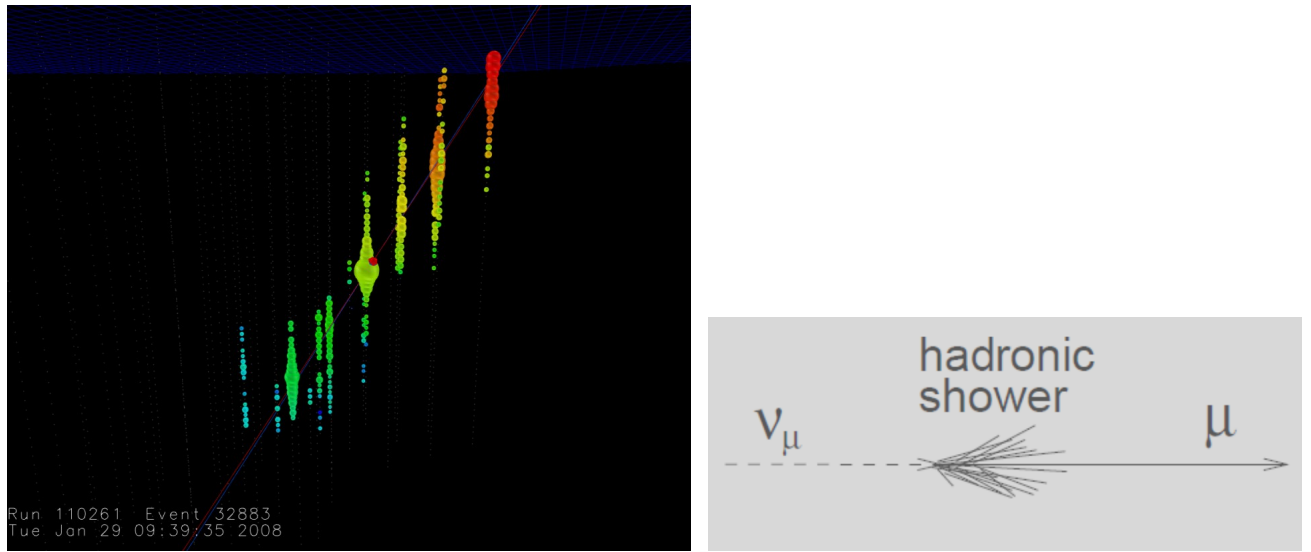


Figure 4.4: **Left** : A track like event record from IceCube. The color coding helps us to understand the temporal behaviour. Red means earliest point of entry, while blue represents latest. We can see that the muon has lit up the DOMs as it passed through the strings. **Right** : A schematic diagram for a track.

- *a cascade*, produced by either i) ν_e CC interactions, ii) a subset of ν_τ CC interactions or iii) NC interactions of all three flavours. Cascades are characterized by their light deposition originating from charged hadrons and leptons, distributed around the interaction vertex in an approximately spherically shaped signature. Such an event is depicted in Fig. 4.5. Since almost all of the energy carrying by the particle is deposited in the detector, energy reconstruction is much better for these events. However they have very poor information about the directionality of the charged particle.

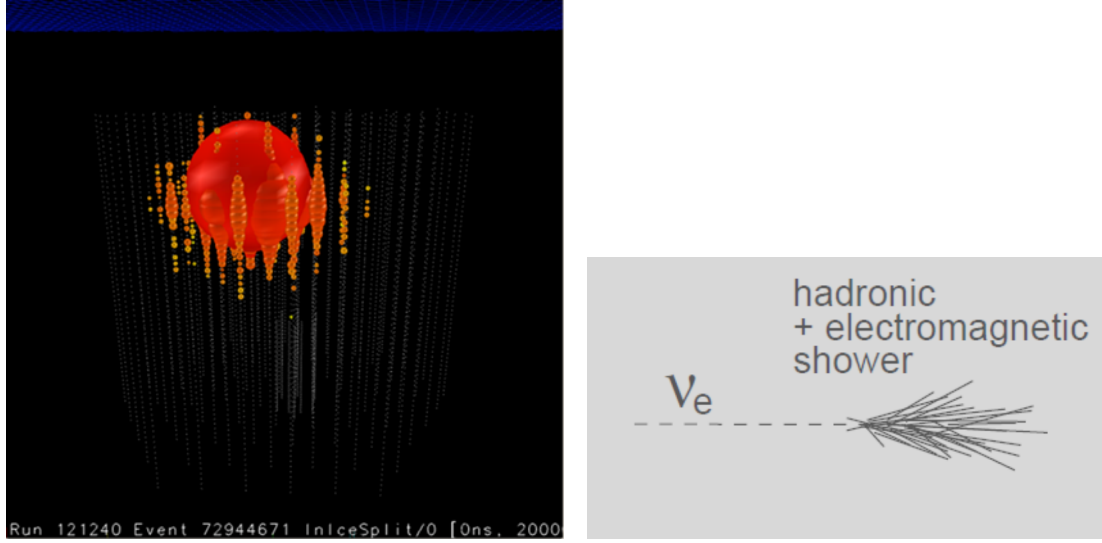


Figure 4.5: **Left** : A cascade like event record from IceCube. . **Right** : A schematic diagram for the same.

This classification allows us to categorize most events. There are other, potentially important types of events, however, which have not yet been observed; *e.g.* the *double bang* events signalling the CC production of a highly energetic τ lepton [209] (see Fig. 4.6), and the *pure muon* and *contained lollipop* [210] events which would unambiguously signal the detection of the Glashow resonance [192, 211, 212].

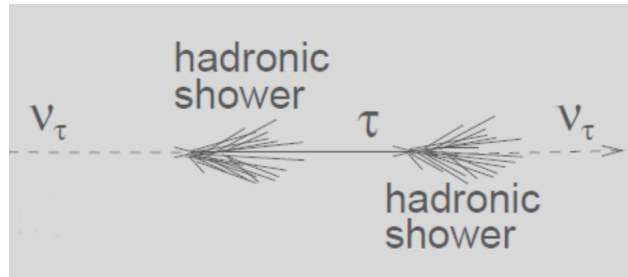


Figure 4.6: A schematic diagram of a double bang event as produced by a τ lepton.

Additionally, in spite of the belief that sources do not produce ν_τ , the flavour ratios for neutrinos are rendered close to 1 : 1 : 1 at earth due to oscillations over large distance scales. In this situation, cascade events are expected to constitute about 75–80% of the total observed sample [213]. The background to these events is provided by the rapidly falling atmospheric neutrino flux and the muons created in cosmic-ray showers in the atmosphere.

The 988-day IC data reveals 37 events (9 track, 28 cascades) with energies between 30

TeV and 2 PeV, consistent with a diffuse neutrino flux given by

$$E^2 \phi_\nu(E) = 0.95 \pm 0.3 \times 10^{-8} \text{ GeV cm}^{-2} \text{ s}^{-1} \text{ sr}^{-1}, \quad (4.6)$$

in the energy range 60 TeV–3 PeV, where ϕ_ν represents the per-flavor flux. A purely atmospheric/cosmic-ray shower origin of these events is rejected at the 5.7σ level. The events are shown in Fig. 4.7.

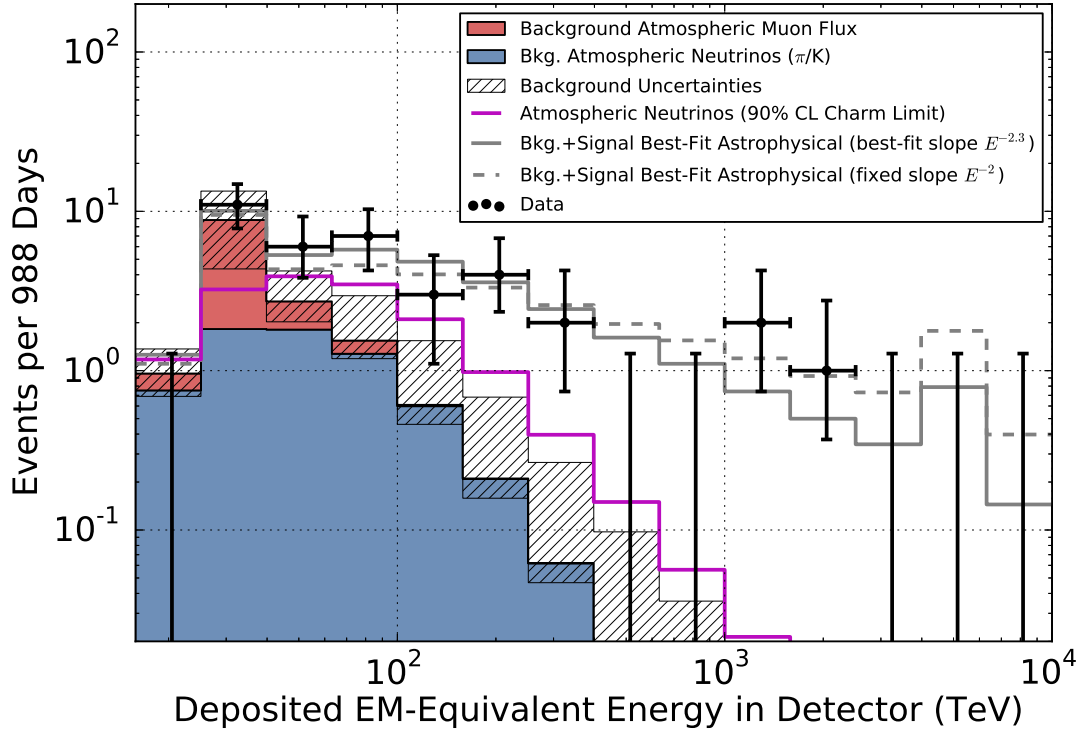


Figure 4.7: IC events for 988 days of data collection. The background arising from atmospheric neutrinos is shown in blue shaded and brick red region. The grey and the dashed grey curves are the IC astrophysical best-fit. The latter predicts events in the high energy bins in contrast to what observed [14].

We mention three characteristics of the event sample which will be pertinent to us below: *a)* the three highest energy events are closely clustered, with energies of 1 PeV, 1.1 PeV and 2.1 PeV, *b)* there are no events between 400 TeV and 1 PeV, a gap which can be statistically realised in 43% of continuous power-law spectrum predictions [14, 205], and *c)* there are no events beyond 2 PeV, although 3 events are expected between 3–10 PeV for an unbroken E^{-2} spectrum.⁵

⁵This expectation is due to the Glashow resonance [210, 214, 215].

The precise origin of these events is as yet unknown. There is weak evidence of a slight Galactic bias in the directionality, but the overall distribution over the entire sample is consistent with a diffuse isotropic flux. Possible astrophysical sources including both from within our galaxy [216–222] and from outside the galaxy [223–230] have been considered as explanations for the origin of these high energy particles. Some models of astrophysical sources, *e.g.*, for galaxy clusters [231] and starburst galaxies [232], also predict a break in the neutrino spectrum at energies above ~ 1 PeV consistent with IC observations. In addition, the possibility that such UHE events might originate from the decay/annihilation of super-heavy DM into standard model particles has also been investigated [199, 233–236].

4.3.3 PeV events: Fitting the DM-prediction to the IC observation

We next determine the values of the parameters G^2 and τ_ϕ that fits the number of DM events from our prediction with the IC PeV events. The energy at which the χ flux should peak is determined by requiring that the event rates peak at around 1.1 PeV; in turn, this requires that the flux peak at around energies of

$$E_{\text{peak}} = 1.1 / \left[\langle y \rangle \big|_{E_\chi^{\text{in}}=1.1 \text{ PeV}} \right] = 2.53 \text{ PeV},$$

which implies, $m_\phi = 5.06 \text{ PeV}$.

The total number of events in a given IC bin increases proportionally with the incident flux and the interaction rate of the incident particles with the ice nuclei relevant to the corresponding bin energies. Since, in addition, the FDM flux $\Phi \propto \tau_\phi^{-1}$ [Eq. (4.1) and (4.2)] and $d\sigma/dy \propto G^2$ [Eq. (4.5)], the ratio G^2/τ_ϕ of the undetermined parameters G and τ_ϕ can be ascertained by normalising the number of events predicted due to the FDM flux at deposited energies $E^{\text{dep}} \geq 1 \text{ PeV}$ against those seen at the IC. We find that for a reasonable decay lifetime of $\tau_\phi = 5 \times 10^{21} \text{ s}$, we need to set $G = 0.047$ to obtain the 3 PeV+ events from the FDM flux seen over the 988-day IC runtime. The values of the parameters thus determined are well within the allowed parameter-space, given constraints on the coupling constant from perturbativity and on the lifetime from model independent considerations for heavy DM decaying to relativistic particles: $\tau_\phi \geq 10^{18} \text{ s}$ [237]. The corresponding nature of the FDM extragalactic flux is shown in Fig. 4.8. The bigger the value of τ_ϕ , the larger would G need to be, to match the IC PeV+ event rate, with the upper bound to the coupling constant and, by consequence, the upper bound to τ_ϕ , being set by unitarity limits on G .

4.3.4 Sub-PeV Events: Neutrinos from extra-galactic sources

While the events corresponding to deposited energies $E_{\text{dep}} \geq 1$ PeV are accounted for by the FDM flux, the sub-PeV events up to 400 TeV are consistent with a power-law flux of incident particles, and are, likely, representative of a diffuse flux of neutrinos from extragalactic sources. The term “best-fit” has limited validity at this point in time since given the limited statistics, it is at present unclear if the flux is truly diffuse and extragalactic, or a superposition of individual extended sources or a combination of these alternatives [238]. Indeed, using only the sub-PeV events to determine the best-fit $E^{-\alpha}$ spectrum, we find that the IC observation is closely matched by a more steeply falling astrophysical flux spectrum than that in Eq. (4.6), *i.e.*, the best-fit is instead given by (Fig. 4.8)⁶

$$d\Phi_{\text{astro}}/dE_{\text{in}} = 1.21 \times 10^{-3} E^{-3.0} \text{ GeV}^{-1} \text{ cm}^{-2} \text{ s}^{-1} \text{ sr}^{-1}. \quad (4.7)$$

We note here that while Eq. (4.7) represents the best possible fit to the sub-PeV events

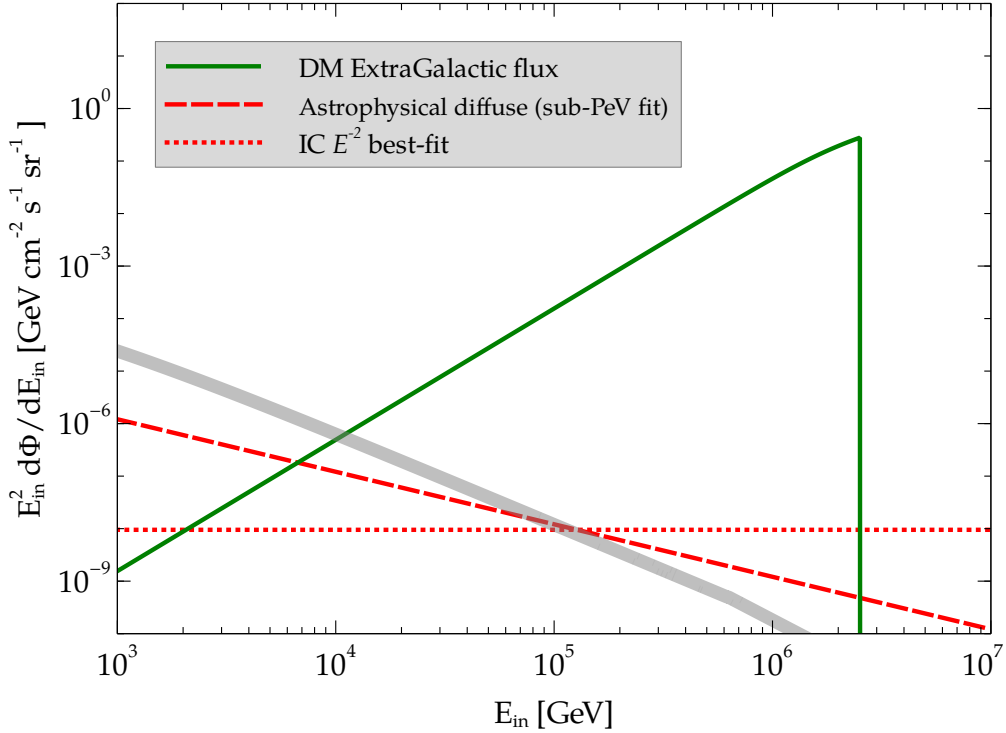


Figure 4.8: The TeV-scale diffuse neutrino flux and the extra-galactic FDM flux at PeV+ energies for decay lifetime $\tau_\phi = 5 \times 10^{21}$ s. The thick light-gray curve indicates the estimated conventional atmospheric $\nu_\mu + \bar{\nu}_\mu$ flux.

⁶Theoretically we can encounter a flux spectrum that is softer than E^{-2} .

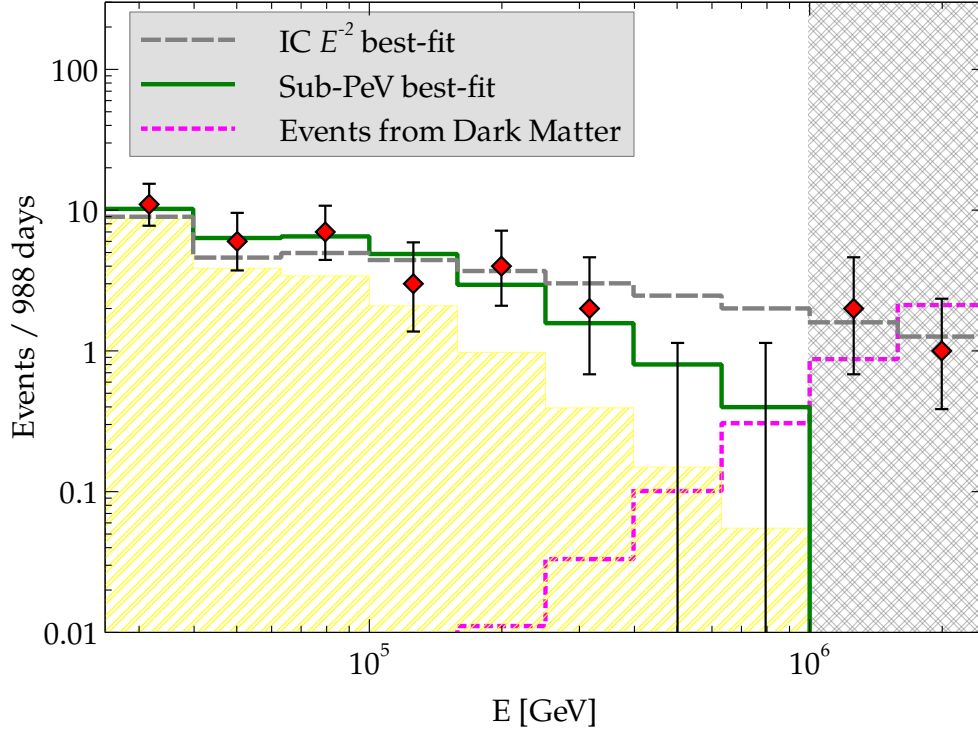


Figure 4.9: Predicted and observed total event rates at the IceCube. The gray shaded region represents energies at which we expect events predominantly from the DM sector. The green line shows event-rate predictions from our best fit flux to the sub-PeV event-rates observed at IC, with the flux given by Eq. (4.7). The event rates predicted due to the IC best-fit E^{-2} flux (gray dashed line) and the observed data (red diamonds) are shown. The IC-estimate for the atmospheric background events is shown as the yellow shaded region.

from a power-law, any soft spectra with index $\alpha \leq 2.5$ and appropriate normalization would be compatible with the data, within a 1σ confidence level, although with slightly poorer goodness-of-fit measures. Due to the softness of the spectral shape, the astrophysical flux drops to below the single-event threshold at energies higher than 400 TeV, rendering it naturally consistent with the lack of events at subsequent energies up to the PeV. The FDM flux itself does not contribute appreciably to the sub-PeV event-rate (see figure 4.9).

We note here that the gap in the event-spectrum between 400 TeV–1 PeV is not yet statistically significant and, therefore, a diffuse astrophysical flux with less steep spectra $\alpha \approx 2$ –2.3 would also be consistent with the sub-TeV event-spectra should this gap fill up in the future.

4.4 Discussion and Conclusions

Given present-day constraints on DM, it is possible that it may not be WIMP-like and thermal in nature. In the scenario proposed in this chapter, we have focussed on the possible direct detection of high energy DM particles. Such particles cannot form the bulk of DM, which must be non-relativistic, but may be a small population that lends itself to detection via methods different from those currently implemented at current DM detectors. One possible way such a component could exist at and around a specific high energy, would be due to its creation by the decay of another significantly more massive non-thermal DM relic. If the lighter DM particle interacts with nucleons, its cross-section at high energies may be detectable as neutrino-like cascades in a massive detector like IC. Using the neutrino-nucleon NC deep inelastic cross-section as a guiding analogy, we have applied this to the cluster of three \sim PeV events seen at IC.

Thus, this cluster of three events has a different origin from the remainder of the IC event sample, which we assume to be primarily astrophysical extra-galactic neutrinos. It results in a softer astrophysical spectral best-fit than the one which includes the full-event sample. In this picture, the gap currently seen in the data between 400 TeV–1 PeV is physical, and the result of two distinct spectra. While it may partially get filled in or otherwise modified due to future data, it would remain as a demarcating feature between 2 fluxes of different origins, a UHE neutrino flux with a softer than currently estimated spectrum, and a DM flux that generates cascade interactions in the detector. Additionally, the PeV events should continue to cluster in the 1–3 PeV region, with a galactic bias [199] due to the fact that about half of the DM induced PeV flux contribution is expected to be galactic. We note that at present 2 of the 3 events appear to come from the direction of the galaxy. This scenario also provides a natural explanation for the lack of events beyond 3 PeV. Other recent proposals, in addition to certain models of astrophysical sources referred to previously, which also account for the cut-off at PeV energies are discussed in [233, 234, 239–243].

It is also to be noted that DM induced events will for the most part not contain energetic muon tracks, and will mostly be cascade-like. Thus, over time, if the IC sample contains a mixture of such events along with an astrophysical neutrino event component, the overall data will manifest a deficit in the ratio of muon track to cascades compared to the standard IC expectation of 1 : 3.

Additionally, for DM events in the 1–3 PeV range, some extra-galactic contribution of cascades could come from the Northern hemisphere, because the lower DM-matter cross-section does not cause their flux to attenuate significantly in the earth at PeV energies,

unlike neutrinos. These predictions separate the present scenario from other DM induced indirect detection proposals [233, 234]), and can be tested as IC gathers more data.

In conclusion, we have studied the possibility of detecting DM using large neutrino detectors, via a relativistic and high energy component that may exist in addition to the bulk of non-relativistic (and non-thermal) DM. As a specific example of the concept, we have applied it to recent events reported by IC, and also pointed out testable features of the scenario which can be used, with future data, to rule it out.

Chapter 5

Boosted Dark matter and IceCube : Detailed analysis

5.1 Introduction and Motivation

In this chapter, we shall begin with a summary of the 1347-day IceCube (IC) high-energy starting event (HESE) neutrino data, focussing on events with deposited energies greater than around 30 TeV, and discuss some of its features, especially those that are of particular interest for this study. We shall then introduce two possible scenarios of boosted dark matter, which, in combination with a power-law astrophysical flux, can provide a good fit to these features. In the previous chapter we briefly introduced the concept of a boosted dark matter scenario and how can it explain the IceCube ultra-high energy PeV events. There we worked with 988 days of data unlike in this chapter where we have used 1347 days of data. Also, in this chapter, we extend our boosted dark matter scenario not only to explain the PeV events, but also some sub-PeV excesses as well (details later).

5.1.1 IceCube High Energy Starting Events (HESE) and features of the 1347-day data

The observation of 54 HESE (*i.e.*, events with their νN interaction vertices inside the detector) [15, 244], with deposited energies between 30 TeV to a maximum energy of 2.1 PeV by the IceCube experiment (IC) has opened an unprecedented window to the universe at high energies.¹ The data constitute an approximately 7σ signal in favour of a

¹ In addition to the analysis presented by the IceCube collaboration in [15, 244], a recent analysis of the HESE data may be found in [245].

non-atmospheric and extra-terrestrial origin of the events.² It is generally believed, but not conclusively known, that the highest energy cosmic rays ($E \geq 10^6$ GeV), for which observations now extend to $E \sim 10^{11}$ GeV, and ultra-high energy (UHE) neutrinos with energies greater than $\mathcal{O}(20)$ TeV, share common origins and are produced by the same cosmic accelerators. The specific nature of these accelerators, however, remains unknown, although over the years, anticipating their detection, several classes of highly energetic cosmic astrophysical sources have been studied as possible origins of these particles. For general discussions of this topic, we refer the reader to [246–256].

Subsequently, based on the recent IC data, many authors have considered a host of source classes and possibilities for explaining both the origin and some emerging spectral features in the IC data. These efforts have been motivated, at least in part, by evidence that the data, to an extent, diverge from expectations. The considered candidate sources include gamma-ray bursts [230,256–265], star-burst galaxies [225,266–269], active galactic nuclei [228,270–278], remnants of hyper-novae [279] and of supernovae [280], slow-jet supernovae [281], microquasars [282], neutron star mergers [283], blackholes [284], cosmic-ray interactions [220,285–290], the galactic halo [216], galaxy clusters [291], dark matter decay [233,234,292–306], and exotic particles, processes or possibilities [240–242,307–323].

It is generally accepted, however, that the charged particles in a source which link the acceleration of cosmic-rays to the acceleration of astrophysical neutrinos attain their high energies via Fermi shock acceleration [324], and as a generic consequence, the neutrinos resulting from them are expected to follow a E^{-2} spectrum [246,247]. Some variation from this general spectral behaviour may occur, however, depending on the details of the source, as discussed, for instance, in [325].

We now describe the significant features of 1347 days of the HESE data (Fig. 5.1), some of which are fairly firm even at the present level of statistics, and others which, while interesting and suggestive, are emergent and need further confirmation via more observations before they can be considered as established. (We note that the energies quoted below refer to those deposited by the primary in IC.)

- The data, to a high level of significance (about 7σ , as mentioned earlier), indicate that above a few tens of TeV, the sources of the events are primarily non-atmospheric and extra-terrestrial in nature.

²The statistical significance is dependent upon the largely theoretically modelled upper limits of the prompt neutrino flux from heavy meson decays. The 7σ value corresponds to the scenario where the prompt flux is assumed to be absent. Nonetheless, even with the highest upper limits from present computations, the statistical significance of a new signal over and above the atmospheric background is well above 5σ .

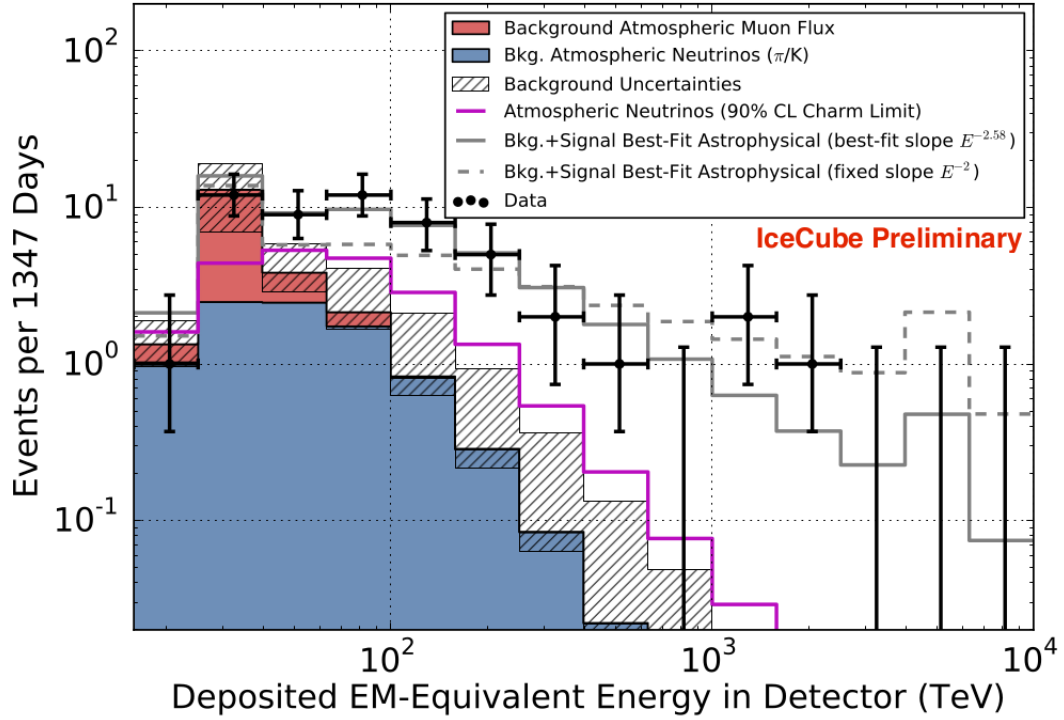


Figure 5.1: IC events for 1347 days of data collection. The background arising from atmospheric neutrinos is shown in blue shaded and brick red region. The grey and the dashed grey curves are the IC astrophysical best-fit. The latter predicts events in the high energy bins in contrast to what observed [15].

- Due to the lack of multi-PeV events, including those from the Glashow Resonance [210, 214, 215] in the range 6-10 PeV, a single power-law fit to the flux underlying the observed events now disfavors the expected spectral index from Fermi shock acceleration considerations, $\gamma = -2$, by more than 4σ . Indeed, for an assumed E^{-2} spectrum, and with the corresponding best-fit normalization to the flux, about 3 additional cascade events are expected between 2 PeV and 10 PeV, largely due to the expected presence of the Glashow resonance. However, in spite of IceCube's high sensitivity at these energies, none have been observed thus far. The present best fit value of γ is consequently significantly steeper, being around $\gamma = -2.58$ [15, 326].
- The data, when subjected to directional analyses [15, 199, 217–219, 293, 327–336], at its present level of statistics, is compatible with an isotropic diffuse flux, although several studies among the ones cited above indicate the presence of a small galactic bias. The accumulation of more data will be able to ascertain whether the galactic

bias is real, in which case it would imply important (and possibly new) underlying physics.

- The three highest energy events [15], with the estimated (central value) of the deposited energies of 1.04 PeV, 1.14 PeV and 2.0 PeV are all cascade events from the southern hemisphere. At these energies, *i.e.* $E_\nu \gtrsim 1$ PeV, the earth becomes opaque to neutrinos, thus filtering out neutrinos coming from the northern hemisphere.
- Below 1 PeV, there appears to be a dip in the spectrum, with no cascade events between roughly 400 TeV and 1 PeV.³
- At lower energies, in the approximate range of 50 – 100 TeV, there appears to be an excess, with a bump-like feature (compared to a simple power-law spectrum), which is primarily present in events from the southern hemisphere [338]. The maximum local significance of this excess is about 2.3σ , which is obtained when the lowest estimates for the conventional atmospheric neutrino background is adopted, with the prompt component of the background assumed to be negligible [339].
- Finally, and importantly, the data when interpreted as being due to a single astrophysical power-law neutrino flux, appears to require an unusually high normalization for this flux, which is at the level of the Waxman-Bahcall (WB) bound [340,341] for neutrino fluxes from optically thin sources of high energy cosmic rays and neutrinos. This is an aspect that is difficult to understand within the confines of the standard interpretive mechanism, which connects ultra-high energy neutrino fluxes to observations of the highest energy cosmic-rays⁴.

5.1.2 Deep Inelastic Scattering of Boosted Dark Matter in IceCube

As proposed in [295], if there is a source of long-lived, highly relativistic and energetic neutral particles in the present Universe which can interact with quarks or gluons, the signal produced by them in IceCube would, in all likelihood, be indistinguishable from the NC DIS cascade of a neutrino primary. To the extent that the astrophysical neutrino flux is expected to follow a simple power-law behaviour, one could argue that features

³A recent analysis [337] statistically reinforces the presence of a break in the spectrum in the region 200 - 500 TeV, which could have a bearing on this feature.

⁴The WB bound is valid for sources which produce neutrinos as a result of pp or $p\gamma$ interactions. It assumes that they are optically thin to proton photo-meson and proton-nucleon interactions, allowing protons to escape. Such sources are characterized by an optical depth τ which is typically less than one. As explained in [341], the bound is conservative by a factor of $\sim 5/\tau$.

in the HESE data (as described in the previous subsection) which deviate from this, such as statistically significant excesses, spectral breaks or line-like features, could indicate the presence of such a particle⁵. Although there are strong constraints on the presence of additional relativistic degrees of freedom during the epochs of recombination and big bang nucleosynthesis, such particles might be injected at later times by the slow decay of a heavy particle, which, overall, is the approach we adopt here.

We consider the case where this heavy particle constitutes a significant part of the dark matter (DM) density of the Universe. Its late-time decay produces a highly energetic flux of light dark matter (LDM) particles, which can then give rise to a subset of the NC DIS events at IC. We note that this is different from the scenario where the heavy dark matter (HDM) particle directly decays to standard model particles, leading to a neutrino flux in IC, as discussed in, for instance [233, 234, 292–294, 296, 297, 299–301, 303–306, 342]. In the scenario(s) discussed here, in order to have NC DIS scattering with nuclei, the LDM particles need to couple to the SM quarks (or gluons) with appropriate strength. It is then possible that these interactions could keep them in chemical equilibrium with the SM sector in the early Universe. Thus, the standard thermal freeze-out mechanism will give rise to a relic density of the LDM particles as well in the present Universe, though the exact value of their present-day density would in general depend upon all the annihilation modes open and the corresponding annihilation rates. It is important to note that the couplings relevant for the IC analysis provide only a lower bound on the total annihilation rate. For our purpose, the precise relic density of LDM is not of particular relevance, and we simply need to ensure that it annihilates sufficiently fast in order not to overclose the Universe, while its relic abundance should not be too high, in order to allow for a sufficient HDM presence in the universe. The latter is needed to produce enough of the relativistic LDM flux from its late time decays. In other words, scenarios where the LDM abundance is small are preferred but not required. Similarly, for phenomenological analysis of the IC data, the production mechanism of the HDM particle does not play any essential role. Therefore, we abstain from discussing specific cosmological models for HDM production in this article, and instead refer the reader to possibilities discussed in Refs. [343–346]. We further note that general considerations of partial-wave unitarity of scattering amplitudes imply an upper bound on the mass of any DM particle that participates in standard thermal equilibrium production processes and then freezes out. Such a particle should be lighter than a few hundred TeV, as discussed in [191]. As we shall see,

⁵Alternatively, such features could, of course, also indicate that the conventional neutrino astrophysical flux, while originating in standard physics, is much less understood than we believe, and may have more than one component.

the HDM under consideration here is necessarily non-thermal due to this reason⁶.

In what follows, we pursue two specific realizations (labelled Scenario I and II below) of such a dark matter sector, which, in combination with a power-law astrophysical component, provide a good description to the features in the IC data described in the previous subsection. For each realization, we perform a likelihood analysis to fit the IC HESE data and its observed features, in terms of a combination of four distinct fluxes. These fluxes are:

1. **Flux-1:** An underlying power-law flux of astrophysical neutrinos, $\Phi_{\text{Ast}} = N_{\text{Ast}} E^{-\gamma}$, whose normalization (N_{Ast}) and index (γ) are left free.
2. **Flux-2:** A flux of boosted light dark matter (LDM) particles (χ), which results from the late-time decay of a heavy dark matter (HDM) particle (ϕ). When χ is much lighter than ϕ , its scattering in IC resembles the NC DIS scattering of an energetic neutrino, giving rise to cascade-like events.
3. **Flux-3:** The flux of secondary neutrinos resulting from three-body decay of the HDM, where a mediator particle is radiated off a daughter LDM particle. The mediator then subsequently decays to SM particles, producing neutrinos down the decay chain. Since the NC DIS scattering that results from Flux-2 requires a mediator particle which couples to both the LDM and the SM quarks, such a secondary neutrino flux is always present.
4. **Flux-4:** The conventional, fixed, and well-understood, atmospheric neutrino and muon background flux, which is adapted from IC analyses [15, 244].

Scenario I : PeV events originating from DIS scattering of boosted LDM at IC

In Scenario I, the three highest energy PeV events, which are cascades characterized by energy depositions (central values) of 1.04 PeV, 1.14 PeV and 2.0 PeV, are assumed to be due to Flux-2 above, requiring an HDM mass of $\mathcal{O}(5)$ PeV. Both Flux-1 and Flux-3 contribute to account for rest of the HESE events, including the small bump-like excess

⁶We note that a two-component *thermal* WIMP-like DM scenario, with the lighter particle (of mass $\mathcal{O}(1)$ GeV) being boosted after production (via annihilation in the galactic halo of its heavier partner of mass $\mathcal{O}(100)$ GeV) and subsequently detected in neutrino experiments has been discussed in [347]. Boosted thermal DM detection from the sun and the galactic center due to annihilation of a heavier counterpart at similar masses and energies has been discussed in [348–350].

in the 30 – 100 TeV range. This scenario, in a natural manner, allows for the presence of a gap, or break in the spectrum between 400 TeV to 1 PeV⁷.

A similar scenario has previously been studied in Refs. [295, 298], in which the 988-day HESE data were taken into account. While Ref. [295] ascribed the events below a PeV upto tens of TeV entirely to the astrophysical flux (Flux-1), Ref. [298], ascribed these as being generated by the secondary neutrino flux from three-body HDM decay (Flux-3). In this study we do not make any assumption regarding the specific origin of these sub-PeV events, and allow any viable combination of Flux-1 and Flux-3 in the fitting procedure. As we shall see later, one of our main results from the fit to the HESE data within Scenario I is that with the current level of statistics, a broad range of combinations of Flux-1 and Flux-3 can fit the sub-PeV events, while the PeV events are explained by Flux-2. We note in passing that, in Ref. [298] the DM model parameter space was guided by the requirement that the LDM annihilation in the present Universe explain the diffuse gamma ray excess observed from the Galactic centre region [352] in the Fermi-LAT data. In the present study, the focus is entirely on satisfactorily fitting the IC events.

Scenario II : PeV events from an astrophysical flux and the 30 – 100 TeV excess from LDM DIS scattering

In Scenario II, we relax the assumption made regarding the origin of the three PeV events in Scenario I, and perform a completely general fit to both the PeV and the sub-PeV HESE data, with all four of the flux components taken together. Essentially, this implies that the mass of the HDM particle is now kept floating in the fit as well. We find that both the best-fit scenario and the statistically favoured regions correspond to a case where the PeV events are explained by the astrophysical neutrino flux (Flux-1), while the excess in the 30 – 100 TeV window primarily stems from the LDM scattering (Flux-2). Flux-3, which now populates the low 1–10 TeV bins becomes inconsequential to the fit, since the IC threshold for the HESE events is 30 TeV. Expectedly, in order for the astrophysical flux to account for the PeV events, the slope of the underlying power-law spectrum in Scenario II is significantly flatter compared to that in Scenario I.

In addition to performing general fits to the PeV and sub-PeV HESE data as described above, we also explore, for both Scenarios I and II, the extent to which different Lorentz

⁷The statistical significance of such a break has now increased due to the recent release of six-year muon track data [351]; see, for instance, the discussion in [337]. Additionally, as we shall see below, by providing a significant fraction of the events directly (via Flux 2) or indirectly (via Flux 3) from DM, this scenario does not require the astrophysical neutrino flux to be pushed up uncomfortably close to the Waxman-Bahcall bound, unlike the standard single power-law interpretation.

structures of the LDM coupling with the SM quarks impact the results. While a vector mediator coupling to the SM quarks and the LDM was considered in Ref. [295], a pseudo-scalar mediator was employed in Ref. [298]. Adopting a more general approach, we consider scalar, pseudo-scalar, vector and axial-vector mediators. However, we find (expectedly) that if the LDM relic density is appreciable, strong limits on the spin-independent coherent elastic scattering cross-section with nuclei of the relic LDM component come into play and restrict the available parameter space for scalar and vector mediators. There are also interesting differences between the pseudo-scalar and axial-vector scenarios insofar as fitting the IC data, as we shall show in later sections.

Finally, as emphasized in Ref. [298], the three-body decay of the HDM particles that gives rise to the secondary neutrino flux (Flux-3 above), also produces a flux of diffuse gamma-rays in a broad energy range, which is constrained from the measurements by the Fermi-LAT telescope [353] at lower energies, and by the cosmic ray air shower experiments (KASCADE [354] and GRAPES-3 [355]) at higher energies [356]. We find that the parameter space of the proposed dark matter scenarios that can fit the IC data is significantly constrained by the upper bounds on residual diffuse gamma ray fluxes⁸.

The rest of this chapter is organized as follows: Sec. 5.2 examines the different ways the LDM particle can interact with SM quarks, and summarizes the current constraints on the effective couplings and the mass parameters, using gamma ray and collider data. We also discuss the general method used to calculate the contribution made by the HDM three-body decay to galactic and extra-galactic gamma-ray fluxes. Sec. 5.3 focusses on Scenario I and describes our procedure for deriving best-fits to the observed IC HESE data for it, and the results obtained for different choices of the mediator. The validity of these results is then examined in the light of various constraints. Similarly, Sec. 5.4 repeats this for Scenario II. Although the focus of this work is on understanding the HESE data, IC has recently released a statistically independent sample of high energy muon track events [351] for the neutrino energies between 190 TeV to 9 PeV, where the interaction vertex is allowed to be outside the detector. Sec. 5.5, examines both the scenarios considered here in the light of this data sample. Finally, our findings are recapitulated and summarized in Sec. 5.6.

⁸We note that stronger constraints, based on IC data and Fermi-LAT, as discussed recently in [357] are evaded in our work since they are derived assuming the two-body decay of dark matter directly to SM particles, *e.g.* $b\bar{b}$.

5.2 LDM interaction with quarks: simplified models and current constraints

This section provides further details on how we model the interaction of the LDM with the SM quarks. In what follows, we shall work with a representative model where the HDM (ϕ) is described by a real scalar field, and the LDM (χ) is a neutral Dirac fermion, both of which are singlets under the standard model gauge interactions. The interaction of the heavy dark matter particle with the LDMs is described by an Yukawa term of the form $g_{\phi\chi\chi}\phi\bar{\chi}\chi$.

We further assume that the LDM particles are stabilized on the cosmological scale by imposing a Z_2 symmetry, under which the LDM field is odd, and all other fields are even. The LDM can interact with the SM fermions (quarks in particular) via scalar, pseudo-scalar, vector, axial-vector or tensor effective interactions. To describe such effective interactions we introduce a simplified model, where the interactions are mediated by a Z_2 even spin-0 or spin-1 particle. The LDM can also couple to SM fermions via a Z_2 odd mediator, which carries the quantum numbers of the SM fermion it couples to. We do not consider the t-channel models or the tensor type interaction in this study.

In the following sub-sections we shall describe the simplified model setup and mention the generic constraints on the couplings of a spin-0 or spin-1 mediator to the LDM and the SM fermions. Such constraints on the coupling and mass parameters can be modified within the context of a specific UV complete scenario, especially if it necessarily involves other light degrees of freedom not included in the simplified model. However, since the primary focus of this study is to determine the combination of different fluxes which can fit the features observed in the IC data, the simplified models chosen are sufficient for this purpose. Our approach allows us to draw general conclusions regarding the possible contributions of LDM scattering and the secondary neutrino fluxes, while being broadly consistent with constraints from experiments and observations.

5.2.1 Spin-0 mediators

The parity-conserving effective interaction Lagrangian (after electroweak symmetry breaking) of the LDM χ with SM fermions f , involving a scalar mediator S or a pseudo-scalar mediator A can be written as follows:

$$\mathcal{L}_S = \sum_f \frac{g_{Sf}m_f}{v} S\bar{f}f + g_{S\chi} S\bar{\chi}\chi \quad (5.1)$$

$$\mathcal{L}_P = \sum_f \frac{ig_{Pf}m_f}{v} A \bar{f} \gamma_5 f + ig_{P\chi} A \bar{\chi} \gamma_5 \chi \quad (5.2)$$

Here m_f is the mass of the SM fermion f , $g_{S\chi}$ ($g_{P\chi}$) represents the coupling of the LDM with the scalar (pseudoscalar) mediator, and v (≈ 246 GeV) stands for the vacuum expectation value of the SM Higgs doublet (in the presence of other sources of electroweak symmetry breaking the definition of v will be appropriately modified). The sum over fermion flavours can in principle include all SM quarks and leptons, although for our current study, the quark couplings are more relevant. We shall take the coupling factors g_{Sf} and g_{Pf} , which appear in the coupling of fermion flavour f with the scalar and the pseudo-scalar mediators respectively, to be independent of the quark flavour for simplicity.

A SM singlet spin-0 mediator cannot couple in a gauge-invariant way to SM fermion pairs via dimension-four operators. One way to introduce such a coupling is via mixing with the neutral SM-like Higgs boson after electroweak symmetry breaking. Such a mixing, if substantial, can however modify the SM-like Higgs properties leading to strong constraints from current LHC data. Other possible ways include introducing a two Higgs doublet model (and mixing of the singlet scalar with the additional neutral scalar boson(s)), or introducing new vector-like fermions to which the singlet scalar couples, and which in turn can mix with the SM fermions [358]. In all such cases the couplings of the singlet-like scalar to SM fermions should be proportional to the fermion Yukawa couplings in order to be consistent with the assumption of minimal flavour violation, thus avoiding flavour-changing neutral current (FCNC) constraints [359].

5.2.2 Spin-1 mediators

The effective interaction Lagrangian involving a spin-1 mediator, Z' , to SM fermions f and the LDM χ can be written as follows:

$$\mathcal{L} = \bar{\chi} (g_{V\chi} \gamma^\mu + g_{A\chi} \gamma^\mu \gamma_5) \chi Z'_\mu + \sum_f \bar{f} \gamma^\mu (g_{Lf} P_L + g_{Rf} P_R) f Z'_\mu. \quad (5.3)$$

Here the subscripts V , A , L , and R refer to vector, axial-vector, left-chiral and right-chiral couplings respectively. The left and right handed SM fermion currents are invariant under the SM $SU(3)_C \times SU(2)_L \times U(1)_Y$ gauge transformations. Therefore, in general, both vector and axial-vector interactions are present with coefficients $g_{Vf} = g_{Rf} + g_{Lf}$ and $g_{Af} = g_{Rf} - g_{Lf}$. In order to obtain only vector or axial-vector SM fermion currents at a low energy scale, we need to set $g_{Rf} = g_{Lf}$ or $g_{Rf} = -g_{Lf}$, respectively.

If the Z' couples to charged leptons, there are strong upper bounds on its mass from collider searches for dilepton resonances from the LHC. In order to avoid them, we assume the leptonic couplings to be absent. In a minimal scenario with only the SM Higgs doublet giving mass to all the SM fermions, we encounter further relations from $U(1)'$ gauge invariance (here, Z' is the gauge field corresponding to the $U(1)'$ gauge interaction) on the coupling coefficients to quarks and leptons [360]. This is because if left and right handed SM fermions have different charges under the new gauge group, the SM Higgs doublet needs to be charged under $U(1)'$ as well. Thus, when a single Higgs doublet gives rise to the mass of both SM quarks and charged leptons, if the quarks are charged under $U(1)'$, so would be the leptons. However, such constraints can be avoided in a non-minimal scenario, for example in a two Higgs doublet model, where different Higgs bosons are responsible for giving mass to quarks and leptons, thereby making their $U(1)'$ charges uncorrelated. We keep in view such considerations related to ultra-violet completion for this study, although we do not fully flesh out their consequences.

5.2.3 Constraints on the couplings and the mass parameters

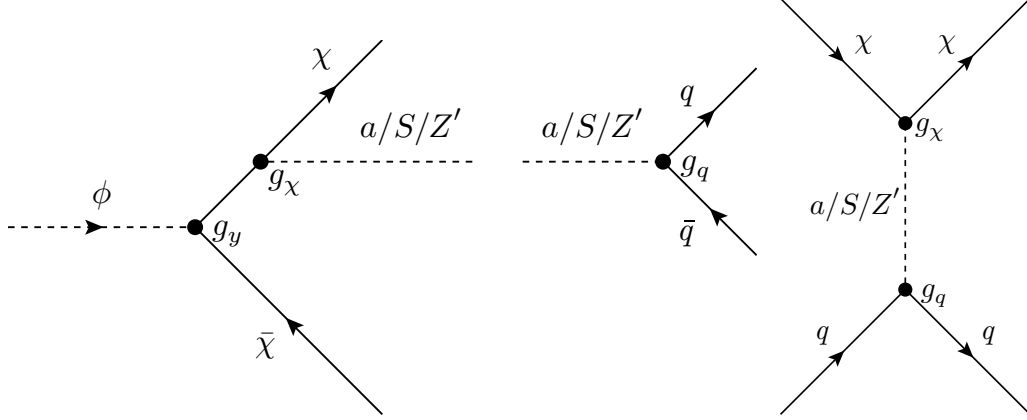


Figure 5.2: The interactions corresponding to ϕ decay (left), mediator decay (centre) and χq scattering (right) involving a generic mediator, along with relevant coupling constants.

Figure 1 shows the main interaction vertices which are relevant for both Scenario I and II. g_y represents the coupling between the HDM and LDM leading to the slow decay of the former, with lifetime τ_ϕ . The other couplings shown correspond to the vertices of either (a) SM quarks or (b) the LDM interacting with a generic mediator, which can be a pseudo-scalar (a) or a scalar (S) or a spin-1 boson (Z') which couples via vector and/or axial-vector couplings, as discussed in the previous section.

The rate of LDM DIS scattering at IC is proportional to $(g_q g_\chi)^2$, where g_q and g_χ are the mediator-quark pair and mediator-LDM pair couplings, respectively. It is also proportional to g_y^2 , or, equivalently, inversely proportional to τ_ϕ ⁹. Finally, the IC event rates are also proportional to the fractional contribution of the HDM to the total DM density, $f_\phi = \Omega_\phi/\Omega_{\text{DM}}$. Here, $\Omega_{\text{DM}} = 0.1198/h^2$ (with h being the normalized Hubble constant) from recent PLANCK results [5].

From the above considerations, the IC event rate from LDM DIS scattering, for a given choice of mediator mass m_M , is determined by the quantity $F = f_\phi g_q^2 g_\chi^2 / \tau_\phi$. It is useful to determine its maximum allowed value. In order to keep the couplings perturbative, we require $g_{\chi,q} < 4\pi$. We also require the lifetime of the HDM to be longer than the age of the Universe $\tau_\phi \gtrsim 4.35 \times 10^{17}$ seconds. And since $f_\phi < 1$, we obtain the upper bound, $F \lesssim 5.7 \times 10^{-14} \text{ s}^{-1}$. If the value of F exceeds this maximum, the couplings will not be perturbative, or the HDM would have decayed too quickly to have an appreciable density in the present Universe.

The secondary neutrino flux from the three-body decay of ϕ (Flux-3 in Sec. 5.1.2), is proportional to g_χ^2 (again, in the limit where the two-body decay width is much larger than the three-body width). It is also inversely proportional to the life-time of the HDM, τ_ϕ . In addition to the mass of the ϕ , τ_ϕ is determined by $g_{\phi\chi\chi}$ when the two body decay to LDM pairs dominate. Thus, the parameters relevant for fitting the features in the IC data in our work are g_q, g_χ , mass of the mediator particle (m_M), and τ_ϕ . The results do not depend on m_χ , as long as it is significantly lower than m_ϕ .

It is useful to examine the ball-park numerical values of some of the quantities which are used to fit the IC events using DIS χ -nucleon scattering. The cross section depends essentially on F and the mediator mass, m_M . Hence, given a certain value of m_M , and a value for the factor F , one could obtain minimum value of the couplings needed to fit an observed number of cascade events. This is given by $g_q g_\chi \gtrsim (F \times 4.35 \times 10^{17})^{(1/2)}$, assuming $f_\phi < 1$, and $\tau_\phi \gtrsim 4.35 \times 10^{17}$ seconds. A typical value that occurs in the fits is, for instance, $F \sim 10^{-26} \text{ s}^{-1}$, and using this leads to a lower bound $g_q g_\chi \gtrsim 6.6 \times 10^{-5}$. Assuming, for simplicity, $g_q \sim g_\chi = g$, each coupling should thus be greater than about 8×10^{-3} .

As mentioned earlier, (in Sec. 5.1.2), the most restrictive constraint on the value of F comes from the upper bound on the flux of diffuse gamma rays. We defer a detailed discussion of our computation of the gamma ray flux from the three-body decay of the HDM, and the resulting constraints to Sec. 5.2.3. Significant constraints also arise from collider experiments, where the mediator and the LDM particles can be directly produced, and

⁹This assumes that the two-body decay to χ is the dominant mode.

we discuss these in the next sub-section.

The relic density of χ , which we denote as $f_\chi = \Omega_\chi/\Omega_{\text{DM}}$, is not of direct relevance to our study, which focusses on the IC events coming either from DIS scattering of the LDM in IC, and on the flux of secondary neutrinos from the three-body decay of the HDM. However, direct detection constraints can be important if there is a significant density of the LDM in the current Universe. It is well-known that if f_χ is significant, the spin-independent direct detection bounds on the scalar and vector interactions are very strong, and thus would force us to focus on either pseudo-scalar or axial-vector couplings (or relegate us to corners of m_χ values which are not yet probed by the direct detection experiments). For our purpose, we could either assume that this is the case, or, equivalently, that the χ density is indeed small. If the latter, within the simplified model setup discussed above, the relic density of χ can be diluted to very small values in two ways. The first is by increasing g_χ , and restricting to values of $m_\chi > m_M$, such that the dominant annihilation mode of χ is to the mediator pair, which can then decay to the SM fermions even via a small g_q . The second way (albeit fine-tuned), is by setting m_χ close to $m_M/2$, thereby allowing for a resonant annihilation of LDM pairs to SM quarks. Since the IC event rates do not depend upon m_χ as long as it is significantly smaller than the HDM mass, both these approaches do not affect the IC event rates. Finally, there can always be additional annihilation modes of the LDM not described by the simplified models which do not affect the IC computations, but help make f_χ small.

With respect to the choices of mediators, we note that as far as the IC DIS scattering cross-sections are concerned, the exact Lorentz structure of the couplings is not important. However, as we shall see later, the two-body branching ratio of the HDM to LDM pair is sensitive to the Lorentz structure.

Collider constraints

The collider constraints are sensitive to the interplay of several couplings and mass parameters relevant to our study, specifically, g_q, g_χ, m_χ and m_M . A scalar or pseudo-scalar mediator particle which dominantly couples to heavy fermions can be produced in association with one or two b-quarks (involving the parton level processes $g b(\bar{b}) \rightarrow b(\bar{b}) S/A$ and $g g \rightarrow b\bar{b} S/A$ respectively). Such a final state may be accessible to LHC searches if the (pseudo-)scalar decays further to an LDM pair $S/A \rightarrow \chi\bar{\chi}$. However, in case, $m_\chi > m_{S/A}$, the (pseudo-)scalar would decay back to the SM fermion pairs, thereby making the search considerably harder due to large SM backgrounds. On the other hand, off-shell S/A production does lead to a cross-section in the one or two b-jet(s) and missing transverse mo-

momentum (MET) channel. Furthermore, an effective coupling of S/A to gluon pairs is also generated by the top quark loop, and therefore, mono-jet and missing energy searches are also relevant. These bounds have been computed in, for example, Ref. [361]. The current bounds from these searches are weaker than $g_q g_\chi \lesssim \mathcal{O}(0.1)$, across the range of m_M and m_χ of our interest [361]. As we shall see later, the coupling values required in our study are well within the current collider limits. For individual couplings, values of $\mathcal{O}(0.3)$ should be allowed, although the LHC bounds are very sensitive to the ratio g_χ/g_q , which determines the rate of events with MET.

In the case of a spin-1 mediator with either vector or axial vector couplings to SM quarks, the strongest collider constraints come from dijet resonance searches, where the mediator is produced on-shell, and decays back to the SM quarks. Depending upon the values of g_χ and g_q , monojet and MET searches could also be important, especially if a) the mediator width is large, making the resonance searches harder, or if b) $g_\chi > g_q$ for a given value of the product $g_\chi g_q$, such that the branching ratio to LDM pairs dominates the on-shell mediator decay (when $m_M > 2m_\chi$). Bounds on couplings in the axial-vector case have been discussed in Ref. [362], which combines the results of different experiments spanning a range of centre of mass energies, including (8 TeV) LHC (ATLAS and CMS), Tevatron and UA2. Similar considerations and bounds would apply to the vector mediator case. For $\mathcal{O}(1)$ values of $g_q g_\chi$, bounds from dijet searches cover $M_{Z'}$ masses in the range of 100 GeV to 2 – 3 TeV, depending upon the ratio g_χ/g_q , across the range of m_χ values. For a detailed discussion of these bounds for different values of $g_q g_\chi$ and g_χ/g_q , we refer the reader to Ref. [362]. With the recent 13 TeV 15.7 fb⁻¹ LHC data, ATLAS limits on the Z' coupling to quarks vary in the range of 0.1 to 0.33, as $M_{Z'}$ is varied in the range 1.5 to 3.5 TeV, when the mediator decay to LDM pairs is absent [363]. Thus, we conclude that the collider bounds on the spin-1 boson couplings are in the range of $\mathcal{O}(0.1)$, and the values required to fit the IC event rates are very much allowed by collider constraints.

Contributions to Galactic and Extra-Galactic Gamma-Ray Fluxes from HDM Decay

The three-body decay of the HDM to a pair of LDMs and a mediator particle (where the mediator particle is radiated by an LDM in the final state), will necessarily contribute to a diffuse gamma ray flux spanning a wide range of energies. This sub-section describes the general method we use to calculate these contributions. The mediator particles lead to hadronic final states via their decays to quark pairs or to hadronically decaying tau pairs, with gamma rays originating from the decays of neutral pions produced in the cascade. Leptonic decays of the mediator can also give rise to high-energy photons via

bremsstrahlung and inverse Compton scattering. In the computation of the gamma ray constraints, we only consider the hadronic decay modes of the mediator via quark final states, since the coupling of the mediator to quarks is essential to explaining the IC events in our scenario. For the case of a (pseudo)scalar mediator, the leptonic couplings are expected to be small due to the smaller Yukawa couplings of the charged leptons, while for the case of (axial-)vector mediators, as discussed in Sec. 5.2.2, consistency with dilepton resonance search constraints favour a setup in which the leptonic couplings are absent. We note in passing that the same three body decays would also lead to signatures in cosmic rays, and there can be additional constraints from measurements of positron and anti-proton fluxes. Due to the large uncertainties in diffusion and propagation models of cosmic rays, we do not include these constraints in our analysis.

The gamma ray flux, like the secondary neutrino flux which we calculate below in Section 3, has a galactic and an extra-galactic component [364]:

$$\frac{d\Phi_{\text{Isotropic}}}{dE_\gamma} = \frac{d\Phi_{\text{ExGal}}}{dE_\gamma} + 4\pi \frac{d\Phi_{\text{Gal}}}{dE_\gamma d\Omega} \Big|_{\text{Min}} \quad (5.4)$$

The extra-galactic flux is isotropic and diffuse (after subtracting out contributions from known astrophysical sources), while the minimum of the galactic flux is an irreducible isotropic contribution to the diffuse flux [364]. Since the most important constraints on very high-energy gamma-rays come from air-shower experiments, observations of which are confined to the direction opposite to the Galactic center, we take this minimum to be the flux from the anti-Galactic center, following Refs. [364, 365].

Unlike the neutrino flux, the extra-galactic gamma-ray component suffers significant attenuation due to pair creation processes, and consequently in the energy region of interest here, one finds the galactic component to be the dominant one from any given direction in the sky. This is given by

$$\frac{d\Phi_{\text{Gal}}}{dE_\gamma d\Omega} = \frac{1}{4\pi} \frac{\Gamma_{\text{dec}}}{M_{\text{DM}}} \int_{\text{los}} ds \rho_{\text{halo}}[r(s, \psi)] \frac{dN}{dE_\gamma} \quad (5.5)$$

where, Γ_{dec} is the total decay width of the HDM, M_{DM} is its mass, and the line of sight integral over the DM halo density $\rho_{\text{halo}}[r(s, \psi)]$ is performed along the direction of the anti-GC. We take the DM density profile in our galaxy to be described by a Navarro-Frenk-White distribution [366]:

$$\rho_{\text{NFW}}(r) = \rho_s \frac{r_s}{r} \left(1 + \frac{r}{r_s} \right)^{-2} \quad (5.6)$$

with the standard parameter choices, $\rho_s = 0.18 \text{ GeV cm}^{-3}$ and $r_s = 24 \text{ kpc}$. Here, dN/dE_γ

represents the gamma-ray spectra per decay of the HDM in the HDM rest frame. We take the prompt gamma ray energy distribution in the rest frame of the mediator from PPFC4 [164], and then subsequently fold it with the three-body differential energy distribution of the mediator obtained using CalcHEP [367], and finally boost the resulting gamma ray spectra to the rest frame of the decaying HDM.

The extra-galactic component of the flux is given by [364]

$$\frac{d\Phi_{\text{ExGal}}}{dE_\gamma} = \frac{\Omega_{\text{DM}}\rho_{c,0}}{M_{\text{DM}}\tau_{\text{DM}}} \int_0^{\text{inf}} dz \frac{e^{-\tau(E_\gamma(z),z)}}{H(z)} \frac{dN}{dE_\gamma}(E_\gamma(z),z) \quad (5.7)$$

where, the Hubble constant is given by $H(z) = H_0 \sqrt{\Omega_M(1+z)^3 + \Omega_\Lambda}$, with H_0 being the present Hubble expansion rate, and $\Omega_M, \Omega_{\text{DM}}$ and Ω_Λ are the matter, DM and dark energy densities respectively, in terms of the present critical density, $\rho_{c,0}$. We take the values of all relevant cosmological parameters from recent Planck best fits [5, 368]. The attenuation factor $e^{-\tau(E_\gamma(z),z)}$ describes the absorption of gamma rays described above, as a function of the redshift z and observed gamma-ray energy E_γ , which we take from PPFC4 tables [164].

Having established the framework and general considerations for our study, and outlined the constraints to which it is subject, in the sections to follow we proceed with the specific calculations necessary to demonstrate how IC data may be understood in scenarios combining boosted dark matter and astrophysical neutrinos.

5.3 Scenario I: PeV events caused by LDM scattering on Ice and its implications

In this section we consider a scenario where boosted DM scattering off ice-nuclei leads to the three events at energies above a PeV seen in the 1347-day HESE sample. In the present data-set, these events are somewhat separated from the others, since there appear to be no HESE events in the region $400 \text{ TeV} \leq E_{\text{dep}} \leq 1 \text{ PeV}$, providing some justification for considering them as disparate from the rest.

Both a) the details of the scattering cross-section of the LDM with ice-nuclei, and b) the three-body spectrum leading to the secondary neutrino flux in sub-PeV energies depend on the particle mediating the χN interaction. Thus we first examine different mediator candidates — pseudo-scalar, scalar, vector and axial vector — and determine how the corresponding fits and parameters change when a specific choice is made.

As discussed in Sec. 5.2.3, for the (dominant) two-body decay of the HDM (ϕ) into a pair of LDM ($\chi\bar{\chi}$), the corresponding event rate for χN scattering is proportional to

$F = f_\phi (g_\chi g_q)^2 / \tau_\phi$. The observed rate of the PeV events in IC, along with their deposited energies, then determines a) the ratio of couplings and lifetime F , and b) the mass (m_ϕ) of the HDM (ϕ), using the usual two-body decay kinematics [295]. Specifically, if the mean inelasticity of the interaction of the LDM with the ice-nuclei, mediated by a particle a is given by $\langle y_a \rangle$, then we require the LDM flux from HDM decay to peak around energies $E_{\text{PeV}} / \langle y_a \rangle$, where E_{PeV} represents an estimated average deposited energy at IC for such events.

In this scenario, events in the sub-PeV energy range are then explained by a combination of events from Flux-1 (an astrophysical power-law neutrino flux), Flux-3 (the secondary flux of neutrinos from three-body HDM decay) and Flux-4 (the standard atmospheric neutrino and muon flux), as outlined in Sec. 5.1.2. For Flux-4, we use the best-fit background estimates from the IC analysis. We determine the best-fit combination of Flux-1 and Flux-3, which, when folded in with the IC-determined best-fit Flux-4 will explain all the sub-PeV observed events in the 1347-days HESE sample. The parameters relevant to this sub-PeV best-fit are m_a , $(f_\phi g_\chi^2 / \tau_\phi)$, N_{Ast} (the number of sub-PeV events from Flux-1), and γ (the power-law index for Flux-1).

The total number of shower events within each IC energy bin is given by [369]:

$$N_\chi^{\text{cascade}, NC} = T N_A \int_{E_{\min}}^{m_\phi/2} dE_\chi M^{NC}(E_\chi) \frac{d\Phi_\chi}{dE_\chi} \int_{y_{\min}}^{y_{\max}} dy \frac{d\sigma^{NC}(E_\chi, y)}{dy} \quad (5.8)$$

Here y is the inelasticity parameter, defined in the laboratory frame by $y = E_{\text{dep}} / E_\chi$, with E_{dep} being the energy deposited in the detector and E_χ denotes the energy of the incident dark matter, T the runtime of the detector (1347 days) and N_A is the Avogadro number. The limits of the integration are given by $y_{\min} = E_{\min}^{\text{dep}} / E_\chi$ and $y_{\max} = \min(1, E_{\max}^{\text{dep}} / E_\chi)$. E_{\min}^{dep} and E_{\max}^{dep} are the minimum and maximum deposited energies for an IC energy-bin. $M^{NC}(E_\chi)$ is the energy dependent effective detector mass for neutral current interactions obtained from [244]. $d\sigma^{NC}(E_\chi, y)/dy$ is the differential χN scattering cross-section, which we quantify below.

The total flux $d\Phi_\chi/dE_\chi$ is composed of two parts, the Galactic component $d\Phi_\chi^{\text{GC}}/dE_\chi$ and the red-shift (z) dependant extra-Galactic component $d\Phi_\chi^{\text{EG}}/dE_\chi$. They are given by [198, 234]:

$$\begin{aligned} \frac{d\Phi_\chi^{\text{GC}}}{dE_\chi} &= D_G \frac{dN_\chi}{dE_\chi} \\ \frac{d\Phi_\chi^{\text{EG}}}{dE_\chi} &= D_{\text{EG}} \int_0^\infty dz \frac{1}{H(z)} \frac{dN_\chi}{dE_\chi} [(1+z)E_\chi], \end{aligned} \quad (5.9)$$

where,

$$D_G = 1.7 \times 10^{-8} \left(\frac{1 \text{ TeV}}{m_\phi} \right) \left(\frac{10^{26} \text{ s}}{\tau_\phi} \right) \text{ cm}^{-2} \text{ s}^{-1} \text{ sr}^{-1}$$

and

$$D_{EG} = 1.4 \times 10^{-8} \left(\frac{1 \text{ TeV}}{m_\phi} \right) \left(\frac{10^{26} \text{ s}}{\tau_\phi} \right) \text{ cm}^{-2} \text{ s}^{-1} \text{ sr}^{-1}.$$

For the two-body decay $\phi \rightarrow \bar{\chi}\chi$, the flux at source is given by :

$$\frac{dN_\chi}{dE_\chi} = 2\delta \left(E_\chi - \frac{1}{2}m_\phi \right), \quad (5.10)$$

where, E_χ denotes the incident energy at IC for each χ particle.

We next describe the computation of the secondary neutrino flux due to the $\phi \rightarrow \chi\bar{\chi}a$ three-body decay mode, where one of the daughters (a) is the mediating particle in χN scattering. The general procedure is the same as outlined in [298]. In our representative calculation here, a is assumed to decay to a $q\bar{q}$ pair, which by further hadronisation and decays leads to the secondary neutrino spectrum. It is straightforward to obtain the resulting neutrino flux in the rest frame of a (see, *e.g.*, [164]), using event generators that implement the necessary showering and hadronisation algorithms, such as PYTHIA8 [370]. This flux is then boosted to the lab-frame, which is, approximately, the ϕ rest frame.

This boosted flux in the ϕ rest frame is used in conjunction with Eq. 5.9 to get the final flux of the secondary neutrinos. The neutrino event rates from this source are determined by folding this flux with the effective area and the exposure time of the detector [244].

Having obtained the event rates for the secondary neutrinos, one defines the χ^2 necessary to quantify our goodness of fit to the observed data:

$$\begin{aligned} \chi^2 &\equiv \chi^2(m_a, f_\phi g_\chi^2/\tau_\phi, N_{\text{Ast}}, \gamma) \\ &= [N^{\text{sub-PeV}}(m_a, f_\phi g_\chi^2/\tau_\phi, N_{\text{Ast}}, \gamma) - N_{\text{obs}}^{\text{sub-PeV}}]^2 / N^{\text{sub-PeV}}(m_a, f_\phi g_\chi^2/\tau_\phi, N_{\text{Ast}}, \gamma) \end{aligned} \quad (5.11)$$

Minimizing this χ^2 determines the best-fit point in the parameter space of $\{m_a, f_\phi g_\chi^2/\tau_\phi, N_{\text{Ast}}, \gamma\}$. It should be noted that the sub-PeV events in Scenario I are due both to the decay of the mediator and a uniform power-law spectrum typical of diffuse astrophysical sources, which is why the overall χ^2 function is dependent on all the four parameters shown above.

We now turn to discussing the results for specific mediators.

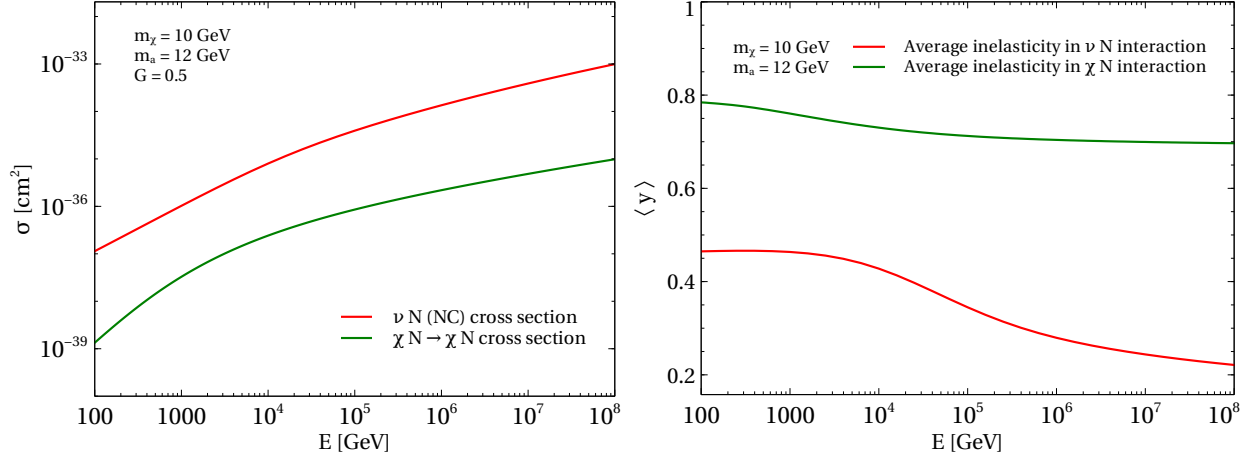


Figure 5.3: Representative plots showing the relative behaviour of χN and νN neutral current cross sections (left). Average inelasticities are also plotted for both cases (right).

5.3.1 Pseudoscalar mediator

When the mediator is a pseudo-scalar particle, the corresponding double differential cross-section is given by :

$$\frac{d^2\sigma}{dx dy} = \sum_q \frac{1}{32\pi x M_N} \frac{E_\chi}{(E_\chi^2 - m_\chi^2)} \frac{(g_\chi g_q)^2 (Q^2)^2}{(Q^2 + m_a^2)^2} f_q(x, Q^2) \quad (5.12)$$

where x is the Bjorken scaling parameter, M_N, m_χ and m_a are the masses of the nucleon, LDM, and the mediator respectively, and $Q^2 = 2xyM_N E_\chi$. $f_q(x, Q^2)$ is the parton distribution function (PDF) of the quark q in the nucleon. We henceforth use the CT10 PDFs [202] throughout our work.

Eq. (5.12) allows us to compute the event rates (using Eq. (5.8)) and the mean inelasticity of the χN scattering process. In Fig. 5.3 we show the total deep inelastic $\chi N \rightarrow \chi N$ cross section and the average inelasticity ($\langle y \rangle$), and compare them with the $\nu N \rightarrow \nu N$ case [192, 193, 371].

Fig. 5.4 shows the individual flux components that contribute to the PeV and the sub-PeV events in Scenario I. This is a representative plot, and the parameters that were used while calculating the fluxes are the best-fit values shown in Table. 5.1.

As discussed previously, in Scenario I, the sub-PeV events depend on the mediator mass m_a , the ratio $f_\phi g_\chi^2 / \tau_\phi$ and on the HDM mass m_ϕ . The three PeV events, on the other hand depend on m_a , the ratio $F = f_\phi g_\chi^2 g_q^2 / \tau_\phi$ and as well as on m_ϕ . Treating the PeV events as arising from two-body decay of the ϕ to $\chi\bar{\chi}$ using gives us $m_\phi \simeq 5.3$ PeV. A major fraction of the sub-PeV events arise from the secondary neutrino flux, and for

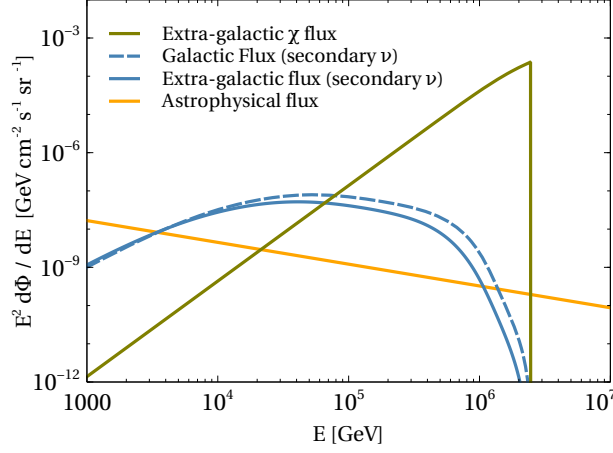


Figure 5.4: Relevant fluxes that contribute towards the PeV and the sub-PeV events in Scenario I. The galactic χ flux is not shown since it originates from the two body decay of ϕ , and is given by the simple form in Eq. 5.10, unlike the extra-galactic flux, which exhibits a z dependance. The values of parameters used to calculate the fluxes are given in Table. 5.1.

Parameter	m_a [GeV]	g_q	$f_\phi g_\chi^2 / \tau_\phi$ [s^{-1}]	γ	\tilde{N}_{ast} (all flavour)
$a \rightarrow b\bar{b}$	12.0	0.32	1.23×10^{-26}	2.57	1.21×10^{-9}
$a \rightarrow c\bar{c}$	5.3	0.50	5.02×10^{-27}	2.61	5.40×10^{-9}

Table 5.1: The best fit values of relevant parameters in case of a pseudoscalar mediator a , when it dominantly decays to $b\bar{b}$ and $c\bar{c}$ respectively. \tilde{N}_{Ast} is given in units of $GeV\ cm^{-2}\ s^{-1}\ sr^{-1}$.

this we carry out calculations in two different kinematic regions: *a*) where the mediator mass lies above the $b\bar{b}$ production threshold, and *b*) where it lies below this threshold, making $c\bar{c}$ the main decay mode. The results for best fits to the data using events from all of the above fluxes, and considering both kinematic regions, are shown in Fig. 5.5. The solid red line represents the total of the contributions from the various fluxes, and we find that it provides a good description to the data across the energy range of the sample. The best fit values of the parameters are given in Table 5.1. The corresponding normalisation of the astrophysical flux is shown in terms of the flux at the 100 TeV bin $\tilde{N}_{Ast} = E^2 \Phi_{Ast}|_{100\ TeV} GeV\ cm^{-2}\ s^{-1}\ sr^{-1}$.

We note the following features of Fig 5.5, which also conform to emergent features of

IC data:

- The secondary neutrino event spectrum has a shape that would allow it to account for a ‘bump’, or excess, such as presently seen in the vicinity of 30–100 TeV.
- The astrophysical neutrino contribution, especially in the $b\bar{b}$ case, is not a major component. This is unlike the standard situation where only astrophysical neutrinos account for events beyond 30 TeV, requiring a flux very close to the Waxman-Bahcall bound.
- A dip in the region 400–1000 TeV occurs naturally due to the presence of fluxes of different origin in this region.
- Over the present exposure period, no HESE events are expected in the region beyond 2–3 PeV, since the only contributing flux here is the astrophysical flux, which is significantly lower in this scenario as opposed to the IC best-fits. With more exposure, some astrophysical events can be expected to show up in this region.

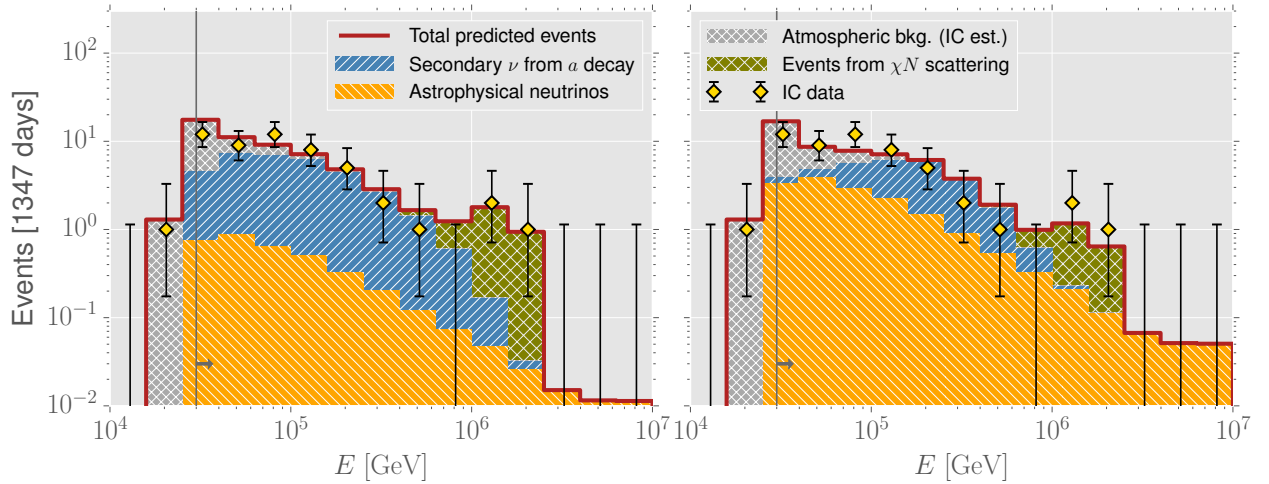


Figure 5.5: Best-fit events (stacked bars) from a combination of secondary ν 's, astrophysical ν 's and background in the sub-PeV energies, with LDM events explaining the PeV+ events. The best-fit value of $m_\phi = 5.34$ PeV. **Left:** Decays to $b\bar{b}$. **Right:** The mediator mass limited to below $b\bar{b}$ production threshold, so that it can dominantly decay only to $c\bar{c}$ pairs.

Parameter correlation analyses

It is useful to examine the parameter space for Scenario I allowed by IC data. We use the case of a pseudo-scalar mediator as representative, and examine the correlations and degeneracies between the parameters. We give contour plots between pairs of parameters for each of the LDM decay scenarios considered above, *i.e.* for decay to $b\bar{b}$ and to $c\bar{c}$. Noting that the sub-PeV events in the HESE sample that do not have their origin in the atmosphere are, in our scenario, either from the secondary neutrino flux or from the astrophysical (power-law) neutrino flux, we denote the total number (in the 1347-day sample) of the former by N_{DM} , and that of the latter by N_{Ast} .

For each case we start with the best-fit values obtained in the previous section for each of the parameters in the set: $\{N_{\text{DM}}, m_a, N_{\text{Ast}}, \gamma, m_\phi, g_q\}$. We note that N_{DM} is proportional to $(f_\phi g_\chi^2)/\tau_\phi$, whereas the primary DM component of the event spectrum, coming from χ scattering off ice nuclei at PeV energies is related to $m_\phi, f_\phi (g_\chi g_q)^2/\tau_\phi$ and m_a . For a fixed γ , specifying the N_{Ast} is tantamount to specifying the overall astrophysical flux normalisation A in the uniform power-law spectrum $\Phi_{\text{Ast}} = AE^{-\gamma}$.

The total number of signal events observed in the 1347-day IC sample is 35 at its best-fit value, with a 1σ (3σ) variation of 29–42 (20–57). This assumes the conventional atmospheric background is at the expected best-fit, and the prompt background is zero. Selecting two parameters for each analysis, we vary their values progressively from their best-fits, while marginalizing over the other parameters over their allowed 1σ (3σ) ranges. For each pair of the chosen two-parameter subset, we compute the $\Delta\chi^2(p_a, p_b) = \chi^2(p_a, p_b) - \chi_{\text{b.f.}}^2$ where p_a, p_b represent the value of the two chosen parameters in the iteration. With the resulting $\Delta\chi^2$ we plot 1σ and 3σ contours enclosing the allowed variation of these parameters (Fig. 5.6, Fig. 5.7 and Fig. 5.8). Due to the sparse statistics presently available, the 3σ allowed regions in these plots permit the IC data to be fit well for a wide range of values of the chosen variables.

Following the discussion in Sec. 5.2.3, the only major constraint on the parameters in the pseudo-scalar mediator scenario stems from the upper bound on diffuse gamma-ray fluxes, while the current collider constraints restrict the values of the couplings to $\mathcal{O}(0.1)$ values. The sum of the galactic and extragalactic gamma ray fluxes corresponding to the best fit parameter points are shown in Fig. 5.9. They are compared with both the Fermi-LAT data [353] at lower energies, and cosmic ray air shower experiment (KASCADE [354] and GRAPES-3 [355]) data at higher energies. These constraints significantly restrict the available parameter-space, and, indeed, our best-fit values for the N_{DM} lie

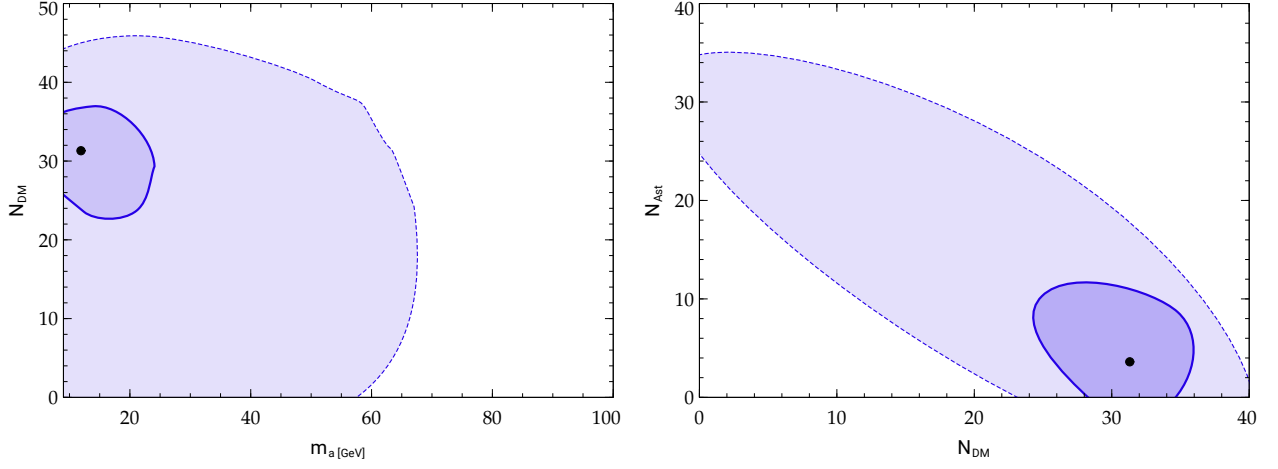


Figure 5.6: 1σ and 3σ allowed regions for parameters N_{ψ_1} and m_a (left) and N_{ψ_1} and N_{Ast} (right) for mediator decays to $b\bar{b}$. The solid dot in each case represents the corresponding best-fit point in the parameter subspace.

in a disfavoured region. We find, however, that a reasonable region of the allowed 3σ parameters-space is nonetheless consistent with these constraints, and that the allowed region for $b\bar{b}$ is larger than that for $c\bar{c}$. Fig. 5.8 reflects these conclusions.

5.3.2 Scalar mediator

In this section we explore the case when the mediator a in Scenario I is a scalar. The relevant double differential χN scattering cross-section in this case is given by:

$$\frac{d^2\sigma}{dx dy} = \sum_q \frac{1}{32\pi} \frac{E_\chi}{x M_N (E_\chi^2 - m_\chi^2)} \frac{(g_\chi g_q)^2}{(Q^2 + m_a^2)^2} \times [16m_\chi^2 m_q^2 + (Q^2)^2 + 4Q^2(m_\chi^2 + m_q^2)] f_q(x, Q^2) \quad (5.13)$$

where, the various quantities used are as before (Eq. (5.12)).

The parameter values at the best-fit point are shown in Table 5.2, and we show the corresponding event rates in Fig 5.10. It is interesting to note that, compared to the pseudo-scalar case, due to the additional terms contributing to the differential χN scattering cross-section (in particular, the $4Q^2 m_\chi^2$ term), the best fit value for g_q turns out be smaller in the scalar case, while rest of the relevant parameters take similar values.

The gamma-ray constraints on the scalar mediator case are found to be similar to the pseudo-scalar case, and as discussed in Sec. 5.2.3, the collider constraints on the coupling parameters are also of similar magnitude. As further explained in Sec. 5.2.3, although

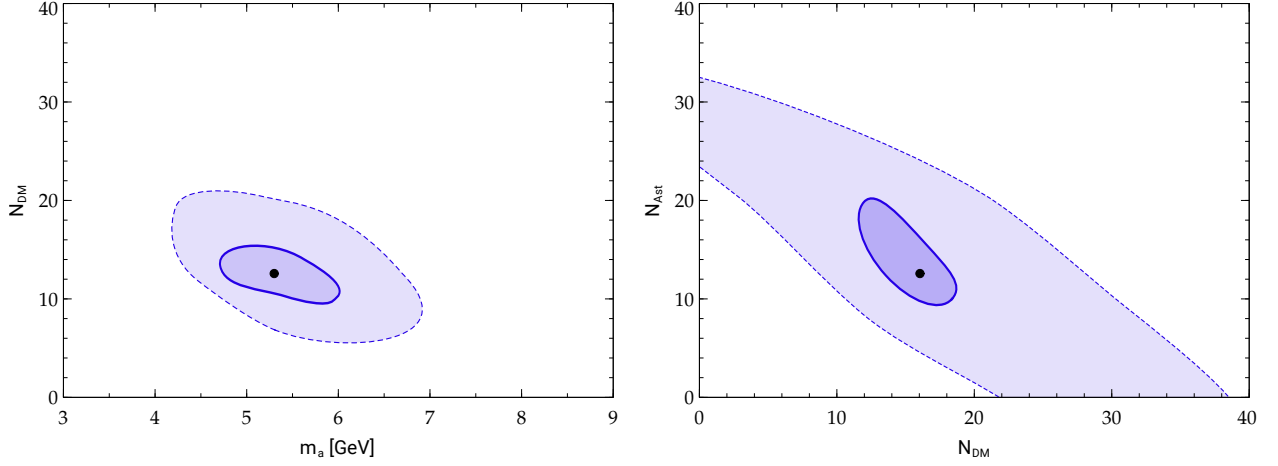


Figure 5.7: 1σ and 3σ allowed regions for parameters N_{ψ_1} and m_a (left) and N_{ψ_1} and N_{Ast} (right) for mediator decays to $c\bar{c}$. The solid dot in each case represents the corresponding best-fit point in the parameter subspace.

Best fit parameters	m_a [GeV]	g_q	$f_\phi g_\chi^2 / \tau_\phi$ [s^{-1}]	γ	\tilde{N}_{ast} (all flavour)
$a \rightarrow c\bar{c}$	5.3	0.29	4.88×10^{-27}	2.63	5.41×10^{-9}

Table 5.2: The best fit values of relevant parameters in the case of a scalar mediator a , when it decays dominantly to $c\bar{c}$. The best fit value of m_ϕ here is ~ 5.3 PeV. \tilde{N}_{Ast} is given in terms of $\text{GeV cm}^{-2} \text{s}^{-1} \text{sr}^{-1}$.

we restrict ourselves to regions of parameter space where f_χ is very small, for parameter values where f_χ becomes appreciable, there are additional constraints from relic density requirements as well as direct detection bounds. The spin-independent direct detection bounds in particular are very stringent in the scalar mediator scenario, unless the DM mass lies below $\mathcal{O}(10 \text{ GeV})$, where the nuclear-recoil experiments lose sensitivity. Overall, stronger constraints notwithstanding, we find that the best-fit point lies in an allowed region of the parameter space, and provides an excellent fit to the data, with explanations for the observed features identical to those described in the last subsection.

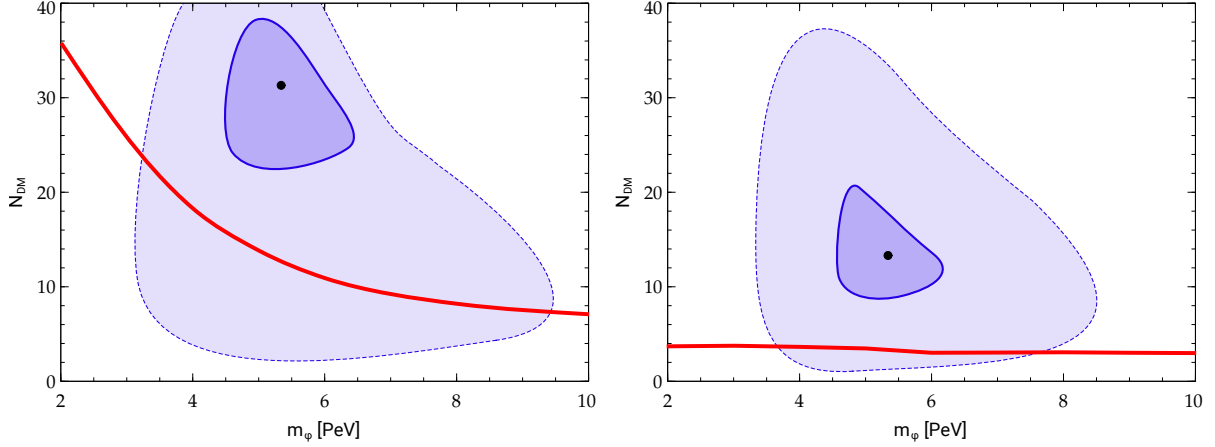


Figure 5.8: Plot showing allowed regions satisfying gamma ray constraints in the case when pseudoscalar mediator decays to $b\bar{b}$ (Left) and to $c\bar{c}$ (Right). Regions above the red line are constrained by observations of the diffuse gamma ray flux.

5.3.3 Vector and axial-vector mediators

The double differential cross section in the case of a vector mediator is given by:

$$\begin{aligned} \frac{d^2\sigma}{dxdy} = & \sum_q \frac{1}{32\pi} \frac{1}{x M_N E_\chi} \frac{(g_\chi g_q)^2}{(Q^2 + m_{Z'}^2)^2} \\ & \times \left(\frac{(Q^2)^2}{2} + s^2 - s Q^2 \right) f_q(x, Q^2). \end{aligned} \quad (5.14)$$

where, g_q is the coupling of Z' to the quark q , and $s \approx 2x E_\chi M_N$.

To evade the strong bounds particular to vector (and axial-vector) mediators coming from dijet resonance searches in collider experiments, as discussed in Sec. 5.2.3, we impose a penalty on the χ^2 computation whenever the combination of the coupling constant and $M_{Z'}$ extends into a region disfavoured at more than 90% confidence level. Once we have thus determined the allowed region of the parameter space, we show the results (Fig. 5.11) corresponding to a benchmark point in this space, defined by the values in Table 5.3, that maximises the contribution from secondary neutrinos from DM decay (Flux-3), and correspondingly deems the astrophysical neutrino component insignificantly small (which we consequently do not show). An increased flux for the latter can be accommodated by a corresponding scaling down of the value of $f_\phi g_\chi^2 / \tau_\phi$ and so on.

As seen in Fig. 5.11, unlike the pseudo-scalar and the scalar cases, we note that the galactic and the extra galactic secondary flux events remain approximately flat with decreasing energy below ≈ 1 PeV. This results in the absence of a dip or deficit in the region

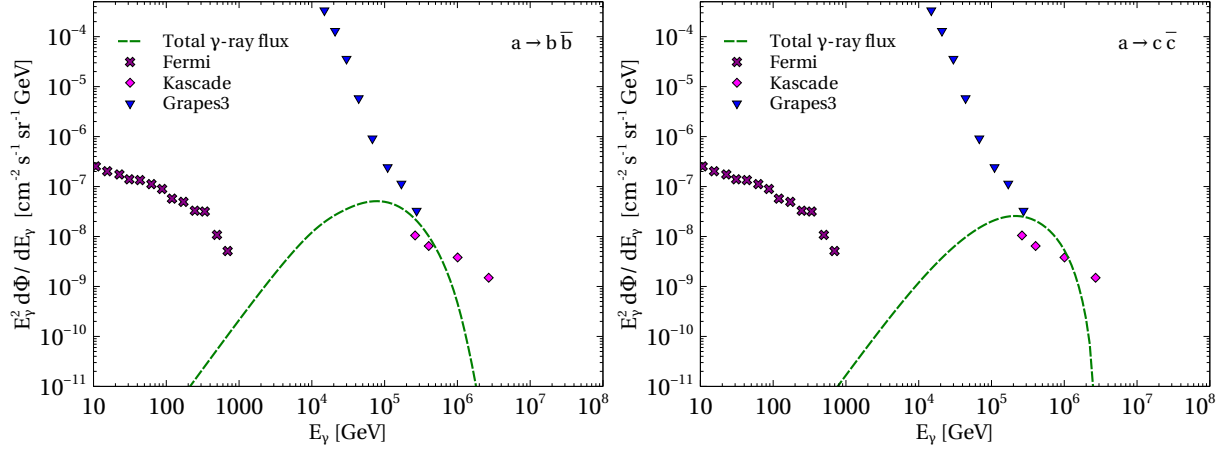


Figure 5.9: Diffuse gamma-ray flux for the best-fit parameter choice in the pseudo-scalar mediator scenario, where the mediator a dominantly decays to $b\bar{b}$ (left) and $c\bar{c}$ (right). The current constraints from Fermi-LAT data at lower energies, and cosmic ray air shower experiment (KASCADE and GRAPES-3) data at higher energies are also shown.

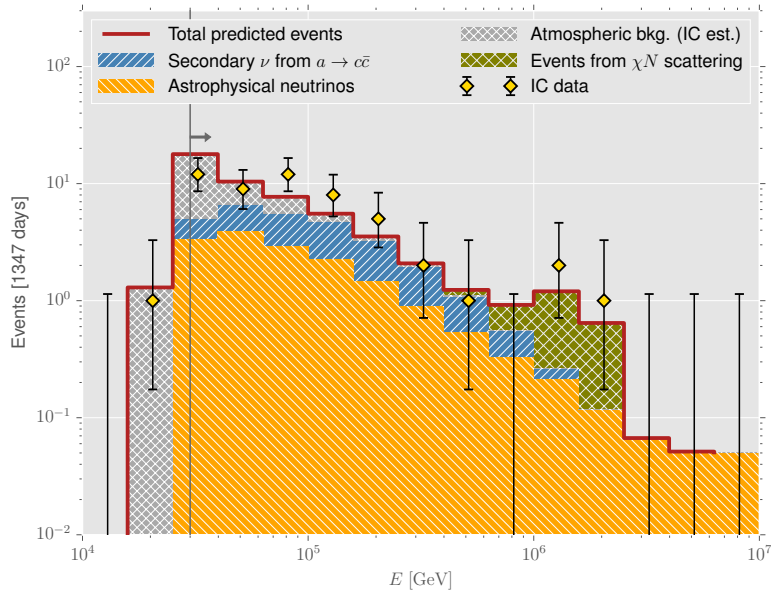


Figure 5.10: Same as Fig. 5.5, for the scalar mediator scenario, with the mediator dominantly decaying to $c\bar{c}$.

400 TeV–1 PeV which is one of the features of the present IC data that we would like to reproduce in Scenario I. This can be mitigated by increasing the mass of the mediator (see Fig 5.12). A comparison with the pseudoscalar mediator event spectrum, where this

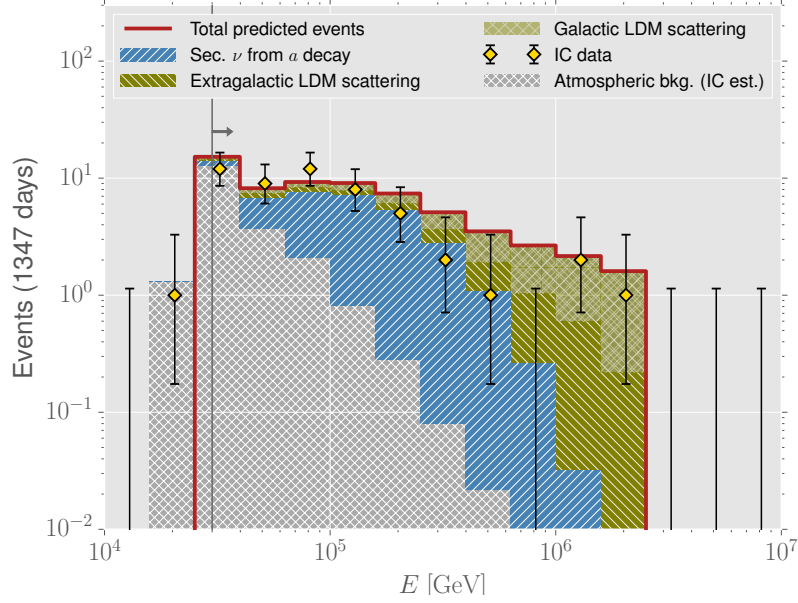


Figure 5.11: Event rates for the benchmark parameter values shown in Table 5.3. In keeping with the description in text, the correspondingly tiny number of events from the astrophysical flux have not been shown here.

problem is absent, is shown for a fixed mass, in the right panel Fig. 5.12.

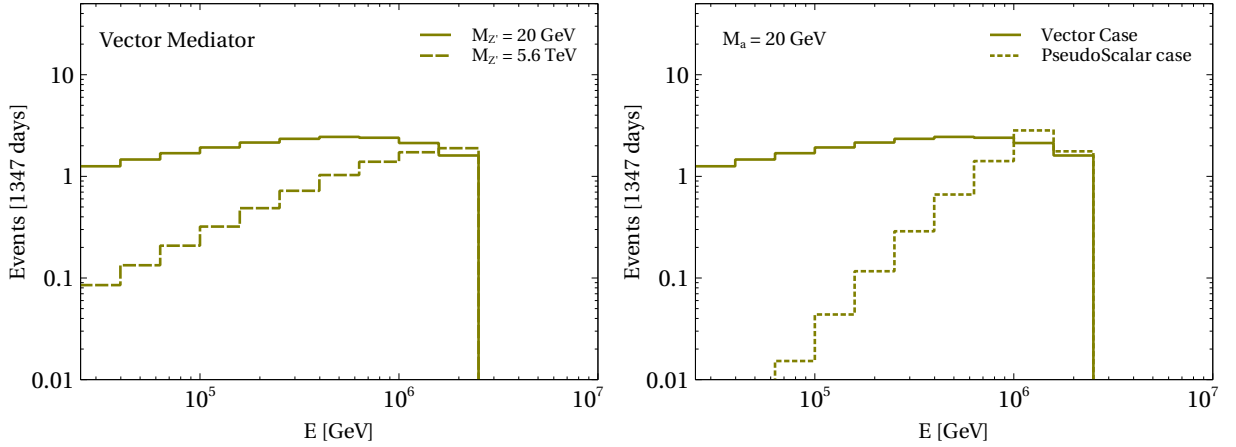


Figure 5.12: **Left:** PeV events in the vector mediator scenario, with different choices for the Z' mass. A larger value of the Z' mass is more likely to explain the *dip* at around PeV. **Right:** PeV events in vector and pseudoscalar case with a mediator mass fixed to 20 GeV. The pseudoscalar scenario, as discussed earlier, explains the *dip* more accurately because of its sharply falling event rates, unlike in the vector scenario.

Benchmark Values	$M_{Z'}$ [GeV]	g_q	$f_\phi g_\chi^2 / \tau_\phi$ [s ⁻¹]
$Z' \rightarrow q\bar{q}$	20	3.3×10^{-3}	2.5×10^{-27}

Table 5.3: Benchmark values of relevant parameters in the case of a vector mediator Z' , when it decays to all possible $q\bar{q}$ pairs. The value of m_ϕ used here is ~ 5.0 PeV. As noted in the text, we have chosen a benchmark point in the parameter space that maximises the secondary ν contribution from DM decay, and consequently deems the astrophysical flux negligible. The latter has therefore not been shown here.

We now turn to the relevant gamma-ray constraints, along the same lines we studied it for the case of a pseudo-scalar mediator. While the differential three-body decay width of the HDM follows somewhat different distributions for different choices of mediator spin and CP properties, the very large boost of the mediator particle washes out these differences to a large extent, and we arrive at a similar spectral shape as discussed for the spin-0 mediators above. We find that the corresponding constraints are not severe, but may have mild tension in some energy regions. As far as relic density and spin-independent direct detection bounds are concerned, similar considerations as in the scalar mediator case would also apply to the vector mediator scenario, and we refer the reader to the discussion in Sec. 5.3.2.

Even though the differential χN cross-section behaves similarly in the vector and axial-vector scenarios (in small m_χ and m_q limit), there are additional important considerations particular to the axial-vector case that limit the available parameter space very stringently. As explained earlier, in order to accommodate the PeV events by χN DIS scattering, we require that the three body decay width of the HDM is much smaller than its two body decay width. However, as shown in Fig. 5.13, the three-body branching ratio starts to dominate for g_χ values as low as 0.01 in the axial-vector case, whereas for scalar, pseudo-scalar or vector mediators, the three-body branching ratio becomes large only for $g_\chi \geq 1$. Thus, since the PeV event rate is proportional to $g_\chi^2 g_q^2 f_\phi / \tau_\phi$, to obtain the required number of events in the PeV region, the value of g_q needs to be pushed higher than its perturbative upper bound of 4π . Ultimately, we find that it is not possible to fit both the PeV and the sub-PeV events while simultaneously satisfying the perturbativity requirement for an axial-vector mediator.

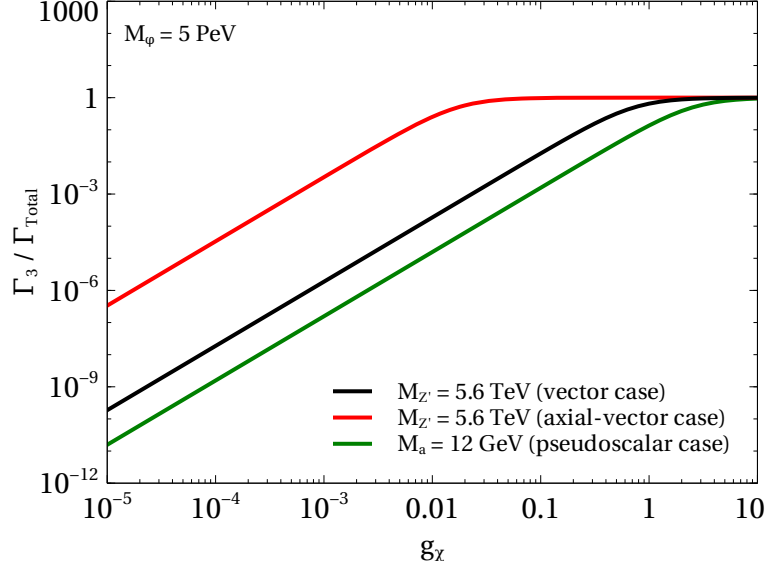


Figure 5.13: Variation of three body branching ratio with g_χ for the vector, axial-vector and the pseudoscalar mediators. The scalar mediator scenario shows a similar behaviour as the pseudo-scalar one.

5.4 Scenario II: Excess events in the 30–100 TeV region caused by LDM scattering on Ice and its implications

As discussed in Sec. 5.1.2, in Scenario II, we relax the assumption made regarding the origin of the three PeV events in Scenario I, and perform a completely general fit to both the PeV and the sub-PeV HESE data, with all four of the flux components taken together. This essentially implies that the HDM mass m_ϕ is also left floating in the fit in the entire range [30 TeV, 2.5 PeV]. Therefore, the space of parameters now comprises the set m_ϕ, F, m_a, γ and N_{ast} .

We find that doing this causes the best-fit HDM mass to float to a value $\mathcal{O}(500)$ TeV, so that the resulting LDM spectra from its decay are naturally able to explain the bump, or excess in the ~ 50 –100 TeV energy range that is seen in the IC data. At the present time, this feature has a statistical significance of about 2.3σ . An important consequence of this is that the flux of secondary neutrinos from mediator decay, which played an important role in Scenario I, now populates the low energy bins (between 1 TeV to 10 TeV) and falls outside the range relevant to our fit (the IC threshold for the HESE events is 30 TeV). This flux is thus subsumed in the atmospheric background. At energies of around a TeV, where the secondary neutrino flux from three-body decays of HDMs in this scenario

might have been otherwise important, the atmospheric neutrino flux is already about a 1000 times higher, and completely overwhelms it. Furthermore, the full-volume IceCube is only sensitive to contained events depositing at least about 10 TeV in the detector, hence this flux is also largely rendered unobservable because it lies outside the HESE sensitivity range.

Note that Scenario II also suggests that the other currently emergent features, the cluster of 3 events close to 1–2 PeV and the dip in the 400 TeV–1 PeV region, which were very important motivations for Scenario I, may not survive with time. Thus, at the current level of statistics, this fit gives primacy to the 50–100 TeV excess. In Scenario I, the PeV events, assumed to arise from the two-body decay of HDM, will (in the form of cascades resembling NC neutrino events) steadily increase in number and manifest themselves as an excess or bump, whereas in Scenario II they would just become part of the overall astrophysical power-law neutrino spectrum without a special origin. The related dip, or deficit, currently seen in the 400 TeV to 1 PeV region would gradually become prominent and significant in Scenario I, but would get smoothed over in Scenario II. Consequently,, in Scenario II the only relevant fluxes are the astrophysical flux and the χ flux originating from the two body decay of ϕ , in addition to, of course, the background atmospheric flux. We show the representative contributing fluxes in Fig. 5.14.

The best fit parameters for the fit in Scenario II are given in Table 5.4, and the corresponding results are shown in Fig. 5.15, for the pseudo-scalar mediator scenario (left column), and the axial-vector mediator scenario (right column). As in Scenario I, the scalar and pseudo-scalar mediators lead to similar fits. However, unlike in Scenario I, since the secondary neutrino flux lies outside the energy range under study, both vector and axial-vector mediators lead to similar results for Scenario II. Therefore, we have not shown the scalar and vector cases separately.

Parameter	m_a [GeV]	m_ϕ [TeV]	$f_\phi g_q^2 g_\chi^2 / \tau_\phi$ [s ⁻¹]	γ	\tilde{N}_{ast} (all flavour)
Pseudoscalar	16.1	680	1.15×10^{-27}	2.31	1.59×10^{-8}
Axial-vector	5.6×10^3	470	2.21×10^{-24}	2.30	1.59×10^{-8}

Table 5.4: The best fit values of relevant parameters in case of a pseudoscalar and axial-vector mediator for Scenario II. \tilde{N}_{ast} is given in units of GeV cm⁻² s⁻¹ sr⁻¹.

The similarity in the number of events originating from DM and from astrophysical neutrinos in the two cases is not surprising. In both cases, only the small excess in the

vicinity of $\sim 50 - 100$ TeV is due to DM cascades, the remaining events conform to the expected astrophysical neutrino spectrum, which then sets the normalization and the index. Consequently, we also note an important difference between the astrophysical fluxes in Scenario II compared to Scenario I, *i.e.* in Scenario I this flux is usually sub-dominant to the secondary neutrino flux, whereas in Scenario II it accounts for all events except those comprising the excess in the range $\sim 50-100$ TeV. The difference in m_ϕ in the two cases is due to the variation in the values of $\langle y \rangle$ for the two type of mediators.

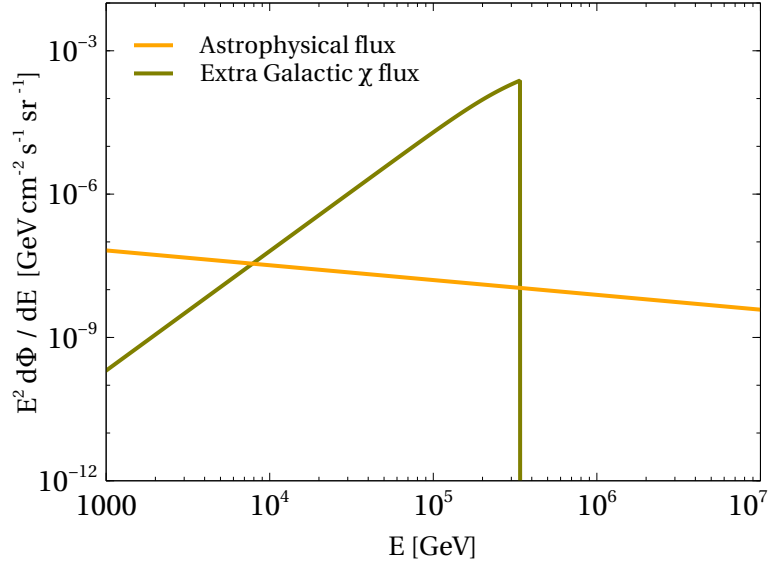


Figure 5.14: Relevant fluxes for Scenario II. The corresponding parameters are given in Table 5.4. As before the monochromatic spike at $m_\phi/2$ due to the galactic χ flux is not shown here.

5.4.1 Gamma-ray constraints on Scenario II

As for Scenario I, the diffuse gamma-ray constraints provide the most significant restrictions on our parameter space, and lead to upper bounds on $f_\phi g_\chi^2 / \tau_\phi$. The behaviour of the differential γ -ray flux is sensitive to the mediator mass and the type of mediator under study, as shown in Fig. 5.16. Using results on the diffuse gamma ray fluxes from Fermi-LAT, KASCADE and GRAPES3 data, we obtain upper bounds on $f_\phi g_\chi^2 / \tau_\phi$ for the pseudo-scalar and axial-vector cases, respectively, as follows :

$$\frac{(g_\chi^2 f_\phi)}{\tau_\phi} \leq \begin{cases} 5.2 \times 10^{-27} \text{ s}^{-1} & \text{for the pseudo-scalar case} \\ 1.2 \times 10^{-29} \text{ s}^{-1} & \text{for the axial-vector case} \end{cases} \quad (5.15)$$

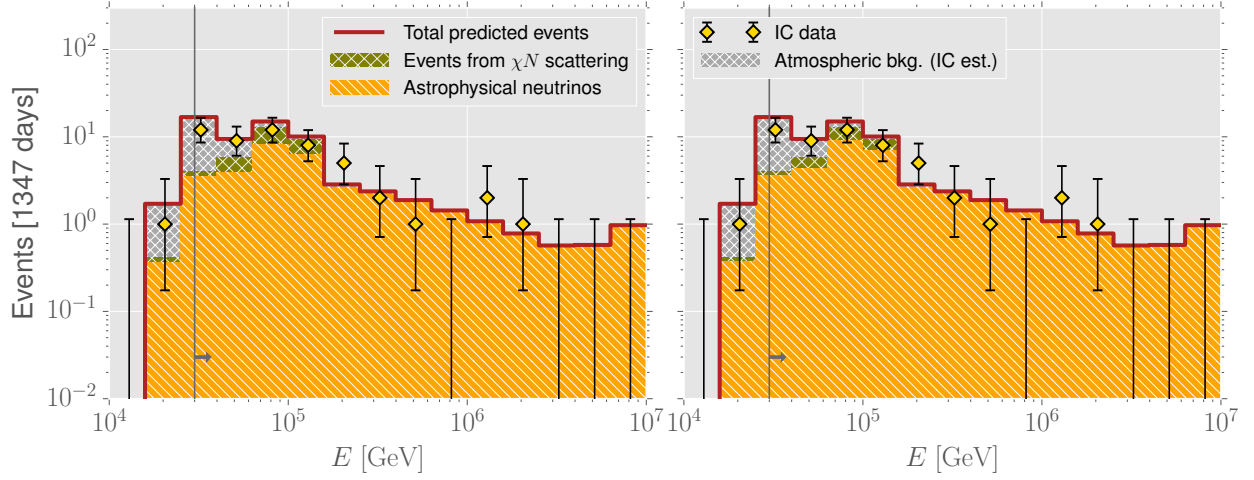


Figure 5.15: The total event rate is shown as the red solid curve. This comprises events from LDM scattering, astrophysical neutrinos and the atmospheric background. Events from the astrophysical power-law spectrum are shown as orange bars and stacked bars shaded in green show the LDM events over and above the astrophysical events. The other events over and above the green/yellow bars are due to atmospheric neutrinos and muons. The left hand side shows the pseudo-scalar case while the right hand side gives the case of an axial-vector type mediator.

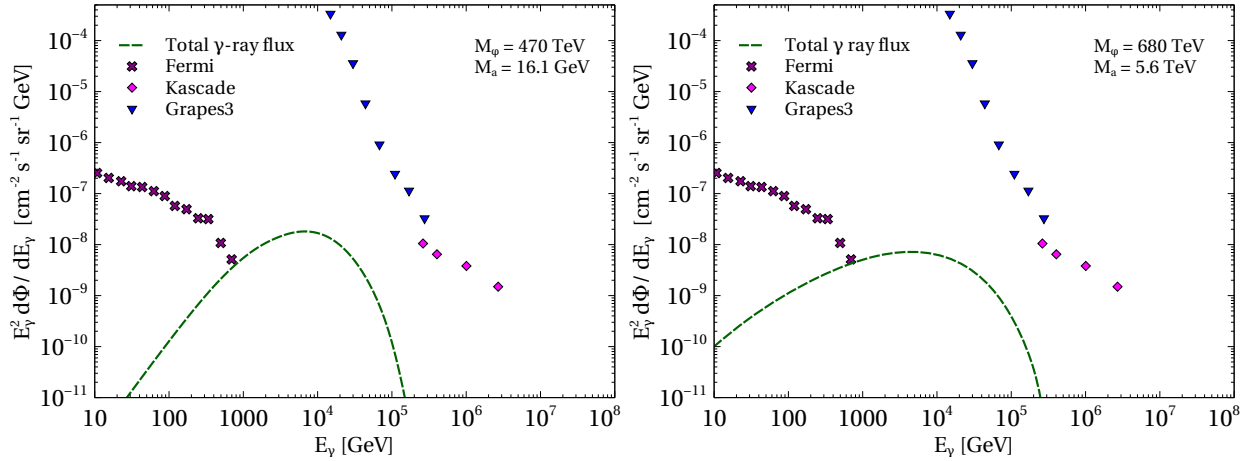


Figure 5.16: Diffuse gamma-ray flux for pseudo-scalar (left) and axial-vector case (right). The maximum allowed values of $(f_\phi g_\chi^2)/\tau_\phi$ have been used for the flux computation here.

The upper bounds on F that result from the above are significantly more stringent for the axial-vector case, and rule out the best-fit case shown in Fig. 5.15 for this mediator. The best-fit shown for the pseudo-scalar case is broadly consistent with the current gamma-

ray constraints.

5.5 Muon-Track events

Our discussion so far has been confined to the HESE events, whose starting vertices are, by definition, contained within the IC instrumented volume. More recently, however, a 6-year analysis of through-going muon track events at IC has been reported [351]. The events in this data sample include those with interaction vertices outside this volume. There are events both in the PeV and the sub-PeV regions. When fit with a uniform astrophysical power-law flux, this sample prefers a stronger astrophysical spectrum, with $\gamma = 2.13 \pm 0.13$. This is notably different from the conclusion from the HESE analysis, which suggests $\gamma = 2.57$, whilst disfavouring a spectrum with $\gamma = 2.0$ at more than 3σ . This tension could, perhaps be a hint for additional flux components which cannot be accounted for in a simple power-law picture. Indeed, as pointed out in [351], a possible reason for the tension could be a flux component from galactic sources, which becomes sub-dominant as the energy increases. We note that the secondary neutrino flux from the galaxy, which dominates the sub-PeV contribution in Scenario I, is a possibility that conforms to this requirement.

While we have not attempted a full comparative study of this sample in the context of our scenarios here, we have tried to get an approximate idea of the track event predictions that Scenario I and II would give. In Scenario I, for example, contributions to these events would arise from the secondary neutrino and astrophysical fluxes. We can then compare the predicted event rates with those predicted by the IC best-fit astrophysical flux (with index 2.13, from [351]). We show the comparisons in Fig. 5.17 for the pseudoscalar mediator in Scenario I. The through-going track events span the energy range from 190 TeV to a few PeV [351]. For both the cases when pseudoscalar $a \rightarrow b\bar{b}$ and $a \rightarrow c\bar{c}$ we have taken a value of $f_\phi g_\chi^2/\tau_\phi$ which satisfies all constraints. For the astrophysical flux, the values of the index and the normalisations were however fixed to their best-fit values (Fig. 5.17).

We find good overlap with the IC prediction (*i.e.*, the red and black curves) in the lower part of the energy range of interest, *i.e.* 190 TeV to ~ 600 TeV (where most of the observations lie); however, for higher energies the curves differ, and Scenario I predicts substantially less through-going muon track events. We note that statistics in higher energy region are sparse, making definitive conclusions difficult. In the multi-PeV region, for instance, the highest energy event in this 6-yr sample [351], has a deposited energy of ~ 2.6 PeV, and an estimated muon energy of about 4.5 PeV. It is difficult to say if this is an unusually high energy event isolated in origin from the rest; for a detailed discussion

of possibilities, see [372].

Similarly, we show the IC prediction along with the expectation for Scenario II in Fig 5.18. Although our Scenario II flux is somewhat lower than the IC fit, the agreement overall is reasonable (given the present level of statistics), since the astrophysical power-law flux is a dominant contributor in Scenario II, unlike in Scenario I. Further confirmation will have to await more data, especially in the high energy region ($E_\nu \geq 3$ PeV).

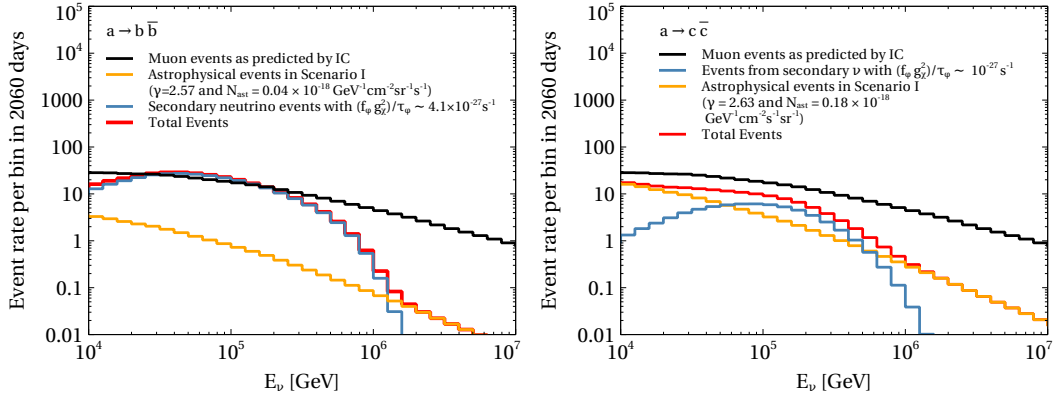


Figure 5.17: Muon track events for the pseudoscalar case in Scenario I and their comparison with the IC predicted best fit. The black line represents the IC power-law prediction and should be compared to our total prediction for throughgoing track events in the energy region 190 TeV to a few PeV (red line).

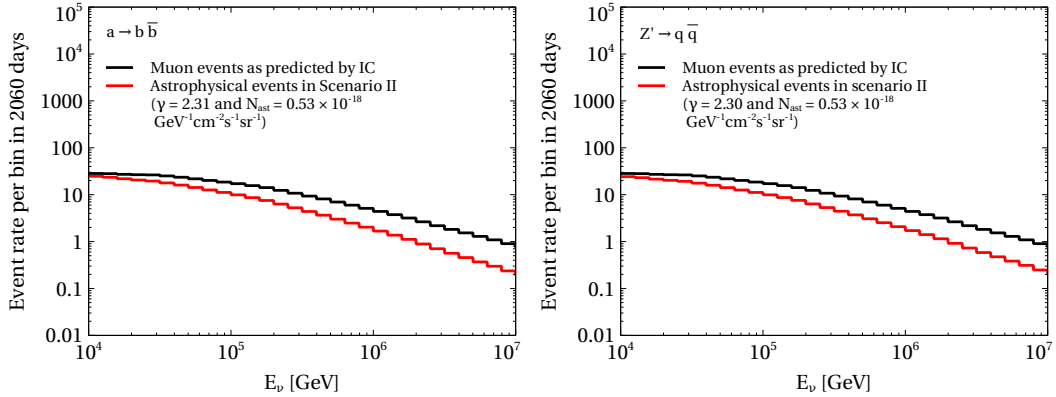


Figure 5.18: Muon track events in Scenario II. Shown for the case of pseudoscalar (left) and axial-vector type mediators (right). In Scenario II, the astrophysical flux is the main contributor to the track events. In our notation $\Phi_{ast} = N_{ast} E^{-\gamma}$. Best fit values of N_{ast} and γ are used in the above plot.

5.6 Summary and Conclusions

By steadily accumulating high energy events over the last four years in the energy range 30 TeV to 2 PeV, IC has conclusively established the presence of a diffuse flux or fluxes which have a non-atmospheric origin and (at least partially) extra-galactic origin, the source(s) of which are at present largely unknown.

Standard expectations dictate that this signal is due to a flux of astrophysical neutrinos, primarily from sources outside of our galaxy, and that it should correspond to a uniform power-law flux, characteristic of Fermi shock acceleration, with index approximately -2 . Features in the data seem to indicate that there are deviations from these expectations, which may signal the presence of one or more additional fluxes. These features include a) a lack of cascade events beyond 2.1 PeV, in spite of both IC's sensitivity in this region, and the presence of the Glashow resonance around 6.3 PeV; b) a possible dip in the spectrum between 400 TeV–1 PeV; c) a low energy excess of around 2.3σ significance over and above the IC best-fit power-law spectrum in the energy range 50–100 TeV. In addition, an overall puzzling feature of the flux is its unexpected proximity to the WB bound, since standard expectations would argue for a neutrino flux that is a factor of a few below this upper limit.

In this work, we have explored the idea that some of the events in IC which cause the overall signal to deviate from the standard power-law originate from the scattering of boosted DM on ice. We have considered two scenarios, both involving the incidence of such fermionic dark matter (LDM), which is produced (in the context of a minimal two-component dark matter sector) from the slow decay of its (significantly) heavier cousin (HDM). The LDM, upon scattering off the ice-nuclei inside IC, mimicks standard model neutrino-nucleon neutral current scattering, but, in general, with weaker interaction strengths. If the HDM has a mass $\sim 5\text{--}10$ PeV, the LDM flux can be shown to peak in a cluster around the 1–2 PeV energies and, with the right parameters, can explain the IC PeV events. This forms the basis of Scenario I, which accounts for the rest of the events (at sub-PeV energies), by a combination of those from astrophysical sources and a secondary neutrino flux originating from the decay of the mediator involved in the LDM-nucleon scattering. It is interesting to note that the secondary neutrinos naturally provide a bump in the region 30–100 TeV once the parameters for the three PeV events from LDM scattering are fixed.

On the other hand, in Scenario II, for lighter masses of the HDM $\sim 500\text{--}800$ TeV, the LDM flux leads to scattering events in the sub-PeV $\sim 30\text{--}100$ TeV energies and is helpful in explaining this low-energy excess over and above a harder (compared to Scenario I)

astrophysical power-law flux. In both scenarios, in order to explain observations, our work incorporates the *direct* detection of boosted DM by IC, in addition to its detecting UHE neutrinos. This allows the standard astrophysical flux to stay appreciably below the WB bound for Scenario I, and, to a lesser extent, for Scenario II.

Four different mediators which connect the SM and DM sectors are considered, specifically, scalar, pseudo-scalar, vector and axial-vector. For Scenario I, we find excellent fits to the IC data in both spin-0 mediator cases — the LDM scattering explains the three PeV events with a hard cut-off set by the HDM mass. It has a soft astrophysical power-law flux that dies out around energies of 400 TeV, and a small but significant neutrino flux from the decay of the mediator that helps explain the small bump around 30-100 TeV, making the full spectrum a better match to the data than a power-law-only spectrum. However, for the pseudo-scalar, stringent constraints from γ -ray observations rule out the region of parameter space where the best-fit itself lies. The allowed 3σ parameter-space region around the best-fit is quite large, nevertheless, and we find that a significant portion of this is as yet allowed by the γ -ray bounds.

For spin-1 mediators, in Scenario I we find significantly increased tension between constraints and best-fit parameters in the vector mediator case, but are, nevertheless, able to fit the IC data well for specific values of the parameters within the allowed regions. The case for the axial-vector mediator is, unfortunately, more pessimistic: we find that perturbativity requirements on the coupling constants prevent a simultaneous fit to the observed PeV and sub-PeV data.

If, with future data, Scenario I were to sustain, we would expect to see a gradual statistical improvement in the evidence for a dip-like structural feature around 400-800 TeV, since this region marks the interface of fluxes of different origins. One would see a paucity of events beyond 2.1 PeV, due to a significantly lower astrophysical flux compared to current IC predictions. In addition, a PeV event spectrum predominantly from LDM scattering (due to HDM decay) predicts i) a significantly enhanced ratio of cascade-to-track events approximately in the (0.75-2.5 PeV) region, ii) a build-up in the number of such cascade events in this region as the HDM decay and LDM scattering proceed, and iii) a small but non-zero number of up-going cascades in this energy region over time from the northern hemisphere compared to the case where these events would have been due to a neutrino flux (because of the relatively lower χ -nucleon cross section and consequent reduced screening by the earth.)¹⁰. Finally, through-going muon track events beyond ~ 3 PeV are also expected to be lower in number in this scenario than what current IC power-

¹⁰We note that IC has already observed an *upgoing* cascade in this energy region, with deposited energy 0.77 ± 0.22 PeV [373]

law fit predictions suggest. The overall signal would also exhibit a gradual galactic bias with more statistics, since generically, in DM scenarios, the contributions from our galaxy and from extra-galactic DM are roughly of the same order. Such a directional bias is not expected in a genuinely isotropic flux¹¹. These features would be in contrast to what one would expect to see if the standard astrophysical power-law flux explanation were indeed responsible for the observed events and will be discernable as statistics increase.

Scenario II, on the other hand, is designed to explain only the event excess at 50–100 TeV energies as being due to DM scattering on ice, with the other events, including those above 1 PeV, attributed to an astrophysical neutrino power-law spectrum. It thus assumes that the other features, including the 400–800 TeV dip and the existence of a cut-off beyond ~ 2 PeV, which are part of Scenario I, would gradually disappear and smooth out over time. It is in good agreement with the HESE data, and because it requires a harder astrophysical spectrum to explain the highest energy events, it is also in better agreement with IC’s six-year through-going muon track data. Indeed, its predictions for both cascade and track events (both starting and through-going) are only slightly below those of the official IC fits. The secondary neutrinos produced from the decays of the mediator in this scenario peak at energies around a TeV and lie in a region dominated by the conventional atmospheric background. They are thus not consequential to our considerations here. With respect to the different types of mediators, this scenario is somewhat less constrained over-all compared to Scenario I. The best-fits we obtain for the vector and axial-vector cases are disallowed by gamma-ray observations; nevertheless, good fits in the 3σ region are possible. The scalar and pseudo-scalar mediators make for better agreement, with their best-fits being allowed.

To conclude, we have shown that present differences in the IC data in comparison to what is expected from standard astrophysical diffuse neutrino fluxes may be explained by assuming that the full spectrum is made up of multiple flux components, with one significant component being the flux of a boosted DM particle. Depending on the HDM mass, the LDM flux either peaks at PeV energies (Scenario I) and explains the PeV events in the 4-yr HESE sample, or at lower energies (Scenario II) and aids in explaining the 50–100 TeV excess. In Scenario I, the excess at 50–100 TeV is naturally accounted for by a secondary neutrino flux from HDM decay. In both cases, the different components conspire in ways that explain the IC data better than any single component flux can. This is in spite of strong constraints from γ -ray observations, which limit but do not completely ex-

¹¹ We stress that in our scenario also, the events due to the astrophysical neutrino flux (Flux-1) will be isotropic in distribution. The directional bias will be exhibited by only those events that originate in DM (Flux-2 and Flux-3).

clude the available 3σ parameter space around the corresponding best-fits. On this note, it is worth mentioning that our work skirts the recent strong constraints [357] on masses and lifetimes of heavy DM decays as explanations of IC events, as they apply to scenarios in which such DM decays directly to SM particles. Finally, we have also discussed signatures that would, with future data, help distinguish each case under consideration from fits with a solely uniform power-law flux. More data over the next few years should be able to conclusively support or veto such multi-component explanations of high-energy observations at IC compared to other, more standard expectations.

Chapter 6

Conclusion

In this thesis, we have studied some aspects of non-thermal dark matter. Non-thermal dark matter scenarios are a new area of investigation for dark matter physicists. Null results from various direct detection experiments which hunt for thermal WIMPs, have led us to consider an altogether different mode of dark matter production. We have investigated how to calculate relic density (along with other quantities of physical interest) of such non-thermal dark matter (under framework of some specific models). Also, since due to very low interaction strengths direct detection of non-thermal candidates is difficult, we have tried to explore some indirect and roundabout ways to detect these feebly interacting particles.

6.1 Non-thermal dark matter in $U(1)_{B-L}$ model

In chapter 2, we have taken-up a well studied and well motivated extension of Standard Model ($U(1)_{B-L}$) and examined whether it can incorporate a non-thermal sterile neutrino dark matter. We have taken the lightest of the three sterile neutrinos as our non-thermal dark matter candidate. Its principle production modes were found to be the decays of W^\pm and Z_{BL} . Of these the latter itself being out of equilibrium (due to very small g_{BL}), we had to solve for coupled set of Boltzmann equations (rate equations). Different relevant constraints were checked as well. A possible way of indirectly detecting this sterile neutrino non-thermal dark matter was also proposed exploiting its three-body decay $N_1 \rightarrow e^+e^-\nu$. It was shown that the 511 keV flux can indeed be explained well in this scenario.

6.2 Calculation of momentum distribution functions of non-thermal dark matter

The methodology for calculation of relic density as discussed in chapter 2 is valid only if we are not too far away from the thermal scenario and this assumption was indeed true for the benchmarks considered therein. However, since this cannot be guaranteed at all times, we showed in chapter 3 how to find the final relic density of dark matters by solving directly for the non-thermal distribution functions themselves. We took a new type of $U(1)_{B-L}$ model this time for demonstrating the technique. This model, unlike the usual $U(1)_{B-L}$ described in chapter 2, instead of having three right handed neutrinos for anomaly cancellation, has four new chiral fermions with appropriate charges. However, the technique presented here is in general applicable to other $U(1)_X$ models as well. As before, we also checked validity of our models in view constraints arising from various aspects like number of extra relativistic degrees of freedom during BBN, invisible decay of extra Z-boson etc.

6.3 Boosted dark matter scenarios

Having developed a detailed framework as how to calculate the relic density of dark matter along with other physical observables in case of a system far from (or approximately near) an equilibrium one, we then turned into systematic study of detecting these non-thermal particles. We shift our perspective now from the details of non-thermal dark matters or the models that can explain it. Instead we take its relic density to be a free parameter and perform a phenomenological study. We turn to IceCube neutrino detector and its observation of ultra high energy events (energy \sim PeV) for hints of detecting dark matter. A dark sector was proposed in chapter 4 which consist of a non-thermal candidate with mass of $\mathcal{O}(\text{PeV})$ (Φ), and a much lighter one of mass $\ll \text{PeV}$ (χ). χ is predominantly produced non-thermally from the late time two body decay of Φ ($\Phi \rightarrow \bar{\chi}\chi$). Hence, the lighter (relativistic) component forms only a small portion of the total dark matter energy budget of the universe, with the heavy one contributing the most. The boosted lighter dark matter hits the ice nucleus with very high energies and shatters it producing Cherenkov radiation detectable by the experimental set-up. Assuming a typical Z' portal interaction of the lighter species with quarks, we were able to explain the IceCube ultra high energy events and its features. We have shown that these dark matter events can indeed clone a neutrino-nucleon event and in this respect we have proposed

a new method of directly detecting a low mass (boosted) dark matter in the ultra high energy regime. This in turn will also lead to an indirect confirmation of the presence of the heavy non-thermal PeV dark matter.

In chapter 5 however, we did a more robust analysis by studying the implications of different types of mediator (mediating the lighter dark matter with quarks) in explaining the IceCube data. This time we used 4 years of IceCube data (in chapter 4 we used 3 years of data) which have few more new features along with a possible excess around TeV energies. We tried to explain all of these features along with the TeV excess by our boosted dark matter scenarios. In the process some mediators proved to be more effective than the others. We also looked into constraints arising from diffuse gamma ray fluxes and they were found to be quite restrictive as well.

Thus, in summary, we have studied methodologies of calculating the relic densities of non-thermal dark matters as well solving for the non-thermal distributions functions. Along with this, we have also proposed a boosted two component dark matter scenario and analysed the same in the setting of IceCube data. We have shown that it is possible to detect a heavy non-thermal dark matter candidate indirectly via the direct detection of the lighter one.

Bibliography

- [1] V. C. Rubin and W. K. Ford, Jr., *Rotation of the Andromeda Nebula from a Spectroscopic Survey of Emission Regions*, *apj* **159** (Feb., 1970) 379.
- [2] M. Markevitch, *Chandra observation of the most interesting cluster in the universe*, [astro-ph/0511345](#).
- [3] D. Clowe, M. Bradac, A. H. Gonzalez, M. Markevitch, S. W. Randall, C. Jones et al., *A direct empirical proof of the existence of dark matter*, *Astrophys. J.* **648** (2006) L109–L113, [[astro-ph/0608407](#)].
- [4] R. H. Cyburt, B. D. Fields, K. A. Olive and T.-H. Yeh, *Big Bang Nucleosynthesis: 2015*, *Rev. Mod. Phys.* **88** (2016) 015004, [[1505.01076](#)].
- [5] PLANCK collaboration, P. A. R. Ade et al., *Planck 2015 results. XIII. Cosmological parameters*, *Astron. Astrophys.* **594** (2016) A13, [[1502.01589](#)].
- [6] SUPERNOVA COSMOLOGY PROJECT collaboration, M. Kowalski et al., *Improved Cosmological Constraints from New, Old and Combined Supernova Datasets*, *Astrophys. J.* **686** (2008) 749–778, [[0804.4142](#)].
- [7] M. Tegmark, M. Zaldarriaga and A. J. S. Hamilton, *Towards a refined cosmic concordance model: Joint 11 parameter constraints from CMB and large scale structure*, *Phys. Rev.* **D63** (2001) 043007, [[astro-ph/0008167](#)].
- [8] E. Kolb and M. Turner, *The Early Universe*, .
- [9] XENON collaboration, E. Aprile et al., *First Dark Matter Search Results from the XENON1T Experiment*, [1705.06655](#).
- [10] P. Cushman et al., *Working Group Report: WIMP Dark Matter Direct Detection*, in *Proceedings, 2013 Community Summer Study on the Future of U.S. Particle Physics:*

Snowmass on the Mississippi (CSS2013): Minneapolis, MN, USA, July 29-August 6, 2013, 2013. [1310.8327](#).

- [11] N. Bernal, M. Heikinheimo, T. Tenkanen, K. Tuominen and V. Vaskonen, *The Dawn of FIMP Dark Matter: A Review of Models and Constraints*, [1706.07442](#).
- [12] L. J. Hall, K. Jedamzik, J. March-Russell and S. M. West, *Freeze-In Production of FIMP Dark Matter*, *JHEP* **03** (2010) 080, [[0911.1120](#)].
- [13] U. o. W. Francis Halzen, Department of Physics, *IceCube Science Team*, .
- [14] ICECUBE collaboration, M. G. Aartsen et al., *Observation of High-Energy Astrophysical Neutrinos in Three Years of IceCube Data*, *Phys. Rev. Lett.* **113** (2014) 101101, [[1405.5303](#)].
- [15] ICECUBE collaboration, M. G. Aartsen et al., *The IceCube Neutrino Observatory - Contributions to ICRC 2015 Part II: Atmospheric and Astrophysical Diffuse Neutrino Searches of All Flavors*, in *Proceedings, 34th International Cosmic Ray Conference (ICRC 2015)*, 2015. [1510.05223](#).
- [16] F. Zwicky, *Die Rotverschiebung von extragalaktischen Nebeln*, *Helvetica Physica Acta* **6** (1933) 110–127.
- [17] V. C. Rubin and W. K. Ford, Jr., *Rotation of the Andromeda Nebula from a Spectroscopic Survey of Emission Regions*, *apj* **159** (Feb., 1970) 379.
- [18] F. D. Kahn and L. Woltjer, *Intergalactic Matter and the Galaxy.*, *apj* **130** (Nov., 1959) 705.
- [19] J. P. Ostriker, P. J. E. Peebles and A. Yahil, *The size and mass of galaxies, and the mass of the universe*, *apj* **193** (Oct., 1974) L1–L4.
- [20] V. C. Rubin, D. Burstein, W. K. Ford, Jr. and N. Thonnard, *Rotation velocities of 16 SA galaxies and a comparison of Sa, Sb, and SC rotation properties*, .
- [21] V. C. Rubin, N. Thonnard and W. K. Ford, Jr., *Extended rotation curves of high-luminosity spiral galaxies. IV - Systematic dynamical properties, SA through SC*, .
- [22] J. A. Tyson, G. P. Kochanski and I. P. Dell’Antonio, *Detailed mass map of CL0024+1654 from strong lensing*, *Astrophys. J.* **498** (1998) L107, [[astro-ph/9801193](#)].

- [23] H. Hoekstra, *Weak gravitational lensing*, *Proc. Int. Sch. Phys. Fermi* **186** (2014) 59–100, [[1312.5981](#)].
- [24] D. Clowe, M. Bradac, A. H. Gonzalez, M. Markevitch, S. W. Randall, C. Jones et al., *A direct empirical proof of the existence of dark matter*, *Astrophys. J.* **648** (2006) L109–L113, [[astro-ph/0608407](#)].
- [25] R. Cooke, M. Pettini, R. A. Jorgenson, M. T. Murphy and C. C. Steidel, *Precision measures of the primordial abundance of deuterium*, *Astrophys. J.* **781** (2014) 31, [[1308.3240](#)].
- [26] R. H. Cyburt, B. D. Fields, K. A. Olive and T.-H. Yeh, *Big Bang Nucleosynthesis: 2015*, *Rev. Mod. Phys.* **88** (2016) 015004, [[1505.01076](#)].
- [27] R. H. Cyburt, B. D. Fields and K. A. Olive, *An Update on the big bang nucleosynthesis prediction for Li-7: The problem worsens*, *JCAP* **0811** (2008) 012, [[0808.2818](#)].
- [28] B. D. Fields, P. Molaro and S. Sarkar, *Big-Bang Nucleosynthesis*, *Chin. Phys.* **C38** (2014) 339–344, [[1412.1408](#)].
- [29] SDSS collaboration, W. J. Percival et al., *Baryon Acoustic Oscillations in the Sloan Digital Sky Survey Data Release 7 Galaxy Sample*, *Mon. Not. Roy. Astron. Soc.* **401** (2010) 2148–2168, [[0907.1660](#)].
- [30] S. D. McDermott, H.-B. Yu and K. M. Zurek, *Turning off the Lights: How Dark is Dark Matter?*, *Phys. Rev.* **D83** (2011) 063509, [[1011.2907](#)].
- [31] K. Kadota, T. Sekiguchi and H. Tashiro, *A new constraint on millicharged dark matter from galaxy clusters*, [1602.04009](#).
- [32] LUX collaboration, D. S. Akerib et al., *First results from the LUX dark matter experiment at the Sanford Underground Research Facility*, *Phys. Rev. Lett.* **112** (2014) 091303, [[1310.8214](#)].
- [33] A. Loeb and N. Weiner, *Cores in Dwarf Galaxies from Dark Matter with a Yukawa Potential*, *Phys. Rev. Lett.* **106** (2011) 171302, [[1011.6374](#)].
- [34] M. Vogelsberger, J. Zavala and A. Loeb, *Subhaloes in Self-Interacting Galactic Dark Matter Haloes*, *Mon. Not. Roy. Astron. Soc.* **423** (2012) 3740, [[1201.5892](#)].

- [35] J. Zavala, M. Vogelsberger and M. G. Walker, *Constraining Self-Interacting Dark Matter with the Milky Way's dwarf spheroidals*, *Mon. Not. Roy. Astron. Soc.* **431** (2013) L20–L24, [[1211.6426](#)].
- [36] S. De Lope Amigo, W. M.-Y. Cheung, Z. Huang and S.-P. Ng, *Cosmological Constraints on Decaying Dark Matter*, *JCAP* **0906** (2009) 005, [[0812.4016](#)].
- [37] S. Banerjee, A. Bhattacharyya, S. K. Ghosh, S. Raha, B. Sinha and H. Toki, *Massive Compact Halo Objects from the relics of the cosmic quark - hadron transition*, *Mon. Not. Roy. Astron. Soc.* **340** (2003) 284, [[astro-ph/0211560](#)].
- [38] MACHO collaboration, C. Alcock et al., *The MACHO project: Microlensing results from 5.7 years of LMC observations*, *Astrophys. J.* **542** (2000) 281–307, [[astro-ph/0001272](#)].
- [39] K. Freese, B. Fields and D. Graff, *Limits on stellar objects as the dark matter of our halo: nonbaryonic dark matter seems to be required*, *Nucl. Phys. Proc. Suppl.* **80** (2000) 0305, [[astro-ph/9904401](#)].
- [40] B. D. Fields, K. Freese and D. S. Graff, *Chemical abundance constraints on white dwarfs as halo dark matter*, *Astrophys. J.* **534** (2000) 265–276, [[astro-ph/9904291](#)].
- [41] EROS-2 collaboration, P. Tisserand et al., *Limits on the Macho Content of the Galactic Halo from the EROS-2 Survey of the Magellanic Clouds*, *Astron. Astrophys.* **469** (2007) 387–404, [[astro-ph/0607207](#)].
- [42] J. R. Primack and M. A. K. Gross, *Hot dark matter in cosmology*, [astro-ph/0007165](#).
- [43] *Review on dark matter*, PDG (2015) .
- [44] G. Jungman, M. Kamionkowski and K. Griest, *Supersymmetric dark matter*, *Phys. Rept.* **267** (1996) 195–373, [[hep-ph/9506380](#)].
- [45] H.-C. Cheng, J. L. Feng and K. T. Matchev, *Kaluza-Klein dark matter*, *Phys. Rev. Lett.* **89** (2002) 211301, [[hep-ph/0207125](#)].
- [46] R. Barbieri, L. J. Hall and V. S. Rychkov, *Improved naturalness with a heavy Higgs: An Alternative road to LHC physics*, *Phys. Rev.* **D74** (2006) 015007, [[hep-ph/0603188](#)].
- [47] Y. G. Kim, K. Y. Lee and S. Shin, *Singlet fermionic dark matter*, *JHEP* **05** (2008) 100, [[0803.2932](#)].

- [48] T. Hambye, *Hidden vector dark matter*, *JHEP* **01** (2009) 028, [[0811.0172](#)].
- [49] J. McDonald, *Gauge singlet scalars as cold dark matter*, *Phys. Rev.* **D50** (1994) 3637–3649, [[hep-ph/0702143](#)].
- [50] A. Dutta Banik, D. Majumdar and A. Biswas, *Possible explanation of indirect gamma ray signatures from hidden sector fermionic dark matter*, *Eur. Phys. J.* **C76** (2016) 346, [[1506.05665](#)].
- [51] D. E. Kaplan, M. A. Luty and K. M. Zurek, *Asymmetric Dark Matter*, *Phys. Rev.* **D79** (2009) 115016, [[0901.4117](#)].
- [52] S. Profumo, *Astrophysical Probes of Dark Matter*, in *Proceedings, Theoretical Advanced Study Institute in Elementary Particle Physics: Searching for New Physics at Small and Large Scales (TASI 2012): Boulder, Colorado, June 4-29, 2012*, pp. 143–189, 2013. [1301.0952](#). DOI.
- [53] J. L. Feng and J. Kumar, *The WIMPlless Miracle: Dark-Matter Particles without Weak-Scale Masses or Weak Interactions*, *Phys. Rev. Lett.* **101** (2008) 231301, [[0803.4196](#)].
- [54] P. Gondolo and G. Gelmini, *Cosmic abundances of stable particles: Improved analysis*, *Nucl. Phys.* **B360** (1991) 145–179.
- [55] M. W. Goodman and E. Witten, *Detectability of certain dark-matter candidates*, *Phys. Rev. D* **31** (Jun, 1985) 3059–3063.
- [56] LUX collaboration, D. S. Akerib et al., *Improved Limits on Scattering of Weakly Interacting Massive Particles from Reanalysis of 2013 LUX Data*, *Phys. Rev. Lett.* **116** (2016) 161301, [[1512.03506](#)].
- [57] XENON100 collaboration, E. Aprile et al., *Dark Matter Results from 225 Live Days of XENON100 Data*, *Phys. Rev. Lett.* **109** (2012) 181301, [[1207.5988](#)].
- [58] DARKSIDE collaboration, P. Agnes et al., *Results from the first use of low radioactivity argon in a dark matter search*, *Phys. Rev.* **D93** (2016) 081101, [[1510.00702](#)].
- [59] CoGENT collaboration, C. E. Aalseth et al., *CoGeNT: A Search for Low-Mass Dark Matter using p-type Point Contact Germanium Detectors*, *Phys. Rev.* **D88** (2013) 012002, [[1208.5737](#)].

- [60] CDMS collaboration, R. Agnese et al., *Silicon Detector Dark Matter Results from the Final Exposure of CDMS II*, *Phys. Rev. Lett.* **111** (2013) 251301, [[1304.4279](#)].
- [61] COUPP collaboration, E. Behnke et al., *First Dark Matter Search Results from a 4-kg CF₃I Bubble Chamber Operated in a Deep Underground Site*, *Phys. Rev.* **D86** (2012) 052001, [[1204.3094](#)].
- [62] M. Felizardo et al., *Final Analysis and Results of the Phase II SIMPLE Dark Matter Search*, *Phys. Rev. Lett.* **108** (2012) 201302, [[1106.3014](#)].
- [63] DAMA, LIBRA collaboration, R. Bernabei et al., *New results from DAMA/LIBRA*, *Eur. Phys. J.* **C67** (2010) 39–49, [[1002.1028](#)].
- [64] R. Bernabei et al., *Final model independent result of DAMA/LIBRA-phase1*, *Eur. Phys. J.* **C73** (2013) 2648, [[1308.5109](#)].
- [65] PICO collaboration, C. Amole et al., *Dark Matter Search Results from the PICO-60 C₃F₈ Bubble Chamber*, *Phys. Rev. Lett.* **118** (2017) 251301, [[1702.07666](#)].
- [66] LUX collaboration, D. S. Akerib et al., *Limits on spin-dependent WIMP-nucleon cross section obtained from the complete LUX exposure*, *Phys. Rev. Lett.* **118** (2017) 251302, [[1705.03380](#)].
- [67] E. Behnke et al., *Final Results of the PICASSO Dark Matter Search Experiment*, *Astropart. Phys.* **90** (2017) 85–92, [[1611.01499](#)].
- [68] L. Goodenough and D. Hooper, *Possible Evidence For Dark Matter Annihilation In The Inner Milky Way From The Fermi Gamma Ray Space Telescope*, [0910.2998](#).
- [69] A. Boyarsky, D. Malyshev and O. Ruchayskiy, *A comment on the emission from the Galactic Center as seen by the Fermi telescope*, *Phys. Lett.* **B705** (2011) 165–169, [[1012.5839](#)].
- [70] K. N. Abazajian and M. Kaplinghat, *Detection of a Gamma-Ray Source in the Galactic Center Consistent with Extended Emission from Dark Matter Annihilation and Concentrated Astrophysical Emission*, *Phys. Rev.* **D86** (2012) 083511, [[1207.6047](#)].
- [71] K. N. Abazajian, *The Consistency of Fermi-LAT Observations of the Galactic Center with a Millisecond Pulsar Population in the Central Stellar Cluster*, *JCAP* **1103** (2011) 010, [[1011.4275](#)].

- [72] Q. Yuan and B. Zhang, *Millisecond pulsar interpretation of the Galactic center gamma-ray excess*, *JHEAp* **3-4** (2014) 1–8, [[1404.2318](#)].
- [73] R. M. O’Leary, M. D. Kistler, M. Kerr and J. Dexter, *Young Pulsars and the Galactic Center GeV Gamma-ray Excess*, [1504.02477](#).
- [74] T. Daylan, D. P. Finkbeiner, D. Hooper, T. Linden, S. K. N. Portillo, N. L. Rodd et al., *The characterization of the gamma-ray signal from the central Milky Way: A case for annihilating dark matter*, *Phys. Dark Univ.* **12** (2016) 1–23, [[1402.6703](#)].
- [75] M. J. L. Turner et al., *The European Photon Imaging Camera on XMM-Newton: The MOS cameras*, *Astron. Astrophys.* **365** (2001) L27–35, [[astro-ph/0011498](#)].
- [76] A. Boyarsky, O. Ruchayskiy, D. Iakubovskiy and J. Franse, *Unidentified Line in X-Ray Spectra of the Andromeda Galaxy and Perseus Galaxy Cluster*, *Phys. Rev. Lett.* **113** (2014) 251301, [[1402.4119](#)].
- [77] E. Bulbul, M. Markevitch, A. Foster, R. K. Smith, M. Loewenstein and S. W. Randall, *Detection of An Unidentified Emission Line in the Stacked X-ray spectrum of Galaxy Clusters*, *Astrophys. J.* **789** (2014) 13, [[1402.2301](#)].
- [78] O. Ruchayskiy, A. Boyarsky, D. Iakubovskiy, E. Bulbul, D. Eckert, J. Franse et al., *Searching for decaying dark matter in deep XMM-Newton observation of the Draco dwarf spheroidal*, *Mon. Not. Roy. Astron. Soc.* **460** (2016) 1390–1398, [[1512.07217](#)].
- [79] E. Bulbul, M. Markevitch, A. R. Foster, R. K. Smith, M. Loewenstein and S. W. Randall, *Comment on “Dark matter searches going bananas: the contribution of Potassium (and Chlorine) to the 3.5 keV line”*, [1409.4143](#).
- [80] A. Biswas, D. Majumdar and P. Roy, *Nonthermal two component dark matter model for Fermi-LAT $\bar{\chi}\chi$ -ray excess and 3.55 keV X-ray line*, *JHEP* **04** (2015) 065, [[1501.02666](#)].
- [81] K. S. Babu and R. N. Mohapatra, *7 keV Scalar Dark Matter and the Anomalous Galactic X-ray Spectrum*, *Phys. Rev.* **D89** (2014) 115011, [[1404.2220](#)].
- [82] D. Borah, A. Dasgupta and R. Adhikari, *Common origin of the 3.55 keV x-ray line and the Galactic Center gamma-ray excess in a radiative neutrino mass model*, *Phys. Rev.* **D92** (2015) 075005, [[1503.06130](#)].
- [83] D. Borah, A. Dasgupta and S. Patra, *Common Origin of 3.55 keV X-ray line and Gauge Coupling Unification with Left-Right Dark Matter*, [1604.01929](#).

- [84] T. E. Jeltema and S. Profumo, *Discovery of a 3.5 keV line in the Galactic Centre and a critical look at the origin of the line across astronomical targets*, *Mon. Not. Roy. Astron. Soc.* **450** (2015) 2143–2152, [[1408.1699](#)].
- [85] E. Carlson, T. Jeltema and S. Profumo, *Where do the 3.5 keV photons come from? A morphological study of the Galactic Center and of Perseus*, *JCAP* **1502** (2015) 009, [[1411.1758](#)].
- [86] J. Knodlseder et al., *Early SPI / INTEGRAL constraints on the morphology of the 511 keV line emission in the 4th galactic quadrant*, *Astron. Astrophys.* **411** (2003) L457–L460, [[astro-ph/0309442](#)].
- [87] T. Siegert, R. Diehl, G. Khachatryan, M. G. H. Krause, F. Guglielmetti, J. Greiner et al., *Gamma-ray spectroscopy of Positron Annihilation in the Milky Way*, *Astron. Astrophys.* **586** (2016) A84, [[1512.00325](#)].
- [88] J. Knodlseder et al., *The All-sky distribution of 511 keV electron-positron annihilation emission*, *Astron. Astrophys.* **441** (2005) 513–532, [[astro-ph/0506026](#)].
- [89] L. Boubekur, S. Dodelson and O. Vives, *Cold Positrons from Decaying Dark Matter*, *Phys. Rev.* **D86** (2012) 103520, [[1206.3076](#)].
- [90] E. J. Chun and H. B. Kim, *Axino Light Dark Matter and Neutrino Masses with R-parity Violation*, *JHEP* **10** (2006) 082, [[hep-ph/0607076](#)].
- [91] D. P. Finkbeiner and N. Weiner, *Exciting Dark Matter and the INTEGRAL/SPI 511 keV signal*, *Phys. Rev.* **D76** (2007) 083519, [[astro-ph/0702587](#)].
- [92] D. Hooper, F. Ferrer, C. Boehm, J. Silk, J. Paul, N. W. Evans et al., *Possible evidence for MeV dark matter in dwarf spheroidals*, *Phys. Rev. Lett.* **93** (2004) 161302, [[astro-ph/0311150](#)].
- [93] N. Prantzos et al., *The 511 keV emission from positron annihilation in the Galaxy*, *Rev. Mod. Phys.* **83** (2011) 1001–1056, [[1009.4620](#)].
- [94] R. J. Wilkinson, A. C. Vincent, C. Boehm and C. McCabe, *Ruling out the light WIMP explanation of the galactic 511 keV line*, *Phys. Rev.* **D94** (2016) 103525, [[1602.01114](#)].
- [95] AMS collaboration, M. Aguilar et al., *Antiproton Flux, Antiproton-to-Proton Flux Ratio, and Properties of Elementary Particle Fluxes in Primary Cosmic Rays Measured*

- with the Alpha Magnetic Spectrometer on the International Space Station, *Phys. Rev. Lett.* **117** (2016) 091103.
- [96] M.-Y. Cui, Q. Yuan, Y.-L. S. Tsai and Y.-Z. Fan, Possible dark matter annihilation signal in the AMS-02 antiproton data, *Phys. Rev. Lett.* **118** (2017) 191101, [[1610.03840](#)].
- [97] G. Giesen, M. Boudaud, Y. GÃl'anolini, V. Poulin, M. Cirelli, P. Salati et al., AMS-02 antiprotons, at last! Secondary astrophysical component and immediate implications for Dark Matter, *JCAP* **1509** (2015) 023, [[1504.04276](#)].
- [98] PAMELA collaboration, O. Adriani et al., An anomalous positron abundance in cosmic rays with energies 1.5-100 GeV, *Nature* **458** (2009) 607–609, [[0810.4995](#)].
- [99] FERMI-LAT collaboration, M. Ackermann et al., Measurement of separate cosmic-ray electron and positron spectra with the Fermi Large Area Telescope, *Phys. Rev. Lett.* **108** (2012) 011103, [[1109.0521](#)].
- [100] C.-H. Chen, C.-W. Chiang and T. Nomura, Dark matter for excess of AMS-02 positrons and antiprotons, *Phys. Lett. B* **747** (2015) 495–499, [[1504.07848](#)].
- [101] M. Di Mauro, F. Donato, N. Fornengo, R. Lineros and A. Vittino, Interpretation of AMS-02 electrons and positrons data, *JCAP* **1404** (2014) 006, [[1402.0321](#)].
- [102] XENON collaboration, E. Aprile et al., Physics reach of the XENON1T dark matter experiment, *JCAP* **1604** (2016) 027, [[1512.07501](#)].
- [103] LZ collaboration, D. S. Akerib et al., LUX-ZEPLIN (LZ) Conceptual Design Report, [1509.02910](#).
- [104] C. E. Aalseth et al., The DarkSide Multiton Detector for the Direct Dark Matter Search, *Adv. High Energy Phys.* **2015** (2015) 541362.
- [105] A. Drukier and L. Stodolsky, Principles and Applications of a Neutral Current Detector for Neutrino Physics and Astronomy, *Phys. Rev. D* **30** (1984) 2295.
- [106] P. Cushman et al., Working Group Report: WIMP Dark Matter Direct Detection, in *Proceedings, 2013 Community Summer Study on the Future of U.S. Particle Physics: Snowmass on the Mississippi (CSS2013): Minneapolis, MN, USA, July 29-August 6, 2013*, 2013. [1310.8327](#).
- [107] W. C. Haxton, R. G. Hamish Robertson and A. M. Serenelli, Solar Neutrinos: Status and Prospects, *Ann. Rev. Astron. Astrophys.* **51** (2013) 21–61, [[1208.5723](#)].

- [108] F. Mayet et al., *A review of the discovery reach of directional Dark Matter detection*, *Phys. Rept.* **627** (2016) 1–49, [[1602.03781](#)].
- [109] L. Covi, J. E. Kim and L. Roszkowski, *Axinos as cold dark matter*, *Phys. Rev. Lett.* **82** (1999) 4180–4183, [[hep-ph/9905212](#)].
- [110] L. Covi, H.-B. Kim, J. E. Kim and L. Roszkowski, *Axinos as dark matter*, *JHEP* **05** (2001) 033, [[hep-ph/0101009](#)].
- [111] K.-Y. Choi, J. E. Kim and L. Roszkowski, *Review of axino dark matter*, *J. Korean Phys. Soc.* **63** (2013) 1685–1695, [[1307.3330](#)].
- [112] R. Kallosh, L. Kofman, A. D. Linde and A. Van Proeyen, *Gravitino production after inflation*, *Phys. Rev.* **D61** (2000) 103503, [[hep-th/9907124](#)].
- [113] G. F. Giudice, A. Riotto and I. Tkachev, *Thermal and nonthermal production of gravitinos in the early universe*, *JHEP* **11** (1999) 036, [[hep-ph/9911302](#)].
- [114] E. W. Kolb, D. J. H. Chung and A. Riotto, *WIMPzillas!*, in *Trends in theoretical physics II. Proceedings, 2nd La Plata Meeting, Buenos Aires, Argentina, November 29-December 4, 1998*, pp. 91–105, 1998. [hep-ph/9810361](#).
- [115] H. Baer, K.-Y. Choi, J. E. Kim and L. Roszkowski, *Dark matter production in the early Universe: beyond the thermal WIMP paradigm*, *Phys. Rept.* **555** (2015) 1–60, [[1407.0017](#)].
- [116] B. Shakya, *Sterile Neutrino Dark Matter from Freeze-In*, *Mod. Phys. Lett.* **A31** (2016) 1630005, [[1512.02751](#)].
- [117] J. McDonald, *Thermally generated gauge singlet scalars as selfinteracting dark matter*, *Phys. Rev. Lett.* **88** (2002) 091304, [[hep-ph/0106249](#)].
- [118] C. E. Yaguna, *The Singlet Scalar as FIMP Dark Matter*, *JHEP* **08** (2011) 060, [[1105.1654](#)].
- [119] F. Elahi, C. Kolda and J. Unwin, *UltraViolet Freeze-in*, *JHEP* **03** (2015) 048, [[1410.6157](#)].
- [120] S. B. Roland, B. Shakya and J. D. Wells, *Neutrino Masses and Sterile Neutrino Dark Matter from the PeV Scale*, *Phys. Rev.* **D92** (2015) 113009, [[1412.4791](#)].

- [121] P. S. Bhupal Dev, A. Mazumdar and S. Qutub, *Constraining Non-thermal and Thermal properties of Dark Matter*, *Front.in Phys.* **2** (2014) 26, [[1311.5297](#)].
- [122] M. Endo and F. Takahashi, *Non-thermal Production of Dark Matter from Late-Decaying Scalar Field at Intermediate Scale*, *Phys. Rev.* **D74** (2006) 063502, [[hep-ph/0606075](#)].
- [123] M. Shaposhnikov and I. Tkachev, *The nuMSM, inflation, and dark matter*, *Phys. Lett.* **B639** (2006) 414–417, [[hep-ph/0604236](#)].
- [124] R. N. Mohapatra and G. Senjanović, *Neutrino mass and spontaneous parity nonconservation*, *Phys. Rev. Lett.* **44** (Apr, 1980) 912–915.
- [125] N. Okada and O. Seto, *Higgs portal dark matter in the minimal gauged $U(1)_{B-L}$ model*, *Phys. Rev.* **D82** (2010) 023507, [[1002.2525](#)].
- [126] T. Basak and T. Mondal, *Constraining Minimal $U(1)_{B-L}$ model from Dark Matter Observations*, *Phys. Rev.* **D89** (2014) 063527, [[1308.0023](#)].
- [127] W. Rodejohann and C. E. Yaguna, *Scalar dark matter in the $B\hat{L}\hat{S}L$ model*, *JCAP* **1512** (2015) 032, [[1509.04036](#)].
- [128] A. Biswas, S. Choubey and S. Khan, *Galactic gamma ray excess and dark matter phenomenology in a $U(1)_{B-L}$ model*, *JHEP* **08** (2016) 114, [[1604.06566](#)].
- [129] S. Dodelson and L. M. Widrow, *Sterile-neutrinos as dark matter*, *Phys. Rev. Lett.* **72** (1994) 17–20, [[hep-ph/9303287](#)].
- [130] R. Essig, E. Kuflik, S. D. McDermott, T. Volansky and K. M. Zurek, *Constraining Light Dark Matter with Diffuse X-Ray and Gamma-Ray Observations*, *JHEP* **11** (2013) 193, [[1309.4091](#)].
- [131] X.-D. Shi and G. M. Fuller, *A New dark matter candidate: Nonthermal sterile neutrinos*, *Phys. Rev. Lett.* **82** (1999) 2832–2835, [[astro-ph/9810076](#)].
- [132] S. B. Roland, B. Shakya and J. D. Wells, *PeV neutrinos and a 3.5 keV x-ray line from a PeV-scale supersymmetric neutrino sector*, *Phys. Rev.* **D92** (2015) 095018, [[1506.08195](#)].
- [133] K. Kadota, *Sterile neutrino dark matter in warped extra dimensions*, *Phys. Rev.* **D77** (2008) 063509, [[0711.1570](#)].

- [134] M. Frigerio and C. E. Yaguna, *Sterile Neutrino Dark Matter and Low Scale Leptogenesis from a Charged Scalar*, *Eur. Phys. J.* **C75** (2015) 31, [[1409.0659](#)].
- [135] A. Merle, V. Niro and D. Schmidt, *New Production Mechanism for keV Sterile Neutrino Dark Matter by Decays of Frozen-In Scalars*, *JCAP* **1403** (2014) 028, [[1306.3996](#)].
- [136] A. Merle and M. Totzauer, *keV Sterile Neutrino Dark Matter from Singlet Scalar Decays: Basic Concepts and Subtle Features*, *JCAP* **1506** (2015) 011, [[1502.01011](#)].
- [137] B. Shuve and I. Yavin, *Dark matter progenitor: Light vector boson decay into sterile neutrinos*, *Phys. Rev.* **D89** (2014) 113004, [[1403.2727](#)].
- [138] K. Kaneta, Z. Kang and H.-S. Lee, *Right-handed neutrino dark matter under the BL gauge interaction*, *JHEP* **02** (2017) 031, [[1606.09317](#)].
- [139] G. Gelmini, S. Palomares-Ruiz and S. Pascoli, *Low reheating temperature and the visible sterile neutrino*, *Phys. Rev. Lett.* **93** (2004) 081302, [[astro-ph/0403323](#)].
- [140] G. Gelmini, E. Osoba, S. Palomares-Ruiz and S. Pascoli, *MeV sterile neutrinos in low reheating temperature cosmological scenarios*, *JCAP* **0810** (2008) 029, [[0803.2735](#)].
- [141] S. Khalil and O. Seto, *Sterile neutrino dark matter in B - L extension of the standard model and galactic 511-keV line*, *JCAP* **0810** (2008) 024, [[0804.0336](#)].
- [142] ATLAS collaboration, G. Aad et al., *Observation of a new particle in the search for the Standard Model Higgs boson with the ATLAS detector at the LHC*, *Phys. Lett.* **B716** (2012) 1–29, [[1207.7214](#)].
- [143] CMS collaboration, S. Chatrchyan et al., *Observation of a new boson at a mass of 125 GeV with the CMS experiment at the LHC*, *Phys. Lett.* **B716** (2012) 30–61, [[1207.7235](#)].
- [144] T. Mondal and T. Basak, *Class of Higgs-portal Dark Matter models in the light of gamma-ray excess from Galactic center*, *Phys. Lett.* **B744** (2015) 208–212, [[1405.4877](#)].
- [145] A. Hook, E. Izaguirre and J. G. Wacker, *Model Independent Bounds on Kinetic Mixing*, *Adv. High Energy Phys.* **2011** (2011) 859762, [[1006.0973](#)].
- [146] L. Basso, A. Belyaev, S. Moretti and C. H. Shepherd-Themistocleous, *Phenomenology of the minimal B-L extension of the Standard model: Z' and neutrinos*, *Phys. Rev.* **D80** (2009) 055030, [[0812.4313](#)].

- [147] M. Carena, A. Daleo, B. A. Dobrescu and T. M. P. Tait, *Z' gauge bosons at the Tevatron*, *Phys. Rev.* **D70** (2004) 093009, [[hep-ph/0408098](#)].
- [148] G. Cacciapaglia, C. Csaki, G. Marandella and A. Strumia, *The Minimal Set of Electroweak Precision Parameters*, *Phys. Rev.* **D74** (2006) 033011, [[hep-ph/0604111](#)].
- [149] ATLAS collaboration, G. Aad et al., *Search for high-mass dilepton resonances in pp collisions at $\sqrt{s} = 8$ TeV with the ATLAS detector*, *Phys. Rev.* **D90** (2014) 052005, [[1405.4123](#)].
- [150] L. J. Hall, K. Jedamzik, J. March-Russell and S. M. West, *Freeze-In Production of FIMP Dark Matter*, *JHEP* **03** (2010) 080, [[0911.1120](#)].
- [151] G. Arcadi and L. Covi, *Minimal Decaying Dark Matter and the LHC*, *JCAP* **1308** (2013) 005, [[1305.6587](#)].
- [152] PARTICLE DATA GROUP collaboration, K. A. Olive et al., *Review of Particle Physics*, *Chin. Phys.* **C38** (2014) 090001.
- [153] P. Bechtle, S. Heinemeyer, O. Stål, T. Stefaniak and G. Weiglein, *Probing the Standard Model with Higgs signal rates from the Tevatron, the LHC and a future ILC*, *JHEP* **11** (2014) 039, [[1403.1582](#)].
- [154] A. Boyarsky, J. Lesgourgues, O. Ruchayskiy and M. Viel, *Lyman-alpha constraints on warm and on warm-plus-cold dark matter models*, *JCAP* **0905** (2009) 012, [[0812.0010](#)].
- [155] U. Seljak, A. Makarov, P. McDonald and H. Trac, *Can sterile neutrinos be the dark matter?*, *Phys. Rev. Lett.* **97** (2006) 191303, [[astro-ph/0602430](#)].
- [156] A. Boyarsky, J. Lesgourgues, O. Ruchayskiy and M. Viel, *Realistic sterile neutrino dark matter with keV mass does not contradict cosmological bounds*, *Phys. Rev. Lett.* **102** (2009) 201304, [[0812.3256](#)].
- [157] K. Abazajian, G. M. Fuller and M. Patel, *Sterile neutrino hot, warm, and cold dark matter*, *Phys. Rev.* **D64** (2001) 023501, [[astro-ph/0101524](#)].
- [158] J. Edsjo and P. Gondolo, *Neutralino relic density including coannihilations*, *Phys. Rev.* **D56** (1997) 1879–1894, [[hep-ph/9704361](#)].
- [159] J. R. Primack, *Dark matter and structure formation*, in *Midrasha Mathematicae in Jerusalem: Winter School in Dynamical Systems Jerusalem, Israel, January 12-17, 1997*, 1997. [astro-ph/9707285](#).

- [160] J. Diemand and B. Moore, *The structure and evolution of cold dark matter halos*, *Adv. Sci. Lett.* **4** (2011) 297–310, [[0906.4340](#)].
- [161] C. Picciotto and M. Pospelov, *Unstable relics as a source of galactic positrons*, *Phys. Lett.* **B605** (2005) 15–25, [[hep-ph/0402178](#)].
- [162] Y. Ascasibar, P. Jean, C. Boehm and J. Knoedlseder, *Constraints on dark matter and the shape of the Milky Way dark halo from the 511-keV line*, *Mon. Not. Roy. Astron. Soc.* **368** (2006) 1695–1705, [[astro-ph/0507142](#)].
- [163] C. Boehm, D. Hooper, J. Silk, M. Casse and J. Paul, *MeV dark matter: Has it been detected?*, *Phys. Rev. Lett.* **92** (2004) 101301, [[astro-ph/0309686](#)].
- [164] M. Cirelli, G. Corcella, A. Hektor, G. Hutsi, M. Kadastik, P. Panci et al., *PPPC 4 DM ID: A Poor Particle Physicist Cookbook for Dark Matter Indirect Detection*, *JCAP* **1103** (2011) 051, [[1012.4515](#)].
- [165] A. Denner, S. Heinemeyer, I. Puljak, D. Rebuszi and M. Spira, *Standard Model Higgs-Boson Branching Ratios with Uncertainties*, *Eur. Phys. J.* **C71** (2011) 1753, [[1107.5909](#)].
- [166] S. Patra, W. Rodejohann and C. E. Yaguna, *A new B-L model without right-handed neutrinos*, *JHEP* **09** (2016) 076, [[1607.04029](#)].
- [167] L. Basso, A. Belyaev, S. Moretti and C. H. Shepherd-Themistocleous, *Phenomenology of the minimal B-L extension of the Standard model: Z' and neutrinos*, *Phys. Rev.* **D80** (2009) 055030, [[0812.4313](#)].
- [168] S. L. Adler, *Axial vector vertex in spinor electrodynamics*, *Phys. Rev.* **177** (1969) 2426–2438.
- [169] R. Delbourgo and A. Salam, *The gravitational correction to pcac*, *Phys. Lett.* **B40** (1972) 381–382.
- [170] M. Magg and C. Wetterich, *Neutrino Mass Problem and Gauge Hierarchy*, *Phys. Lett.* **B94** (1980) 61–64.
- [171] G. Lazarides, Q. Shafi and C. Wetterich, *Proton Lifetime and Fermion Masses in an SO(10) Model*, *Nucl. Phys.* **B181** (1981) 287–300.
- [172] R. N. Mohapatra and G. Senjanovic, *Neutrino Masses and Mixings in Gauge Models with Spontaneous Parity Violation*, *Phys. Rev.* **D23** (1981) 165.

- [173] A. Arhrib, R. Benbrik, M. Chabab, G. Moulhaka, M. C. Peyranere, L. Rahili et al., *The Higgs Potential in the Type II Seesaw Model*, *Phys. Rev.* **D84** (2011) 095005, [[1105.1925](#)].
- [174] J. K  nig, A. Merle and M. Totzauer, *keV Sterile Neutrino Dark Matter from Singlet Scalar Decays: The Most General Case*, *JCAP* **1611** (2016) 038, [[1609.01289](#)].
- [175] A. Biswas and A. Gupta, *Freeze-in Production of Sterile Neutrino Dark Matter in $U(1)_{B-L}$ Model*, *JCAP* **1609** (2016) 044, [[1607.01469](#)].
- [176] J. Edsjo and P. Gondolo, *Neutralino relic density including coannihilations*, *Phys. Rev.* **D56** (1997) 1879–1894, [[hep-ph/9704361](#)].
- [177] ATLAS, CMS collaboration, G. Aad et al., *Measurements of the Higgs boson production and decay rates and constraints on its couplings from a combined ATLAS and CMS analysis of the LHC pp collision data at $\sqrt{s} = 7$ and 8 TeV*, *JHEP* **08** (2016) 045, [[1606.02266](#)].
- [178] A. Merle, V. Niro and D. Schmidt, *New Production Mechanism for keV Sterile Neutrino Dark Matter by Decays of Frozen-In Scalars*, *JCAP* **1403** (2014) 028, [[1306.3996](#)].
- [179] A. Biswas and A. Gupta, *Freeze-in Production of Sterile Neutrino Dark Matter in $U(1)_{B-L}$ Model*, *JCAP* **1609** (2016) 044, [[1607.01469](#)].
- [180] K. Kannike, *Vacuum Stability Conditions From Copositivity Criteria*, *Eur. Phys. J.* **C72** (2012) 2093, [[1205.3781](#)].
- [181] D. S. Akerib et al., *Results from a search for dark matter in the complete LUX exposure*, [1608.07648](#).
- [182] H. Vogel and J. Redondo, *Dark Radiation constraints on minicharged particles in models with a hidden photon*, *JCAP* **1402** (2014) 029, [[1311.2600](#)].
- [183] E. W. Kolb and M. S. Turner, *The Early Universe*, *Front. Phys.* **69** (1990) 1–547.
- [184] D. Cline, *A Brief Status of the Direct Search for WIMP Dark Matter*, [1406.5200](#).
- [185] A. Kusenko and L. J. Rosenberg, *Working Group Report: Non-WIMP Dark Matter*, in *Proceedings, 2013 Community Summer Study on the Future of U.S. Particle Physics: Snowmass on the Mississippi (CSS2013): Minneapolis, MN, USA, July 29-August 6, 2013*, 2013. [1310.8642](#).

- [186] K. M. Nollett and G. Steigman, *BBN And The CMB Constrain Neutrino Coupled Light WIMPs*, *Phys. Rev.* **D91** (2015) 083505, [[1411.6005](#)].
- [187] PLANCK collaboration, P. A. R. Ade et al., *Planck 2013 results. XVI. Cosmological parameters*, *Astron. Astrophys.* **571** (2014) A16, [[1303.5076](#)].
- [188] D. Hooper, F. S. Queiroz and N. Y. Gnedin, *Non-Thermal Dark Matter Mimicking An Additional Neutrino Species In The Early Universe*, *Phys. Rev.* **D85** (2012) 063513, [[1111.6599](#)].
- [189] D. Z. Freedman, *Coherent neutrino nucleus scattering as a probe of the weak neutral current*, *Phys. Rev.* **D9** (1974) 1389–1392.
- [190] J. Billard, L. Strigari and E. Figueroa-Feliciano, *Implication of neutrino backgrounds on the reach of next generation dark matter direct detection experiments*, *Phys. Rev.* **D89** (2014) 023524, [[1307.5458](#)].
- [191] K. Griest and M. Kamionkowski, *Unitarity Limits on the Mass and Radius of Dark Matter Particles*, *Phys. Rev. Lett.* **64** (1990) 615.
- [192] R. Gandhi, C. Quigg, M. H. Reno and I. Sarcevic, *Ultrahigh-energy neutrino interactions*, *Astropart. Phys.* **5** (1996) 81–110, [[hep-ph/9512364](#)].
- [193] R. Gandhi, C. Quigg, M. H. Reno and I. Sarcevic, *Neutrino interactions at ultrahigh-energies*, *Phys. Rev.* **D58** (1998) 093009, [[hep-ph/9807264](#)].
- [194] K. Murase and J. F. Beacom, *Constraining Very Heavy Dark Matter Using Diffuse Backgrounds of Neutrinos and Cascaded Gamma Rays*, *JCAP* **1210** (2012) 043, [[1206.2595](#)].
- [195] C. Rott, K. Kohri and S. C. Park, *Superheavy dark matter and IceCube neutrino signals: Bounds on decaying dark matter*, *Phys. Rev.* **D92** (2015) 023529, [[1408.4575](#)].
- [196] K. Ichiki, M. Oguri and K. Takahashi, *WMAP constraints on decaying cold dark matter*, *Phys. Rev. Lett.* **93** (2004) 071302, [[astro-ph/0403164](#)].
- [197] A. Del Popolo, *Dark matter and structure formation a review*, *Astron. Rep.* **51** (2007) 169–196, [[0801.1091](#)].
- [198] A. Esmaili, A. Ibarra and O. L. G. Peres, *Probing the stability of superheavy dark matter particles with high-energy neutrinos*, *JCAP* **1211** (2012) 034, [[1205.5281](#)].

- [199] Y. Bai, R. Lu and J. Salvado, *Geometric Compatibility of IceCube TeV-PeV Neutrino Excess and its Galactic Dark Matter Origin*, [*JHEP* **01** \(2016\) 161](#), [[1311.5864](#)].
- [200] A. Alves, S. Profumo and F. S. Queiroz, *The dark Z' portal: direct, indirect and collider searches*, [*JHEP* **04** \(2014\) 063](#), [[1312.5281](#)].
- [201] D. Hooper, *Z' Mediated Dark Matter Models for the Galactic Center Gamma-Ray Excess*, [*Phys. Rev.* **D91** \(2015\) 035025](#), [[1411.4079](#)].
- [202] H.-L. Lai, M. Guzzi, J. Huston, Z. Li, P. M. Nadolsky, J. Pumplin et al., *New parton distributions for collider physics*, [*Phys. Rev.* **D82** \(2010\) 074024](#), [[1007.2241](#)].
- [203] M. R. Buckley, D. Hooper, J. Kopp and E. Neil, *Light Z' Bosons at the Tevatron*, [*Phys. Rev.* **D83** \(2011\) 115013](#), [[1103.6035](#)].
- [204] M. Kachelriess, P. D. Serpico and M. A. Solberg, *On the role of electroweak bremsstrahlung for indirect dark matter signatures*, [*Phys. Rev.* **D80** \(2009\) 123533](#), [[0911.0001](#)].
- [205] ICECUBE collaboration, M. G. Aartsen et al., *Evidence for High-Energy Extraterrestrial Neutrinos at the IceCube Detector*, [*Science* **342** \(2013\) 1242856](#), [[1311.5238](#)].
- [206] ANTARES collaboration, S. Adrian-Martinez et al., *Searches for Point-like and extended neutrino sources close to the Galactic Centre using the ANTARES neutrino Telescope*, [*Astrophys. J.* **786** \(2014\) L5](#), [[1402.6182](#)].
- [207] V. Scherini, *Updated results on Ultra-High Energy Neutrinos with the Pierre Auger Observatory*, *PoS Neutel2013* (2013) 058.
- [208] KM3NET collaboration, A. Margiotta, *Status of the KM3NeT project*, [*JINST* **9** \(2014\) C04020](#), [[1408.1132](#)].
- [209] J. G. Learned and S. Pakvasa, *Detecting tau-neutrino oscillations at PeV energies*, [*Astropart. Phys.* **3** \(1995\) 267–274](#), [[hep-ph/9405296](#)].
- [210] A. Bhattacharya, R. Gandhi, W. Rodejohann and A. Watanabe, *The Glashow resonance at IceCube: signatures, event rates and pp vs. $p\gamma$ interactions*, [*JCAP* **1110** \(2011\) 017](#), [[1108.3163](#)].
- [211] S. L. Glashow, *Resonant scattering of antineutrinos*, [*Phys. Rev.* **118** \(Apr, 1960\) 316–317](#).

- [212] V. S. Berezinsky and A. Z. Gazizov, *Neutrino - electron scattering at energies above the W boson production threshold*, *Sov. J. Nucl. Phys.* **33** (1981) 120–125.
- [213] J. F. Beacom and J. Candia, *Shower power: Isolating the prompt atmospheric neutrino flux using electron neutrinos*, *JCAP* **0411** (2004) 009, [[hep-ph/0409046](#)].
- [214] S. L. Glashow, *Resonant Scattering of Antineutrinos*, *Phys. Rev.* **118** (1960) 316–317.
- [215] V. Barger, L. Fu, J. G. Learned, D. Marfatia, S. Pakvasa and T. J. Weiler, *Glashow resonance as a window into cosmic neutrino sources*, *Phys. Rev.* **D90** (2014) 121301, [[1407.3255](#)].
- [216] A. M. Taylor, S. Gabici and F. Aharonian, *Galactic halo origin of the neutrinos detected by IceCube*, *Phys. Rev.* **D89** (2014) 103003, [[1403.3206](#)].
- [217] M. Ahlers and K. Murase, *Probing the Galactic Origin of the IceCube Excess with Gamma-Rays*, *Phys. Rev.* **D90** (2014) 023010, [[1309.4077](#)].
- [218] S. Razzaque, *The Galactic Center Origin of a Subset of IceCube Neutrino Events*, *Phys. Rev.* **D88** (2013) 081302, [[1309.2756](#)].
- [219] C. Lunardini, S. Razzaque, K. T. Theodoseou and L. Yang, *Neutrino Events at IceCube and the Fermi Bubbles*, *Phys. Rev.* **D90** (2014) 023016, [[1311.7188](#)].
- [220] M. Kachelrieß and S. Ostapchenko, *Neutrino yield from Galactic cosmic rays*, *Phys. Rev.* **D90** (2014) 083002, [[1405.3797](#)].
- [221] D. B. Fox, K. Kashiyama and P. M̄szar̄ss, *Sub-PeV Neutrinos from TeV Unidentified Sources in the Galaxy*, *Astrophys. J.* **774** (2013) 74, [[1305.6606](#)].
- [222] M. C. Gonzalez-Garcia, F. Halzen and V. Niro, *Reevaluation of the Prospect of Observing Neutrinos from Galactic Sources in the Light of Recent Results in Gamma Ray and Neutrino Astronomy*, *Astropart. Phys.* **57-58** (2014) 39–48, [[1310.7194](#)].
- [223] V. S. Berezinsky, P. Blasi and V. S. Ptuskin, *Clusters of Galaxies as a Storage Room for Cosmic Rays*, *Astrophys. J.* **487** (1997) 529–535, [[astro-ph/9609048](#)].
- [224] A. Loeb and E. Waxman, *The Cumulative background of high energy neutrinos from starburst galaxies*, *JCAP* **0605** (2006) 003, [[astro-ph/0601695](#)].
- [225] K. Murase, M. Ahlers and B. C. Lacki, *Testing the Hadronuclear Origin of PeV Neutrinos Observed with IceCube*, *Phys. Rev.* **D88** (2013) 121301, [[1306.3417](#)].

- [226] H.-N. He, T. Wang, Y.-Z. Fan, S.-M. Liu and D.-M. Wei, *Diffuse PeV neutrino emission from ultraluminous infrared galaxies*, *Phys. Rev.* **D87** (2013) 063011, [[1303.1253](#)].
- [227] F. W. Stecker, C. Done, M. H. Salamon and P. Sommers, *High-energy neutrinos from active galactic nuclei*, *Phys. Rev. Lett.* **66** (1991) 2697–2700.
- [228] F. W. Stecker, *PeV neutrinos observed by IceCube from cores of active galactic nuclei*, *Phys. Rev.* **D88** (2013) 047301, [[1305.7404](#)].
- [229] E. Waxman and J. N. Bahcall, *High-energy neutrinos from cosmological gamma-ray burst fireballs*, *Phys. Rev. Lett.* **78** (1997) 2292–2295, [[astro-ph/9701231](#)].
- [230] K. Murase and K. Ioka, *TeV–PeV Neutrinos from Low-Power Gamma-Ray Burst Jets inside Stars*, *Phys. Rev. Lett.* **111** (2013) 121102, [[1306.2274](#)].
- [231] K. Murase, S. Inoue and S. Nagataki, *Cosmic Rays Above the Second Knee from Clusters of Galaxies and Associated High-Energy Neutrino Emission*, *Astrophys. J.* **689** (2008) L105, [[0805.0104](#)].
- [232] A. Loeb and E. Waxman, *The Cumulative background of high energy neutrinos from starburst galaxies*, *JCAP* **0605** (2006) 003, [[astro-ph/0601695](#)].
- [233] B. Feldstein, A. Kusenko, S. Matsumoto and T. T. Yanagida, *Neutrinos at IceCube from Heavy Decaying Dark Matter*, *Phys. Rev.* **D88** (2013) 015004, [[1303.7320](#)].
- [234] A. Esmaili and P. D. Serpico, *Are IceCube neutrinos unveiling PeV-scale decaying dark matter?*, *JCAP* **1311** (2013) 054, [[1308.1105](#)].
- [235] J. Zavala, *Galactic PeV neutrinos from dark matter annihilation*, *Phys. Rev.* **D89** (2014) 123516, [[1404.2932](#)].
- [236] A. Bhattacharya, M. H. Reno and I. Sarcevic, *Reconciling neutrino flux from heavy dark matter decay and recent events at IceCube*, *JHEP* **06** (2014) 110, [[1403.1862](#)].
- [237] B. Audren, J. Lesgourgues, G. Mangano, P. D. Serpico and T. Tram, *Strongest model-independent bound on the lifetime of Dark Matter*, *JCAP* **1412** (2014) 028, [[1407.2418](#)].
- [238] M. Ahlers and F. Halzen, *Pinpointing Extragalactic Neutrino Sources in Light of Recent IceCube Observations*, *Phys. Rev.* **D90** (2014) 043005, [[1406.2160](#)].

- [239] Y. Ema, R. Jinno and T. Moroi, *Cosmic-Ray Neutrinos from the Decay of Long-Lived Particle and the Recent IceCube Result*, *Phys. Lett.* **B733** (2014) 120–125, [[1312.3501](#)].
- [240] L. A. Anchordoqui, V. Barger, H. Goldberg, J. G. Learned, D. Marfatia, S. Pakvasa et al., *End of the cosmic neutrino energy spectrum*, *Phys. Lett.* **B739** (2014) 99–101, [[1404.0622](#)].
- [241] K. C. Y. Ng and J. F. Beacom, *Cosmic neutrino cascades from secret neutrino interactions*, *Phys. Rev.* **D90** (2014) 065035, [[1404.2288](#)].
- [242] F. W. Stecker and S. T. Scully, *Propagation of Superluminal PeV IceCube Neutrinos: A High Energy Spectral Cutoff or New Constraints on Lorentz Invariance Violation*, *Phys. Rev.* **D90** (2014) 043012, [[1404.7025](#)].
- [243] J. G. Learned and T. J. Weiler, *A Relational Argument for a \sim PeV Neutrino Energy Cutoff*, [1407.0739](#).
- [244] ICECUBE collaboration, M. G. Aartsen et al., *Evidence for High-Energy Extraterrestrial Neutrinos at the IceCube Detector*, *Science* **342** (2013) 1242856, [[1311.5238](#)].
- [245] A. C. Vincent, S. Palomares-Ruiz and O. Mena, *Analysis of the 4-year IceCube HESE data*, [1605.01556](#).
- [246] J. K. Becker, *High-energy neutrinos in the context of multimessenger physics*, *Phys. Rept.* **458** (2008) 173–246, [[0710.1557](#)].
- [247] F. Halzen and D. Hooper, *High-energy neutrino astronomy: The Cosmic ray connection*, *Rept. Prog. Phys.* **65** (2002) 1025–1078, [[astro-ph/0204527](#)].
- [248] G. Sigl, *High Energy Neutrinos and Cosmic Rays*, *Proc. Int. Sch. Phys. Fermi* **182** (2012) 145–184, [[1202.0466](#)].
- [249] M. D. Kistler, T. Stanev and H. YÄijksel, *Cosmic PeV Neutrinos and the Sources of Ultrahigh Energy Protons*, *Phys. Rev.* **D90** (2014) 123006, [[1301.1703](#)].
- [250] N. Gupta, *Galactic PeV Neutrinos*, *Astropart. Phys.* **48** (2013) 75–77, [[1305.4123](#)].
- [251] R. Laha, J. F. Beacom, B. Dasgupta, S. Horiuchi and K. Murase, *Demystifying the PeV Cascades in IceCube: Less (Energy) is More (Events)*, *Phys. Rev.* **D88** (2013) 043009, [[1306.2309](#)].

- [252] L. A. Anchordoqui, H. Goldberg, M. H. Lynch, A. V. Olinto, T. C. Paul and T. J. Weiler, *Pinning down the cosmic ray source mechanism with new IceCube data*, *Phys. Rev. D* **89** (2014) 083003, [[1306.5021](#)].
- [253] L. A. Anchordoqui et al., *Cosmic Neutrino Pevatrons: A Brand New Pathway to Astronomy, Astrophysics, and Particle Physics*, *JHEAp* **1-2** (2014) 1–30, [[1312.6587](#)].
- [254] K. Murase, *On the Origin of High-Energy Cosmic Neutrinos*, *AIP Conf. Proc.* **1666** (2015) 040006, [[1410.3680](#)].
- [255] W. Winter, *Describing the Observed Cosmic Neutrinos by Interactions of Nuclei with Matter*, *Phys. Rev. D* **90** (2014) 103003, [[1407.7536](#)].
- [256] S. Dado and A. Dar, *Origin of the High Energy Cosmic Neutrino Background*, *Phys. Rev. Lett.* **113** (2014) 191102, [[1405.5487](#)].
- [257] I. Cholis and D. Hooper, *On The Origin of IceCube’s PeV Neutrinos*, *JCAP* **1306** (2013) 030, [[1211.1974](#)].
- [258] R.-Y. Liu and X.-Y. Wang, *Diffuse PeV neutrinos from gamma-ray bursts*, *Astrophys. J.* **766** (2013) 73, [[1212.1260](#)].
- [259] S. Razzaque, *Long-lived PeV–EeV neutrinos from gamma-ray burst blastwave*, *Phys. Rev. D* **88** (2013) 103003, [[1307.7596](#)].
- [260] N. Fraija, *GeV–PeV neutrino production and oscillation in hidden jets from gamma-ray bursts*, *Mon. Not. Roy. Astron. Soc.* **437** (2014) 2187–2200, [[1310.7061](#)].
- [261] M. Petropoulou, D. Giannios and S. Dimitrakoudis, *Implications of a PeV neutrino spectral cutoff in GRB models*, *Mon. Not. Roy. Astron. Soc.* **445** (2014) 570–580, [[1405.2091](#)].
- [262] S. Razzaque and L. Yang, *PeV–EeV neutrinos from GRB blast waves in IceCube and future neutrino telescopes*, *Phys. Rev. D* **91** (2015) 043003, [[1411.7491](#)].
- [263] I. Tamborra and S. Ando, *Diffuse emission of high-energy neutrinos from gamma-ray burst fireballs*, *JCAP* **1509** (2015) 036, [[1504.00107](#)].
- [264] N. Senno, K. Murase and P. Meszaros, *Choked Jets and Low-Luminosity Gamma-Ray Bursts as Hidden Neutrino Sources*, *Phys. Rev. D* **93** (2016) 083003, [[1512.08513](#)].

- [265] I. Tamborra and S. Ando, *Inspecting the supernova–gamma-ray-burst connection with high-energy neutrinos*, *Phys. Rev.* **D93** (2016) 053010, [[1512.01559](#)].
- [266] L. A. Anchordoqui, T. C. Paul, L. H. M. da Silva, D. F. Torres and B. J. Vlcek, *What IceCube data tell us about neutrino emission from star-forming galaxies (so far)*, *Phys. Rev.* **D89** (2014) 127304, [[1405.7648](#)].
- [267] I. Tamborra, S. Ando and K. Murase, *Star-forming galaxies as the origin of diffuse high-energy backgrounds: Gamma-ray and neutrino connections, and implications for starburst history*, *JCAP* **1409** (2014) 043, [[1404.1189](#)].
- [268] X.-C. Chang and X.-Y. Wang, *The diffuse gamma-ray flux associated with sub-PeV/PeV neutrinos from starburst galaxies*, *Astrophys. J.* **793** (2014) 131, [[1406.1099](#)].
- [269] I. Bartos and S. Marka, *Spectral Decline of PeV Neutrinos from Starburst Galaxies*, [1509.00983](#).
- [270] O. E. Kalashev, A. Kusenko and W. Essey, *PeV neutrinos from intergalactic interactions of cosmic rays emitted by active galactic nuclei*, *Phys. Rev. Lett.* **111** (2013) 041103, [[1303.0300](#)].
- [271] C. D. Dermer, K. Murase and Y. Inoue, *Photopion Production in Black-Hole Jets and Flat-Spectrum Radio Quasars as PeV Neutrino Sources*, *JHEAp* **3-4** (2014) 29–40, [[1406.2633](#)].
- [272] F. Krauss et al., *TANAMI Blazars in the IceCube PeV Neutrino Fields*, *Astron. Astrophys.* **566** (2014) L7, [[1406.0645](#)].
- [273] F. Tavecchio, G. Ghisellini and D. Guetta, *Structured jets in BL Lac objects: efficient PeV neutrino factories?*, *Astrophys. J.* **793** (2014) L18, [[1407.0907](#)].
- [274] S. Sahu and L. S. Miranda, *Some possible sources of IceCube TeV–PeV neutrino events*, *Eur. Phys. J.* **C75** (2015) 273, [[1408.3664](#)].
- [275] O. Kalashev, D. Semikoz and I. Tkachev, *Neutrinos in IceCube from active galactic nuclei*, *J. Exp. Theor. Phys.* **120** (2015) 541–548, [[1410.8124](#)].
- [276] F. Tavecchio and G. Ghisellini, *High-energy cosmic neutrinos from spine-sheath BL Lac jets*, *Mon. Not. Roy. Astron. Soc.* **451** (2015) 1502–1510, [[1411.2783](#)].

- [277] S. S. Kimura, K. Murase and K. Toma, *Neutrino and Cosmic-Ray Emission and Cumulative Background from Radiatively Inefficient Accretion Flows in Low-Luminosity Active Galactic Nuclei*, *Astrophys. J.* **806** (2015) 159, [[1411.3588](#)].
- [278] M. Petropoulou, S. Dimitrakoudis, P. Padovani, A. Mastichiadis and E. Resconi, *Photohadronic origin of γ -ray BL Lac emission: implications for IceCube neutrinos*, *Mon. Not. Roy. Astron. Soc.* **448** (2015) 2412–2429, [[1501.07115](#)].
- [279] R.-Y. Liu, X.-Y. Wang, S. Inoue, R. Crocker and F. Aharonian, *Diffuse PeV neutrinos from EeV cosmic ray sources: Semirelativistic hypernova remnants in star-forming galaxies*, *Phys. Rev.* **D89** (2014) 083004, [[1310.1263](#)].
- [280] S. Chakraborty and I. Izaguirre, *Diffuse neutrinos from extragalactic supernova remnants: Dominating the 100 TeV IceCube flux*, *Phys. Lett.* **B745** (2015) 35–39, [[1501.02615](#)].
- [281] A. Bhattacharya, R. Enberg, M. H. Reno and I. Sarcevic, *Charm decay in slow-jet supernovae as the origin of the IceCube ultra-high energy neutrino events*, *JCAP* **1506** (2015) 034, [[1407.2985](#)].
- [282] L. A. Anchordoqui, H. Goldberg, T. C. Paul, L. H. M. da Silva and B. J. Vlcek, *Estimating the contribution of Galactic sources to the diffuse neutrino flux*, *Phys. Rev.* **D90** (2014) 123010, [[1410.0348](#)].
- [283] H. Gao, B. Zhang, X.-F. Wu and Z.-G. Dai, *Possible High-Energy Neutrino and Photon Signals from Gravitational Wave Bursts due to Double Neutron Star Mergers*, *Phys. Rev.* **D88** (2013) 043010, [[1306.3006](#)].
- [284] X.-Y. Wang and R.-Y. Liu, *Tidal disruption jets of supermassive black holes as hidden sources of cosmic rays: explaining the IceCube TeV-PeV neutrinos*, *Phys. Rev.* **D93** (2016) 083005, [[1512.08596](#)].
- [285] A. Neronov, D. V. Semikoz and C. Tchernin, *PeV neutrinos from interactions of cosmic rays with the interstellar medium in the Galaxy*, *Phys. Rev.* **D89** (2014) 103002, [[1307.2158](#)].
- [286] J. C. Joshi, W. Winter and N. Gupta, *How Many of the Observed Neutrino Events Can Be Described by Cosmic Ray Interactions in the Milky Way?*, *Mon. Not. Roy. Astron. Soc.* **439** (2014) 3414–3419, [[1310.5123](#)].

- [287] B. Katz, E. Waxman, T. Thompson and A. Loeb, *The energy production rate density of cosmic rays in the local universe is $\sim 10^{44-45}$ erg Mpc $^{-3}$ yr $^{-1}$ at all particle energies*, [1311.0287](#).
- [288] K. Fang, T. Fujii, T. Linden and A. V. Olinto, *Is the Ultra-High Energy Cosmic-Ray Excess Observed by the Telescope Array Correlated with IceCube Neutrinos?*, *Astrophys. J.* **794** (2014) 126, [[1404.6237](#)].
- [289] L. A. Anchordoqui, *Neutron β -decay as the origin of IceCube's PeV (anti)neutrinos*, *Phys. Rev.* **D91** (2015) 027301, [[1411.6457](#)].
- [290] Y. Q. Guo, H. B. Hu and Z. Tian, *On the Contribution of "Fresh" Cosmic Rays to the Excesses of Secondary Particles*, [1412.8590](#).
- [291] F. Zandanel, I. Tamborra, S. Gabici and S. Ando, *High-energy gamma-ray and neutrino backgrounds from clusters of galaxies and radio constraints*, *Astron. Astrophys.* **578** (2015) A32, [[1410.8697](#)].
- [292] Y. Ema, R. Jinno and T. Moroi, *Cosmic-Ray Neutrinos from the Decay of Long-Lived Particle and the Recent IceCube Result*, *Phys. Lett.* **B733** (2014) 120–125, [[1312.3501](#)].
- [293] A. Esmaili, S. K. Kang and P. D. Serpico, *IceCube events and decaying dark matter: hints and constraints*, *JCAP* **1412** (2014) 054, [[1410.5979](#)].
- [294] A. Bhattacharya, M. H. Reno and I. Sarcevic, *Reconciling neutrino flux from heavy dark matter decay and recent events at IceCube*, *JHEP* **06** (2014) 110, [[1403.1862](#)].
- [295] A. Bhattacharya, R. Gandhi and A. Gupta, *The Direct Detection of Boosted Dark Matter at High Energies and PeV events at IceCube*, *JCAP* **1503** (2015) 027, [[1407.3280](#)].
- [296] Y. Ema, R. Jinno and T. Moroi, *Cosmological Implications of High-Energy Neutrino Emission from the Decay of Long-Lived Particle*, *JHEP* **10** (2014) 150, [[1408.1745](#)].
- [297] J. F. Cherry, A. Friedland and I. M. Shoemaker, *Neutrino Portal Dark Matter: From Dwarf Galaxies to IceCube*, [1411.1071](#).
- [298] J. Kopp, J. Liu and X.-P. Wang, *Boosted Dark Matter in IceCube and at the Galactic Center*, *JHEP* **04** (2015) 105, [[1503.02669](#)].
- [299] K. Murase, R. Laha, S. Ando and M. Ahlers, *Testing the Dark Matter Scenario for PeV Neutrinos Observed in IceCube*, *Phys. Rev. Lett.* **115** (2015) 071301, [[1503.04663](#)].

- [300] A. Esmaili and P. D. Serpico, *Gamma-ray bounds from EAS detectors and heavy decaying dark matter constraints*, *JCAP* **1510** (2015) 014, [[1505.06486](#)].
- [301] L. A. Anchordoqui, V. Barger, H. Goldberg, X. Huang, D. Marfatia, L. H. M. da Silva et al., *IceCube neutrinos, decaying dark matter, and the Hubble constant*, *Phys. Rev.* **D92** (2015) 061301, [[1506.08788](#)].
- [302] S. M. Boucenna, M. Chianese, G. Mangano, G. Miele, S. Morisi, O. Pisanti et al., *Decaying Leptophilic Dark Matter at IceCube*, *JCAP* **1512** (2015) 055, [[1507.01000](#)].
- [303] P. Ko and Y. Tang, *IceCube Events from Heavy DM decays through the Right-handed Neutrino Portal*, *Phys. Lett.* **B751** (2015) 81–88, [[1508.02500](#)].
- [304] M. Chianese, G. Miele, S. Morisi and E. Vitagliano, *Low energy IceCube data and a possible Dark Matter related excess*, *Phys. Lett.* **B757** (2016) 251–256, [[1601.02934](#)].
- [305] P. S. B. Dev, D. Kazanas, R. N. Mohapatra, V. L. Teplitz and Y. Zhang, *Heavy right-handed neutrino dark matter and PeV neutrinos at IceCube*, *JCAP* **1608** (2016) 034, [[1606.04517](#)].
- [306] M. Chianese and A. Merle, *A Consistent Theory of Decaying Dark Matter Connecting IceCube to the Sesame Street*, [1607.05283](#).
- [307] V. Barger and W.-Y. Keung, *Superheavy Particle Origin of IceCube PeV Neutrino Events*, *Phys. Lett.* **B727** (2013) 190–193, [[1305.6907](#)].
- [308] A. N. Akay, U. Kaya and S. Sultansoy, *Color octet neutrino as the source of the IceCube PeV energy neutrino events*, [1402.1681](#).
- [309] I. Alikhanov, *The Glashow resonance in neutrino–photon scattering*, *Phys. Lett.* **B741** (2015) 295–300, [[1402.6678](#)].
- [310] K. Ioka and K. Murase, *IceCube PeV–EeV neutrinos and secret interactions of neutrinos*, *PTEP* **2014** (2014) 061E01, [[1404.2279](#)].
- [311] J. Zavala, *Galactic PeV neutrinos from dark matter annihilation*, *Phys. Rev.* **D89** (2014) 123516, [[1404.2932](#)].
- [312] M. Ibe and K. Kaneta, *Cosmic neutrino background absorption line in the neutrino spectrum at IceCube*, *Phys. Rev.* **D90** (2014) 053011, [[1407.2848](#)].

- [313] T. Araki, F. Kaneko, Y. Konishi, T. Ota, J. Sato and T. Shimomura, *Cosmic neutrino spectrum and the muon anomalous magnetic moment in the gauged $L_\mu - L_\tau$ model*, *Phys. Rev.* **D91** (2015) 037301, [[1409.4180](#)].
- [314] A. N. Akay, O. Cakir, Y. O. Gunaydin, U. Kaya, M. Sahin and S. Sultansoy, *New IceCube data and color octet neutrino interpretation of the PeV energy events*, *Int. J. Mod. Phys.* **A30** (2015) 1550163, [[1409.5896](#)].
- [315] E. Aeikens, H. PÄd's, S. Pakvasa and P. Sicking, *Flavor ratios of extragalactic neutrinos and neutrino shortcuts in extra dimensions*, *JCAP* **1510** (2015) 005, [[1410.0408](#)].
- [316] J. I. Illana, M. Masip and D. Meloni, *A new physics interpretation of the IceCube data*, *Astropart. Phys.* **65** (2015) 64–68, [[1410.3208](#)].
- [317] C. S. Fong, H. Minakata, B. Panes and R. Zukanovich Funchal, *Possible Interpretations of IceCube High-Energy Neutrino Events*, *JHEP* **02** (2015) 189, [[1411.5318](#)].
- [318] F. W. Stecker, S. T. Scully, S. Liberati and D. Mattingly, *Searching for Traces of Planck-Scale Physics with High Energy Neutrinos*, *Phys. Rev.* **D91** (2015) 045009, [[1411.5889](#)].
- [319] A. DiFranzo and D. Hooper, *Searching for MeV-Scale Gauge Bosons with IceCube*, *Phys. Rev.* **D92** (2015) 095007, [[1507.03015](#)].
- [320] G. Tomar, S. Mohanty and S. Pakvasa, *Lorentz Invariance Violation and IceCube Neutrino Events*, *JHEP* **11** (2015) 022, [[1507.03193](#)].
- [321] P. Di Bari, P. O. Ludl and S. Palomares-Ruiz, *Unifying leptogenesis, dark matter and high-energy neutrinos with right-handed neutrino mixing via Higgs portal*, [1606.06238](#).
- [322] U. K. Dey, S. Mohanty and G. Tomar, *Leptoquarks: 750 GeV Diphoton Resonance and IceCube Events*, [1606.07903](#).
- [323] P. S. B. Dev, D. K. Ghosh and W. Rodejohann, *R-parity Violating Supersymmetry at IceCube*, *Phys. Lett.* **B762** (2016) 116–123, [[1605.09743](#)].
- [324] E. Fermi, *On the Origin of the Cosmic Radiation*, *Phys. Rev.* **75** (1949) 1169–1174.

- [325] T. Kashti and E. Waxman, *Astrophysical Neutrinos: Flavor Ratios Depend on Energy*, *Physical Review Letters* **95** (Oct., 2005) 181101, [[astro-ph/0507599](#)].
- [326] F. Halzen, “Particle physics beyond laboratory energies.” Phenomenology 2016 Symposium, University of Pittsburgh, USA, 2016.
- [327] P. Padovani and E. Resconi, *Are both BL Lacs and pulsar wind nebulae the astrophysical counterparts of IceCube neutrino events?*, *Mon. Not. Roy. Astron. Soc.* **443** (2014) 474–484, [[1406.0376](#)].
- [328] M. Ahlers and F. Halzen, *Pinpointing Extragalactic Neutrino Sources in Light of Recent IceCube Observations*, *Phys. Rev.* **D90** (2014) 043005, [[1406.2160](#)].
- [329] Y. Bai, A. J. Barger, V. Barger, R. Lu, A. D. Peterson and J. Salvado, *Neutrino Lighthouse at Sagittarius A**, *Phys. Rev.* **D90** (2014) 063012, [[1407.2243](#)].
- [330] R. Moharana and S. Razzaque, *Angular correlation of cosmic neutrinos with ultrahigh-energy cosmic rays and implications for their sources*, *JCAP* **1508** (2015) 014, [[1501.05158](#)].
- [331] K. Emig, C. Lunardini and R. Windhorst, *Do high energy astrophysical neutrinos trace star formation?*, *JCAP* **1512** (2015) 029, [[1507.05711](#)].
- [332] ICECUBE, VERITAS collaboration, M. Santander, *Searching for TeV gamma-ray emission associated with IceCube high-energy neutrinos using VERITAS*, *PoS ICRC2015* (2016) 785, [[1509.00517](#)].
- [333] A. Neronov and D. V. Semikoz, *Evidence the Galactic contribution to the IceCube astrophysical neutrino flux*, *Astropart. Phys.* **75** (2016) 60–63, [[1509.03522](#)].
- [334] L. S. Miranda, A. R. de LeÅşn and S. Sahu, *Blazar origin of some IceCube events*, *Eur. Phys. J.* **C76** (2016) 402, [[1510.00048](#)].
- [335] ICECUBE, PIERRE AUGER, TELESCOPE ARRAY collaboration, M. G. Aartsen et al., *Search for correlations between the arrival directions of IceCube neutrino events and ultrahigh-energy cosmic rays detected by the Pierre Auger Observatory and the Telescope Array*, *JCAP* **1601** (2016) 037, [[1511.09408](#)].
- [336] A. Neronov and D. Semikoz, *Galactic and extragalactic contributions to the astrophysical muon neutrino signal*, *Phys. Rev.* **D93** (2016) 123002, [[1603.06733](#)].

- [337] L. A. Anchordoqui, M. M. Block, L. Durand, P. Ha, J. F. Soriano and T. J. Weiler, *Evidence for a break in the spectrum of astrophysical neutrinos*, [1611.07905](#).
- [338] ICECUBE collaboration, M. G. Aartsen et al., *Atmospheric and astrophysical neutrinos above 1 TeV interacting in IceCube*, *Phys. Rev.* **D91** (2015) 022001, [[1410.1749](#)].
- [339] M. Chianese, G. Miele and S. Morisi, *Dark Matter interpretation of low energy IceCube MESE excess*, [1610.04612](#).
- [340] E. Waxman and J. N. Bahcall, *High-energy neutrinos from astrophysical sources: An Upper bound*, *Phys. Rev.* **D59** (1999) 023002, [[hep-ph/9807282](#)].
- [341] J. N. Bahcall and E. Waxman, *High-energy astrophysical neutrinos: The Upper bound is robust*, *Phys. Rev.* **D64** (2001) 023002, [[hep-ph/9902383](#)].
- [342] S. M. Boucenna, M. Chianese, G. Mangano, G. Miele, S. Morisi, O. Pisanti et al., *Decaying Leptophilic Dark Matter at IceCube*, *JCAP* **1512** (2015) 055, [[1507.01000](#)].
- [343] K. Harigaya, M. Kawasaki, K. Mukaida and M. Yamada, *Dark Matter Production in Late Time Reheating*, *Phys. Rev.* **D89** (2014) 083532, [[1402.2846](#)].
- [344] Y. Kurata and N. Maekawa, *Averaged Number of the Lightest Supersymmetric Particles in Decay of Superheavy Particle with Long Lifetime*, *Prog. Theor. Phys.* **127** (2012) 657–664, [[1201.3696](#)].
- [345] R. Allahverdi and M. Drees, *Production of massive stable particles in inflaton decay*, *Phys. Rev. Lett.* **89** (2002) 091302, [[hep-ph/0203118](#)].
- [346] R. Allahverdi and M. Drees, *Thermalization after inflation and production of massive stable particles*, *Phys. Rev.* **D66** (2002) 063513, [[hep-ph/0205246](#)].
- [347] K. Agashe, Y. Cui, L. Necib and J. Thaler, *(In)direct Detection of Boosted Dark Matter*, *JCAP* **1410** (2014) 062, [[1405.7370](#)].
- [348] J. Berger, Y. Cui and Y. Zhao, *Detecting Boosted Dark Matter from the Sun with Large Volume Neutrino Detectors*, *JCAP* **1502** (2015) 005, [[1410.2246](#)].
- [349] K. Kong, G. Mohlabeng and J.-C. Park, *Boosted dark matter signals uplifted with self-interaction*, *Phys. Lett.* **B743** (2015) 256–266, [[1411.6632](#)].
- [350] H. Alhazmi, K. Kong, G. Mohlabeng and J.-C. Park, *Boosted Dark Matter at the Deep Underground Neutrino Experiment*, [1611.09866](#).

- [351] ICECUBE collaboration, M. G. Aartsen et al., *Observation and Characterization of a Cosmic Muon Neutrino Flux from the Northern Hemisphere using six years of IceCube data*, [1607.08006](#).
- [352] FERMI-LAT collaboration, M. Ajello et al., *Fermi-LAT Observations of High-Energy γ -Ray Emission Toward the Galactic Center*, *Astrophys. J.* **819** (2016) 44, [[1511.02938](#)].
- [353] FERMI-LAT collaboration, M. Ackermann et al., *The spectrum of isotropic diffuse gamma-ray emission between 100 MeV and 820 GeV*, *Astrophys. J.* **799** (2015) 86, [[1410.3696](#)].
- [354] KASCADE-GRANDE collaboration, Z. Feng, D. Kang and A. Haungs, *Limits on the isotropic diffuse γ -rays at ultra high energies measured with KASCADE*, *PoS ICRC2015* (2016) 823.
- [355] AGRAPES-3 collaboration, S. K. Gupta et al., *The current status of the GRAPES-3 extensive air shower experiment*, *Nucl. Phys. Proc. Suppl.* **196** (2009) 153–158.
- [356] M. Ahlers and K. Murase, *Probing the Galactic Origin of the IceCube Excess with Gamma-Rays*, *Phys. Rev.* **D90** (2014) 023010, [[1309.4077](#)].
- [357] T. Cohen, K. Murase, N. L. Rodd, B. R. Safdi and Y. Soreq, *Gamma-ray Constraints on Decaying Dark Matter and Implications for IceCube*, [1612.05638](#).
- [358] E. Izaguirre, G. Krnjaic and B. Shuve, *The Galactic Center Excess from the Bottom Up*, *Phys. Rev.* **D90** (2014) 055002, [[1404.2018](#)].
- [359] G. D’Ambrosio, G. F. Giudice, G. Isidori and A. Strumia, *Minimal flavor violation: An Effective field theory approach*, *Nucl. Phys.* **B645** (2002) 155–187, [[hep-ph/0207036](#)].
- [360] F. Kahlhoefer, K. Schmidt-Hoberg, T. Schwetz and S. Vogl, *Implications of unitarity and gauge invariance for simplified dark matter models*, *JHEP* **02** (2016) 016, [[1510.02110](#)].
- [361] M. R. Buckley, D. Feld and D. Goncalves, *Scalar Simplified Models for Dark Matter*, *Phys. Rev.* **D91** (2015) 015017, [[1410.6497](#)].
- [362] M. Chala, F. Kahlhoefer, M. McCullough, G. Nardini and K. Schmidt-Hoberg, *Constraining Dark Sectors with Monojets and Dijets*, *JHEP* **07** (2015) 089, [[1503.05916](#)].

- [363] ATLAS collaboration, T. A. collaboration, *Search for New Phenomena in Dijet Events with the ATLAS Detector at $\sqrt{s}=13$ TeV with 2015 and 2016 data*, .
- [364] M. Cirelli, G. Corcella, A. Hektor, G. Hutsi, M. Kadastik, P. Panci et al., *PPPC 4 DM ID: A Poor Particle Physicist Cookbook for Dark Matter Indirect Detection*, *JCAP* **1103** (2011) 051, [[1012.4515](#)].
- [365] M. Cirelli, E. Moulin, P. Panci, P. D. Serpico and A. Viana, *Gamma ray constraints on Decaying Dark Matter*, *Phys. Rev.* **D86** (2012) 083506, [[1205.5283](#)].
- [366] J. F. Navarro, C. S. Frenk and S. D. M. White, *The Structure of cold dark matter halos*, *Astrophys. J.* **462** (1996) 563–575, [[astro-ph/9508025](#)].
- [367] A. Belyaev, N. D. Christensen and A. Pukhov, *CalcHEP 3.4 for collider physics within and beyond the Standard Model*, *Comput. Phys. Commun.* **184** (2013) 1729–1769, [[1207.6082](#)].
- [368] PLANCK collaboration, P. A. R. Ade et al., *Planck 2013 results. XVI. Cosmological parameters*, *Astron. Astrophys.* **571** (2014) A16, [[1303.5076](#)].
- [369] O. Mena, S. Palomares-Ruiz and A. C. Vincent, *Flavor Composition of the High-Energy Neutrino Events in IceCube*, *Phys. Rev. Lett.* **113** (2014) 091103, [[1404.0017](#)].
- [370] T. Sjostrand, S. Mrenna and P. Z. Skands, *A Brief Introduction to PYTHIA 8.1*, *Comput. Phys. Commun.* **178** (2008) 852–867, [[0710.3820](#)].
- [371] A. Cooper-Sarkar, P. Mertsch and S. Sarkar, *The high energy neutrino cross-section in the Standard Model and its uncertainty*, *JHEP* **08** (2011) 042, [[1106.3723](#)].
- [372] M. D. Kistler and R. Laha, *Multi-PeV Signals from a New Astrophysical Neutrino Flux Beyond the Glashow Resonance*, [1605.08781](#).
- [373] A. Ishihara and I. Collaboration, *Extremely high energy neutrinos in six years of icecube data*, *Journal of Physics: Conference Series* **718** (2016) 062027.